Doctoral Dissertation
Doctoral Program in Electrical, Electronics and Communications Engineering
(36th Cycle)

Study on Modeling and Efficient Algorithms for Geomagnetic Induction in AC Transmission Grids and Gas Pipeline Networks

A dissertation submitted to Politecnico di Torino and Xi'an Jiaotong University in partial fulfillment of the requirements for the degree of Doctor of Philosophy

Minzhou Liu

* * * * * *

Supervisors
Prof. Igor Simone Stievano and Prof. Yanzhao Xie, Supervisors
Prof. Flavio Canavero and Prof. Riccardo Trinchero, Co-Supervisors

Doctoral Examination Committee:
Prof. Shengchang Ji, Xi'an Jiaotong University (Chairman)
Prof. Yunqing Pei, Xi'an Jiaotong University
Prof. Bingqiang Li, Northwestern Polytechnical University
Prof. Bing Wei, Xidian University
Prof. Jun Guo, Xi'an Jiaotong University
Prof. Flavia Grassi, Politecnico di Milano
Prof. Paolo Manfredi, Politecnico di Torino

Politecnico di Torino
2024

I hereby declare that, the contents and organisation of this dissertation constitute my own original work and does not compromise in any way the rights of third parties, including those relating to the security of personal data.

…………………………………....

Minzhou Liu
2024

ABSTRACT

Geomagnetic disturbances (GMDs) are wide-area natural hazards caused by solar activity, which induce low-frequency geoelectric fields on the earth's surface. The resulting geomagnetically induced currents (GICs) in the power grid can lead to the half-wave saturation of transformer, and the pipe-to-soil potential may interfere with the cathodic protection system, which may pose a potential threat to the reliable operation of large-scale AC transmission grids and gas pipeline networks. Therefore, understanding the induced voltage and current levels in the energy system due to extreme GMDs is of great significance for further assessment and mitigation of geomagnetic hazards. The increasingly interconnected and coupled transmission grids and gas pipeline networks are subject to complex spatially distributed geoelectric fields, which requires more efficient and generalized geomagnetic induction models. In this respect, this dissertation studies the wide-area spatiotemporal distribution characteristics of the geoelectric fields, proposes several reduced geomagnetic induction models for power grids and pipeline networks, and further establishes a comprehensive induction model that considering the coupling between these two networks.

First, the evaluation scenarios of the geoelectric fields induced by extreme GMD are constructed for the geomagnetic induction analysis of energy networks, considering the intensity of geomagnetic activity and the distribution of three-dimensional earth conductivity. Typical scenarios such as 100-year, 200-year and 10,000-year events are constructed for extreme geomagnetic variations, by combining the extreme value statistical method with the theoretical upper limit of the disturbance storm time index. Then, a Bayesian inversion method for horizontally layered earth structure is proposed, which can quantify the impact of measurement noise and shielding effects on the estimation performance from a statistical perspective. In addition, the nonuniform wide-area geoelectric fields on the earth's surface are calculated considering complex earth resistivity distribution such as the coast.

Then, this study proposes a model reduction method for GIC calculation in lumped parameter circuits of the power grids. A reduced nodal admittance matrix method is proposed for GIC calculation in power grids based on Kron reduction, which reduces the size of GIC model while retaining the positive definiteness and sparsity of the design matrix. Moreover, the impact of transformer reactive power loss caused by GIC on the voltage security of the power system is

---

*This work is supported by National Key R&D Program of China (2016YFC0800100).

evaluated. A compressed surrogate computational model for multiple AC voltages is established based on the generalized polynomial chaos expansion method and principal component analysis, which can speed up the uncertainty quantification of AC voltages in bulk transmission systems during GMD compared to traditional Monte Carlo method.

Furthermore, this study proposes a reduced method for the distributed parameter circuit of buried pipelines. A modified equivalent pi-circuit model for pipelines excited by nonuniform geoelectric field is derived based on transmission line theory, which can efficiently solve the geomagnetic induction in large-scale interconnected pipeline networks in the cases of nonuniform geomagnetic source field and complex earth conductivity distribution. Furthermore, the proposed equivalent circuit can be used to efficiently evaluate the nonlinear polarization effects of coating breakdown. The proposed equivalent circuit is then extended to the calculation of other types of electromagnetic interference on buried pipelines, such as the conductive interference caused by the HVDC earth return currents.

Finally, this study proposes a novel geomagnetic induction calculation model that considers the coupling between the AC transmission system and the pipeline network. The substation grounding currents may interact with the leakage currents from nearby buried pipelines through the earth during GMD, which is not fully considered in classical geomagnetic induction studies. Hence, a more comprehensive nodal voltage analysis is conducted to evaluate the geomagnetic induction in integrated systems, where the conductive coupling between grounded nodes is characterized by ground transfer resistances. The results of several test cases indicate the need to account for the coupling between the substation grounding grid and the buried pipeline in order to predict the distribution of the geomagnetic response accurately.

In summary, in this research activity, more generalized modeling methods are developed for the geomagnetic induction in transmission grids, gas pipeline networks and their integrated systems, by considering the influence of nonuniform geoelectric fields, uncertain input parameters, nonlinear components, and conductive coupling. And the proposed algorithms enable more rigorous evaluation of the response in energy networks and are promising for online applications, which lays the foundation for further GMD risk assessment and mitigation.

KEY WORDS: Geomagnetic disturbances; Geomagnetically induced currents; Pipe-to-soil potentials; Integrated power-gas systems; Model reduction; Uncertainty quantification

TYPE OF DISSERTATION: Application Fundamentals

CONTENTS

List of Figures

List of Tables

Glossary

ρ^{c}	The calculated apparent resistivity
ρ^{m}	The measured apparent resistivity
$\pi_{\mathrm{post}}(\cdot)$	The posterior probability density function
$\pi_{\mathrm{prior}}(\cdot)$	The prior probability density function
AIES	Affine Invariant Ensemble Sampler
$\mathbf{B}$	The geomagnetic fields
B_{H}	The horizontal geomagnetic fields
B_x, B_y	The northward and eastward geomagnetic fields
BAM	Bus Admittance Matrix
BMT	Beijing Ming Tombs
CDF	Cumulative Distribution Function
Dst	Disturbance storm time
DSTL	Distributed Source Transmission Line
$\mathbf{E}$	The geoelectric fields
$\mathbb{E}[\cdot]$	The expectation value
E^{con}	The tangential electric field due to conductive EMI
E^{ind}	The tangential electric field induced by the external source current
E_{t}	The tangential geoelectric fields
E_x, E_y	The northward and eastward geoelectric fields
EHV	Extra-High Voltage
EMI	ElectroMagnetic Interference
EVA	Extreme Value Analysis
f	The computational forward model
FFT	Fast Fourier Transform
$\mathbf{G}$	The ground transfer conductance matrix
GIC	Geomagnetically Induced Currents
GMD	Geomagnetic Disturbances
GPD	Generalized Pareto Distribution
HAD	Hartland

$\mathbf{I}$	The geomagnetically induced currents
I^{bd}	The leakage current of coating breakdown node
$\mathbf{I}^{\mathrm{eff}}$	The transformer effective GIC
$\mathbf{I}^{\mathrm{p}}$	The earthing currents from pipe nodes
$\mathbf{I}^{\mathrm{s}}$	The substation grounding GIC
$\mathbf{I}^{\mathrm{tl}}$	The GIC in power transmission lines
IFFT	Inverse Fast Fourier Transform
IPGS	Integrated Power-Gas Systems
$\mathbf{J}$	The nodal current injections
$\mathbf{J}_{\mathrm{b}}, \mathbf{J}_{\mathrm{p}}, \mathbf{J}_{\mathrm{s}}$	The nodal current injections at bus nodes, pipe nodes and substation grounding grid nodes
$\mathbf{K}$	The magnetotelluric transfer function
L	The likelihood function
LP	Lehtinen-Pirjola
MAP	Maximum A Posteriori
MC	Monte Carlo
MCMC	Markov Chain Monte Carlo
$N_{\mathrm{b}}, N_{\mathrm{p}}, N_{\mathrm{s}}$	The sets of the bus nodes, pipe nodes and substation grounding grid nodes
$n_{\mathrm{b}}, n_{\mathrm{p}}, n_{\mathrm{s}}$	Number of the bus nodes, pipe nodes and substation grounding grid nodes
NAM	Nodal Admittance Matrix
NUR	Nurmijärvi
P	The active power
PCA	Principal Component Analysis
PCE	Polynomial Chaos Expansions
PDF	Probability Density Function
PSP	Pipe-to-Soil Potentials
Q	The reactive injections
Q^{loss}	The reactive power loss of transformer caused by GIC
$\mathbf{R}$	The ground transfer resistance matrix

RNAM	Reduced Nodal Admittance Matrix
$U(\cdot,\cdot)$	The uniform distribution PDF
UHV	Ultra-High Voltage
$\mathbf{V}$	The nodal DC voltages
$\mathbf{V}^{\mathrm{ac}}$	The nodal AC voltages
V^{exc}	The excitation voltage
V^{pol}	The polarization voltage
V^{sca}	The scattered voltage
$\mathbf{V}_{\mathrm{b}}, \mathbf{V}_{\mathrm{p}}, \mathbf{V}_{\mathrm{s}}$	The nodal DC voltages of bus nodes, pipe nodes and substation grounding grid nodes
$\mathbf{x}$	The input vector
$\mathbf{Y}$	The nodal admittance matrix
$\mathbf{y}$	The output vector
Y, Z	The parallel admittance and series impedance of pipeline
Z_{C}, γ	The characteristic impedance and propagation constant of pipeline

1 Introduction

1.1 Research Background and Significance

Geomagnetic disturbance (GMD) is a small-probability, but high-impact global natural hazard caused by solar activities such as coronal mass ejections. According to Faraday's law of electromagnetic induction, the changing magnetic field induces low-frequency (0.1 mHz–0.1 Hz) geoelectric fields on the earth's surface, which drives geomagnetically induced currents (GICs) in the energy systems[1, 2]. GMD may pose a threat to the reliability of the ground-based wide-area energy networks, including AC transmission grids and gas pipeline networks[3-8]. Figure 1-1 shows the mechanism of GMDs and the process of their impact on the energy system.

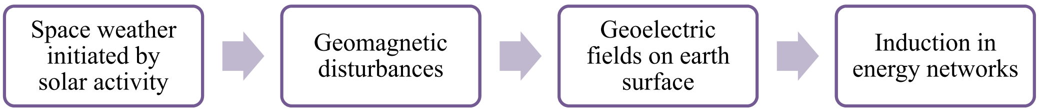

Figure 1-1 Schematic diagram of the process from the origin of GMD to its ultimate impact on the energy system.

GICs in power grids give rise to half-cycle saturation of the transformers, causing hot spot heating[9, 10], increased reactive power loss[11-15] and harmonics injection[16], which may pose a threat to the reliability of the electrical equipment and the power grid. One of the most serious accident resulted from the GMD on power systems occurred in March 1989, which caused the burning of a transformer in the Québec power grid in Canada and a power outage for 9 hours[17]. During strong GMD, the intensity of geomagnetic variations is related to geomagnetic latitude. Generally, the magnitude of geomagnetic variations is greater in high latitudes. Recent studies have found that power grids in low-latitude and middle-latitude regions, such as China[18], South Africa[19], Spain[20], and New Zealand[21], may also be severely interfered by GIC, due to the characteristics of the power grid and the earth resistivity structure. For instance, during the GMD event from November 7 to 9, 2004, the peak value of the neutral GIC measured at the main transformer of Ling'ao substation in China reached 75.5 A[18].

The resulting pipe-to-soil potentials (PSP) and GIC in the pipeline network may accelerate the corrosion of the pipeline, interfere with the cathodic protection system and other electrical equipment along the pipeline, which may have the potential to reduce the service life and even affect the operational safety of the pipeline[22-27]. Hence, calculation of the geomagnetic induction in the pipeline is of great significance for evaluating the impacts of geomagnetic storms and identifying vulnerable pipes for protection.

Modern power and pipeline networks are expanding in size and transmission distance, making them more vulnerable to GMD. In ultra-high voltage and extra-high voltage AC transmission systems, the resistances of transmission lines and transformer windings are generally small in order to reduce losses. As a result, larger GIC levels will occur during GMD. The metal tubes of natural gas pipelines are usually insulated from the soil with the coating to prevent corrosion. Modern coatings with improved quality have large resistivities, which may result in larger induced voltages during GMD.

In recent years, the assessment and mitigation of the GMD impacts on ground-based infrastructure has received widespread attention from the fields of space physics, geophysics, and energy engineering. In 2019, the US National Science and Technology Council released the "National Space Weather Strategy and Action Plan", which requires the establishment of reference space weather events, improving the modeling of its impact on critical infrastructure and improving corresponding protection capabilities[28]. In 2021, the UK Department for Business, Energy & Industrial Strategy released the "UK Severe Space Weather Preparedness Strategy", which requires improving the prediction of space weather events and assessing their effects on the infrastructures[29]. In the European Risk from Geomagnetically Induced Currents (EURISGIC) project carried out from 2011 to 2014, the piecewise uniform one-dimensional layered earth models were established for Europe, which were used to evaluate the GIC levels in the European interconnected power grid[30]. Engineering standards related to the impact of GMD on the power grid are being formulated and revised. In 2015, an IEEE standard for transformer capacity evaluation during GMD was developed to evaluate the operating status of transformers under different levels of load and GIC[31]. In 2020, the North American Electric Reliability Corporation developed the TPL-007 standard, which constructs the benchmark and supplementary 100-year GMD events in North America for long-term planning of the power system[32].

According to the generation mechanism of geomagnetic induction, the modeling of induced currents and voltages in the energy systems can be divided into two relatively independent steps, namely the "geophysical step" and the "engineering step", which are the calculation of the induced electric field and the calculation of induction in the energy networks, respectively[33].

1. In the geophysical step, the induced geoelectric field on the surface is calculated using the space current source model or the magnetic field data recorded by the geomagnetic observatories, combined with the earth conductivity model;
2. In the engineering step, the geoelectric field can be modelled as a DC voltage source

superimposed on the transmission line, thus the GIC in each branch of the network can be calculated through the circuit analysis. For quasi-DC geoelectric field excitation, the power grid and pipeline network are modeled as circuit systems with lumped and distributed parameters, respectively. It depends on their different grounding characteristics: the power grid is discretely grounded through the substation grounding grid, while the pipeline is distributed grounded through the leakage resistance of the coating.

Therefore, the modeling and calculation of geomagnetic induction in large-scale power networks and pipeline networks under extreme GMD scenarios is of great importance, which lays the foundation for further GMD risk assessment and mitigation. On the one hand, it is necessary to construct more reasonable worst-case GMD input scenarios and calculate the corresponding non-uniform distribution of the geoelectric field in a wide area. On the other hand, more general and efficient induction models for energy networks are required. In order to rigorously and comprehensively assess the level of geomagnetic induction in energy networks, it is necessary to consider the influences of non-uniform electric fields, random parameters and nonlinear elements.

1.2 State of the Art of the Research

1.2.1 Existing Study About Modeling Electromagnetic Environments in Extreme GMD Scenarios

It is of great significance to construct typical extreme GMD scenarios to provide guidance for risk assessment of energy systems in engineering practice. Digital geomagnetic data with sampling period of 1-minute or even smaller have been collected for decades worldwide. However, it is usually necessary to consider more serious GMD scenarios for risk assessment. The extreme value analysis (EVA) is widely adopted for generating the 100-year and 200-year GMD events for North America and Europe, etc. Pulkkinen et al. estimated the 100-year return level of the induced geoelectric field using one-dimensional layered earth models based on the assumption of a lognormal distribution[34]. Thomson et al. estimated the 100-year and 200-year return levels of geomagnetic field variations and their rate-of-change using the geomagnetic observations in Europe based on extreme value statistical theory[35]. However, these classical events are not sufficient for safety-critical nodes such as the ultra-high voltage (UHV)/extra-high voltage (EHV) substations and nuclear power plants. In recent years, the 10,000-year GMD event has been concerned by researchers and adopted by engineering standards[36, 37].

Earth resistivity structure is the basis for calculating substation grounding parameters, which is important for ensuring the safety of electrical equipment and operating personnel[38, 39]. The grounding parameters of high-voltage substations depend on the soil resistivity at depths of hundreds of meters, which usually presents a layered structure. In addition, the soil resistivity model also plays a key role in evaluating the electromagnetic interference on the power systems from HVDC earth return currents[40] and geomagnetic disturbances, etc. The electrical sounding method is widely employed to interpret the layered earth, including the resistivity and thickness of each layer. A reasonable soil structure can be inverted by fitting the measured apparent resistivity data. The parameter estimation of a layered structure is usually modeled as a single-objective, multi-parameter, nonlinear optimization problem.

The optimization algorithms for earth inversion can be divided into two categories. The first category is the traditional non-heuristic optimization algorithms, e.g. Newton method[41], quasi-Newton method[42], Levenberg-Marquardt algorithm[43-45], etc. It is computationally efficient, but usually requires the derivative of the objective function. Moreover, it depends on the selection of the initial guess for iterations, which tends to trap in local optima especially for the multilayer structures. Alamo compared the performance of eight non-heuristic optimization methods for the inversion of a two-layer earth[46]. The other category is the heuristic optimization algorithms, e.g. genetic algorithm[47-49], particle swarm optimization[50], differential evolution algorithm[51, 52], simulated annealing algorithm[53] and artificial bee colony algorithm[54], etc. It is more capable of searching the global optimum, but it requires larger computational cost. Several literature further adopted hybrid heuristic algorithms to improve the inversion performance[55-57].

However, the accuracy of optimization methods for soil parameter estimation is challenged by several limitations. The soil parameters obtained by optimization algorithms are usually deterministic without providing their uncertainties. In practice, the observation of apparent resistivity is affected by measurement inaccuracy and local resistivity variation, thus reducing the estimation accuracy. For instance, according to the results in Reference [45, 56], different optimization methods achieve close root mean square errors, but the estimated results in some layers are quite different. Reference [44, 58] tried to calculate the confidence interval of the estimated soil parameter on the basis of linear approximation of the computational model, which may lead to additional errors. Moreover, it is mainly applicable to traditional gradient-based optimization algorithms. Moreover, the inversion of some special soil structures may be ill-conditioned. For example, if a layer with high resistivity or large thickness exists in the earth structure, it may have a certain shielding effect on other layers[57]. The estimated results of the optimization technique may deviate greatly from the actual parameters[57], even regardless of the measurement error.

The induced geoelectric field on the ground surface is usually spatially nonuniform, which is affected by the distribution of both the geomagnetic variation and the earth conductivity. For some types of GMD, such as auroral electrojet in the ionosphere at high latitudes, the space current system as an external source is relatively complex, and the resulting spatial distribution of magnetic field disturbances is less uniform than that at low latitudes[59-61]. Another cause of nonuniform geoelectric field is the complex distribution of earth conductivity[62-67], especially the lateral variations in coasts, lakeshores, and geodetic fault zones, which may lead to a local geoelectric field increase near the interface[67-69]. Some previous studies on GIC measurements and simulations have shown that the nonuniform geoelectric field may greatly affect the induction results in the power grid[60, 62, 64, 65].

Pirjola and Boteler et al. proposed a method to calculate the surface electromagnetic field of uniform and layered earth under the excitation of infinite line and infinite surface space current model[70, 71]. Boteler summarized the evolution of Québec 1D layered earth model and compared the calculated induced geoelectric fields, which illustrates the importance of accurate earth conductivity models[72]. Zheng compared the effects of large and small source current models on surface wave impedance, and showed that the former is suitable for calculation of induced geoelectric fields in mid- and low-latitude areas[59]. The TPL-007 standard evaluated the 100-year peak geoelectric field in different regions of North America for transmission system planning, which is calculated based on the 1D layered earth model[32].

Karami et al. calculated the surface electromagnetic field at the coast generated by the auroral electrojet using a two-dimensional finite element model and compared it with the results of the complex image method[69]. Dong et al. calculated the geoelectric field considering the lateral change of earth conductivity based on the Galerkin method[73]. Wang et al. proposed a simplified calculation method based on the distributed source transmission line model to analyze the coast effect on the geoelectric fields, in which the sedimentary layer, crust layer and mantle layer of the earth are modeled as transmission lines[74].

In summary, it is necessary to construct reasonable worst-case scenarios of the electromagnetic environment during extreme GMD for the purpose of geomagnetic risk assessment of energy systems. Some safety-critical systems, such as ultra-high voltage substations and nuclear power plants, require more extreme GMD scenarios. However, traditional extreme value statistical theory may lead to overly conservative estimates, resulting in uneconomical and unnecessary protection costs. The induced geoelectric field relies on accurate earth conductivity input parameters, whereas the results of traditional optimization-based methods are non-unique and uncertain. In addition, the three-dimensional earth conductivity distribution may lead to great distortion of the surface electric field, which needs to be considered in the worst-case scenarios.

1.2.2 Existing Study About Geomagnetic Induction in Power Grids

GMDs initiated by the solar activity generate GICs in the bulk transmission networks, which may lead to adverse effects such as voltage collapse and transformer hot-spot heating[75, 76]. The assessment of GMD impacts on the AC transmission network includes two steps. First, the quasi-DC current induced by GMD is calculated using a DC model of the power grid, in which only the resistance parameters of the power transmission lines and transformers are considered. Then, the reactive power loss caused by the half-wave saturation of the transformer is incorporated into the AC power flow model of the power system to evaluate the AC voltage security.

Traditional GIC calculations typically rely on assumed deterministic DC parameters of electrical components in the power grid. These GIC results are used to evaluate the impacts on power system voltage stability and transformer temperature rise. Then real-time operation strategies, such as generation redispatch and load shedding, are developed for mitigating GIC effects. However, accurate DC parameters of power components are not easily obtained in engineering practice, which is different from standard AC parameters. The substation grounding resistance is a major source of uncertainty, since it is usually not included in the standard power flow data and varies with multiple factors such as soil moisture. For example, Blake et al. reported that the use of an assumed 0.5 Ω grounding resistance in the Irish power grid resulted in an underestimation of GIC amplitude by a factor of approximately 2.5[77]. This is because a rainfall before the geomagnetic storm event caused a greatly decrease in the substation grounding resistance. Thus, using assumed grounding resistance parameters may result in the calculated GIC amplitude and spatial distribution in the power grid being significantly different from the actual situation. In this way, the operational strategy developed may not be able to adapt to the actual GIC level. In this context, efficient probabilistic GIC analysis plays a key role in developing robust online operational mitigation schemes against uncertain GMD hazards.

The efficiency improvement of power grid GIC calculation has attracted much attention from several scholars in the fields of geophysics and power energy in recent years. The nodal admittance matrix (NAM) method[75] and the Lehtinen-Pirjola (LP) method[76] are derived on the basis of the full-node circuit model, i.e. all the substation grounding grids and buses are regarded as nodes, which results in a large-scale system of linear equations. Recently, Marsal et al.[78] proposed a bus admittance matrix (BAM) method for GIC model reduction, and the newly created matrix to be inverted is asymmetric. The LP method is the earliest proposed method for GIC calculation. It provides a compact form for solving substation grounding GIC without the need to solve for nodal voltages, thus the LP method is still widely adopted in the offline analysis of some small-scale power grids. However, the scale of modern power grid interconnection has expanded to include tens of thousands of nodes, thus higher requirements have been placed on the computational efficiency of GIC. Theoretically, both the NAM method and the BAM method have their own advantages. The NAM method has the advantage of a positive definite design matrix, and the BAM method has the advantage of a smaller design matrix. They will have different performance in computational efficiency under different simulation configurations. Under the simulation configuration of full matrix factorization, the calculation efficiency of forward and backward substitution mainly depends on the size of the factors of the design matrix. Hence, for some small-scale power systems, the calculation efficiency of BAM may be better than that of NAM method when using the full matrix decomposition. However, for large-scale grids with thousands of nodes, the full matrix decomposition is memory intensive and usually takes more time than sparse matrix decomposition.

Horton et al. established a Benchmark power grid case with multiple voltage levels, and provided the induced voltage and current results under uniform geoelectric fields, which can be used to verify different GIC algorithms[79]. Boteler proposed an equivalence method for GIC calculations of two-area interconnected power grids, and the results illustrate the need to preserve the induced voltage and resistance of the first power transmission line to the neighbor power system[80]. Boteler and Pirjola demonstrated the equivalence of the LP method and the NAM method, and discussed the modeling methods for transmission networks with multiple voltage levels[76]. Guo et al. compared the GICs in UHV power grids when considering and ignoring the EHV power grid, and the results showed that accurate GIC calculation requires not only the power grid with the highest voltage level, but also other power grids with lower voltage levels[81]. Overbye et al. quantified the sensitivity of the transformer effective GIC to the geoelectric field on each power line, and the results showed that it was mainly affected by the electric field on adjacent lines[75]. Kazerooni et al. validated the power grid GIC model by comparing the geoelectric field estimated from the measured GIC and from the measured magnetic field, and detected outliers in the measurements[82]. Klauber et al. estimated the multi-zone geoelectric fields from transformer neutral GIC measurements based on linear least squares method[11, 83].

In order to analyze the influence of GIC on the power system operation, many scholars have studied the transformer half-cycle saturation characteristics. Rezaei-Zare proposed a field-circuit coupled model for medium and low frequency transient simulation of transformer, considering the non-linearity and frequency-dependent parameters of the iron core and tank, etc[84]. The field-circuit coupled model simulates the flux path in iron core, which is helpful for analyzing the influence of magnetic circuit structure and magnetization characteristics on transformer reactive power loss. The field-circuit coupled model has the advantages of high accuracy, but it requires a large number of input parameters of transformer's structure and materials as well as complex simulation process[9, 10]. Bernabeu discussed the magnetizing current and harmonic characteristics of single-phase transformer under the influence of GMD[85]. Haddadi et al. established an electromagnetic transient simulation model for IEEE 118 power grid test case affected by induced geoelectric fields[86], and compared the accuracy of load-flow, transient stability type, and electromagnetic transient type methods[87].

The reactive loss of transformer changes linearly with GIC within a certain range and the proportionality coefficient between them is defined as K-value. Dong et al. first proposed K-value calculation method based on comparative study of the relationship between GIC and reactive loss of single-phase, three-phase shell-type, three-phase three-limb and three-phase five-limb transformers[88]. Overbye et al. improved the K-value calculation method by considering the influence of AC voltages on the reactive loss and evaluated their impact on the power system voltage stability via power flow analysis[89]. K-value method has the advantage of ease of implementation and is suitable for fast calculation of transformer reactive loss in a large-scale power grid.

In summary, efficient computational models are important for evaluating GIC and its impact on the voltage security of transmission systems, especially when dealing with a large numbers of random input parameters. In the DC model of the power grid, traditional power grid GIC analysis does not fully account for the influence of uncertainty in substation ground resistance parameters, which may lead to underestimation of the tail risk of GIC. In addition, the impact of GMD on the AC voltage of the power system in traditional studies is usually based on determined power system operating modes. However, the AC load in the power system also fluctuates during a GMD event. Therefore, it is important to quantify the uncertainty of GIC and AC voltages in the power grid during extreme GMD by comprehensively considering random inputs such as external geoelectric fields, substation ground resistances, and AC loads. It requires repeated calculations of DC and AC models of the power system, however, traditional methods are high-order and time-consuming.

1.2.3 Existing Study About EMI Calculation for Gas Pipeline Networks

For the pipeline induction analysis, the transmission line model is usually required to obtain the PSP and GIC along the pipeline, which is different from the lumped circuit model used for GIC calculation in the power grid[3, 90, 91]. The interconnection of pipelines forms a complex network, which requires efficient induction algorithms for large-scale network analysis. Boteler and Cookson first proposed the distributed source transmission line (DSTL) model for geomagnetic induction in pipeline in 1986[22]. Pulkkinen et al. adopted the equivalent Thevenin circuit model of the pipeline, and compared the induction results under different types of discontinuities such as the bends, junctions and branch points[23]. Boteler proposed the equivalent-pi circuit model of the pipeline under the uniform geoelectric field in 2013, which is more suitable for the induction calculation of large-scale pipeline networks[24]. However, few studies exist on the nonuniform geoelectric field induction in complex pipeline networks.

Yu et al. measured the stray current and PSP of pipelines during GMD, and the results showed that GMD can bring strong interference to buried pipelines at mid- and low-latitudes, which is worthy of further study[26]. Ingham et al. analyzed the changes in the output of the cathodic protection system on the New Zealand pipeline network during GMD[92, 93]. The results showed that the induction in the pipeline not only depends on the local electric field, but is also affected by the geoelectric field on the whole pipeline network. The authors highlighted that the disbonding of coating and hydrogen induced cracking may also occur in pipelines during GMD[93], in addition to the corrosion effects that are traditionally concerned. Trichtchenko et al. evaluated pipeline corrosion caused by telluric currents generated in GMD at different latitudes, and the results showed that some pipelines at low latitudes also face high corrosion risks caused by GMD[94].

For buried pipelines with distributed parameters, a complete distribution of induced voltages and currents along the pipeline is often required for corrosion assessment. Thus, it is more sensitive to the influence of local non-uniform electric fields, which is not fully considered in traditional modeling. Traditional modeling generally considers pipeline models to be linear. However, the insulation coating may break down with age in service. The nonlinear polarization effects occur where pipe steel and soil are in direct contact, which may affect the accuracy of PSP and GIC results along the pipeline.

In addition to GMD, the gas pipeline networks are subject to various low-frequency external electromagnetic interference (EMI). Especially nowadays, pipelines and other energy infrastructures are built in increasingly confined spaces, such as common corridors with power lines; thus the pipelines may be continuously exposed to strong EMI stresses. The resulting voltage and current responses may accelerate the corrosion of pipelines and interfere with cathodic protection devices, etc. Assessing their electromagnetic effects and deploying cost-effective mitigation measures have long been topics of interest in engineering practice. Rigorous evaluation of the electromagnetic response in the pipeline network is the first step to support these work.

Low-frequency EMI to pipelines can be electrically classified into three categories: capacitive, inductive and conductive[95, 96]. For buried pipelines, the capacitive coupling occurs only for pipelines exposed during installation or maintenance, and can generally be ignored during normal operation due to the shielding effect of the ground. Thus, this research mainly focuses on the latter two coupling mechanisms. The inductive coupling is caused by time-varying magnetic flux generated by external current sources, e.g., fundamental frequency AC and harmonic currents in nearby power lines[97-101], ionospheric source currents associated with geomagnetic activity[22-24, 102], etc. The conductive coupling is triggered by the soil potential rise due to ground fault currents from the power grid[103, 104], HVDC earth return currents[105-109], metro stray currents[110], etc. The external electromagnetic environment may have a wide footprint with spatially nonuniform distribution. For instance, the currents from HVDC electrodes can affect pipelines several kilometers away, and geomagnetic disturbances initiated by space weather can produce interference on even continental levels. Moreover, the affected pipeline networks to be evaluated are usually large-scale and multi-branch.

EMI coupling to buried pipelines can usually be analyzed by using the transmission line (TL) model with distributed parameters. Noteworthy here is that the arrangement of the excitation source is different in the circuits used for inductive and conductive coupling: the former is in the longitudinal branch, whereas the latter is in the transverse branch. Taflove et al.[97] proposed the TL model for the inductive coupling of pipelines resulting from nearby power lines. The model was subsequently extended by Boteler and Cookson[22] for geomagnetic induction in pipelines. Lagace et al.[105] proposed the TL model for the conductive interference caused by HVDC earth return currents. Analytical solutions for voltage and current responses can be acquired simply for a single pipeline, however, it is difficult for networks with complex topology. The nodal voltage analysis based on discretization of pipelines usually yields large-scale computational models. In contrast, the equivalence-based algorithms become a more efficient scheme.

Several equivalence methods have been developed specifically for inductive or conductive coupling to a pipeline. An equivalent Thevenin circuit is normally adopted for the single-port equivalence of a pipeline to analyze the inductive coupling due to AC power lines[97] and geomagnetic disturbances[23]. It usually starts from a pipe located at the edge of the network and is then performed sequentially according to the network topology. In addition, an equivalent-pi circuit was proposed for the two-port equivalence of the pipeline excited by external electric fields, and the analytical solutions of its parameters were derived in the cases of uniform[24] geoelectric field induced by geomagnetic disturbances. The two-port equivalence can be applied to each single-conductor pipeline individually without considering their interaction, which is more suitable for the large-scale networks. Some efforts have been made for the unified modeling of inductive and conductive coupling. Haubrich et al.[111] presented a universal two-port equivalent model for inductive and conductive interference through voltage and current transformations. However, it assumes that the electric field along each pipeline is constant.

Furthermore, the literature on pipeline equivalents mentioned above assume the linearity of all elements in the network while ignoring the nonlinear polarization of coating breakdown[112]. The results given by Li et al.[108, 109] show that the neglect of nonlinear polarization can result in rather conservative estimates of the responses for the analysis of HVDC earth return currents, which implies uneconomic mitigation measures.

In summary, there are some limitations in traditional methods for the calculation of geomagnetic induction in pipelines. The original distributed parameter circuit model is high-order for large-scale pipeline networks. The effect of nonuniform geoelectric fields on the geomagnetic induction of buried pipelines is not fully considered, which may result in an underestimate of the response for some segments for long-distance pipelines crossing complex geological areas. In addition, the nonlinear polarization effect occurring between the metal and soil at the damaged part of coating is not considered in GMD analysis. Finally, the traditional geomagnetic induction models are developed separately for the AC transmission system and gas pipeline network, without considering the coupling between the substation grounding grids and the buried pipelines. Therefore, there is a need to develop more general and efficient geomagnetic induction calculation models in order to accurately evaluate the geomagnetic response in pipelines.

1.3 Major Research Content and Organization of the Dissertation

The research objective is to investigate the voltage and current response of the power grids and gas pipeline networks to GMD hazards, as shown in the Figure 1-2. To achieve this goal, the accurate benchmark GMD scenarios are first required as input, and then several generalized and efficient models needs be developed to calculate the geomagnetic induction in energy systems, including the power grids, gas pipeline networks, and their integrated systems.

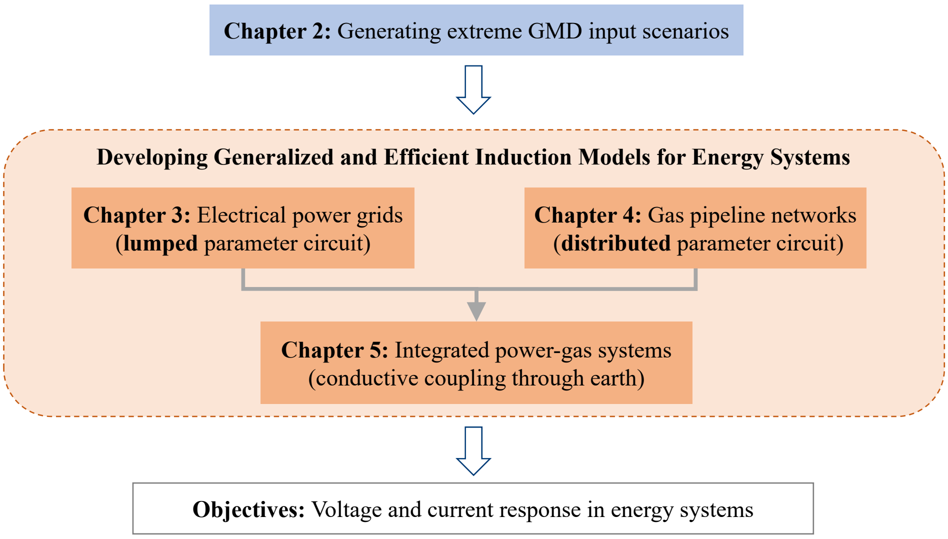

Figure 1-2 Main research content of the dissertation.

However, the accurate calculation is challenged by several gaps. Firstly, the observations of the geomagnetic field and earth parameters are limited. In addition, high-order induction models need be created for large-scale system, and the existing induction models are developed separately for power grids and pipeline networks. To address these problems, correspondingly, the statistical methods are adopted to generate more reasonable worst-case input scenarios. Then, several more efficient induction models are developed for the circuit system with lumped and distributed parameters. Finally, the interaction between the power grid and pipeline network is modeled in geomagnetic induction analysis.

In Chapter 2, more reasonable GMD input scenarios are constructed. The peak values of extreme geomagnetic variations are predicted by combining extreme value statistics and theoretical upper limit of Disturbance storm time (Dst) index. Then, a Bayesian inversion method is presented for the layered earth structure, which can provide more comprehensive statistical properties of the soil parameters, e.g. confidence intervals, correlation coefficients, marginal and joint probability distributions. Finally, the spatio-temporal distribution of the geoelectric field is calculated by considering the three-dimensional complex earth conductivity.

In Chapter 3, a novel reduced nodal admittance matrix (RNAM) method is proposed for the GIC model reduction of large-scale AC transmission grid based on Kron reduction. The proposed RNAM method has a smaller and positive-definite design matrix, which combines the advantages of both the BAM method and the NAM method. The novel method is compared with the classical algorithms including the NAM method, the LP method, and the BAM method, and its efficiency improvement is illustrated with several power grid test cases. Then, the GIC impacts on power system voltage stability is evaluated based on polynomial chaos expansions

(PCE), considering uncertain geoelectric fields, substation grounding resistances and AC loads. The sparse regression method is used to reduce the number of polynomial expansion terms to avoid the curse of dimensionality. For bulk power systems with a large number of buses of interest, principal component analysis (PCA) is further used to compress the multiple outputs, which can reduce the number of PCE-based surrogate models that need to be built.

In Chapter 4, we propose a more general equivalent-pi circuit model for the induction calculation of pipeline networks excited by the spatially nonuniform geoelectric field based on the transmission line theory, and study the influence of non-uniformity of geoelectric field on PSP and GIC along the pipelines. Then, the equivalent-pi model is extended to other types of EMI analysis of large-scale pipeline networks, which is capable of handling the inductive or conductive EMI as well as the co-existence of both. Furthermore, the pipeline network is divided into linear pipe segments and nonlinear grounded branches due to locally damaged coatings. The linear pipe segment excited by electric fields can be reduced to an equivalent-pi circuit. It is applicable to arbitrary nonuniform electric fields without necessarily being constant or in a specific function form. The nodal voltage analysis can be performed more efficiently for large-scale pipeline networks with nonlinear polarization, given each linear pipeline segment has been simplified as a lumped circuit, thus considerably reducing the model order of the system of nonlinear equations to be solved.

In Chapter 5, a comprehensive nodal voltage analysis method is proposed for the geomagnetic induction modeling in the IPGS considering the interaction between the power grids and pipelines. The conductive coupling of grounded nodes in the IPGS, including substation grounding grids and buried pipelines, is modeled with the ground transfer resistance. Several IPGS test cases are used to illustrate the impacts of the interaction on the induced voltages and currents. The influences of spatial patterns and resistance parameters of IPGS as well as earth resistivity structures on the interaction are discussed.

The last chapter presents a summary and a list of the future work.

2 Modeling Electromagnetic Fields During Extreme GMD Scenarios

The geoelectric fields on the earth’s surface induced by extreme GMD can cause adverse effects on wide-area transmission grids and pipeline networks. The spatiotemporal distribution of the geoelectric field depends on the intensity of geomagnetic activity and the distribution of the earth conductivity. The occurrence of geomagnetic storms is random, and its intensity and frequency can be inferred statistically from measured geomagnetic data. For long return periods such as 10,000 years, extreme value statistical methods may produce overly conservative results. In addition, the earth conductivity parameters obtained by using traditional optimization methods may be biased, which are affected by measurement errors and shielding effects.

To address these issues, in Section 2.1, the extreme return levels of geomagnetic variations are estimated by combining extreme value statistics and theoretical upper limit of the Dst index, which are used to generate 100-year, 200-year and 10,000-year typical scenarios. Section 2.2 details the proposed earth structure inversion method based on Bayesian regression, which can quantify the probability distribution of soil parameters, and its performance is illustrated with some earth cases. In Section 2.3, the surface induced geoelectric field is calculated taking into account the complex conductivity distribution. Finally, Section 2.4 concludes the chapter.

2.1 Generation of Worst-Case Extreme GMD Scenarios

2.1.1 Method for Estimating the Return Levels of Geomagnetic Variations

It is of great significance to construct typical extreme GMD scenarios to provide guidance for risk assessment of energy systems in engineering practice. To ensure the long-term reliable operation of energy infrastructure, attention should be paid not only to their response in historical geomagnetic disturbance events, but also to the potential maximum stress levels in the future.

Here is a brief introduction to the procedure for generating the extreme GMD scenario and assessing its impacts on the energy networks. Firstly, the extreme geomagnetic variation is estimated by combining the EVA and theoretical upper limit of GMD. Then, the largest historical GMD event observed is scaled according to the peak geomagnetic variation. Finally, it can be used to evaluate the geoelectric field and GIC levels by combining of the earth conductivity model and power grid and pipeline network model.

1） Extreme Values Analysis of Geomagnetic Observation

Extreme statistical analysis, especially the generalized Pareto distribution (GPD), is widely used to estimate the occurrence of extreme GMD scenarios, whose cumulative probability distribution function is as shown in equation (2-1).

$$F(x;\mu,\sigma,\xi) = 1 - \left(1 + \xi\frac{x-\mu}{\sigma}\right)^{-1/\xi}, \quad (x \geq \mu, 1 + \xi\frac{x-\mu}{\sigma} > 0) \tag{2-1}$$

where x is the random variable, μ denotes the location parameter (i.e., threshold), ξ and σ represents the shape parameter and the scale parameter, respectively.

During the GPD modeling process, observed data exceeding a certain threshold are selected, resulting in only a small amount of data available for parameter estimation. The estimates and confidence intervals for GPD model parameters can be obtained using the maximum likelihood estimation method[113, 114].

In fact, there exists uncertainty in the estimation of the return level by EVA due to the small sample size. The Wald confidence interval is used to characterize the uncertainty of the return level, which is based on the asymptotic normality of the parameter estimators.

2） Data Preprocessing for GPD Analysis

Before performing parameter estimation for the Pareto distribution, some data preprocessing is needed, including threshold selection and data declustering[35].

During the GPD modeling process, observed data exceeding a certain larger threshold are selected for parameter estimation, so the selection of the threshold is a key issue. If the threshold is too large, there are only a few excesses, and the variance of the estimator is larger; if the threshold is too small, the distribution of the excesses may be different from the GPD, resulting in a biased estimate. Therefore, for threshold selection, it is necessary to take into account the relationship between bias and variance.

The mean excess function $e(u)$ based on the GPD model is a commonly used method for threshold selection, which is defined as follows

$$e(u) = \frac{1}{N_u}\sum_{X_i > u}(X_i - u), u > 0 \tag{2-2}$$

where N_u is the number of excess. The point set $\{(u, e_n(u)) : u < x_{1,n}\}$ is called the mean residual life plot. The threshold can be selected according to the following method: if the excess for a certain threshold u_0 follows the GPD, then for $u > u_0$, the excess function of the sample is approximately a straight line.

Another method of threshold selection is based on the change in the estimator caused by the threshold u. If the excess for a certain threshold u_0 follows the GPD, then for $u > u_0$, the estimated value of the shape parameter $\hat{\xi}$ and the scale parameter $\hat{\sigma}$ should be stable within a certain range. This method requires model parameter estimation for a series of different thresholds which leads to a relatively higher computational cost.

In this study, the threshold is selected for one-minute geomagnetic data based on the mean excess function, since it is much less computationally expensive than the method based on parameter estimators.

Moreover, we decluster the geomagnetic data above the threshold to eliminate the dependency between data, which means extremes separated by fewer than 12 h non-extremes belong to the same cluster, and only the maximum in each cluster is considered[35].

3） Statistical Inference of GPD Model

Estimates and confidence intervals for GPD model parameters and return levels can be obtained using the maximum likelihood estimation method[113, 114]. Assuming that $X_1, X_2, \ldots, X_{Nu}$ are independent and identically distributed observed data, the log likelihood function of the GPD with parameters ξ and σ can be obtained as

$$L(\sigma, \xi) = -N_u \log \sigma - \left(\frac{1}{\xi} + 1\right) \sum_{i=1}^{N_u} \log\left(1 + \frac{\xi}{\sigma} x_i\right) \tag{2-3}$$

The maximum likelihood estimation of the parameters $\hat{\xi}$ and $\hat{\sigma}$ can be obtained by using a numerical method.

One of the main purposes of EVA is to estimate quantile x_p, defined by equation (2-4). The estimated value of quantile x_p can be derived from the parameter estimation of GPD. For the statistical analysis of GMD, floods and other natural disasters, the return level corresponding to the return period of $T = 1/(1-p)$ years, commonly known as the 1-in-T-year event needs to be estimated. For instance, the 100-year and 200-year return levels correspond to quantile $x_{0.99}$ and $x_{0.995}$, respectively. This extrapolation is a significant advantage of extreme value statistics, and the return period T concerned can be much greater than the historical observation time T_0.

$$P\left(x \geq x_p\right) = \int_{x_p}^{\infty} f(x)\,\mathrm{d}x = 1 - p \tag{2-4}$$

where $f(x)$ is the probability density function of variable x.

4） Theoretical Upper Limit for Dst Index

Reference[115] proposed the theoretical upper limit for the largest imaginable geomagnetic storm, corresponding to the value of Dst index of -2500 nT, which has been adopted by some studies on GICs in the UK power grids[36, 116]. The Dst index indicates the strength of the ring current, which is one of the main sources of GMD at low latitudes. Thus, the upper limit of the Dst index provides a valuable reference for GIC study in China.

The geomagnetic variation estimates based on the Dst index can provide scale factors to study the 1-in-10,000-year extreme event. Assuming a simple dipolar ring current model on the plane of geomagnetic equator[116], the horizontal geomagnetic variation at geomagnetic latitude ϕ can be simplified as $\Delta B_H \cos\phi$, where ΔB_H is the horizontal geomagnetic variation on the geomagnetic equator.

2.1.2 Extreme GMD Scenarios For Sanhua Area

1） Geomagnetic Observation in Sanhua Area

The 1-minute geomagnetic data at Beijing Ming Tombs (BMT, 40.3°N 116.2°E) observatory from 1996 to 2019 are used for EVA. Compared with other observatories in China, BMT has the advantages of closer distance to the Sanhua UHV grid, relatively higher latitude and longer measurement time. Moreover, the BMT data are representative since the spatial distribution of geomagnetic variation at low latitude is relatively uniform[59]. However, for high latitude areas, it is necessary to use averaging or interpolation methods to integrate the geomagnetic data from multiple observatories at the similar geomagnetic latitude, since the spatial distribution of geomagnetic variation is much more complicated.

The geomagnetic data from SuperMAG have already removed the annual and daily baselines to reduce the impacts of other interferences[117]. The historical time series of variation ΔB are shown in Figure 2-1. Some statistical results about BMT data are provided in Table 2-1. As some studies on sudden impulse storms have pointed out, the 1-minute data used in this study may not be able to fully capture high-frequency variations[118, 119], which will be considered in future studies.

Table 2-1 Maximum variation and rate-of-change of geomagnetic field observed at BMT

Component	$\max(\Delta B_i)$/nT ($i = x, y, \mathrm{H}$)	$\max(\mathrm{d}B_i/\mathrm{d}t)$/nT·min^{-1}
Northward B_x	546	130
Eastward B_y	170	85
Horizontal B_H	547	132

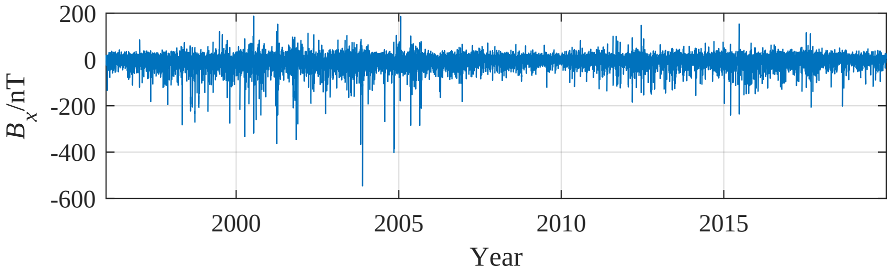

(a) Northward geomagnetic variations

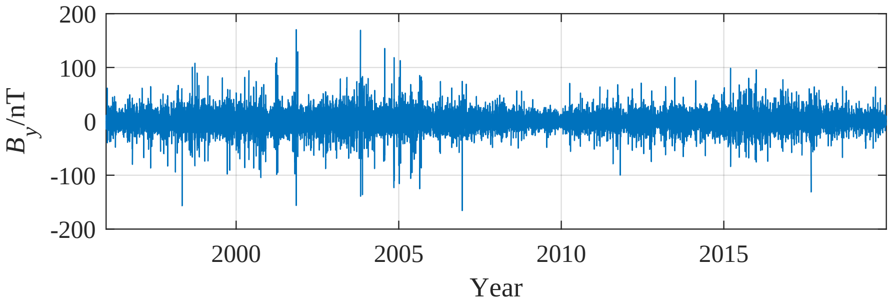

(b) Eastward magnetic variations

Figure 2-1 Time series of the geomagnetic variations in the north and east directions at BMT observatory from 1996 to 2019.

2） Estimating Geomagnetic Variation Using Extreme Value Analysis

Both the magnitude of variation and rate-of-change of the magnetic field can characterize the intensity of GMD, and the former is adopted for EVA in this study. Before performing parameter estimation for the Pareto distribution, some data preprocessing is needed, including threshold selection and data declustering[35].

The selection of the threshold is relatively subjective but a key issue. That is, if the threshold is too large, there are only a few excesses, then the variance of the estimator is larger; if the threshold is too small, the distribution of the excesses may be different from the GPD, resulting in a biased estimate. Therefore, it is necessary to take into account the relationship between the bias and the variance for threshold selection. In this study, the 0.9997 quantile of the geomagnetic variation is used as the threshold.

Moreover, we decluster the geomagnetic data above the threshold to eliminate the dependency between data, which means extremes separated by fewer than 12 h non-extremes belong to the same cluster, and only the maximum in each cluster is considered.

The ‘extRemes’ package in R is used in this study[114]. The 100, 200 and 10,000-year return levels for the geomagnetic variation and corresponding confidence intervals at BMT observatory are shown in Figure 2-2 and Table 2-2. In this study, the magnetic variation and

GIC estimates are rounded to the nearest ten digits. From Figure 2-2, we can observe that there is a large uncertainty in the estimation of the 10,000-year return level. This can be explained by the fact that the digital geomagnetic data are only available for a few decades. The upper bound of 95% Wald confidence interval is adopted to account for modeling uncertainties.

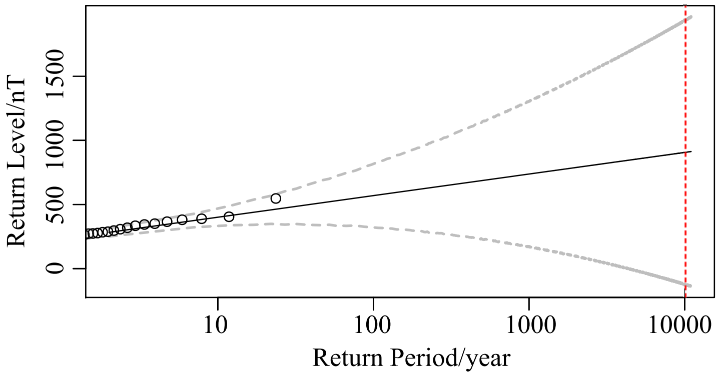

Figure 2-2 The return level (black curve) of horizontal magnetic variation at BMT and its 95% Wald confidence interval (gray dashed curves). (The circles indicate the empirical return level, and the red dashed line represents the 10,000-year return period.).

Table 2-2 Return level and confidence interval of magnetic variation at BMT

Return period/year	Return level/nT	95% confidence interval/nT
100	570	[330, 810]
200	620	[290, 950]
10,000	910	[-120, 1930]

3） Theoretical Upper Limit of Magnetic Variation in Sanhua Area

The upper limit of geomagnetic variation at BMT observatory is 2150 nT, which is larger than the upper bound of 95% Wald confidence interval of 10000-year scenarios. For Sanhua area, the geomagnetic latitude ranges from 15.06~33.88°N, and the corresponding upper limit of geomagnetic variation is 2080~2410 nT.

Taking into account all the above-mentioned elements, 1930 nT estimated by EVA is used in the following GIC study since it has not reached the theoretical upper limit. The theoretical upper limit 2410 nT may be adopted if more conservative situations need to be considered.

4） 1-in-10,000-year Geomagnetic Time Series

A typical historical GMD event at BMT observatory that occurred on July 15-16, 2000 shown in Figure 2-3, is chosen for the following GIC study, which is scaled to 1930 nT for 10,000-year scenario, resulting in a scale factor of 6.0.

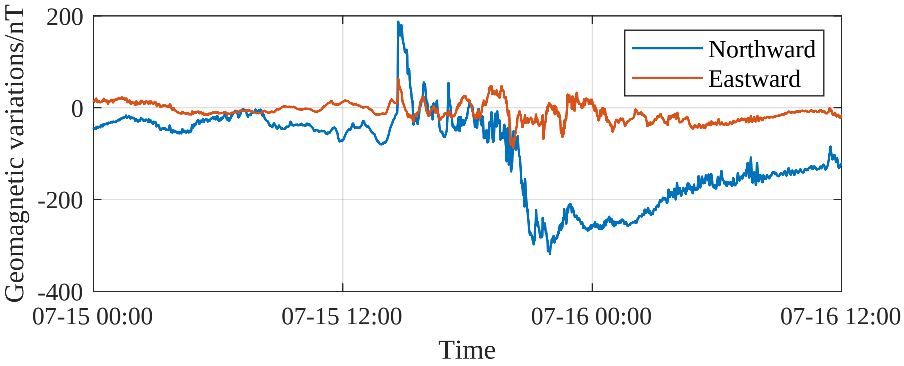

Figure 2-3 Time series of the geomagnetic variations at BMT observatory during the GMD event occurred on July 15-16, 2000.

2.1.3 Extreme GMD Scenarios For the UK

In this case, the magnitude of the horizontal magnetic field change rate is used as a measure of the intensity of the geomagnetic storm. The 1-minute sampling geomagnetic data at Hartland (HAD) geomagnetic observatory from 1983 to 2017 (35 years in total) are collected, as shown in Figure 2-4. And the maximum value of the historical measured data is 327 nT/min.

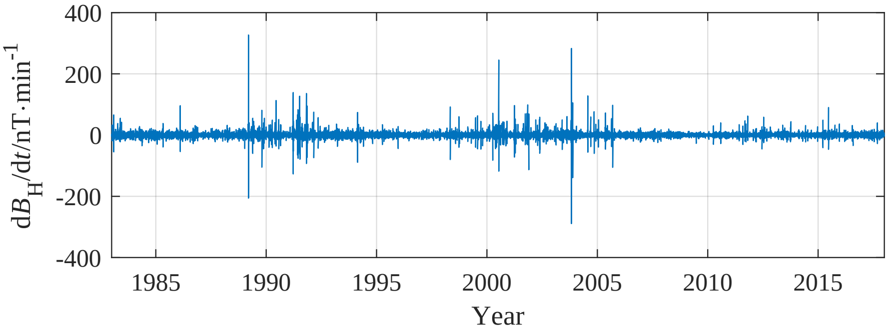

Figure 2-4 Rate-of-change of horizontal geomagnetic fields at HAD observatory from 1983 to 2017.

According to the extreme value theory, the 100, 200 and 10,000-year return levels for the rate-of-change of horizontal magnetic field at HAD are shown in Table 2-3.

Table 2-3 Return level and confidence interval of magnetic variation at HAD

Return period/year	Return level/$nT\cdot min^{-1}$	84% quantile/$nT\cdot min^{-1}$
100	470	610
200	630	840
10,000	3260	5150

In the actual geomagnetic storm event, the duration of extreme conditions of high change rate of the magnetic field is short, usually only tens of seconds to minutes. For the period of time during which the magnetic field changes drastically, a single frequency approximation waveform is used for simplification[120].

Assuming that the magnetic field in the horizontal direction is sinusoidal as shown by equation (2-5), the magnetic field strength H_0 corresponding to the period T can be calculated from the average rate of change of the magnetic field according to equation (2-6).

$$B_{\mathrm{H}} = H_0 \sin\left(2\pi t/T\right) \tag{2-5}$$

$$\mathrm{d}B_{\mathrm{H}}/\mathrm{d}t = H_0 \frac{\sqrt{2}\pi}{T} \tag{2-6}$$

Assuming that the period T is 10 minutes, the magnetic field amplitudes corresponding to the 100, 200 and 10,000-year return periods are 1360, 1880 and 11600 nT.

From theoretical arguments Vasyliūnas has suggested a theoretical upper limit for the largest geomagnetic storm possible corresponding to a Dst of -2500 nT[115], which is adopted by British Geological Survey study[36, 116]. And the magnetic variation estimates based on the Dst index can provide scale factors to study the 1-in-10,000-year extreme event. The estimated variation of the horizontal component at UK HAD observatory using the exponential extrapolation method and the contribution from the ring current (RC) method are 4000 and 6080 nT, respectively[116]. And the latter conservative one is adopted in our GIC study.

Then extreme geomagnetic storm scenarios in the UK are modeled combining the 0.84 quantiles and theoretical upper limit. The results at HAD when T=10 min are shown in Table 2-4. For the 10000-year return level of geomagnetic disturbances, the estimated result from the theoretical upper limit is smaller than that via extreme statistical theory, which can alleviate the conservatism of the latter method.

Table 2-4 The 100, 200 and 10,000-year return levels of the horizontal magnetic variation at HAD when T=10 min

Return period/year	EVA only/nT	EVA & theoretical upper limit/nT
100	1360	1360
200	1880	1880
10,000	11600	6080

The intensity of geomagnetic variations varies with the excitation period, and the estimated results at other periods of geomagnetic fields are presented in Table 2-5. At periods of 0.5 min and 2 min, the levels of geomagnetic variation estimated based on extreme value statistical theory are relatively small and do not exceed the theoretical upper limit.

Table 2-5 The 10,000-year return levels of the horizontal magnetic variation at HAD at different period of magnetic field

Period of magnetic field/min	EVA only/nT	EVA & theoretical upper limit/nT
0.5	580	580
2	2320	2320
10	11600	6080

2.2 Parameter Estimation of a Horizontal Multilayer Earth Using Bayesian Inference

The inversion of earth resistivity structure is of great importance for the electromagnetic interference and grounding analysis. This research presents a Bayesian regression approach for the parameter estimation of horizontal multilayer soils. It provides not only the optimal point estimate of soil parameters, but also more comprehensive statistical properties. The posterior probability distribution of the soil parameters is inferred by combining their prior knowledge with the measured apparent resistivity from Wenner’s method. It allows for statistically quantifying the influence of measurement errors and shielding effects, thus providing a more comprehensive understanding of the soil parameters for robust EMI prediction and substation grounding design. Several multi-layer earth structure cases are used to illustrate the performance of the Bayesian inference method.

We propose a novel method for earth structure inversion based on Bayesian inference[121-124]. The apparent resistivity measurements are used to update the prior knowledge of the parameters to infer their posterior distribution. It can provide not only a point estimate of soil parameters, but also the joint probability distributions to describe parameter uncertainties. To quantify the impact of measurement errors and model inaccuracy on the inversion, an additional random variable representing the model discrepancy is incorporated into the statistical model.

Then, the Markov chain Monte Carlo (MCMC) algorithm is employed to infer the generalized posterior distributions of soil parameters numerically, not limited to the Gaussian distribution assumptions. The original nonlinear computational model of the apparent resistivity is adopted in the inversion, thus avoiding additional errors caused by model linearization.

Furthermore, the information criterion[125] is adopted to determine the optimal number of soil layers to avoid under-fitting or over-fitting issues, by considering the goodness-of-fit, model complexity, and the availability of observations.

The rest of this section is organized as follows. Section 2.2.1 formulates the problem of earth resistivity interpretation from Wenner's method and presents the classical optimization-based inversion model. Section 2.2.2 details the proposed Bayesian inference method for soil inversion. Section 2.2.3 demonstrates the applicability of the proposed method with some layered earth structure cases.

2.2.1 Problem Formulation of Earth Structure Estimation

1） Measured Apparent Resistivity Using Wenner's Method

In the electrical sounding method, an excitation current is injected to the soil, and the unknown soil parameters can be interpreted from the resulting electrical potential. The Wenner's method is recommended by IEEE Standard[39] due to its high precision. The four electrodes C_1, C_2, P_1 and P_2 are arranged at equal intervals along a line, as shown in Figure 2-5.

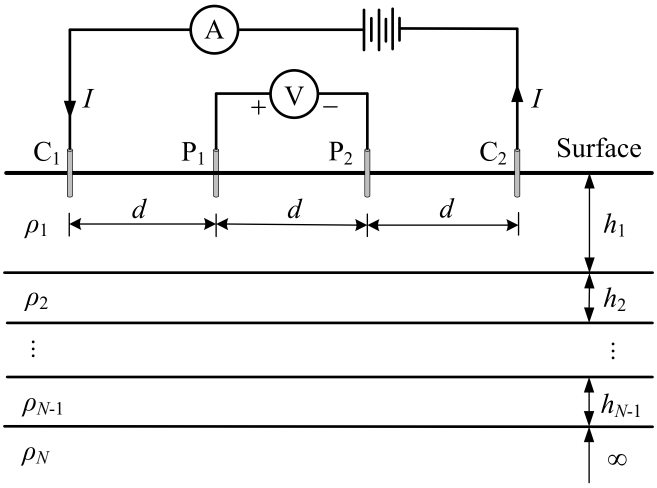

Figure 2-5 Schematic diagram of Wenner's method for measuring the apparent resistivity of a layered earth structure.

Let us denote the distance between adjacent electrodes as d. If it is much larger than the buried depth, the measured apparent resistivity is given by[39]

$$\rho^{\mathrm{m}} = 2\pi d\frac{V}{I} \tag{2-7}$$

where I is the current injected from electrode C_1 and returned from C_2, which is generated by an external DC source, and V is the voltage measured between electrodes P_1 and P_2.

Suppose the apparent resistivity is measured at M different electrode spacings, where d_i and ρ_i^{m} represent the i-th electrode spacing and measured apparent resistivity, respectively. Then, all measurement data obtained from Wenner's method can be written as a set of observations in a compact form as follows

$$\mathbf{y} = \{\mathbf{y}_i\}_{i=1}^{M} = \{(d_i, \rho_i^{\mathrm{m}})\}_{i=1}^{M} \tag{2-8}$$

Generally, when the electrode spacing is small, the apparent resistivity is dominated by the surface soil; whereas when the electrode spacing is large, the apparent resistivity is mainly affected by the deep soil. It depends on the distribution of current density in the earth.

2） Theoretical Apparent Resistivity

For a layered earth structure with known parameters, the apparent resistivity can be calculated analytically using electromagnetic field theory. Assume that the earth has a N layer structure, where ρ_i and h_i are the resistivity and thickness of the i-th layer, respectively. For a two-layer earth, the calculated apparent resistivity can be derived as[38]

$$\rho^{\mathrm{c}} = \rho_1 \left\{ 1 + 4 \sum_{n=1}^{\infty} \left[\frac{K^n}{\sqrt{1 + (2nh_1/d)^2}} - \frac{K^n}{\sqrt{1 + (2nh_1/d)^2}} \right] \right\} \tag{2-9}$$

where $K = (\rho_2 - \rho_1)/(\rho_2 + \rho_1)$ is the reflection coefficient.

For a N-layer earth structure ($N \geq 2$), a more generalized formula for the apparent resistivity can be derived as[42]

$$\rho^{\mathrm{c}} = \rho_1 \left\{ 1 + 2d \int_0^{\infty} \beta(\lambda) \cdot [J_0(\lambda d) - J_0(2\lambda d)] \mathrm{d}\lambda \right\} \tag{2-10}$$

where $J_0(\cdot)$ is the zero-order Bessel’s function of the first kind, and the kernel function $\beta(\lambda) = \alpha_1(\lambda) - 1$ can be calculated recursively from the bottom layer to the top layer:

$$\begin{aligned} \alpha_n = & \frac{1 + K_n e^{-2\lambda h_n}}{1 - K_n e^{-2\lambda h_n}},\ K_n = \frac{\rho_{n+1}\alpha_{n+1} - \rho_n}{\rho_{n+1}\alpha_{n+1} + \rho_n}, \\ & (n = 1, \ldots, N-2) \\ \alpha_{N-1} = & \frac{1 + K_{N-1} e^{-2\lambda h_{N-1}}}{1 - K_{N-1} e^{-2\lambda h_{N-1}}},\ K_{N-1} = \frac{\rho_N - \rho_{N-1}}{\rho_N + \rho_{N-1}} \end{aligned} \tag{2-11}$$

Given the Sommerfeld integral in (2-10), direct numerical integration is computationally expensive[45]. Several techniques have been proposed to simplify its calculation by fitting the kernel function, e.g. complex image method[42], power series approach[48], Chebyshev polynomial method[52] and segmented 3-order fitting method[126], etc. The complex image method is adopted in this research, where the kernel function is fitted with a series of N_{CIM} exponential terms:

$$\beta(\lambda) \approx \sum_{t=1}^{N_{\mathrm{CIM}}} b_t \exp(a_t \lambda) \tag{2-12}$$

where the coefficients a_t and b_t are estimated from some samples of $\beta(\lambda)$.

Then, using the Lipschitz's integration for Bessel functions

$$\int_0^{\infty} \exp(-\lambda|c|) J_0(\lambda d) \mathrm{d}\lambda = 1/\sqrt{c^2 + d^2} \tag{2-13}$$

equation (2-10) can be simplified as[42]

$$\rho^{\mathrm{c}} \approx \rho_1 \left\{ 1 + 2d \sum_{t=1}^{N_{\mathrm{CIM}}} b_t \left[\frac{1}{\sqrt{a_t^2 + d^2}} - \frac{1}{\sqrt{a_t^2 + 4d^2}} \right] \right\} \tag{2-14}$$

3） Classical Optimization-based Soil Estimation

Soil parameters can be estimated by fitting the measured apparent resistivity data in (2-8) with the theoretical model of apparent resistivity. For a N-layer earth, all 2N-1 soil parameters to be estimated can be denoted as a vector:

$$\mathbf{x} = (\rho_1, \rho_2, \ldots, \rho_N, h_1, h_2, \ldots, h_{N-1})^{\mathrm{T}} \tag{2-15}$$

And the calculated apparent resistivity ρ^{c} in (2-9) and (2-10) can be written as a computational forward model f as

$$f: \mathbf{x} \in D_{\mathbf{x}} \rightarrow \rho^{\mathrm{c}} = f(\mathbf{x}, d) \tag{2-16}$$

where $D_{\mathbf{x}}$ the feasible region of the parameters.

Thus, a regression model can be formulated for the measured apparent resistivity data as follows:

$$\rho_i^{\mathrm{m}} = f(\mathbf{x}, d_i) + \varepsilon_i, \ i = 1, 2, \ldots, M \tag{2-17}$$

where ε_i is the residual between the i-th measurement and the model output.

Soil parameters can be estimated by solving a nonlinear optimization problem as in (2-18). The normalized residuals are adopted in the objective function since the measured apparent resistivity at different electrode spacings may vary greatly, and they can even span multiple orders of magnitude[43].

$$\hat{\mathbf{x}} = \arg\min_{\mathbf{x} \in D_{\mathbf{x}}} \sum_{i=1}^{M} \left[\frac{\rho_i^{\mathrm{m}} - f(\mathbf{x}, d_i)}{\rho_i^{\mathrm{m}}} \right]^2 \tag{2-18}$$

2.2.2 Bayesian Inference of Earth Resistivity Parameters

1） A Bayesian Framework for Soil Parameter Estimation

Soil parameters estimated by classical optimization methods are usually deterministic. In this section, we develop a Bayesian framework for earth resistivity inversion, where the measurement error and parameter uncertainty are characterized statistically. It can provide a more comprehensive insight into the soil parameters from available measurements.

Given the characteristics of measured apparent resistivity, a constant relative error model[121] is adopted to describe the residuals in (2-17), i.e. they are assumed to satisfy the following Gaussian distribution independently:

$$\varepsilon_i \sim \mathrm{Normal}(0, (\sigma f(\mathbf{x}, d_i))^2),\ i = 1, 2, \ldots, M \tag{2-19}$$

where σ is the relative error factor. In this model, the base value is taken as the output of the computational model $f(\mathbf{x}, d_i)$ to suppress the influence of noises, instead of the measured value ρ_i^{m} used in (2-18).

Thus, the observation in (2-17) is a realization of the following Gaussian distribution:

$$\rho_i^{\mathrm{m}} \sim \mathrm{Normal}(f(\mathbf{x}, d_i), (\sigma f(\mathbf{x}, d_i))^2),\ i = 1, 2, \ldots, M \tag{2-20}$$

In the Bayesian framework, both the soil parameter $\mathbf{x}$ and the relative error factor σ are quantities of interest, which yields an augmented parameter vector to be estimated:

$$\boldsymbol{\xi} = (\mathbf{x}, \sigma) \tag{2-21}$$

The observations are then used to update the prior knowledge of the parameters to infer their posterior distributions. It is reasonable to assume a prior-independence between $\mathbf{x}$ and σ. Their prior probability density functions are denoted as $\pi_{\text{prior}}(\mathbf{x})$ with support $D_{\mathbf{x}}$ and $\pi_{\text{prior}}(\sigma)$ with support D_σ, respectively. The prior distribution can be specified by expert experience or historical measurements, etc. Otherwise, the non-informative prior can be used, such as the parameters are assumed to be uniformly distributed within a certain range.

Given the observation $\mathbf{y}$ of apparent resistivity, the posterior probability density function of the parameters can be derived using Bayes' theorem[122] as

$$\pi_{\text{post}}(\mathbf{x}, \sigma|\mathbf{y}) \propto \pi_{\text{prior}}(\mathbf{x})\pi_{\text{prior}}(\sigma)L(\mathbf{x}, \sigma; \mathbf{y}) \tag{2-22}$$

where the likelihood function $L(\mathbf{x}, \sigma; \mathbf{y})$ is the sampling probability of observation $\mathbf{y}$ given parameters $\mathbf{x}$ and σ

$$L(\mathbf{x}, \sigma; \mathbf{y}) = \pi_{\text{like}}(\mathbf{y}|\mathbf{x}, \sigma) = \prod_{i=1}^{M} \pi_{\text{like}}(\mathbf{y}_i|\mathbf{x}, \sigma) \tag{2-23}$$

and the sampling probability of the i-th measurement can be calculated as follows according to (2-20):

$$\pi_{\text{like}}(\mathbf{y}_i|\mathbf{x}, \sigma) = \frac{1}{\sqrt{2\pi}\sigma\mathcal{M}(\mathbf{x}, d_i)} \exp\left\{-\frac{\left[\rho_i^{\text{m}} - \mathcal{M}(\mathbf{x}, d_i)\right]^2}{2\left[\sigma\mathcal{M}(\mathbf{x}, d_i)\right]^2}\right\} \tag{2-24}$$

Then, the maximum a posteriori (MAP), as the statistically optimal point estimate, can be obtained from the posterior distribution as follows:

$$(\mathbf{x}_{\text{MAP}}, \sigma_{\text{MAP}}) = \arg\max_{\mathbf{x}, \sigma} \pi_{\text{post}}(\mathbf{x}, \sigma|\mathbf{y}) \tag{2-25}$$

and the posterior distribution of soil parameters $\mathbf{x}$ can be calculated by

$$\pi_{\text{post}}(\mathbf{x}|\mathbf{y}) = \int_{D_\sigma} \pi_{\text{post}}(\mathbf{x}, \sigma|\mathbf{y}) \mathrm{d}\sigma \tag{2-26}$$

Furthermore, for a substation grounding parameter of interest $h : \mathbb{R}^{2N-1} \to \mathbb{R}$, we can predict its probability distribution using the posterior distribution of $\mathbf{x}$. And the conditional expectation of $h(\mathbf{x})$ can then be derived as

$$\mathbb{E}[h(\mathbf{x})|\mathbf{y}] = \int_{D_\mathbf{x}} h(\mathbf{x}) \pi_{\text{post}}(\mathbf{x}|\mathbf{y}) \mathrm{d}\mathbf{x} \tag{2-27}$$

The procedures described above for Bayesian earth structure inversion are summarized in Figure 2-6.

2） MCMC Algorithm

The posterior distributions of soil parameters in (2-22) are typically non-Gaussian and difficult to calculate analytically even if the residuals are normally distributed, since the computational model f of apparent resistivity is highly nonlinear. Instead, it can be calculated using numerical methods such as MCMC. Its basic idea is to create a Markov chain with an invariant distribution equal to the posterior distribution of the parameters. This is proven to hold if the Markov chain satisfies the following detailed balance condition[122, 123]:

$$\pi_{\text{post}}(\boldsymbol{\xi}^{(t)}|\mathbf{y})\mathrm{P}(\boldsymbol{\xi}^{(t+1)}|\boldsymbol{\xi}^{(t)}) = \pi_{\text{post}}(\boldsymbol{\xi}^{(t+1)}|\mathbf{y})\mathrm{P}(\boldsymbol{\xi}^{(t)}|\boldsymbol{\xi}^{(t+1)}) \tag{2-28}$$

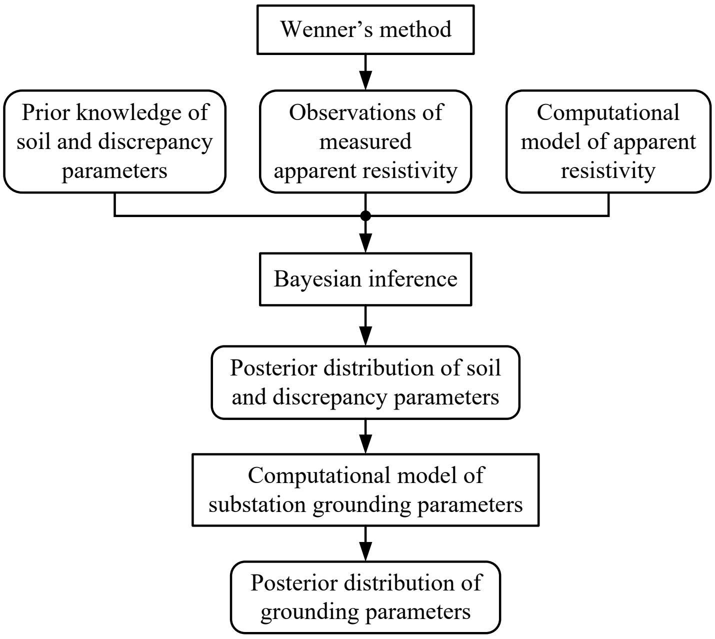

Figure 2-6 Flowchart for Bayesian inference of a multilayer earth structure.

where $\mathrm{P}(\xi^{(t+1)}|\xi^{(t)})$ is the transition probability from $\xi^{(t)}$ at the step t to $\xi^{(t+1)}$ at the subsequent step $t+1$.

Practical MCMC methods include Metropolis-Hastings algorithm, Hamiltonian Monte Carlo algorithm, and affine invariant ensemble sampler (AIES)[122, 124], etc. The AIES algorithm shows better convergence if there is a strong correlation between the posterior distributions of different parameters, thus it is adopted for soil parameter estimation in this research.

The AIES algorithm runs an ensemble of N_{chains} chains simultaneously, and they walk alternately to obtain samples from the posterior distribution. Their transition probabilities are constructed by using the following procedures to satisfy the detailed balance condition. For the i-th chain, a new candidate is preliminarily proposed at step t:

$$\xi_i^{(\star)} = \xi_i^{(t)} + z(\xi_j^{(t)} - \xi_i^{(t)}) \tag{2-29}$$

where j is randomly selected from other chains, and z is sampled from the following probability distribution

$$p(z) = \begin{cases} \frac{1}{\sqrt{z}(2\sqrt{a}-2/\sqrt{a})}, & \text{if } z \in [1/a, a], \\ 0, & \text{otherwise} \end{cases} \tag{2-30}$$

where the tuning parameter $a > 1$.

Then, the candidate is accepted with the probability $\alpha(\xi_i^{(\star)}, \xi_i^{(t)}, z)$ as in (2-31), otherwise it is rejected and the i-th chain keeps the value $\boldsymbol{\xi}_i^{(t)}$ at step $t+1$.

$$\alpha(\boldsymbol{\xi}_i^{(\star)}, \boldsymbol{\xi}_i^{(t)}, z) = \min\left\{1, z^{2N-1}\frac{\pi_{\text{post}}(\boldsymbol{\xi}_i^{(\star)}|\mathbf{y})}{\pi_{\text{post}}(\boldsymbol{\xi}_i^{(t)}|\mathbf{y})}\right\} \tag{2-31}$$

The chains draw samples from the posterior distribution, providing more information about the soil parameters compared to individual point estimates. They can be further used to calculate substation grounding parameters by quantifying and propagating the uncertainty of soil parameters during the measurement process. The numerical procedures for Bayesian inversion of the soil parameters are summarized in Algorithm 2-1.

Algorithm 2-1 Bayesian inference of a layered earth structure via AIES-based MCMC algorithm

```
Data: Observations $\mathbf{y}$ of measured apparent resistivity, computational model $f$, and
      prior probabilistic distribution $\pi_{\text{prior}}(\mathbf{x})$ and $\pi_{\text{prior}}(\sigma)$; MCMC configurations,
      including the number of steps $N_{\text{steps}}$, the number of chains $N_{\text{chains}}$, and the
      tuning parameter $a$.
Result: Posterior distribution of soil parameters $\mathbf{x}$, descrepancy parameter $\sigma$, and
        substation grounding parameters of interest $h(\mathbf{x})$.
Initialize the seed points $\boldsymbol{\xi}_i^{(0)} (i = 1, 2, ..., N_{\text{chains}})$ for all chains;
for $t = 0, 1, \ldots, N_{\text{steps}} - 1$ do
    for $i = 1, 2, \ldots, N_{\text{chains}}$ do
        Select $j$ from other chains $\{1, 2, \ldots, N_{\text{chains}}\} \setminus \{i\}$ randomly;
        Generate $z$ from $p(z)$ in (2-30);
        Propose a new candidate $\boldsymbol{\xi}_i^{(\star)} = (\mathbf{x}_i^{(\star)}, \sigma_i^{(\star)})$ via (2-29);
        Calculate the apparent resistivity $f\left(\mathbf{x}_i^{(\star)}, d_k\right)$, $(k = 1, 2, \ldots, M)$ using (2-9)
          or (2-10);
        Calculate the likelihood function $L(\mathbf{x}_i^{(\star)}, \sigma_i^{(\star)}; \mathbf{y})$ via (2-23);
        Calculate the acceptance probability $\alpha(\boldsymbol{\xi}_i^{(\star)}, \boldsymbol{\xi}_i^{(t)}, z)$ via (2-31);
        Draw $u$ from the standard uniform distribution;
        if $u < \alpha(\boldsymbol{\xi}_i^{(\star)}, \boldsymbol{\xi}_i^{(t)}, z)$ then
            $\boldsymbol{\xi}_i^{(t+1)} = \boldsymbol{\xi}_i^{(\star)}$;
        else
            $\boldsymbol{\xi}_i^{(t+1)} = \boldsymbol{\xi}_i^{(t)}$;
        end
    end
end
Calculate the posterior distribution, MAP and confidence intervals of parameters $\mathbf{x}$
  and $\sigma$ from the MCMC samples as in (2-25) and (2-26);
Predict the probability distribution and expectation of substation grounding
  parameters via (2-27);
```

3） Earth Model Selection via Information Criterion

In this subsection, we further discuss a quantitative method for determining the optimal number of layers using the information criterion. For some alternative numbers of layers, the posterior distributions of the parameters in these models are calculated separately using Algorithm 2-1 firstly. Then, the optimal model can be selected by minimizing the information criterion[125]. Several information criteria are discussed:

Akaike information criterion (AIC)[125] contains two terms, as defined in (2-32). The first term describes the deviance of the fitted model to the observations, and the second term penalizes the model complexity using the number of parameters.

$$\mathrm{AIC} = -2\log \pi_{\mathrm{like}}(\mathbf{y}|\boldsymbol{\xi}_{\mathrm{MLE}}) + 2N_{\mathrm{p}} \tag{2-32}$$

where the number of parameters $N_{\mathrm{p}} = 2N$. The maximum likelihood estimation (MLE) $\boldsymbol{\xi}_{\mathrm{MLE}}$ is given by (2-33), and it is equal to the MAP estimate if the flat priors are used.

$$\boldsymbol{\xi}_{\mathrm{MLE}} = \arg\max_{\boldsymbol{\xi}} L(\boldsymbol{\xi};\mathbf{y}) = \arg\max_{\boldsymbol{\xi}} \pi_{\mathrm{like}}(\mathbf{y}|\boldsymbol{\xi}) \tag{2-33}$$

Bayesian information criterion (BIC)[123] uses a slightly different penalty term that further takes into account the number of observations M:

$$\mathrm{BIC} = -2\log \pi_{\mathrm{like}}(\mathbf{y}|\boldsymbol{\xi}_{\mathrm{MLE}}) + N_{\mathrm{p}}\log M \tag{2-34}$$

2.2.3 Earth Structure Case Studies

1） Case Study A: Two-Layer Earth Structures

Six two-layer earth cases in [46] are used to illustrate the performance of the adopted Bayesian method. As shown in Table 2-6, the MAP results of soil parameters are very close to the optimal solution in [46]. The slight difference arises from the different objective functions (2-25) and (2-18) of the two methods.

The details of the fourth two-layer earth case are presented as a demonstration example. Table 2-7 shows field readings of apparent resistivity from [41]. The prior distributions of the four parameters used for Bayesian inference are given in Table 2-8. $U(a,b)$ denotes the uniform distribution in the interval $[a,b]$. The ranges of the three soil parameters ρ_1, ρ_2 and h_1 are taken from [47]. The range of relative error factor σ is assumed to be [0, 0.05]. Independent uniform prior assumptions are adopted for these four parameters.

Table 2-6 Comparison of the MAP with the best optimization methods in [46] for two-layer structures

Case	$\rho_1/\Omega\cdot$m	$\rho_2/\Omega\cdot$m	h_1/m	σ	Method
1	372.729	145.259	2.690	-	8th[46]
	374.804	146.154	2.677	0.037	MAP
2	246.836	1058.620	2.139	-	7th[46]
	247.189	1045.105	2.108	0.043	MAP
3	57.343	96.712	1.651	-	5th[46]
	58.739	98.123	1.828	0.055	MAP
4	494.883	93.663	4.370	-	7th[46]
	496.308	94.946	4.327	0.038	MAP
5	160.776	34.074	1.848	-	8th[46]
	161.545	32.866	1.868	0.050	MAP
6	125.526	1093.080	2.713	-	8th[46]
	126.670	1102.604	2.733	0.053	MAP

Table 2-7 Measured apparent resistivity—Case study A[46]

No.	d/m	$\rho^{m}/\Omega\cdot$m
1	2.5	451.6
2	5.0	366.7
3	7.5	250.2
4	10.0	180.0
5	12.5	144.2
6	15.0	120.2
7	20.0	115.5
8	25.0	96.5

Table 2-8 Prior probability distribution of the parameters—Case study A

Parameter	Prior distribution
$\rho_1/\Omega\cdot$m	$U(0, 1200)$
$\rho_2/\Omega\cdot$m	$U(0, 1200)$
h_1/m	$U(0, 6)$
σ	$U(0, 0.05)$

Then, these prior distributions are updated using Bayesian method. The AIES algorithm in UQLab[122] is adopted for the soil parameter estimation. Figure 2-7 depicts the posterior one- and two-dimensional marginal probability distributions and correlation coefficients of parameters inferred from the MCMC samples. The MAP and 95% confidence interval of the parameters are given in Table 2-9, which are compared with the results obtained by the optimization method in [46]. It can be seen that the MAP of soil parameters is very close to the optimal solution in [46]. The slight difference arises from the different objective functions (2-25) and (2-18) of the two methods. Compared to optimization methods, Bayesian methods comprehensively quantify the uncertainty of parameter estimation.

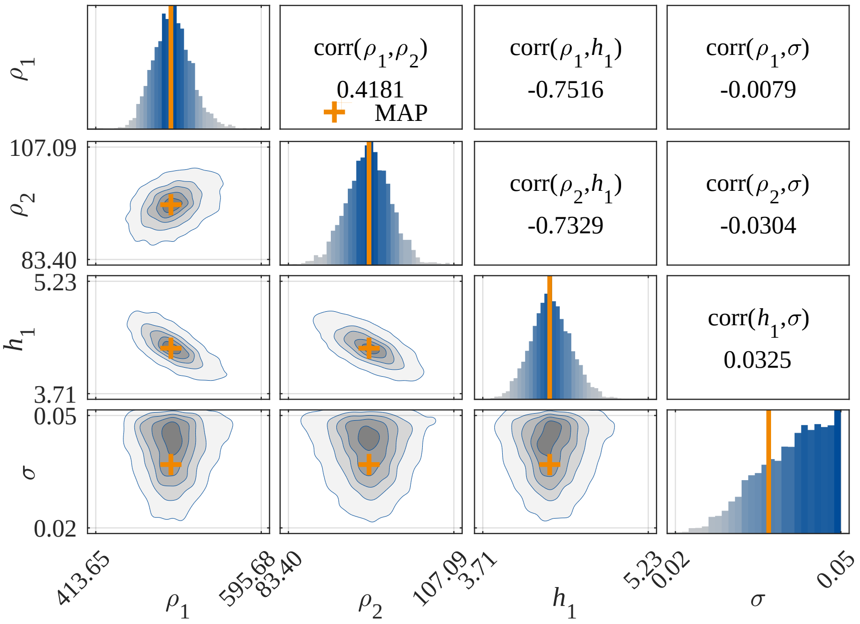

Figure 2-7 One- and two-dimensional posterior marginals and correlation coefficients of parameters obtained by the Bayesian method—Case study A.

Table 2-9 Estimated results of the parameters—Case study A

Parameter	Results in [46]	Bayesian posterior results	
		MAP	95% confidence interval
$\rho_1/\Omega\cdot\text{m}$	494.883	496.308	[458.803, 543.577]
$\rho_2/\Omega\cdot\text{m}$	93.663	94.946	[88.569, 101.094]
h_1/m	4.370	4.327	[3.985, 4.733]
σ	-	0.0378	[0.0289, 0.0496]

Furthermore, the MCMC samples of the soil parameters $\mathbf{x}$ are used to predict the posterior distribution of the calculated apparent resistivity at electrode spacing d, namely $\pi_{\text{post}}(f(\mathbf{x}, d))$. Other grounding parameters of interest can be evaluated similarly. The posterior means and confidence intervals of the calculated apparent resistivity are compared with the measurements in Figure 2-8, which illustrates the accuracy of the Bayesian posterior results.

The classical optimization methods are affected by the measurement error since they can not distinguish whether the error is caused by soil model or measurement data[56]. On the contrary, the adopted Bayesian method can distinguish the contributions of uncertainty in soil parameters and discrepancy parameters. Figure 2-9 compares the posterior distribution of ap-

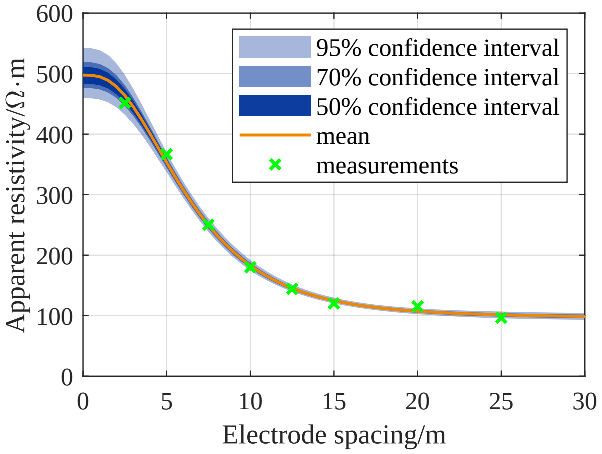

Figure 2-8 Bayesian posterior predictive distribution and measured apparent resistivity—Case study A.

parent resistivity with and without residuals at spacing $d_i (i = 1, 2, \ldots, M)$, which are defined as $\pi_{\text{post}}\left(f(\mathbf{x}, d_i) + \varepsilon_i\right)$ and $\pi_{\text{post}}(f(\mathbf{x}, d_i))$, respectively. The residual ε_i are drawn from the Gaussian distribution in (2-19) using the posterior samples of $\mathbf{x}$ and σ. The extra impact of these residuals is clearly shown in Figure 2-9.

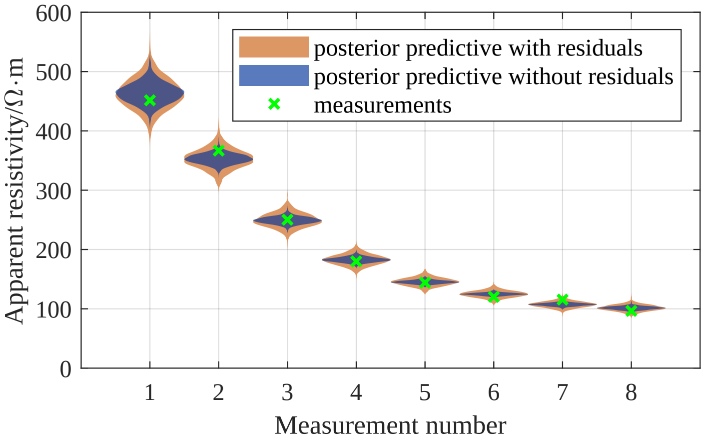

Figure 2-9 Posterior predictive apparent resistivity with and without residuals—Case study A.

2） Case Study B: A Three-Layer Earth

Then, a three-layer earth with known parameters from [57] is used to discuss the shielding effect. As shown in Table 2-10, the second layer has significantly larger resistivity compared to the other layers. The resulting shielding effect brings difficulties in the estimation of other soil parameters. The results in [57] show that the deep soil parameters estimated by the optimization method may deviate from the actual values in this case.

In this research, initially, the theoretical apparent resistivity at eleven electrode spacings

Table 2-10 Synthetic three-layer earth—Case study B[57]

Layer	Resistivity/Ω·m	Thickness/m
1	100	2.5
2	500	50
3	50	∞

are used to synthesize the measurements by adding Gaussian noise with a standard deviation of 2% of the mean. The electrode spacing values are taken from [57]. The actual and measured apparent resistivity are given in Table 2-11.

Table 2-11 Synthetic apparent resistivity measurements for Case study B

No.	d/m	Actual apparent resistivity/Ω·m	Measured apparent resistivity/Ω·m
1	1	103.09	101.75
2	10	285.54	292.28
3	20	371.86	366.22
4	30	397.75	388.93
5	40	393.76	387.10
6	50	373.08	368.81
7	60	343.64	339.80
8	70	310.61	311.71
9	80	277.29	276.20
10	90	245.70	248.58
11	100	216.90	213.21

In this case, the uncertainty in the soil parameters is emphasized, and the prior distribution of σ is set to constant 0.02. The posterior estimation of the soil parameters are depicted in Table 2-12 and Figure 2-10. The parameters ρ_3 and h_2 have large uncertainties, and they are highly correlated.

Table 2-12 Estimated results of the parameters in Case study B from eleven measurements

Parameter	Actual	Bayesian posterior results	
		MAP	95% confidence interval
ρ_1/Ω·m	100	96.99	[92.77, 102.62]
ρ_2/Ω·m	500	459.52	[444.22, 502.32]
ρ_3/Ω·m	50	5.37	[3.62, 77.04]
h_1/m	2.5	2.14	[1.88, 2.55]
h_2/m	50	62.82	[45.92, 65.04]

Figure 2-11 compares the posterior predictive distribution and measurements of apparent resistivity, and it clearly shows the uncertainty at electrode spacing beyond 100 m due to shielding effects and limited observations.

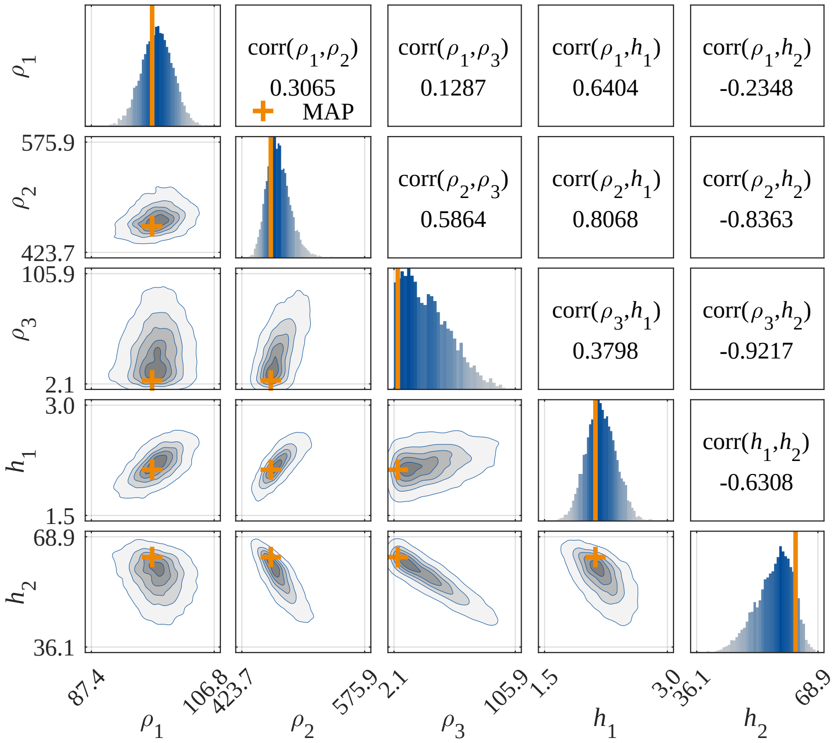

Figure 2-10 One- and two-dimensional posterior marginals and correlation coefficients of parameters in Case study B using eleven measurements.

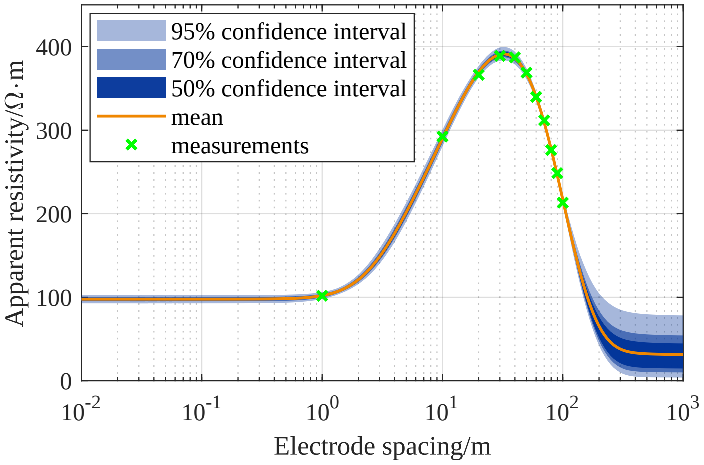

Figure 2-11 Bayesian posterior predictive distribution and measured apparent resistivity in Case study B using eleven measurements.

The performance of soil inversion can be improved by increasing measurements at electrode spacing where the posterior predictive apparent resistivity has a wide confidence interval. Table 2-13 supplements the apparent resistivity measurements at five large electrode spacings. Then, the posterior results obtained with sixteen data are shown in Figure 2-12 and Table 2-14. The MAP of parameters ρ_3 and h_2 are close to the actual values, and their confidence intervals are narrow. The one-dimensional posterior marginal probability distribution of parameters ρ_3 and h_2 is less skewed compared to the results in Figure 2-10. Correspondingly, the uncertainty of the posterior predictive apparent resistivity is also reduced, as shown in Figure 2-13.

Table 2-13 Supplement apparent resistivity measurements for Case study B

No.	*d*/m	Actual apparent resistivity/Ω·m	Measured apparent resistivity /Ω·m
12	160	108.79	110.53
13	220	71.05	68.91
14	280	58.72	59.75
15	340	54.41	54.14
16	400	52.66	52.84

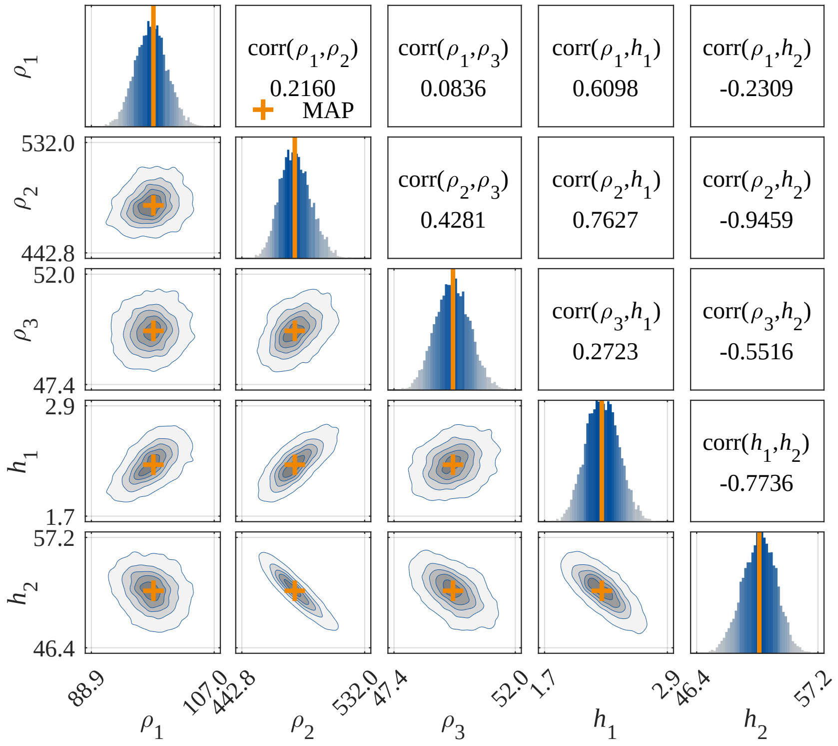

Figure 2-12 One- and two-dimensional posterior marginals and correlation coefficients of parameters in Case study B using sixteen measurements.

Table 2-14 Estimated results of the parameters in Case B from sixteen measurements

Parameter	Actual	Bayesian posterior results	
		MAP	95% confidence interval
ρ_1/Ω·m	100	98.07	[93.18, 102.37]
ρ_2/Ω·m	500	481.19	[461.47, 504.93]
ρ_3/Ω·m	50	49.62	[48.33, 50.91]
h_1/m	2.5	2.28	[1.99, 2.60]
h_2/m	50	52.01	[49.01, 54.81]

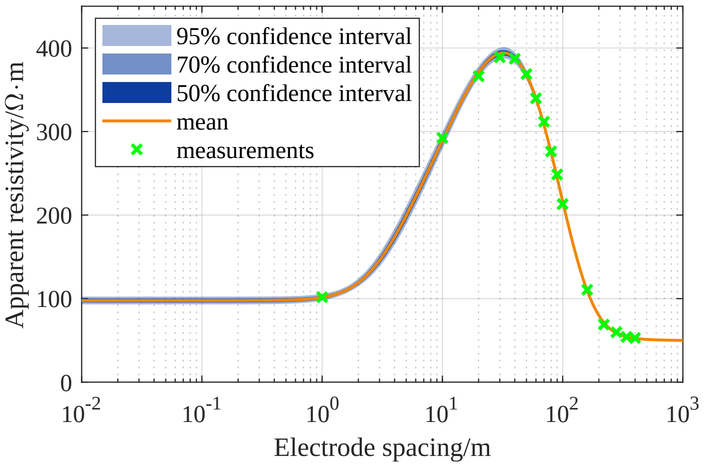

Figure 2-13 Bayesian posterior predictive distribution and measured apparent resistivity in Case study B using sixteen measurements.

3） Case Study C: A Four-Layer Earth

A four-layer earth structure is further used to illustrate the applicability of the Bayesian approach. The measured apparent resistivity data can be found in [42]. Table 2-15 shows the estimated soil parameters using different optimization methods in [42] and [45]. They achieve close goodness-of-fit, with root mean square errors of 2.52% and 2.02%[45], respectively. However, the estimated results of parameters ρ_2, ρ_3 and h_3 are quite different.

Table 2-15 Estimated results of the parameters—Case study C

Parameter	Results in [42]	Results in [45]	Bayesian posterior results	
			MAP	95% confidence interval
ρ_1/Ω·m	235.32	233.90	235.26	[227.04, 247.19]
ρ_2/Ω·m	3518.28	3185.18	4055.47	[2098.71, 5531.67]
ρ_3/Ω·m	205.53	102.11	194.03	[88.28, 382.15]
ρ_4/Ω·m	1504.71	1438.67	1417.62	[1219.84, 2221.60]
h_1/m	1.20	1.17	1.24	[1.10, 1.32]
h_2/m	5.33	6.30	4.64	[3.20, 9.28]
h_3/m	21.06	9.36	19.20	[8.60, 50.24]
σ	-	-	0.0132	[0.0130, 0.0451]

The Bayesian posterior results are given in Table 2-15 and Figure 2-14, where the above three parameters show large uncertainties. The estimate results in [42] and [45] are all enveloped by the 95% confidence interval of the posterior distribution. Figure 2-15 compares the posterior predictive distribution and measured data of apparent resistivity in this case.

The Bayesian results can be used to evaluate the sufficiency of the measured apparent resistivity data for achieving accurate estimation of soil parameters. In Case study A, the measurement points are adequate for a 2-layer simple earth structure. Thus, both the point

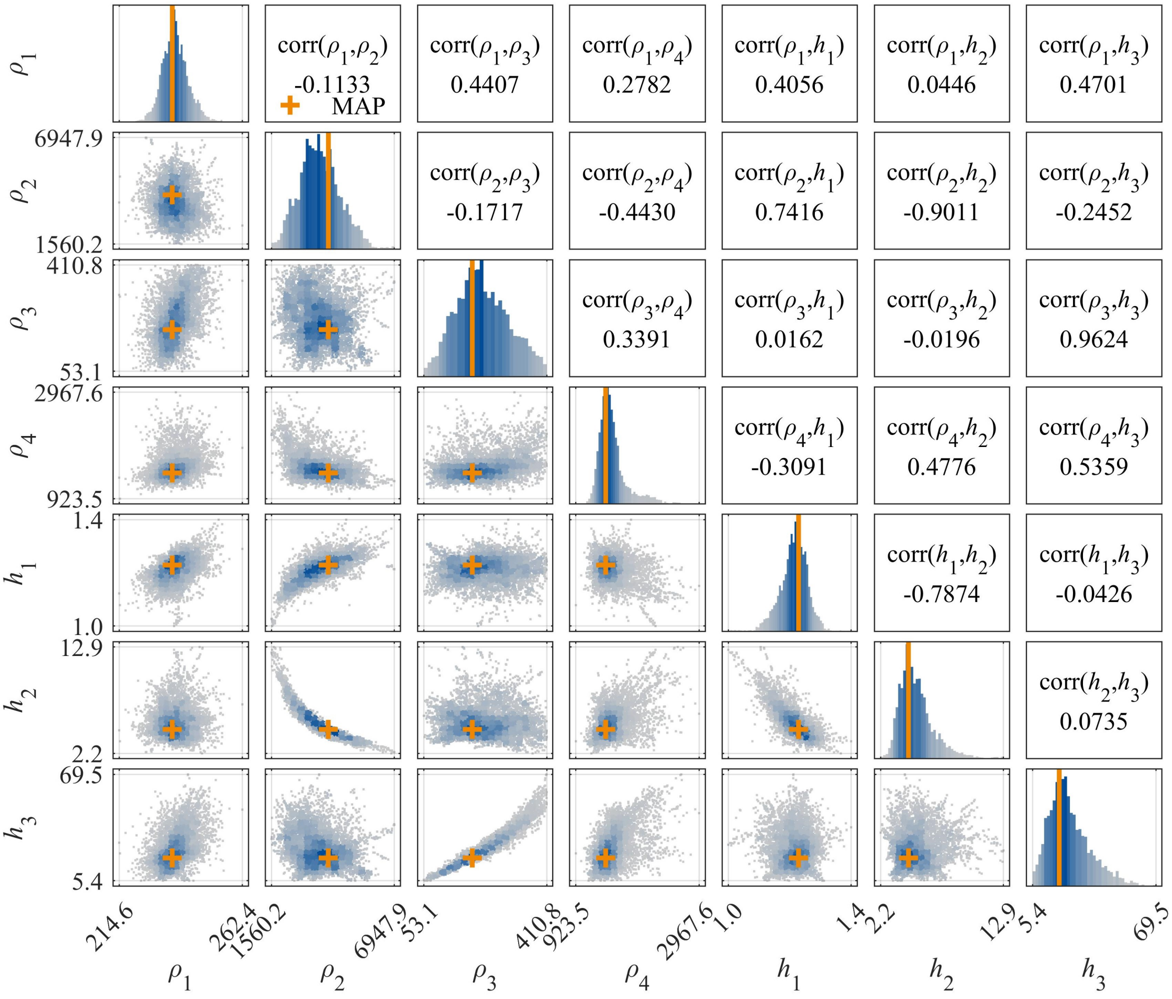

Figure 2-14 One- and two-dimensional posterior marginals and correlation coefficients of parameters obtained by the Bayesian method—Case study C.

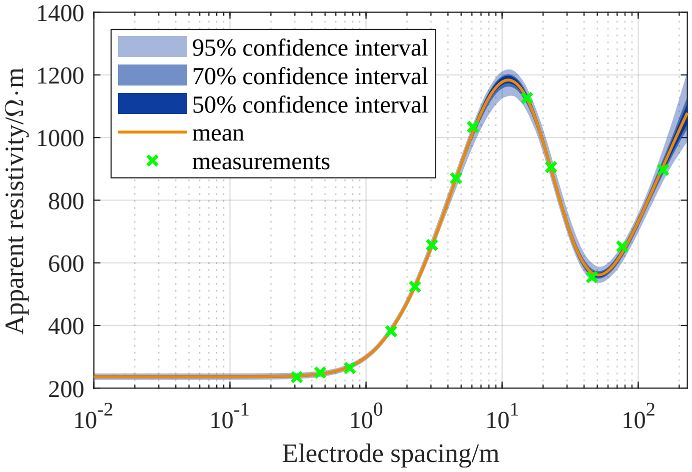

Figure 2-15 Bayesian posterior predictive distribution and measured apparent resistivity—Case study C.

estimation of the optimization method and the MAP of the Bayesian method can interpret the earth structure accurately, and the posterior confidence intervals of the soil parameters using Bayesian methods are relatively narrow. In other cases, the measured data may not capture the full details of the changes at some local extreme points in the apparent resistivity curve, especially when the earth presents a complex multilayer structure, which may limit the performance of the optimization method. The Bayesian posterior confidence interval of the apparent resistivity characterizes the uncertainty around the corresponding electrode spacing, and new measurements can be added at the electrode spacings with relatively wide confidence interval to improve the estimation accuracy.

4） Case Study D

In this case, the layer number of earth structures is further selected based on information criterion. The original apparent resistivity data from case TE1 in [55] are fitted with earth structures ranging from two to six layers. The MAP results are presented in Table 2-16, and the corresponding calculated apparent resistivity curves are compared with the measurements in Figure 2-16.

The maximum log-likelihood and information criteria for the earth models with different layer numbers are shown in Table 2-17. It can be seen that as the number of layers increases, the increase in maximum log-likelihood gradually slows down. Finally, the three-layer model is selected according to the minimum AIC and BIC with a penalty for complex models. It can also be seen from Figure 2-16 that when the number of layers exceeds 3, the MAP estimation results only change the fitting performance for very few measurements, which may lead to overfitting of noise parts.

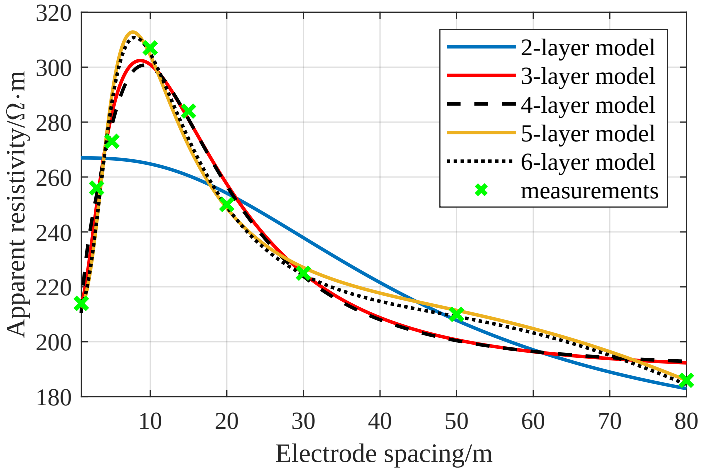

Figure 2-16 Calculated apparent resistivity curves of the earth models with different layer numbers—Case study D.

Table 2-16 Estimated MAP results of the earth models with different layer numbers—Case study D

Parameters	2-layer	3-layer	4-layer	5-layer	6-layer
$\rho_1/\Omega\cdot$m	266.96	209.93	62.94	210.76	210.71
h_1/m	26.85	2.26	0.10	2.27	2.34
$\rho_2/\Omega\cdot$m	160.54	389.11	243.19	384.49	388.76
h_2/m	∞	7.07	4.11	9.11	10.03
$\rho_3/\Omega\cdot$m		187.63	1024.78	129.17	78.80
h_3/m		∞	1.73	19.92	5.28
$\rho_4/\Omega\cdot$m			188.96	1385.03	96.34
h_4/m			∞	10.97	7.34
$\rho_5/\Omega\cdot$m				13.20	1371.79
h_5/m				∞	11.46
$\rho_6/\Omega\cdot$m					13.89
h_6/m					∞
σ	0.094	0.027	0.026	0.018	0.016

Table 2-17 Information criteria of the earth models with different layer numbers—Case study D

Number of layers	Maximum log-likelihood	AIC	BIC
2	-40.90	89.81	90.60
3	-29.62	71.23	72.42
4	-28.84	73.69	75.27
5	-26.01	72.03	74.00
6	-25.98	75.96	78.33

2.3 Calculation of Surface Geoelectric Fields Induced by GMD

2.3.1 Modeling and Calculation Method for Induced Geoelectric Field

1） Geoelectric Fields Using Different Earth Conductivity Models

During the geomagnetic storm, the geoelectric field is generated by the current source in space and its induced currents in the ground. The induced geoelectric field on the earth's surface is affected by the earth conductivity structure with a depth of hundreds of kilometers. Since the actual geoelectric structure is highly complex, it is necessary to simplify the earth conductivity structure when modeling the geoelectric field induced by GMD within a wide area. The widely used earth conductivity models for induced geoelectric field calculation consist of one-dimensional (1D) models, two-dimensional models and three-dimensional models.

For GMD study, the 1D earth model is mostly adopted due to its simplicity and acceptable accuracy. The variable conductivity of the earth can be modeled by a series of horizontal layers with specified conductivity and thickness. If there is a large lateral variation in the earth conductivity, especially in the coastal area, the induced geoelectric field on the land side could be significantly enhanced, which is called the coast effect, and its influence range is within a few kilometers from the coast.

As the one-dimensional model includes the uniform conductivity model and the 1D layered conductivity model, the analytical methods such as the plane wave method and the complex image method (CIM) can be used to calculate the induced geoelectric field. The former applies to low-latitude areas with large field to source distances, while the latter applies to areas with relatively small field to source distances. For geoelectric field modeling in a wide area, the piecewise 1D earth model can be used, that is, the conductivity in each sub-region is uniform in the horizontal direction, and the geoelectric field in each sub-region is solved separately.

For the geomagnetic induction analysis of the pipe network and power grid, the induced horizontal electric field $\mathbf{E} = [E_x, E_y]^{\mathrm{T}}$ on the ground surface is required, which can be calculated by combining the horizontal magnetic field $\mathbf{B} = [B_x, B_y]^{\mathrm{T}}$ and the earth conductivity model. Their relationship at frequency f is as follows[3, 63]:

$$\mathbf{E}(f, \mathbf{x}) = \mathbf{K}(f, \mathbf{x}) \cdot \mathbf{B}(f, \mathbf{x}) \tag{2-35}$$

where $\mathbf{K}(f, \mathbf{x})$ is the magnetotelluric transfer function (TF), also called magnetotelluric impedance in practical magnetotellurics[63], which can be inferred from electromagnetic measurements or numerical simulations; $\mathbf{x}$ is the spatial coordinates on the ground surface; and sub-x and sub-y refer to the components in the north and east directions. The spatial distribution of the magnetic field can be calculated from the space source currents[3, 59], or obtained by spatial interpolation from the measurements at one or multiple geomagnetic observatories[61].

For the earth with 3-D complex distribution of conductivity, the response $\mathbf{K}(f, \mathbf{x})$ is usually a full matrix as in (2-36), and changes with the spatial coordinates[63]. In this case, the magnetic field and electric field on the earth surface are usually not orthogonal, thus resulting in a spatially nonuniform geoelectric field.

$$\mathbf{K}(f, \mathbf{x}) = \begin{bmatrix} K_{xx} & K_{xy} \\ K_{yx} & K_{yy} \end{bmatrix} (f, \mathbf{x}) \tag{2-36}$$

For a uniform or 1-D horizontally layered earth model, the TF is reduced to (2-37), which can be calculated by the plane wave method[3].

$$\mathbf{K}(f,\mathbf{x}) = \begin{bmatrix} 0 & K \\ -K & 0 \end{bmatrix}(f,\mathbf{x}) \tag{2-37}$$

2） Plane Wave Method

The plane wave method[3] has been proved to be suitable for low latitude areas. The electromagnetic field on the earth surface generated by space surface current can be calculated by using the plane wave theory. The effect of space surface current on the earth can be equivalent to a plane electromagnetic wave incident perpendicular to the semi-infinite earth.

For a uniform earth, the following equation can be obtained based on Maxwell’s equations:

$$\frac{\partial^2 E(\omega)}{\partial z^2} = \mathrm{j}\omega\mu_0\sigma E(\omega)\ , \quad \frac{\partial^2 B(\omega)}{\partial z^2} = \mathrm{j}\omega\mu_0\sigma B(\omega) \tag{2-38}$$

The general solution form of the electric field in formula (2-38) is given by

$$E(\omega) = Ce^{-kz} + De^{kz} \tag{2-39}$$

where $k = \sqrt{\mathrm{j}\omega\mu_0\sigma}$ represents the propagation constant of electromagnetic wave in the earth, σ denotes the earth conductivity.

For the earth with uniform conductivity, the relationship between the surface electric field and the surface magnetic field in the frequency domain can be obtained

$$E_y(\omega) = -\sqrt{\frac{\mathrm{j}\omega}{\mu_0\sigma}}B_x(\omega), \qquad E_x(\omega) = \sqrt{\frac{\mathrm{j}\omega}{\mu_0\sigma}}B_y(\omega) \tag{2-40}$$

For a 1-D horizontally layered earth with N layers, the geoelectric field and the geomagnetic field on the earth surface are orthogonal. The transfer function K can be simulated via plane wave method. First, the transfer function on the upper surface of the bottom half space can be calculated according to equation (2-41). Then, recursive calculation is performed to obtain the transfer function of the upper layer based on formula (2-42). Finally, the transfer function $K = K_1$ on the surface can be obtained.

$$K_N = \frac{\mathrm{j}\omega}{k_N} = \sqrt{\frac{\mathrm{j}\omega}{\mu_0\sigma_N}} \tag{2-41}$$

$$K_n = \eta_n \frac{K_{n+1}\left(1+e^{-2k_nh_n}\right) + \eta_n\left(1-e^{-2k_nh_n}\right)}{K_{n+1}\left(1-e^{-2k_nh_n}\right) + \eta_n\left(1+e^{-2k_nh_n}\right)} \tag{2-42}$$

where σ_n, h_n, $k_n = \sqrt{\mathrm{j}\omega\mu_0\sigma_n}$, and $\eta_n = \mathrm{j}\omega/k_n$ refer to the conductivity, thickness, propagation constant and characteristic function of the n-th layer, respectively.

For the actual waveform of geomagnetic field in the time domain, it can be first transformed into the frequency domain by Fast Fourier Transform (FFT), and then the geoelectric field results in the frequency domain are calculated by using the transfer function of earth model. Finally, the geoelectric field results in the time domain are obtained by Inverse Fast Fourier Transform (IFFT).

For the online calculation of geoelectric field, the recursive formulation in the time domain is more suitable than the frequency domain method. Reference [127, 128] proposes the methods for fitting the earth responses, and then the geoelectric field can be obtained by recursive convolution in the time domain.

The transfer function $K(s)$ can be approximated by a rational function based on vector fitting method[129], expressed in the pole-residue form as

$$K(s) \approx r_0 + \sum_{i=1}^{n_{\mathrm{vf}}} \frac{r_i}{s - p_i} \tag{2-43}$$

where s is the Laplace variable; n_{vf} is the order of vector fitting; r_i and p_i are the residue and pole of i-th order.

Then the impulse response of the earth model is

$$\kappa(t) = r_0 \cdot \delta(t) + \sum_{i=1}^{n_{\mathrm{vf}}} r_i \cdot e^{p_i t} \tag{2-44}$$

where $\delta(t)$ is the impulse function.

Let us take the northward geoelectric field E_x as an example, which can be calculated by (2-45) at discrete instants $t_k = k\Delta t (k = 0, 1, \ldots, +\infty)$ to match the actual discrete input measurement.

$$\begin{aligned} E_x(t_k) &= \left(\kappa * B_y\right)(t_k) = \int_0^{t_k} \kappa(t_k - \tau) B_y(\tau)\mathrm{d}\tau \\ &= r_0 B_y(t_k) + \sum_{i=1}^{n_{\mathrm{vf}}} \left(\int_0^{t_k} r_i e^{p_i(t_k - \tau)} B_y(\tau)\mathrm{d}\tau \right) \end{aligned} \tag{2-45}$$

The i-th convolution term can be defined as an intermediate state $x_i (i = 1, 2, \ldots, n_{\mathrm{vf}})$, which can be computed recursively[130] by

$$x_i(t_k) := \int_0^{t_k} r_i e^{p_i(t_k - \tau)} B_y(\tau)\mathrm{d}\tau = e^{p_i \Delta t} x_i(t_{k-1}) + \int_{t_{k-1}}^{t_k} r_i e^{p_i(t_k - \tau)} B_y(\tau)\mathrm{d}\tau \tag{2-46}$$

3） Finite Element Method

If there is a large lateral variation in the earth resistivity, especially in the coastal area, the induced geoelectric field on the land side with high resistivity may be significantly enhanced. As the conventional analytical methods are usually unable to consider the effect of lateral variation in earth resistivity in the 2-D and 3-D earth model, numerical methods like the finite element analysis are needed to solve the geoelectric field induced by GMD. The following is a brief introduction to the basic equations and boundary conditions of the finite element method (FEM)[66, 67] for modelling the induced geoelectric fields in the frequency domain. In this study, the geomagnetic coordinate system is adopted, that is, the north and the east are the positive directions of the x-axis and the y-axis, respectively, and the z-axis represents the depth direction of the earth, and $z = 0$ at the surface. Assuming that the field source changes at an angular frequency ω, the basic equation of the eddy current field is

$$\begin{cases} \nabla \times \frac{1}{\mu} \nabla \times \dot{\mathbf{A}} + \sigma \left(\mathrm{j}\omega \dot{\mathbf{A}} + \nabla \dot{\phi} \right) = \dot{\mathbf{J}}_{\mathrm{S}} \\ \nabla \cdot \sigma \left(\mathrm{j}\omega \dot{\mathbf{A}} + \nabla \dot{\phi} \right) = 0 \end{cases} \tag{2-47}$$

where $\dot{\mathbf{A}}$ is the magnetic vector potential, $\dot{\phi}$ is the electric scalar potential, μ is the magnetic permeability, σ is the conductivity, and $\dot{\mathbf{J}}_{\mathrm{S}}$ is the current source in the non-conductor region. If the surface is taken as the upper boundary, $\dot{\mathbf{J}}_{\mathrm{S}}$ is 0. At the interface between two different conductivity regions in the ground, the interface conditions are as follows:

$$\mathbf{e}_n \times \left(\frac{1}{\mu_0} \nabla \times \dot{\mathbf{A}}_2 - \frac{1}{\mu_0} \nabla \times \dot{\mathbf{A}}_1\right) = 0 \tag{2-48}$$

$$\dot{\mathbf{A}}_2 = \dot{\mathbf{A}}_1 \tag{2-49}$$

$$\dot{\phi}_2 = \dot{\phi}_1 \tag{2-50}$$

$$\sigma_2 \left(\mathrm{j}\omega \dot{\mathbf{A}}_2 + \nabla \dot{\phi}_2 \right) \cdot \mathbf{e}_n = \sigma_1 \left(\mathrm{j}\omega \dot{\mathbf{A}}_1 + \nabla \dot{\phi}_1 \right) \cdot \mathbf{e}_n \tag{2-51}$$

where $\mathbf{e}_n$ is the normal unit vector at the interface.

（1） Upper Boundary

If the surface magnetic field is known, the surface can be taken as the upper boundary, and equation (2-52) and (2-53) can be obtained according to the continuity condition of the current.

$$\mathbf{e}_n \times \left(\frac{1}{\mu_0} \nabla \times \dot{\mathbf{A}}\right) = \dot{\mathbf{K}} \tag{2-52}$$

$$\sigma\left(\mathrm{j}\omega\dot{\mathbf{A}}+\nabla\dot{\phi}\right)\cdot\mathbf{e}_n=0 \tag{2-53}$$

where $\dot{\mathbf{K}}$ is the equivalent surface current density based on surface geomagnetic data.

（2） Lower Boundary

The electromagnetic field at the lower boundary of the model decays to a small extent, so its boundary condition is set as

$$\dot{\mathbf{A}}=0 \tag{2-54}$$

（3） Horizontal Boundary

The change of the geomagnetic field can be divided into the components of change along the north-south direction and the east-west direction, which are denoted as ΔB_x and ΔB_y, respectively. For the above two components, the horizontal boundary conditions are set separately to solve the model, and then the induced geoelectric field results of the two cases are superimposed. Taking case ΔB_x as an example, at the east and west boundary of the earth model, the magnetic field is parallel to the boundary surface.

$$\mathbf{e}_n\times\dot{\mathbf{A}}=0 \tag{2-55}$$

The current in the earth induced by ΔB_x is a circulation along the east-west direction. Therefore, in the solution process, the potentials of the east-west boundary surface must be equal to satisfy the current continuity condition[67] as

$$\dot{\phi}_E=\dot{\phi}_W \tag{2-56}$$

where $\dot{\phi}_E$ and $\dot{\phi}_W$ represent the potential values on the east and the west boundary surfaces, respectively.

At the southern and the northern boundaries of the earth model, the magnetic flux is perpendicular to the boundary surface as

$$\mathbf{e}_n\times\left(\frac{1}{\mu_0}\nabla\times\dot{\mathbf{A}}\right)=0 \tag{2-57}$$

For the calculation of the geoelectric field induced by ΔB_y, the horizontal boundary conditions are set similarly.

2.3.2 Results of Geoelectric Fields Considering Lateral Conductivity Variations

1） A Simple Coast Test Case

The lateral variation of the earth conductivity causes the distortion of the geoelectric field near the interface, which affects the induction results in power grids and pipeline networks. Figure 2-17 presents the thin-sheet coast model from Reference [67] adopted for demonstration. The parameters in the model are set as follows: The space source current is a uniform surface current at 100 km in height, with an amplitude of 1 A/m and a cosine waveform at 0.001 Hz; the depths of sea and land are 5 km and 500 km, and the conductivity is 4 S/m and 0.01 S/m, respectively. The finite element method[66, 67, 69] is used to calculate the spatial distribution of the induced geoelectric field on the earth surface, and the block model is used as a comparison to illustrate the additional influence of ocean, i.e., the geoelectric fields on the surface of land and sea are calculated separately by the plane wave method without considering their mutual influence[3, 62].

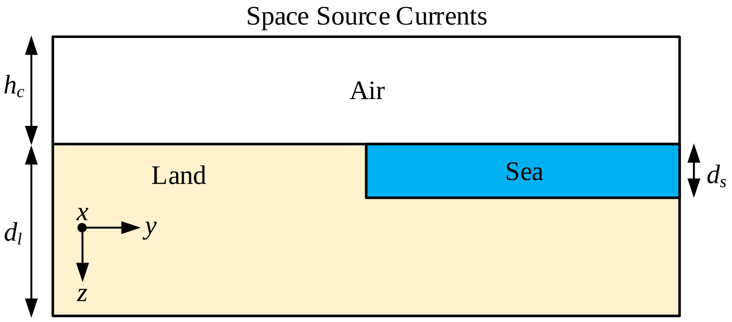

Figure 2-17 Schematic diagram of coast model excited by space source currents. The earth surface is on the $z = 0$ plane, and the coast is along the north direction at $y = 0$. The height of the space source currents, the depth of the ocean and land are h_c, d_s and d_l, respectively.

The direction of the space source currents is taken as east and north respectively, and the resulting surface geoelectric field distribution is shown in Figure 2-18. In the two cases, the geoelectric fields near the interface show different changes. For the space source currents perpendicular to the coast, i.e., along the east direction, an eastward geoelectric field is induced on the earth surface, and the H-polarization[67] causes the geoelectric field to increase on the land side near the interface. For the space source currents parallel to the coast, a northward geoelectric field is induced on the earth surface, and the E-polarization[66] causes the geoelectric field distortion, whose changes are opposite to the H-polarization case.

The ratio of geoelectric field on the land side near the coast obtained by thin-sheet model and block model E_{3D}/E_{1D} is used to illustrate the extent of the coast effect. As shown in

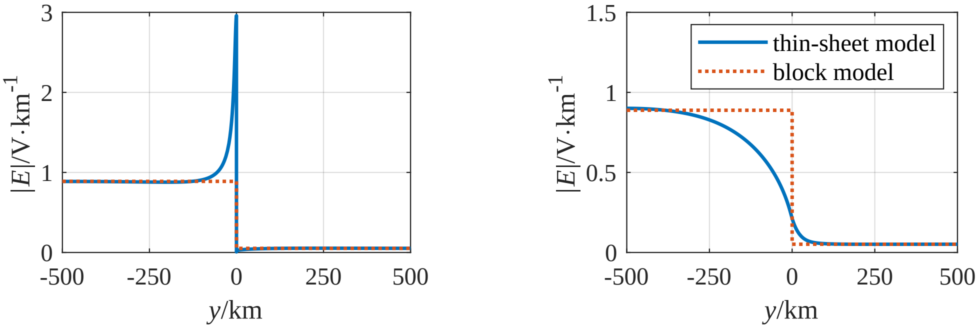

(a) Geoelectric field, H-polarization (b) Geoelectric field, E-polarization

Figure 2-18 Comparison of geoelectric field at 0.001 Hz based on thin-sheet and block earth model.

Figure 2-19, with the frequency increases, the enhancement effect of the H-polarization on the geoelectric field gradually decreases, whereas the weakening effect of the E-polarization on the geoelectric field tends to grow gradually stronger.

The effective distances of the coast effect, defined as the distance from the coast within which the difference between E_{3D} and E_{1D} on the land is greater than 10%[67], at different frequencies are shown in Fig 2-20. The effective distance of the E-polarization is larger than that of the H-polarization, and both generally tend to decrease as the frequency increases.

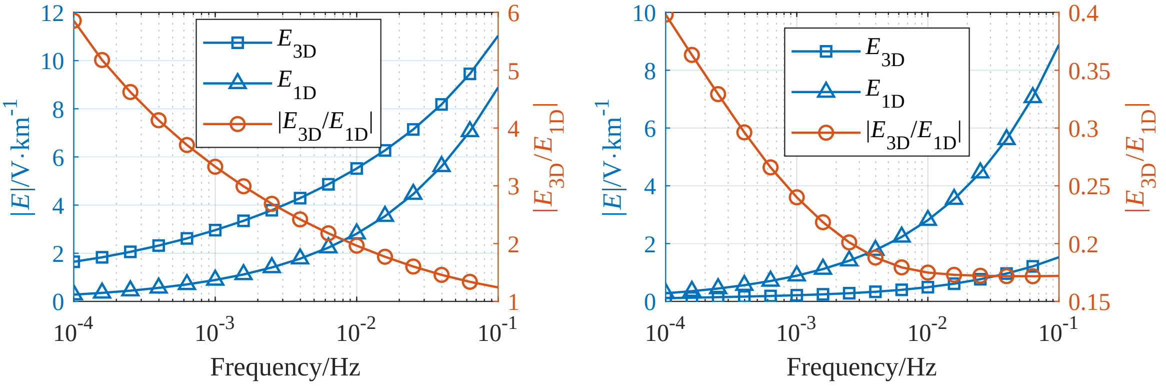

(a) Geoelectric field, H-polarization (b) Geoelectric field, E-polarization

Figure 2-19 Comparison of geoelectric field results on the land side near the coast using 3-D and 1-D earth model with respect to the frequencies.

2） Geoelectric Field Waveforms Due to Coast Effect

Then the impact of the coast effect on the time domain waveform of the geoelectric field is analyzed. The following waveform[68] of the horizontal magnetic field B_H generated by the electrojet is used as excitation:

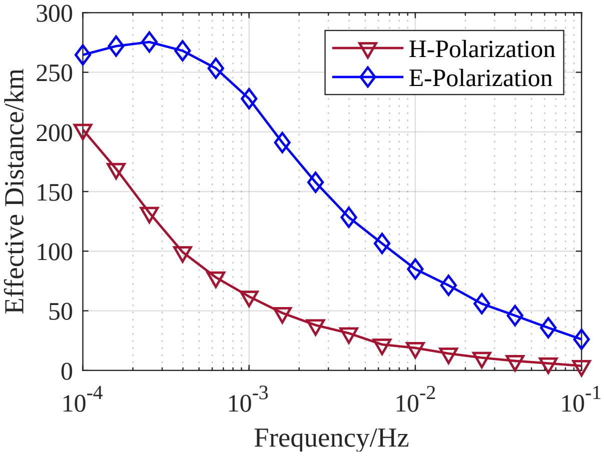

Figure 2-20 Effective distance of coast effect at different frequencies.

$$B_\mathrm{H}(t) = \frac{701\exp(0.05(t-100))}{1+\exp(0.0531(t-100))} \tag{2-58}$$

The corresponding waveforms of the magnetic field and its rate-of-change are shown in Figure 2-21. The peak values of the magnetic field and its rate-of-change are 561.2 nT and 500.0 nT/min respectively. In this test case, the 4-layer conductivity model in Table 2-18 is used as the base earth, which is adjacent to the ocean with a depth of 5 km.

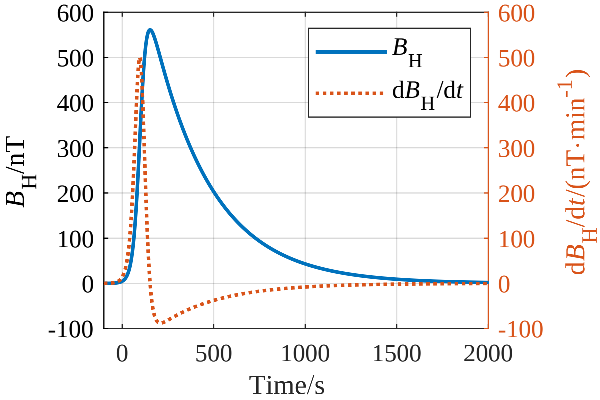

Figure 2-21 Waveform of magnetic variation and its rate-of-change generated by electrojet.

Table 2-18 One-dimensional layered earth model[131]

Layer	Thickness/km	Conductivity/S·m^{-1}
1	30	0.005
2	60	0.013
3	60	0.04
4	∞	0.3

When the magnetic field source is parallel to the coast, the waveforms of the electric field at different distances from the land side to the coast are shown in Figure 2-22. It can be seen that the amplitude of the geoelectric field waveform near the coast is significantly enhanced due to the influence of H polarization, which illustrates the importance of 3D earth modeling. As the distance to the coast increases, the peak value and duration of the geoelectric field waveform gradually become smaller and tend to the results of the 1D model.

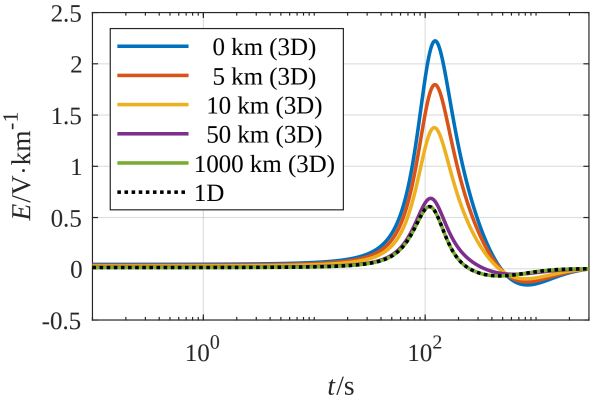

Figure 2-22 Waveforms of the electric field at different distances from the land side to the coast when the magnetic field source is parallel to the coast.

In contrast, when the magnetic field is perpendicular to the coast, the waveforms of the electric field at different distances from the land side to the coast are shown in Figure 2-23. In this case, the amplitude of the geoelectric field waveform near the coast is significantly weakened due to the influence of E polarization, which is opposite to the trend in the case of H polarization. When the distance to the coastline is far enough, the results of the 3D model tend to be those of the 1D model due to the weakening of the coast effect. The above results provide a reference for analyzing the impact of complex 3D earth conductivity distribution on the geoelectric field induced by GMD.

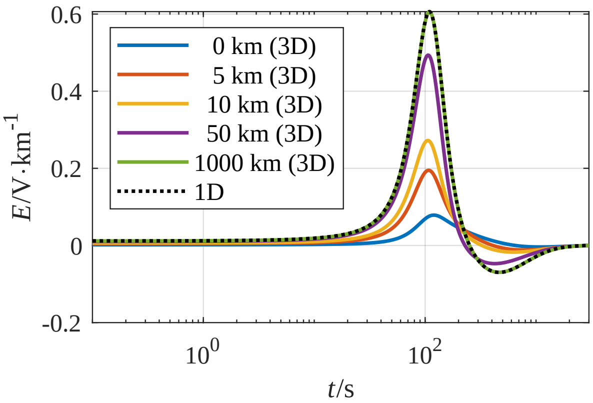

Figure 2-23 Waveforms of the electric field at different distances from the land side to the coast when the magnetic field source is perpendicular to the coast.

3） Geoelectric Field Results Considering 3D Complex Conductivity Distribution

The earth conductivity model of the UK is established taking into account the lateral variations on the surface caused by the ocean around the UK. The conductivity of the surface layer is based on the BGS2012 model[36, 132], as shown in Figure 2-24. The UK deep earth conductivity model adopts the GM one-dimensional layered earth model from [133]. Combined with the above surface and deep earth conductivity models, the finite element model of the UK is established.

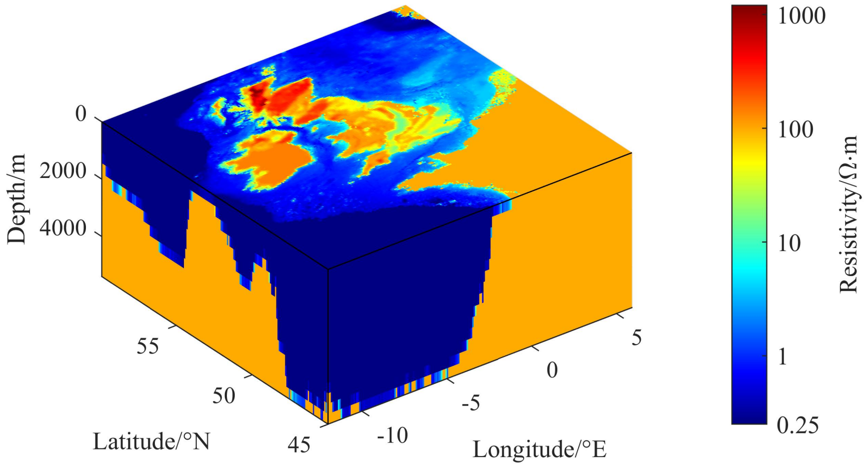

Figure 2-24 Surface earth resistivity model of UK.

In the case of a 200-year return period geomagnetic storm in the UK, the rate of change of the magnetic field is 840 nT/min. Assuming a period of 10 minutes, the corresponding amplitude H_0 = 1880 nT is used for the calculation of the induced electric field in the UK.

It should be noted that for the UK, since the auroral electrojet system mainly flows in the east-west direction, the large magnetic field eastward component may only appear in local areas. In this study, a more rigorous situation is considered that the surface eastward magnetic field is uniform.

The induced electric field distribution in the UK is studied below in the case of the northward and the eastward magnetic fields, respectively. The magnetic field in any other direction on the surface can be divided in these two directions, and then superimposed to obtain the actual inductive electric field distribution.

According to the geoelectric field distribution shown in Figure 2-25, the induced geoelectric field on the east and the west coasts generally increases significantly under the northward magnetic field excitation, while the induced geoelectric field on the north and the south coasts generally increases significantly under the eastward magnetic field excitation. The impact range of the coast effect is about tens of kilometers. Moreover, the finite element model used can take into account the enhancement of the geoelectric field induced by the coast effect in the UK.

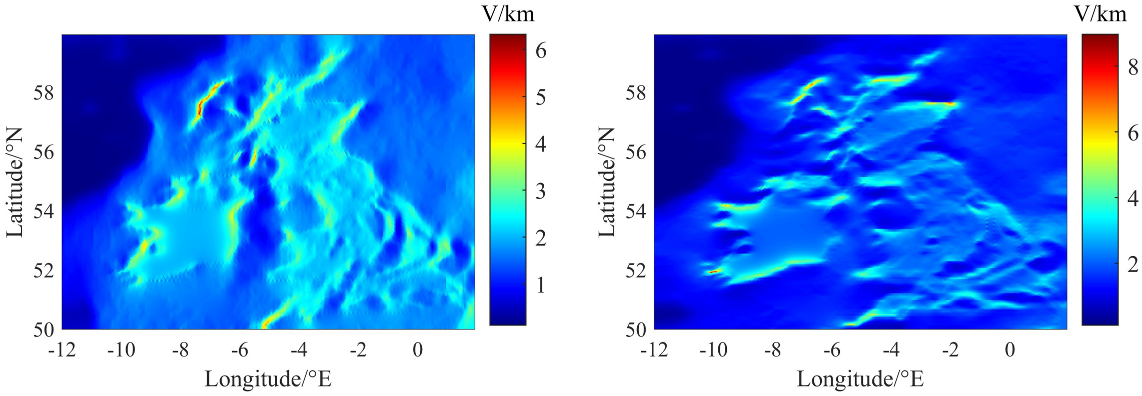

(a) Northward magnetic fields

(b) Eastward magnetic fields

Figure 2-25 Comparison of the induced geoelectric fields in cases of magnetic source fields with different directions.

2.4 Concluding Remarks

In this chapter, first, the extreme GMD scenario is established by combining extreme value statistics and theoretical upper limit method, which may provide a useful reference for risk assessment and mitigation measures for critical assets in power system. The 10,000-year GMD scenarios are generated to complement the classical 100-year and 200-year events. The 10,000-year GMD event is required for safety-critical nodes such as the UHV/EHV substations and nuclear power plants, etc. The return level of geomagnetic variation is estimated using the geomagnetic observations based on extreme value theory, which is then combined with the theoretical upper limit of the disturbance storm time (Dst) index to establish the 10,000-year GMD scenarios.

Then, a Bayesian inversion method is presented for the layered earth structure. Compared to classical optimization techniques, it can provide more comprehensive statistical properties, e.g. confidence intervals, correlation coefficients, marginal and joint probability distributions. It can quantify the uncertainty in soil parameters caused by measurement noises and shielding effects. Furthermore, the posterior samples of soil parameters can be used to predict the probability distribution of the grounding parameters of interest.

Finally, the peak value and spatio-temporal distribution of the geoelectric field on the surface in extreme GMD scenarios are modeled taking into account the vertical and horizontal variations of the earth conductivity. The results show that the geoelectric field near the coast can be distorted due to differences in conductivity between seawater and land. The increase or decrease of the geoelectric field is influenced by the direction of the geomagnetic interference source. We compared the relative contribution and effective distance of coastal effects on geoelectric field distortion at different frequencies. These results provide a basis for predicting voltage and current responses in energy networks to GMD hazards.

3 Efficient Analysis of GICs in Power Grids and Their Impacts on AC Voltage Security

GIC in the power grid during GMD can cause the half-cycle saturation of the transformer. It leads to a collective increase in the additional reactive power losses of the transformer, thereby affecting the voltage stability of the power system. The GMD impact assessment is affected by a large number of uncertain factors such as the intensity of geomagnetic source field variations, substation ground resistances, and AC loads, etc. It needs to be considered in the analysis of GIC flow and power flow of the power system. Thus, efficient probabilistic GIC analysis in power grids provides tools for assessing and mitigating small-probability tail risks of geomagnetic disturbances, especially in early warning and real-time scenarios.

In this chapter, first, a reduced nodal admittance matrix (RNAM) method is proposed to speed up GIC calculation based on Kron reduction. Moreover, the proposed RNAM method is used to achieve a more efficient analysis of probabilistic GICs, which considers the uncertainty of the substation grounding resistances. The novel method is compared with the classical algorithms including the nodal admittance matrix method, the Lehtinen-Pirjola method, and the bus admittance matrix method, and its efficiency improvement is illustrated with several power grid test cases.

Then, we evaluate the impacts of transformer effective GICs on the AC voltage security of power system. The sparse polynomial chaos expansion (PCE) method is used to quantify the impacts of uncertain input parameters, which is more efficient than Monte Carlo method. For bulk power systems with a large number of buses of interest, principal component analysis (PCA) is further used to compress the multiple outputs, which can reduce the number of surrogate models that need to be built.

This chapter is organized as follows. Section 3.1 details the proposed reduced nodal admittance matrix method for accelerating the calculation of GIC in power grids based on Kron reduction. In Section 3.2, the uncertainty quantification model for AC voltage evaluation is established, taking into account the random parameters in the DC and AC models of power grids. Then, an efficient algorithm based on PCE and PCA is further used to efficiently infer the probability distribution of AC voltage. Section 3.3 illustrates the computational efficiency advantages of the proposed methods with several power system test cases. Finally, Section 3.4 summarizes this chapter.

3.1 Reduced Nodal Admittance Matrix Method for Probabilistic GIC Analysis

This section proposes a more efficient GIC calculation method based on Kron-reduced nodal admittance matrix (RNAM)[134], which can be easily implemented on the basis of the classical full-node NAM method. It can reduce the size of the computational model and preserve the positive definiteness of the matrix, thus it can be efficiently solved by utilizing Cholesky decomposition. Furthermore, the proposed RNAM method is applied to the probabilistic GIC analysis considering the uncertainty of substation grounding resistance parameters[82]. The calculation procedure is accelerated by the proposed RNAM method, which is demonstrated by several power grid test cases[79, 81, 86, 135].

3.1.1 Classical Full-Node Admittance Matrix Method

In early research on geomagnetic induction modeling and calculation, the geoelectric field on the earth’s surface was usually calculated using a uniform or one-dimensional horizontally layered earth model due to a lack of knowledge of the earth’s resistivity. In addition, the components in the power grid and pipeline network are considered linear and the parameters are considered known. In this way, the induced voltages and currents in energy systems excited by uniform electric fields can be calculated using the linear superposition method. First, the induced current and voltage are evaluated under the conditions of 1 V/km northward and eastward electric field, respectively. Then, the induction results in the case of a geoelectric field with arbitrary direction and magnitude can be simply calculated using their linear combination.

In power networks with lumped parameters, the substation grounding and transformer effective GIC are the quantities of interest. The effect of GMD is modeled as a lumped voltage source on the transmission line and can be calculated by integrating the horizontal geoelectric field along the line. Traditionally, it is assumed that geoelectric field fluctuations caused by local changes in earth resistivity can be smoothed out by integration. Nowadays, however, long-distance transmission lines may span multiple geological regions, which are subject to more complex spatial distribution of geoelectric fields. In particular, the geoelectric field is strongly distorted in areas with sudden geological changes such as coasts. Some measurement and simulation studies illustrate differences in GIC results in power grids using one-dimensional and three-dimensional earth models[60, 65]. In addition, substation ground resistance is often uncertain due to local resistivity fluctuations and seasonal changes[136]. Thus, uncertainty quantification of GIC and its effect on AC voltage is necessary, which is usually time-consuming and requires efficient algorithms.

Consider a transmission network affected by GMD, including n_s substations, n_b buses and n_t transformers in the GIC flow path. The effect of the wide-area distributed horizontal geoelectric field **E** can be modeled as a voltage source in the power line:

$$V_{ik}^{\mathrm{tl,\,s}} = \int_{L_{ik}} \mathbf{E} \cdot \mathbf{dl} \tag{3-1}$$

where L_{ik} is the geographic path of the power line (i, k).

The single line diagram of the equivalent circuit of the power line (i, k) excited by the external electric field is shown in Figure 3-1, where y_{ik} is the equivalent admittance of a three-phase power line, which is the product of the per-unit-length admittance and its length. Usually, only the resistance part of the power line is considered in GIC analysis due to the very low frequency of the geoelectric field.

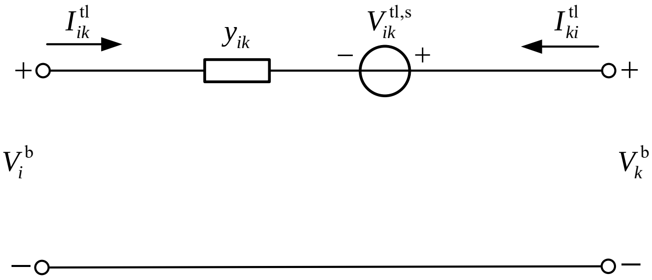

Figure 3-1 Equivalent circuit of power line (i, k) excited by external electric field.

Then the voltage source can be converted into the current injections at buses $\mathbf{J}^\mathrm{b}$ with Norton equivalent system, whereas the current injections at the substation grounding grid nodes $\mathbf{J}^\mathrm{s}$ are zero:

$$\mathbf{J}^\mathrm{b} = \mathbf{\Gamma}^\mathrm{b}\mathbf{E},\ \mathbf{J}^\mathrm{s} = \mathbf{0} \tag{3-2}$$

where $\mathbf{\Gamma}^\mathrm{b} \in \mathbb{R}^{n_\mathrm{b} \times 2n_\mathrm{z}}$ is the incident matrix; $\mathbf{E} \in \mathbb{R}^{2n_\mathrm{z} \times n_T}$ is the induced geoelectric field matrix, n_z is the number of geological zones, and n_T is the number of time instants.

In the classical GIC model for a power grid with multiple voltage levels, the substation grounding grid node set N_s and the bus node set N_b are combined into a full-node set $N_\mathrm{s} \cup N_\mathrm{b}$. Then, the full-node voltages $\mathbf{V} \in \mathbb{R}^{(n_\mathrm{s}+n_\mathrm{b}) \times n_T}$ can be calculated by the NAM method[75]:

$$\mathbf{YV} = \mathbf{J} = \begin{bmatrix} \mathbf{J}^\mathrm{s} \\ \mathbf{J}^\mathrm{b} \end{bmatrix} \tag{3-3}$$

where the nodal admittance matrix $\mathbf{Y} \in \mathbb{R}^{(n_\mathrm{g}+n_\mathrm{b}) \times (n_\mathrm{g}+n_\mathrm{b})}$ is sparse symmetric positive definite, and its nonsingularity needs to be guaranteed by a preprocessing step, i.e. removing the isolated bus nodes.

Further, the obtained full-node voltages can be used to calculate the transformer effective GICs[75] as follows

$$\mathbf{I}^{\mathrm{eff}} = |\mathbf{\Phi V}| = |\mathbf{\Phi Y}^{-1}\mathbf{J}| \tag{3-4}$$

where $\mathbf{\Phi} \in \mathbb{R}^{n_{\mathrm{t}} \times (n_{\mathrm{s}}+n_{\mathrm{b}})}$ is the transformation matrix for the transformer effective GICs.

The substation grounding GICs, depending on the voltages of the substation grounding grid nodes, can be calculated by

$$\mathbf{I}^{\mathrm{s}} = \begin{bmatrix} \mathbf{Y}^{\mathrm{s}} & \mathbf{0} \end{bmatrix} \mathbf{V} = \begin{bmatrix} \mathbf{Y}^{\mathrm{s}} & \mathbf{0} \end{bmatrix} \mathbf{Y}^{-1}\mathbf{J} \tag{3-5}$$

where $\mathbf{Y}^{\mathrm{s}} = \mathrm{diag}(R_{\mathrm{g},1}^{-1}, \ldots, R_{\mathrm{g},n_{\mathrm{g}}}^{-1}) \in \mathbb{R}^{n_{\mathrm{s}} \times n_{\mathrm{s}}}$ is the substation grounding conductance matrix, $R_{\mathrm{g},i}$ is the grounding resistance of the i-th substation, and $\mathbf{0} \in \mathbb{R}^{n_{\mathrm{s}} \times n_{\mathrm{b}}}$ is a zero matrix.

3.1.2 Proposed Model Reduction for Probabilistic GIC Analysis

1） RNAM method for Nodal Voltage Calculation

In this section, we detail the model order reduction method for GIC calculation based on Kron reduction[134]. If we partition the matrices by node type, the nodal voltage equations in (3-3) can be rewritten as:

$$\left[\begin{array}{c|c} \mathbf{Y}^{\mathrm{ss}} & \mathbf{Y}^{\mathrm{sb}} \\ \hline \mathbf{Y}^{\mathrm{bs}} & \mathbf{Y}^{\mathrm{bb}} \end{array}\right] \cdot \left[\begin{array}{c} \mathbf{V}^{\mathrm{s}} \\ \hline \mathbf{V}^{\mathrm{b}} \end{array}\right] = \left[\begin{array}{c} \mathbf{0} \\ \hline \mathbf{J}^{\mathrm{b}} \end{array}\right] \tag{3-6}$$

It is worth noting that block $\mathbf{Y}^{\mathrm{ss}}$ is a positive diagonal matrix since the coupling between the grounding grids of the substations through the earth can usually be ignored. Thus, its inverse $(\mathbf{Y}^{\mathrm{ss}})^{-1}$ is easy to find.

Using the voltage equations for substation grounding nodes N_{s}, $\mathbf{V}^{\mathrm{s}}$ can be expressed by the bus voltages $\mathbf{V}^{\mathrm{b}}$ as

$$\mathbf{V}^{\mathrm{s}} = -(\mathbf{Y}^{\mathrm{ss}})^{-1}\mathbf{Y}^{\mathrm{sb}}\mathbf{V}^{\mathrm{b}} \tag{3-7}$$

Substituting (3-7) into the bus voltage equations in (3-6), the calculation of $\mathbf{V}^{\mathrm{b}}$ can be reduced to

$$\widetilde{\mathbf{Y}}\mathbf{V}^{\mathrm{b}} = \mathbf{J}^{\mathrm{b}} \tag{3-8}$$

where the reduced nodal admittance matrix $\widetilde{\mathbf{Y}} := \mathbf{Y}^{\mathrm{bb}} - \mathbf{Y}^{\mathrm{bs}}(\mathbf{Y}^{\mathrm{ss}})^{-1}\mathbf{Y}^{\mathrm{sb}} \in \mathbb{R}^{n_{\mathrm{b}} \times n_{\mathrm{b}}}$ is the Schur complement of the block $\mathbf{Y}^{\mathrm{ss}}$ of the matrix $\mathbf{Y}$[134].

The above mathematical transformation automatically modifies the topology of each substation, i.e. eliminating the internal grounding grid node, as depicted in Figure 3-2. The proposed RNAM method has the following advantages:

1. The size of the reduced matrix $\widetilde{\mathbf{Y}}$ is less than that of the full-node matrix $\mathbf{Y} \in \mathbb{R}^{(n_{\mathrm{s}}+n_{\mathrm{b}})\times(n_{\mathrm{s}}+n_{\mathrm{b}})}$ in (3-3), thus it may reduce the storage requirements and speed up the GIC simulation without compromising the computational accuracy.
2. The matrix $\widetilde{\mathbf{Y}}$ preserves positive definiteness according to the Schur complement lemma[134].
3. The matrix $\widetilde{\mathbf{Y}}$ preserves sparsity since eliminating N_{s} does not create new non-zero entries between the buses in different substations.
4. The current injections at the bus nodes $\mathbf{J}^{\mathrm{b}}$ remain unchanged.

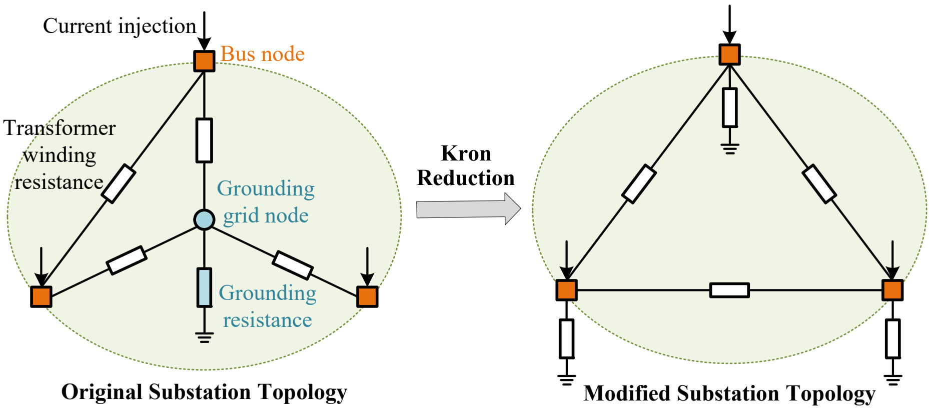

Figure 3-2 Schematic diagram of substation topology modification by eliminating the substation grounding grid node based on Kron reduction.

Furthermore, the interconnected power grid may involve multiple transmission system operators. Suppose we are interested in the GMD impacts on one sub-network whose bus set is denoted as $N_{\mathrm{b}1}$. The other buses $N_{\mathrm{b}2} = N_{\mathrm{b}} \backslash N_{\mathrm{b}1}$ belong to the neighboring sub-networks. Then (3-8) can be partitioned as

$$\left[\begin{array}{c|c} \widetilde{\mathbf{Y}}_{11} & \widetilde{\mathbf{Y}}_{12} \\ \hline \widetilde{\mathbf{Y}}_{21} & \widetilde{\mathbf{Y}}_{22} \end{array}\right] \cdot \left[\begin{array}{c} \mathbf{V}_1^{\mathrm{b}} \\ \hline \mathbf{V}_2^{\mathrm{b}} \end{array}\right] = \left[\begin{array}{c} \mathbf{J}_1^{\mathrm{b}} \\ \hline \mathbf{J}_2^{\mathrm{b}} \end{array}\right] \tag{3-9}$$

where the subscripts 1 and 2 in $\widetilde{\mathbf{Y}}_{ij}$, $\mathbf{V}_i^{\mathrm{b}}$ and $\mathbf{J}_i^{\mathrm{b}} (i,j = 1,2)$ correspond to the bus subsets $N_{\mathrm{b}1}$ and $N_{\mathrm{b}2}$, respectively.

Then the voltage $\mathbf{V}_1^{\mathrm{b}}$ of interest can be calculated by eliminating the bus set $N_{\mathrm{b}2}$ as follows:

$$\left(\widetilde{\mathbf{Y}}_{11} - \widetilde{\mathbf{Y}}_{12}\widetilde{\mathbf{Y}}_{22}^{-1}\widetilde{\mathbf{Y}}_{21}\right)\mathbf{V}_1^{\mathrm{b}} = \mathbf{J}_1^{\mathrm{b}} - \widetilde{\mathbf{Y}}_{12}\widetilde{\mathbf{Y}}_{22}^{-1}\mathbf{J}_2^{\mathrm{b}} \tag{3-10}$$

2） RNAM-based GIC Calculation

The subsequent GIC calculation can be simplified by using the RNAM in (3-8). If we partition the transformation matrix by node types as $\mathbf{\Phi} = \left[\mathbf{\Phi}^{\mathrm{s}}|\mathbf{\Phi}^{\mathrm{b}}\right]$, the formula (3-4) for the transformer effective GICs can be simplified as

$$\mathbf{I}^{\mathrm{eff}} = |\mathbf{\Phi}\mathbf{V}| = |\widetilde{\mathbf{\Phi}}\mathbf{V}^{\mathrm{b}}| = |\widetilde{\mathbf{\Phi}}\widetilde{\mathbf{Y}}^{-1}\mathbf{J}^{\mathrm{b}}| \tag{3-11}$$

where $\widetilde{\mathbf{\Phi}} := \mathbf{\Phi}^{\mathrm{b}} - \mathbf{\Phi}^{\mathrm{s}}(\mathbf{Y}^{\mathrm{ss}})^{-1}\mathbf{Y}_{\mathrm{sb}} \in \mathbb{R}^{n_{\mathrm{t}}\times n_{\mathrm{b}}}$ is the reduced transformation matrix.

Similarly, the formula (3-5) for the substation grounding GICs can be reduced to

$$\mathbf{I}^{\mathrm{s}} = \mathbf{Y}^{\mathrm{s}}\mathbf{V}^{\mathrm{s}} = -\mathbf{Y}^{\mathrm{s}}(\mathbf{Y}^{\mathrm{ss}})^{-1}\mathbf{Y}^{\mathrm{sb}}\mathbf{V}^{\mathrm{b}} = -\mathbf{Y}^{\mathrm{s}}(\mathbf{Y}^{\mathrm{ss}})^{-1}\mathbf{Y}^{\mathrm{sb}}\widetilde{\mathbf{Y}}^{-1}\mathbf{J}^{\mathrm{b}} \tag{3-12}$$

Alternatively, the substation grounding GIC can also be calculated by eliminating the bus nodes

$$\mathbf{I}^{\mathrm{s}} = -\mathbf{Y}^{\mathrm{s}}(\mathbf{Y}^{\mathrm{ss}} - \mathbf{Y}^{\mathrm{sb}}(\mathbf{Y}^{\mathrm{bb}})^{-1}\mathbf{Y}^{\mathrm{bs}})^{-1}\mathbf{Y}^{\mathrm{sb}}(\mathbf{Y}^{\mathrm{bb}})^{-1}\mathbf{J}^{\mathrm{b}} \tag{3-13}$$

where matrix $\mathbf{Y}^{\mathrm{ss}} - \mathbf{Y}^{\mathrm{sb}}(\mathbf{Y}^{\mathrm{bb}})^{-1}\mathbf{Y}^{\mathrm{bs}} \in \mathbb{R}^{n_{\mathrm{g}}\times n_{\mathrm{g}}}$ is typically dense. Hence, equation (3-12) is more preferred than (3-13) for GIC calculation due to the more sparse matrix and the fewer times of inversion.

The GIC flow in the transmission lines can be useful for model validation by differential magnetometry[20]. The GIC in power line (i, k) can be calculated as:

$$I_{ik}^{\mathrm{tl}} = y_{ik}\left(V_i^{\mathrm{b}} - V_k^{\mathrm{b}} + V_{ik}^{\mathrm{tl,\,s}}\right) \tag{3-14}$$

where y_{ik} is the admittance of the power line (i, k), and V_i^{b} and V_k^{b} are the voltages of buses i and k, respectively.

3） Uncertainty Quantification of GIC

The proposed RNAM method is applied to the probabilistic GIC analysis that considers uncertain resistance parameters in the power grid. Substation grounding resistance values are a major source of GIC uncertainty, since they are usually not included in the standard power flow data and are time-varying depending on local soil conductivity[82].

The resulting uncertainty of GIC can be quantified by using the Monte Carlo method. For each sample of substation grounding resistances, we modify the substation grounding conductance matrix $\mathbf{Y}^{\mathrm{s}}$ and block $\mathbf{Y}^{\mathrm{ss}}$. The latter is further used to update the reduced admittance matrix

$\widetilde{\mathbf{Y}}$ and the reduced transformation matrix $\widetilde{\mathbf{\Phi}}$. Finally we can obtain the probability distribution of the GICs with the RNAM method.

3.2 Voltage Security Analysis Based on Probabilistic Power Flow

In this section, the impacts of transformer GICs on the static voltage security is evaluated considering the uncertain factors including the geomagnetic electric fields, substation ground resistances, and AC loads, etc. Given the local effects of most random inputs during geomagnetic storms, the sparse regression method is used to reduce the number of polynomial expansion terms to avoid the curse of dimensionality. For bulk power systems with a large number of buses of interest, principal component analysis (PCA) is further used to compress the multiple outputs, which can reduce the number of surrogate models that need to be built. The accuracy and efficiency of the adopted algorithm are illustrated by 150-node and 500-node power system test cases.

3.2.1 Deterministic Power Flow Model During GMD

GICs flowing through the transformer cause the half-cycle saturation due to the nonlinear excitation characteristics of the iron core. The resulting additional reactive power losses can affect the voltage stability of the power system. The transformer neutral GIC cannot directly characterize the saturation degree of the autotransformer since the series winding and the common winding have a direct electrical connection. In comparison, the effective GIC flowing through the transformer t can be chosen as a more general metric:

$$I_t^{\mathrm{eff}} = \left| I_t^{\mathrm{high}} + \frac{I_t^{\mathrm{low}}}{\alpha_t} \right| \tag{3-15}$$

where I_t^{high} and I_t^{low} are the GICs flowing through the high-voltage and low-voltage coils, and α is the turns ratio.

Then, the additional reactive losses of the transformer t can be calculated using the effective GIC as follows[87, 137]

$$Q_t^{\mathrm{loss}} = g_t(I_t^{\mathrm{eff}}, V_i^{\mathrm{ac}}) \tag{3-16}$$

where $g_t(\cdot)$ depends on the core type of the transformer t, and V_i^{ac} is the AC voltage magnitude of the high-voltage side bus i of the transformer.

For a single-phase two-limb transformer, the function $g_t(\cdot)$ can be simplified to a linear relationship[138-140]:

$$Q_t^{\text{loss}} = k_t I_t^{\text{eff}} V_i^{\text{ac}} \tag{3-17}$$

where the factor k_t depends on the voltage level, structure and material of the transformer.

The additional reactive losses are further integrated into the power flow equations of the power system to evaluate their impacts on the AC voltage. In the power flow calculation, all buses are divided into three categories, including PQ, PV and slack buses. The bus on the high-voltage side of the transformer usually belongs to the PQ type, i.e. the active and reactive power injection are known, whereas the magnitude and phase angle of the AC voltage are quantities to be determined. However, the additional reactive losses caused by GIC are AC voltage-dependent, which need to be taken into account in the establishment and solving of the power flow equations.

During GMD, bus i needs to satisfy the following balance equations for nodal active power and reactive power injections:

$$\Delta P_i = P_{\mathrm{G}i} - P_{\mathrm{L}i} - P_i = 0, \quad i \in N_{\mathrm{PQ}}^{\mathrm{b}} \cup N_{\mathrm{PV}}^{\mathrm{b}} \tag{3-18}$$

$$\Delta Q_i = Q_{\mathrm{G}i} - Q_{\mathrm{L}i} - Q_{\mathrm{T}i} - Q_i = 0, \quad i \in N_{\mathrm{PQ}}^{\mathrm{b}} \tag{3-19}$$

where $N_{\mathrm{PQ}}^{\mathrm{b}}$ and $N_{\mathrm{PV}}^{\mathrm{b}}$ represent the PQ bus set and PV bus set; $P_{\mathrm{G}i}$ and $Q_{\mathrm{G}i}$ are the active and reactive power injection of the generator on bus i; $P_{\mathrm{L}i}$ and $Q_{\mathrm{L}i}$ are the active and reactive loads on bus i; P_i and Q_i are the active and reactive power flowing from node i to other branches, which can be calculated as follows

$$P_i = V_i^{\text{ac}} \sum_{j=1}^{n_{\mathrm{b}}} V_j^{\text{ac}} (G_{ij} \cos\theta_{ij} + B_{ij} \sin\theta_{ij}) \tag{3-20}$$

$$Q_i = V_i^{\text{ac}} \sum_{j=1}^{n_{\mathrm{b}}} V_j^{\text{ac}} (G_{ij} \sin\theta_{ij} - B_{ij} \cos\theta_{ij}) \tag{3-21}$$

$Q_{\mathrm{T}i}$ is the additional reactive power loss of the transformer due to GIC, which depends on the AC voltage magnitude of the high-voltage side

$$Q_{\mathrm{T}i} = \sum_{t=1}^{n_{\mathrm{t}}} \sigma_{it} Q_t^{\text{loss}} = \sum_{t=1}^{n_{\mathrm{t}}} \sigma_{it} g_t(I_t^{\text{eff}}, V_i^{\text{ac}}) \tag{3-22}$$

where σ_{it} is 1 if the high voltage side of transformer t is connected to bus i and 0 otherwise.

Then the nodal power balance equations for all buses in the power system can be summarized as the following vector form. The quantities to be solved include the voltage magnitudes of the PQ buses and PV buses, $\mathbf{V}^{\text{ac}} \in \mathbb{R}^{n_{\mathrm{PQ}}+n_{\mathrm{PV}}}$, and the phase angle of PQ buses relative to the slack bus, $\boldsymbol{\theta} \in \mathbb{R}^{n_{\mathrm{PQ}}}$.

$$\begin{bmatrix} \Delta\mathbf{P} \\ \Delta\mathbf{Q} \end{bmatrix} = \mathbf{f}\left(\begin{bmatrix} \boldsymbol{\theta} \\ \mathbf{V}^{\mathrm{ac}} \end{bmatrix}\right) = \mathbf{0} \in \mathbb{R}^{2n_{\mathrm{PQ}}+n_{\mathrm{PV}}} \tag{3-23}$$

where n_{PQ} and n_{PV} are the numbers of PQ-type and PV-type buses.

The state in the above nonlinear AC power flow equations can be solved by the Newton-Raphson method or the decoupled PQ method. The correction at step k is given by

$$\begin{bmatrix} \Delta\boldsymbol{\theta}^{(k)} \\ \Delta\mathbf{V}^{\mathrm{ac}(k)} \end{bmatrix} = -\mathbf{J}^{(k)} \begin{bmatrix} \Delta\mathbf{P}^{(k)} \\ \Delta\mathbf{Q}^{(k)} \end{bmatrix} \tag{3-24}$$

where $\mathbf{J}^{(k)}$ is the Jacobian matrix at step k, which can be calculated by

$$\mathbf{J}^{(k)} = \begin{bmatrix} \partial\Delta\mathbf{P}/\partial\boldsymbol{\theta} & \partial\Delta\mathbf{P}/\partial\mathbf{V}^{\mathrm{ac}} \\ \partial\Delta\mathbf{Q}/\partial\boldsymbol{\theta} & \partial\Delta\mathbf{Q}/\partial\mathbf{V}^{\mathrm{ac}} \end{bmatrix}\Bigg|_{\boldsymbol{\theta}^{(k)},\mathbf{V}^{\mathrm{ac}(k)}} \tag{3-25}$$

The absolute values of the elements in the diagonal submatrices of $\mathbf{J}^{(k)}$ are generally much larger than those of the elements in the off-diagonal submatrices. The reactive power loss caused by GIC needs to be considered when calculating the diagonal elements of the sub-matrix $\partial\Delta\mathbf{Q}/\partial\mathbf{V}^{\mathrm{ac}}$, and it mainly affects the AC voltage magnitude.

$$\frac{\partial Q_{\mathrm{T}i}}{\partial V_i^{\mathrm{ac}}} = \sum_{t=1}^{n_{\mathrm{t}}} \sigma_{it} \frac{\partial g_t(I_t^{\mathrm{eff}}, V_i^{\mathrm{ac}})}{\partial V_i^{\mathrm{ac}}} \tag{3-26}$$

After solving the AC voltages of the power system, it is necessary to further determine the reactive power output of the generator connected to the PV bus. If it violates the output limit of the generator, the bus needs to be converted from PV type to PQ type, and then the power flow equation needs to be resolved.

In summary, we need to carry out the analysis of the DC circuit and AC circuit of the power system sequentially during GMD, as shown in Figure 3-3. Finally we can obtain the AC voltage magnitude of the bus of interest as the output $y \in \mathbb{R}$. The overall computational forward model involves a large number of uncertain input parameters, including (a) induced geoelectric fields, (b) substation ground resistances, and (c) AC loads. They can affect the accuracy of the calculation of the AC voltage magnitude. These random inputs can be collectively represented as a vector $\boldsymbol{\xi} \in \mathbb{R}^{M}$, and they follows the joint probability density distribution $f(\boldsymbol{\xi})$. Thus, a more robust assessment of AC voltages can be carried out by taking into account the uncertainty propagation through the following computational model.

$$y = f(\boldsymbol{\xi}) \in \mathbb{R} \tag{3-27}$$

where the computational model f contains the steps of GIC flow and power flow analysis in Figure 3-3.

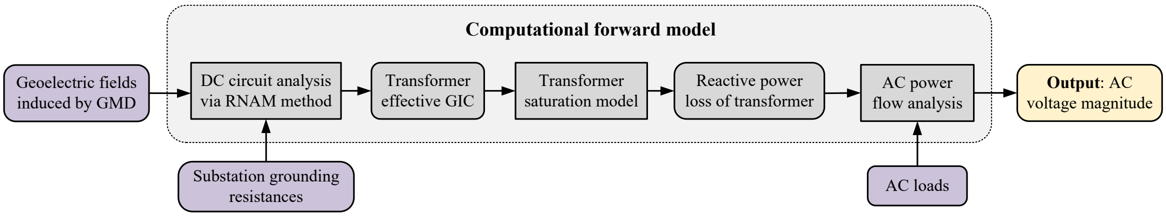

Figure 3-3 Flowchart of the computational forward model to assess the AC voltages of the power systems during GMD.

3.2.2 PCE Surrogate Model for Single AC Voltage Output

For the uncertainty quantification of AC voltages during GMD, it is time-consuming to solve the original nonlinear power flow equations of large-scale power grids using Monte Carlo (MC) method. PCE provides an efficient surrogate model $\tilde{f}$ by approximating the original computational model f with a series of multivariate polynomials[141].

$$y \approx \tilde{f}(\boldsymbol{\xi}) = \sum_{k=0}^{P} c_k \Psi_k(\boldsymbol{\xi}) \tag{3-28}$$

where $c_k \in \mathbb{R}$ is the coefficient of the multivariate polynomial, and the polynomial basis $\Psi_k(\boldsymbol{\xi})$ can be expressed as a product of each univariate orthonormal polynomials:

$$\Psi_k(\boldsymbol{\xi}) := \prod_{i=1}^{M} \varphi_{d_i}(\xi_i),\ d_i = 0, 1, \ldots, d \tag{3-29}$$

where any order polynomial basis of variable ξ_i are orthogonal, given its marginal probability density function $f_i(\xi_i)$.

$$\int_{\mathbb{R}} \varphi_r(\xi_i)\varphi_s(\xi_i) f_i(\xi_i)\mathrm{d}\xi_i = \begin{cases} 1, & \text{if } r = s \\ 0, & \text{otherwise} \end{cases} \tag{3-30}$$

For some common standard random distributions, such as uniform, normal and log-normal distribution, the orthogonal polynomial basis can be found in Table 3-1.

Table 3-1 Orthogonal polynomial basis of some random distributions[141]

Random distributions	Orthogonal polynomials	Support
Uniform	Legendre	$[-1, 1]$
Gaussian	Hermite	$[-\infty, +\infty]$
Gamma	Laguerre	$[0, \infty)$

In the case of d-order truncation, the total number of polynomials generated by the default tensor product expansion method in (3-29) is $P+1 = (d+1)^M$. In comparison, the total-degree truncation scheme only considers polynomials whose total order is less than d as in (3-31), thus its total number of multivariate polynomials is $P+1 = (M+d)!/M!/d!$.

$$\sum_{i=1}^{M} d_i \le d \tag{3-31}$$

In these truncation schemes, the total number of polynomials increases exponentially with the number of input parameters M, which leads to the curse of dimensionality. Hence, it is difficult to be directly applied to the analysis of large-scale power grids during GMD. And some additional constraints regarding are introduced to further reduce the size of the surrogate model. The hyperbolic truncation scheme is a more general scheme that uses q-norm conditions to reduce the number of polynomials.

$$(\sum_{i=1}^{M} d_i^{\,q})^{1/q} \le d \tag{3-32}$$

If we take $q < 1$, it can further restrict the existence of higher-order multivariate polynomials. And the total-degree truncation scheme is a special case when q is 1.

In the PCE model $\tilde{f}$, the polynomial basis can be determined by the probability distribution of random inputs. Their coefficients need to be fitted by fitting the training set obtained through the original calculation model f. Assuming that a training set $\{\xi_i, y_i\}_{i=1}^{L}$ with L samples is obtained in advance, the following equation can be established according to (3-28).

$$\begin{bmatrix} \Psi_0(\xi_1) & \Psi_1(\xi_1) & \dots & \Psi_P(\xi_1) \\ \Psi_0(\xi_2) & \Psi_1(\xi_2) & \dots & \Psi_P(\xi_2) \\ \vdots & \vdots & \ddots & \vdots \\ \Psi_0(\xi_L) & \Psi_1(\xi_L) & \dots & \Psi_P(\xi_L) \end{bmatrix} \cdot \begin{bmatrix} c_1 \\ c_2 \\ \vdots \\ c_P \end{bmatrix} = \begin{bmatrix} y_1 \\ y_2 \\ \vdots \\ y_L \end{bmatrix} \tag{3-33}$$

It can be rewritten in matrix form as follows:

$$\mathbf{H}\mathbf{c} = \mathbf{y} \tag{3-34}$$

Then, the coefficient $\mathbf{c}$ can be obtained by solving the linear equations using the least squares method.

$$\hat{\mathbf{c}} = \arg\min_{\mathbf{c}} ||\mathbf{H}\mathbf{c} - \mathbf{y}||_2^2 = (\mathbf{H}^{\mathrm{T}}\mathbf{H})^{-1}\mathbf{H}^{\mathrm{T}}\mathbf{y} \tag{3-35}$$

In order to further obtain a compact surrogate model with the smallest possible number of multivariate polynomials, a sparse PCE can be implemented by adding a regularization term in the objective function.

$$\hat{\mathbf{c}} = \arg\min_{\mathbf{c}} ||\mathbf{H}\mathbf{c} - \mathbf{y}||_2^2 + \lambda||\mathbf{c}||_1 \tag{3-36}$$

Then, the expected value and variance of the output y can be directly calculated from the polynomial coefficients via (3-37)-(3-38). And the full probability distributions can be evaluated by using the MC samples via the efficient PCE surrogate model.

$$\mathbb{E}[y] = c_0 \tag{3-37}$$

$$\mathrm{Var}[y] = \sum_{k=1}^{P} c_k^2 \tag{3-38}$$

3.2.3 Compressed Surrogate Models for Multiple AC Voltage Outputs Using Principal Component Analysis

GMD hazards with global impacts can threaten the voltage stability of large-scale transmission networks. In this case, there may be a large number of buses of concern. It usually requires a lot of work to build surrogate models for each output individually. To this end, we adopt a compact scheme based on principal component analysis (PCA)[142, 143] in order to achieve uncertainty quantification for large-scale power grids with multiple outputs during GMD.

Let us denote the outputs of the computational model as a vector $\mathbf{y} = (y_1, y_2, \ldots, y_N)^{\mathrm{T}}$, which collects the AC voltages of multiple buses. This can be calculated using the following original computational forward model $\mathbf{y} = f(\boldsymbol{\xi}) \in \mathbb{R}^N$.

A training set $\{\boldsymbol{\xi}_i, \mathbf{y}_i\}_{i=1}^{L}$ can be obtained in the experimental design stage. These outputs can be expressed as a matrix $\mathbf{Y}^{\mathrm{train}} \in \mathbb{R}^{N\times L}$ arranged as in (3-39), where the elements Y_{ni}^{train} represents the m-th output of the i-th sample.

$$\mathbf{Y}^{\text{train}} = \begin{bmatrix} \mathbf{y}_1 & \mathbf{y}_2 & \dots & \mathbf{y}_L \end{bmatrix} \tag{3-39}$$

The mean of the output vectors in the training set, $\boldsymbol{\mu} = (\mu_1, \mu_2, \dots, \mu_N)^{\mathrm{T}}$, can be calculated as

$$\boldsymbol{\mu} = \frac{1}{L}\sum_{i=1}^{L} \mathbf{y}_i \in \mathbb{R}^N \tag{3-40}$$

Thus, the output matrix can be normalized by subtracting the sample mean

$$\widetilde{\mathbf{Y}}^{\text{train}} = \begin{bmatrix} \mathbf{y}_1 - \boldsymbol{\mu} & \mathbf{y}_2 - \boldsymbol{\mu} & \dots & \mathbf{y}_L - \boldsymbol{\mu} \end{bmatrix} \tag{3-41}$$

Then, the economy-size singular value decomposition (SVD) is used to extract the principal components in the outputs

$$\widetilde{\mathbf{Y}}^{\text{train}} = \mathbf{U}\boldsymbol{\Sigma}\mathbf{V}^{\mathrm{T}} \tag{3-42}$$

where $\mathbf{U}$, $\boldsymbol{\Sigma}$, and $\mathbf{V}$ are the decomposed factors.

The diagonal matrix $\boldsymbol{\Sigma}$ collects the singular values, which characterize the contribution of each element in the vector after linear transformation to the total variance. We can select N' principal components using a threshold ε as follows:

$$\frac{\sigma_n}{\sigma_1} < \varepsilon, \ \forall n > N' \tag{3-43}$$

It allows to compress the original output $\mathbf{y} \in \mathbb{R}^N$ of the computational model into a new output $\mathbf{z} \in \mathbb{R}^{N'}$ through a linear transformation as follows

$$\mathbf{z} = f_{\text{PCA}}(\boldsymbol{\xi}) = (\mathbf{U}')^{\mathrm{T}}(f(\boldsymbol{\xi}) - \boldsymbol{\mu}) \in \mathbb{R}^{N'} \tag{3-44}$$

where the matrix $\mathbf{U}'$ consists of the first N' columns of the matrix $\mathbf{U}$.

In this way, we can use the training set $\{\boldsymbol{\xi}_i, \mathbf{z}_i\}_{i=1}^{L}$ about the compressed outputs to build the PCE model in (3-45). It can significantly reduce the number of surrogate models.

$$\mathbf{z} \approx \tilde{f}_{\text{PCE}}\left(\boldsymbol{\xi}\right) \tag{3-45}$$

This compressed vector $\mathbf{z}$ has no actual physical meaning and is just to save computational costs. In the subsequent uncertainty quantization, for a new input sample $\boldsymbol{\xi}$, we can reconstruct the AC voltage magnitudes of interest as follows:

$$\mathbf{y} = \mathbf{U}'\mathbf{z} + \boldsymbol{\mu} = \mathbf{U}'\tilde{f}_{\mathrm{PCE}}\left(\boldsymbol{\xi}\right) + \boldsymbol{\mu} \tag{3-46}$$

The process of uncertainty quantification of AC voltages during GMD based on the compressed surrogate model can be summarized as follows:

1. Construct a multivariate orthogonal polynomial basis using the probability distribution of each random input;
2. Obtain a training set $\{\boldsymbol{\xi}_i, \mathbf{y}_i\}_{i=1}^{L}$ using original computational model via MC method;
3. Compress the output using PCA method to obtain a new training set $\{\boldsymbol{\xi}_i, \mathbf{z}_i\}_{i=1}^{L}$;
4. For the compressed output of each dimension, determine the final set of main polynomial orthogonal basis and the coefficients from the training set based on the sparse regression method;
5. Generate a large number of random input samples using MC method, and calculate the compressed output using the efficient PCE surrogate models;
6. Reconstruct the bus voltage from the compressed outputs, and then calculate their statistical properties, e.g. the mean, standard deviation, confidence interval and probability distribution of the bus voltage.

3.3 Power Grid Case Studies

3.3.1 Results of GIC in Sanhua UHV Grid During Extreme GMD Scenarios

1） Results of Geoelectric Field in Sanhua Area

The plane wave method has been proved to be suitable for low latitude areas. The geoelectric field on the earth surface can be obtained by combining the measured geomagnetic field with the surface impedance. The 1-D layered earth conductivity model, as shown in Table 3-2[91], is used for modeling the geoelectric field in Sanhua region of China based on the plane wave method. The calculated results of geoelectric field during the GMD event from July 15th to 16th, 2000 are shown in Figure 3-4, with a peak value of 0.37 V/km.

Table 3-2 1-D layered earth conductivity model for Sanhua area[91]

Layer	Resistivity/Ω·m	Thickness/km
1	2000	30
2	770	60
3	2000	60
4	3	∞

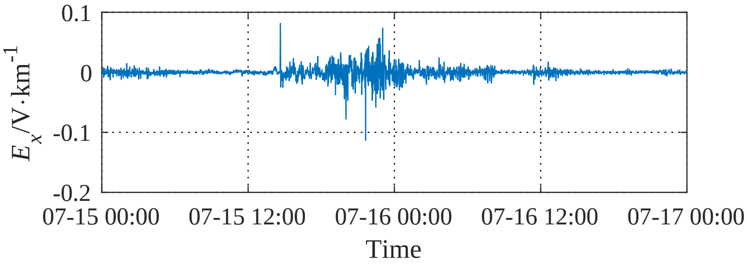

(a) Northward geoelectric field

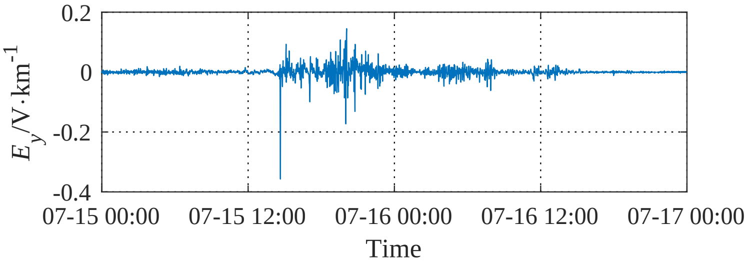

(b) Eastward geoelectric field

Figure 3-4 Time series of northward and eastward geoelectric fields for Sanhua area during July 15-16, 2000.

2） Characteristics of 10,000-year GICs in Sanhua Grid

The GIC flows in the grid rely on many factors like the geomagnetic source field, the earth conductivity structure and the characteristics of the power grid. GIC is mainly related to the DC resistance parameters of the power grid components, including the transmission lines, the transformer windings and the substation grounding grids. The planned Sanhua UHV power grid in China is used as the test case, which includes 36 substations and 46 lines[91]. Assume that there are two transformers in each substation, and the DC resistances of the series winding and common winding are 0.1827 and 0.1415 Ω, respectively. Moreover, the grounding resistance is 0.1 Ω for all substations.

The spatial distribution and time-varying characteristics of the GIC in the typical historical magnetic storm scenario are evaluated, as shown in Figure 3-5 and Figure 3-6. The nodes with large GIC are located at the edges and “corners” of the UHV grid, and the largest three-phase GIC is 137 A at Shanghai substation, which verifies the “corner effect”[144].

By scaling the above results, the largest and the average 10,000-year GICs in Sanhua UHV grid are 830 A and 300 A, respectively. For critical nodes in the UHV grid, appropriate mitigation measures need to be taken, since the possible GICs exceed the common threshold of the transformer in engineering standards, such as 75 A/phase of effective GIC in North American Electric Reliability Corporation (NERC) standard[32].

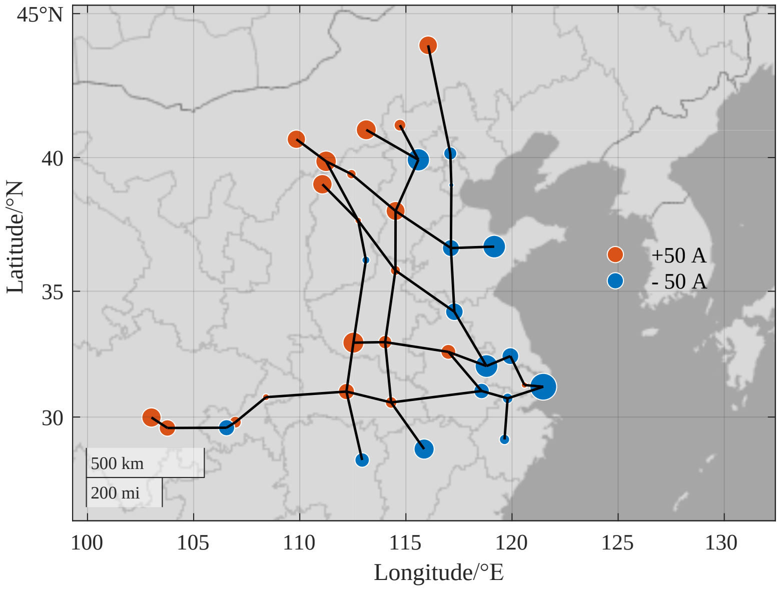

Figure 3-5 A snapshot of the GIC distribution in Sanhua grid at the moment of the largest GIC during the GMD event on July 15-16, 2000. (The positive GIC indicates it flow into the earth from the neutral point of the substation.)

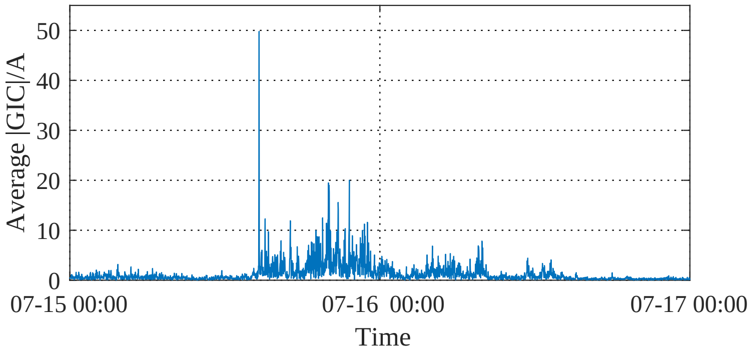

Figure 3-6 Time series of average GIC in Sanhua grid during the GMD event on July 15-16, 2000.

3.3.2 Probabilistic GIC Results Considering Uncertain Substation Grounding Resistances

1） Probabilistic GICs in EPRI-21 Power Grid Test Case

The probabilistic GICs in the EPRI-21 test case[79] during the GMD event on 2015/08/15 are analyzed for illustration. The geomagnetic data with 1-second time cadence at Yellowknife observatory from INTERMAGNET are used as inputs. The induced geoelectric fields are then calculated by using the Québec 1D layered conductivity model[72].

The substation grounding resistances are assumed to be independently log-normally distributed. Let $\ln R_{g,i} \sim \text{Normal}\left(\ln \bar{R}_{g,i}, (0.5 \ln \alpha)^2\right)$, where $\bar{R}_{g,i}$ is the base grounding resistance of i-th substation from[79], and α is the scaling factor. Thus, the 95% confidence interval of $R_{g,i}$

is $[\bar{R}_{g,i}/\alpha, \alpha\bar{R}_{g,i}]$. We take $\alpha = 2$ as a typical example, then the uncertainty of GIC is quantified by the Monte Carlo method. Figure 3-7 depicts the grounding GIC of substation 4. The GIC magnitude at 11:33:03 is 175.6 A using base resistance value, and its 95% confidence interval is [98.4, 291.1] A, which highlights the importance of uncertainty quantification for GIC.

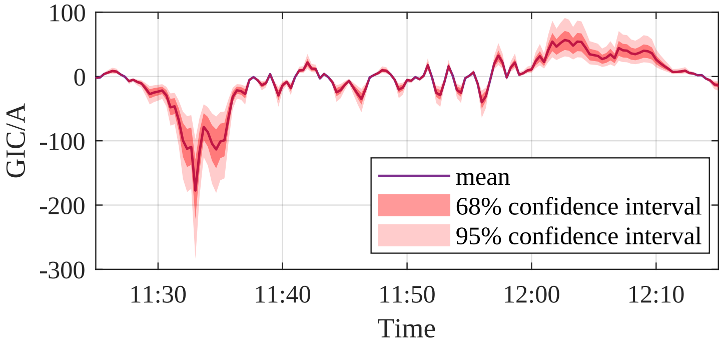

Figure 3-7 Mean and confidence intervals of grounding GIC of substation 4 in EPRI-21 test case[79] during the GMD event on 2015/08/15.

2） Comparison of Four GIC Calculation Methods

We have compared the performance of LP, NAM, BAM and RNAM methods in calculating the substation grounding GICs. The GIC results of the four methods are strictly consistent. Table 3-3 compares the GIC results in EPRI-21 power grid test case[79] under 1 V/km eastward geoelectric field using four calculation methods.

Table 3-3 Comparison of GIC results in EPRI-21 power grid test case[79] under 1 V/km eastward geoelectric field using four calculation methods

Substation number	Substation grounding GIC/A				
	Results in [79]	LP	NAM	BAM	RNAM
2	-189.29	-189.29	-189.29	-189.29	-189.29
3	-109.49	-109.50	-109.50	-109.50	-109.50
4	-124.58	-124.58	-124.58	-124.58	-124.58
5	-65.46	-65.45	-65.45	-65.45	-65.45
6	354.52	354.52	354.52	354.52	354.52
8	134.30	134.30	134.30	134.30	134.30

The design matrices of linear equations in the four methods are decomposed by different methods. The LU decomposition is used for the matrix in the LP method and the BAM method due to their asymmetry. The Cholesky decomposition, which is more efficient than the general LU decomposition, is adopted for the matrix $\mathbf{Y}$ in the NAM method (3-3) and the matrix $\tilde{\mathbf{Y}}$ in the RNAM method (3-8), since they are symmetric positive definite. Then the nodal voltages and GICs can be solved using the forward and backward substitution techniques.

In addition to the size and positive definiteness of the design matrix, its sparsity also affects the computational efficiency. Table 3-4 shows the size and number of non-zero entries of the design matrices of the four GIC calculation methods. Size n is the abbreviation for a $n \times n$ square matrix. It can be seen that for all the four power grid test cases, the design matrix of the proposed RNAM method has the least number of non-zero entries.

Table 3-4 Size and number of non-zero entries of the design matrices of the four methods

Test cases	Size				Number of non-zero entries			
	LP	NAM	BAM	RNAM	LP	NAM	BAM	RNAM
EPRI-21[79]	17	17	11	11	63	63	54	43
IEEE 118-GMD[86]	225	225	118	118	797	797	532	476
Sanhua UHV-EHV[81]	279	279	186	186	851	851	715	572
ACTIVSg2000[135]	2,801	2,801	1,551	1,551	10,083	10,083	7,483	6,117

For the ACTIVSg2000 power grid test case[135], the sparsity of the design matrices of the four methods is compared in Figure 3-8. It can be seen that the design matrices of the LP and NAM methods have the same sparsity. BAM method reduces the size of the design matrix at the cost of potentially introducing a large number of new non-zero entries compared to the matrix block $\mathbf{Y}_{\mathrm{bb}}$, whereas only few new non-zero entries are introduced in the RNAM method as shown in Figure 3-8(d).

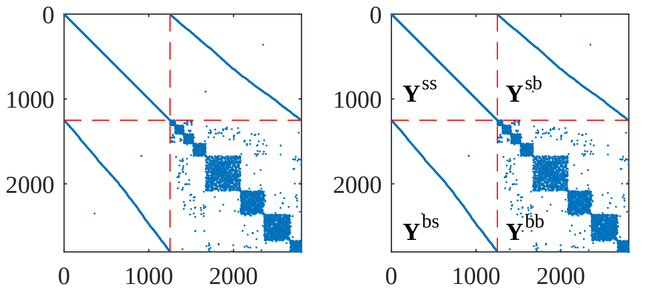

(a) LP (b) NAM

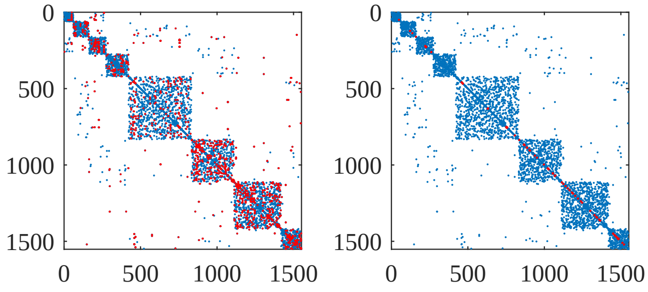

(c) BAM (d) RNAM

Figure 3-8 Sparsity of the design matrices of the four GIC calculation methods for the ACTIVSg2000 power grid case[135]. In subfigures (a) and (b), the red dashed lines depict the boundary between the substation grounding grid nodes and the buses. In subfigures (c) and (d), the red scatter points show the new non-zero entries in the design matrix of the BAM and RNAM methods compared to the matrix block $\mathbf{Y}^{\mathrm{bb}}$.

In addition, the condition numbers of the design matrices of the four methods are compared in Table 3-5, which may affect the numerical stability of the solution. It can be seen that RNAM method has the smallest condition number.

Table 3-5 Condition numbers of the design matrices of the four methods

Test cases	Condition number of the design matrix			
	LP	NAM	BAM	RNAM
EPRI-21[79]	7.81E+12	421.89	324.86	276.99
IEEE 118-GMD[86]	3.83E+12	652.27	2544.03	84.34
Sanhua UHV-EHV[81]	2.92E+12	184.41	92.23	91.71
ACTIVSg2000[135]	1.90E+13	3.46E+03	4.10E+04	1.42E+03

The current injections at the buses, calculated by using the geoelectric fields in this subsection, are added with random components to characterize the influence of spatially nonuniform geoelectric fields. And the number of time instants is taken as $3,600 \times 24 = 86,400$ (1-second time cadence and 1-day duration).

The GIC algorithms are tested using MATLAB R2020b software on a desktop with a 4.0 GHz Intel i7-6700K CPU and 64 GB RAM. Table 3-6 compares the total calculation time, including design matrix factorization and substation grounding GIC calculation, of the four methods for several power grid test cases.

Table 3-6 Comparison of algorithm performance of four GIC calculation methods

Test cases	Number of MC samples	Calculation time/s			
		LP	NAM	BAM	RNAM
EPRI-21[79]	1,000	29.2	11.5	20.9	8.5
IEEE 118-GMD[86]	1,000	397	164	253	99
Sanhua UHV-EHV[81]	1,000	478	210	353	141
ACTIVSg2000[135]	2,000	14,620	6,329	11,012	4,269

MATLAB provides two built-in functions “lu” and “decomposition” for LU factorization, and two built-in functions “chol” and “decomposition” for Cholesky factorization. The calculation time here refers to the best result of different functions for sparse matrix factorization in MATLAB R2020b software. Note that the efficiency ranking of the NAM and BAM methods may change when using the full matrix factorization. It can be seen that the RNAM method is more efficient than the classical methods. Taking the IEEE 118-GMD test case as an example, the RNAM method decreases the calculation time to 60.4% of the NAM method, 24.9% of the LP method, and 39.1% of the BAM method.

3） GIC Calculation of Multi-Area Power System

The proposed RNAM method can also be used to simplify the calculation of GIC of multi-area power grids. In this case, only subsystems within one area may be of concern. Boteler proposed a GIC calculation method when two-area power grids are interconnected through a single tie line, in which the external power grid can be equivalent to a single-port Thevenin circuit[80]. In comparison, our proposed RNAM method is suitable for multi-area power grids interconnected by multiple tie lines.

A three-area IEEE 118 power grid test case, as shown in Figure 3-9, is used to illustrate the feasibility of the RNAM method. It is assumed that the power grid in Area 1 is of concern, and it is connected to external power grids through multiple tie lines.

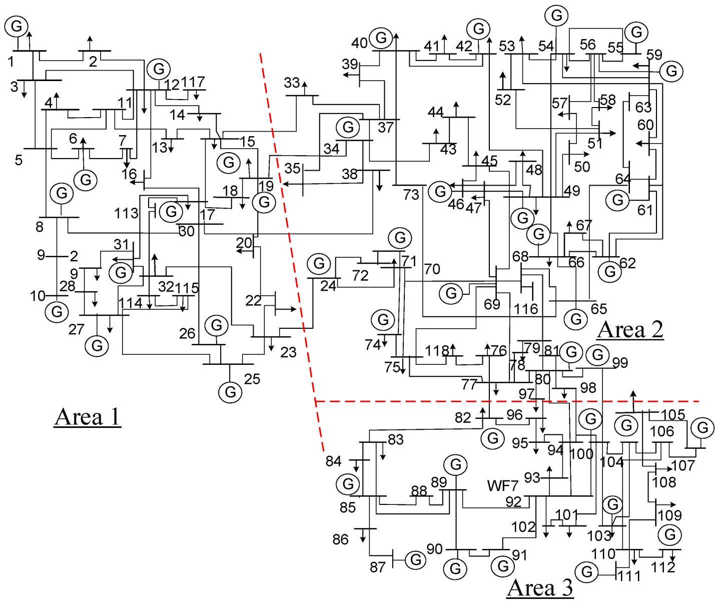

Figure 3-9 Three-area IEEE 118 power grid test case[145].

Then the bus nodes of the external power grid can be eliminated using equation (3-10). Figure 3-10 compares the substation GIC results in Area 1 calculated by the full power grid model and the reduced model. The results of the two models show consistency, which illustrates the feasibility of the RNAM method for dealing with multi-area power grids.

3.3.3 Results of Probabilistic AC Voltages in Power Grids During GMD

1） 150-Bus Power System Case

First, we evaluate the impact of substation grounding resistance and AC load uncertainties on the AC voltages in a 150-node power grid test case[146], as shown in Figure 3-11. The geoelectric field induced by GMD is taken to be 6 V/km, and the direction is set to north.

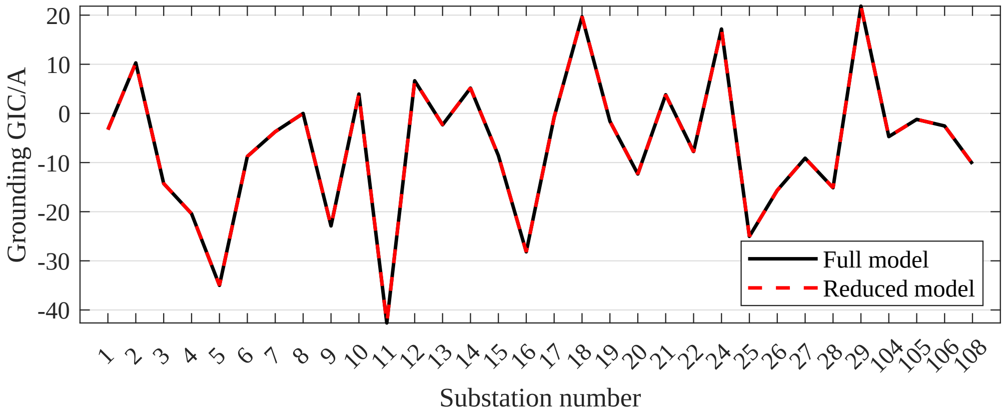

Figure 3-10 Comparison of substation grounding GIC in Area 1 of IEEE 118 power grid test case using full and reduced models.

The random inputs include 26 substation ground resistances and 90 AC loads. The grounding resistance is assumed to follow a lognormal distribution as described in Section 3.3.2. And the AC loads are assumed to be Gaussian distributed with a standard deviation of 5% of the base value. The outputs of interest are the AC voltage magnitudes of buses 13, 75, 78 and 89.

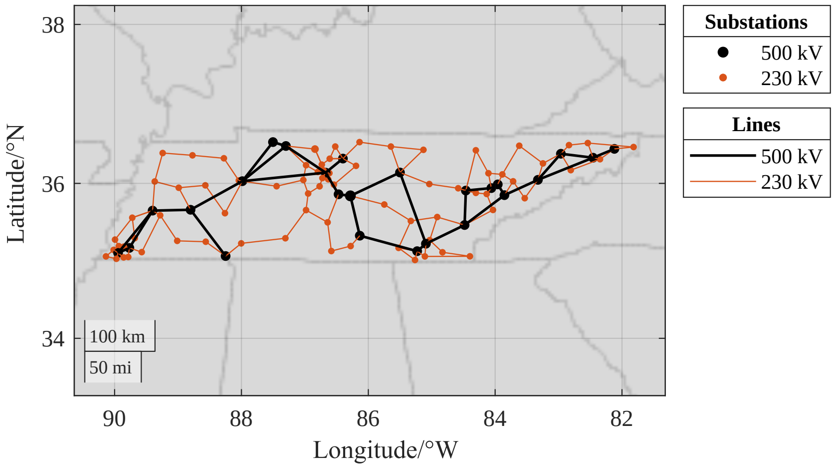

Figure 3-11 Topology diagram of the 150-node power system test case[146].

A second-order PCE surrogate model is built for each output of interest to achieve fast uncertainty quantification of AC voltage. To estimate the coefficients of the PCE models, the sample size of the training set was chosen to be 580, which is 5 times the number of random inputs. The creation of the training set and estimation of the PCE models took 8.23 s and 1.08 s, respectively.

Then, a validation set with 10,000 input samples was used to test the fitting accuracy of the PCE model, and was also used to calculate the probability distribution of the AC voltages. Figure 3-12 compares the cumulative distribution function (CDF) of the outputs obtained by the two models, and they show good consistency. The calculation times of the PCE method and MC method on the validation set are 0.15 s and 142.03 s, respectively. Thus, the total calculation time of the PCE method is 9.46 s. In fact, the training set can be obtained offline in advance, and the resulting surrogate model can be used for rapid online voltage security assessment.

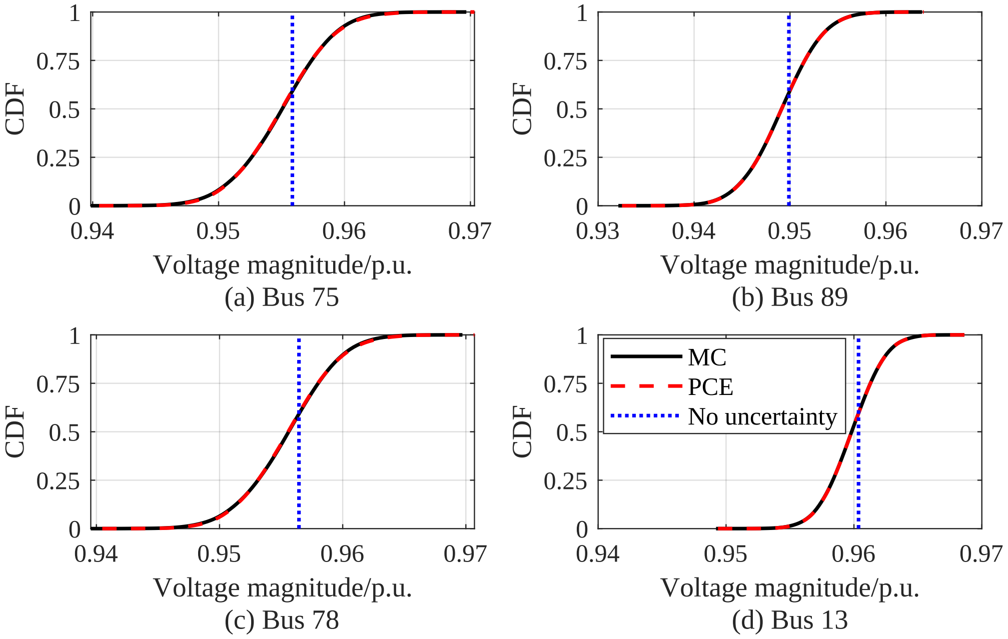

(a) Bus 75
(b) Bus 89
(c) Bus 78
(d) Bus 13

Figure 3-12 CDF of the AC voltage magnitude outputs obtained by the MC and PCE methods—150-node power system case.

In addition, the output obtained by ignoring the input uncertainty is taken as the base value in Figure 3-12. The AC voltage of the power system usually adopts 0.95 p.u. as the lower limit to ensure operational safety. Taking buses 75 and 78 as an example, their AC voltages are greater than 0.95 p.u. using the average value of the ground resistance and AC load. On the contrary, they have a certain risk of limit violation due to the uncertainty of parameters in DC and AC circuits.

2） 500-Bus Power System Case

A larger 500-node power system test example[147], as depicted in Figure 3-13, is adopted to further illustrate the applicability of the adopted PCE method. In this case, the outputs of interest are the AC voltage magnitudes of all PQ buses, the total number of which is 410. We consider a more conservative GMD evaluation scenario: the amplitude of the geoelectric field is 8 V/km, and its direction is random within the interval [0, 360°]. The total number of random inputs is 249, including 1 geoelectric field direction variable, 48 grounding resistances, and 200

AC loads. The maximum output of active and reactive power of generators is scaled by a factor of 1.2 as a preventive measure against GMD hazard.

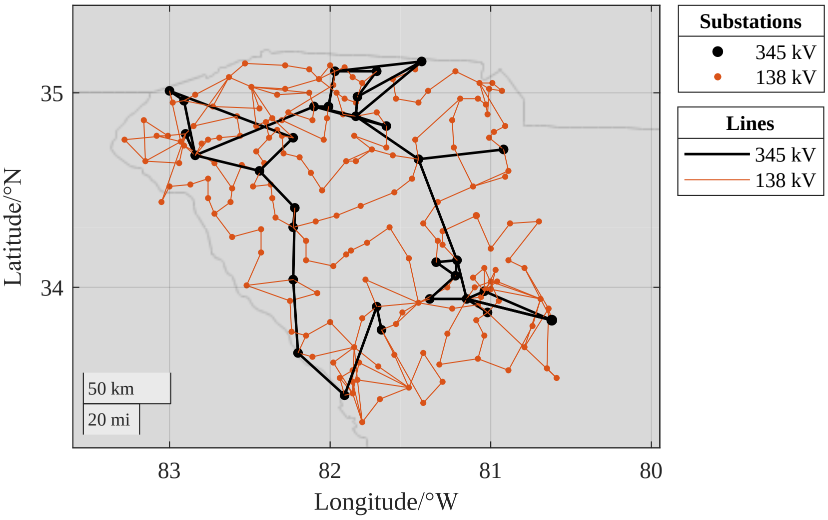

Figure 3-13 Topology diagram of the 500-node power system test case[147].

The sample size of the training set is chosen to be 5 times the number of random inputs, and the calculation time of this step is 51.81 s. The resulting output matrix of the training set is compressed using PCA. The threshold of the singular values is selected as 0.01, and the output dimension can be compressed from 410 to 34, as shown in Figure 3-14.

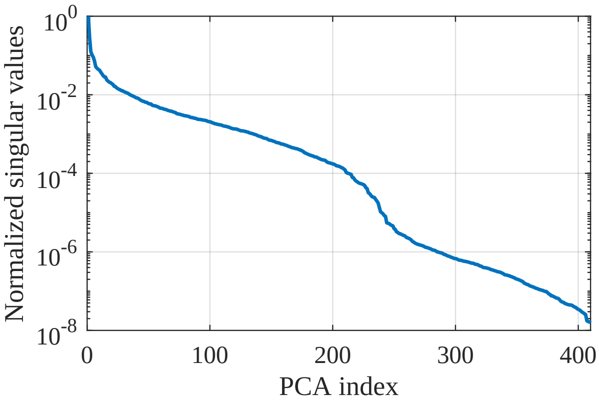

Figure 3-14 Normalized singular values of the training set's output matrix—500-node power system case.

Then, the PCE model is built for each compressed output, which took a total of 82.05 s. Finally, the probability distribution of the AC voltages is obtained using 50,000 input samples. The calculation times of the MC method via the original model and the PCE method via the surrogate model are 2112.60 s and 3.30 s, respectively. In terms of total time, the PCE method achieves a speed up of more than 15.5 times. Figure 3-15 shows the mean and 95% confidence interval of the output obtained by the PCE method, where the AC voltage magnitudes at some buses have large variability due to the random input parameters. Figure 3-16 and Figure 3-17 compares the mean and standard deviation of the AC voltage magnitudes obtained by the two methods, respectively.

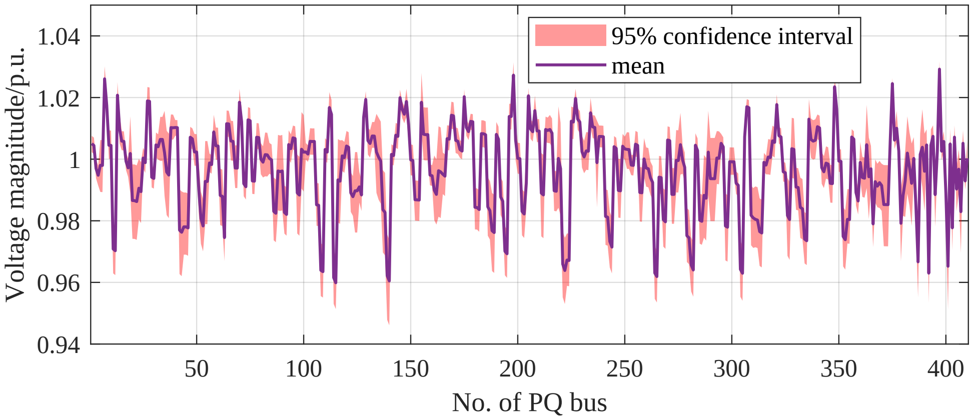

Figure 3-15 Mean and 95% confidence interval of the AC voltage magnitudes obtained by the PCE methods—500-node power system case.

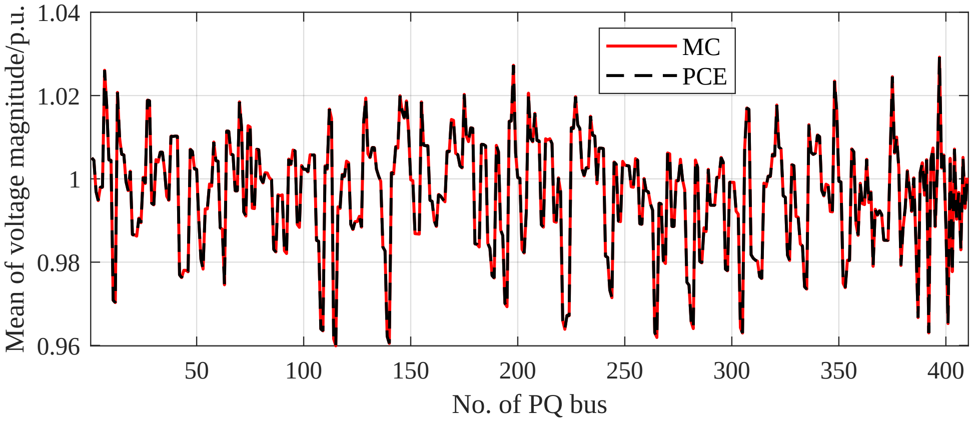

Figure 3-16 Comparison of the mean of the AC voltage magnitudes obtained by the MC and PCE methods—500-node power system case.

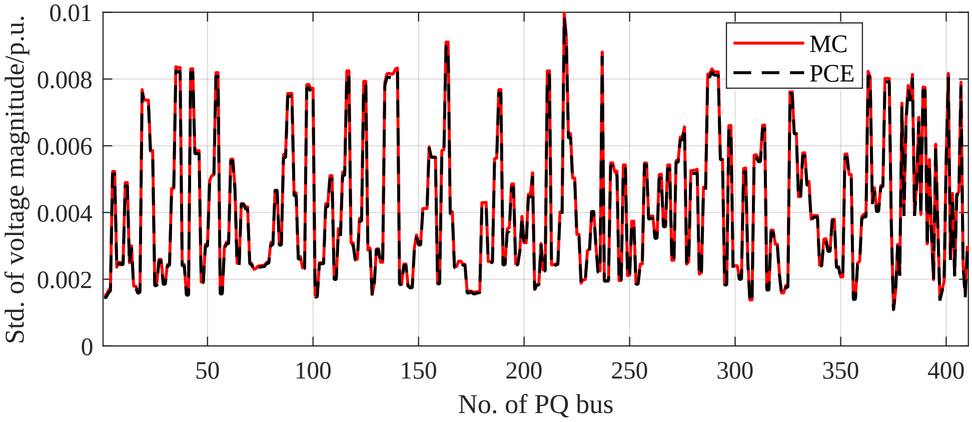

Figure 3-17 Comparison of the standard deviation of the AC voltage magnitudes obtained by the MC and PCE methods—500-node power system case.

Figure 3-18 shows the probability distribution of the AC voltages of all buses, which can be used to analyze the voltage safety margin of the overall system. These comparisons illustrate the accuracy of the compressed PCE method.

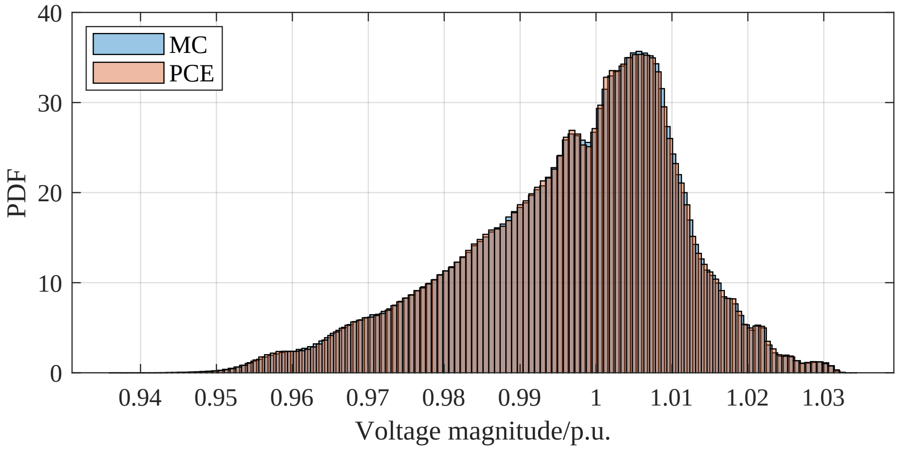

Figure 3-18 PDF of the AC voltage magnitude of all PQ buses obtained by the MC and PCE methods—500-node power system case.

3.4 Concluding Remarks

In this chapter, first, we propose a RNAM method for uncertainty quantification of GICs in power grids. The method makes GIC calculation more efficient than the classical full-node models, which is beneficial to time-critical online operation and control to mitigate GIC impacts. The results of several test cases show that it can save about 25%-40% of the simulation time compared with the classical full-node NAM method. It can provides an uncertainty quantification method for the power grid GIC, considering the uncertainty of substation grounding resistance parameters. It can provide the probability distribution of GIC for each substation rather than a single estimate, thus giving a more comprehensive understanding of tail risk with small probability but high impact. For some important transformers, the upper bound of the confidence interval of GIC can be used to evaluate the small-probability tail risk. The proposed RNAM method can help to formulate robust online operation strategies against uncertain GIC hazards in a more timely manner. For example, the probability distribution of GIC can be used as an input for robust optimization of power systems to develop more resilient GIC effect mitigation schemes.

Then, we evaluate the impacts of transformer effective GICs on the AC voltage security of power system. The GMD impact assessment is affected by a large number of random factors such as the intensity of geomagnetic source field variations, substation ground resistances, and

AC loads, etc. An efficient algorithm based on PCE and PCA is adopted to efficiently quantify the resulting uncertainty of AC voltages in bulk power system. The accuracy and efficiency of the adopted algorithm compared to classical Monte Carlo method are illustrated by 150-node and 500-node power system test cases.

4 Generalized Equivalence Method for Geomagnetic Induction Calculation in Gas Pipeline Networks

The geomagnetic induction may accelerate the corrosion of the pipeline, interfere with the cathodic protection system and other electrical equipment along the pipeline, which may have the potential to reduce the service life and even affect the operational safety of the pipeline[22-27]. Therefore, calculation of the geomagnetic induction in the pipeline is of great significance for evaluating the impacts of geomagnetic storms and identifying vulnerable pipes for protection. However, few studies exist on the induction in complex pipeline networks excited by nonuniform geoelectric fields. And the influence of nonlinear polarization of coating breakdown on the geomagnetic induction are not discussed in existing literature. These factors may significantly affect the level and distribution of geomagnetic response, which requires the development of more general and efficient models for large-scale pipeline networks.

This chapter is organized as follows. Section 4.1 details the proposed equivalent pi-circuit model of pipeline under nonuniform geoelectric field, and summarizes the algorithm of induction in pipeline networks. Section 4.2 discusses the generalized TL model of a pipeline for inductive and conductive EMI analysis and details the proposed algorithm to solve the voltage and current responses of a pipeline network considering nonlinear polarization effect. Then, the induction in the pipe network with nonuniform geoelectric field caused by geomagnetic source field and lateral conductivity variation is analyzed in Section 4.3. And Section 4.4 presents several illustrative pipeline network cases subjected to the geomagnetic disturbances and HVDC earth return currents, as typical examples of inductive and conductive interference, respectively. Finally, Section 4.5 concludes the chapter.

4.1 Calculation Model of Induction in Pipeline Networks Excited by Nonuniform Geoelectric Field

In this section, we propose a more general induction calculation model of pipeline networks under the spatially nonuniform geoelectric field based on the transmission line theory, and study the influence of non-uniformity of geoelectric field on PSP and GIC along the pipelines. Firstly, the equivalent pi-circuit of the pipeline with a nonuniform geoelectric field is established. Secondly, a nodal admittance matrix method for large-scale pipeline network analysis is proposed, and then the induced voltage and current along each pipeline can be obtained. Finally, the proposed algorithm is summarized and verified using a pipeline example.

The calculation formulas for the uniform geoelectric field, as a special case, are listed in this section, and are consistent with the results in Reference [24].

4.1.1 Derivation of Modified Equivalent PI-Circuit for a Pipeline Excited by Nonuniform Geoelectric Field

To analyze the geomagnetic induction of the pipeline, we need to establish the transmission line model due to the weak conductivity of the external insulating coating of the pipeline in practice. In this section, the pipeline is represented as a 1-D transmission line along the x-axis for ease of expression. The DSTL model of the geomagnetic induction in a pipeline[23, 24] is shown in Figure 4-1, where $E_t(x)$ is the tangential component of the geoelectric field along the pipeline, Z and Y are the per-unit-length series impedance and parallel admittance of the pipeline respectively, depending on the resistivity and geometric parameters of the steel and coating. In addition, the reactance and susceptance in the DSTL model are usually ignored because of the relatively low frequency of GMD (0.1 mHz-0.1 Hz).

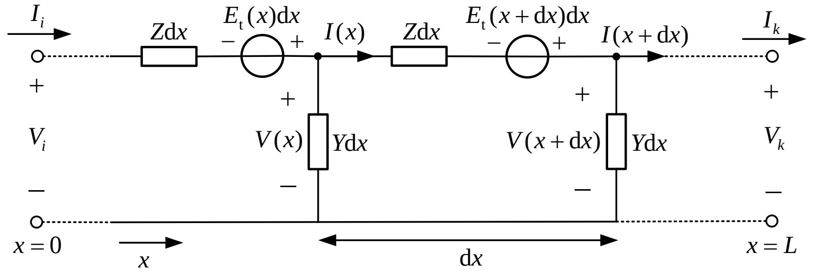

Figure 4-1 Schematic diagram of DSTL model of geomagnetic induction in a pipeline with nonuniform geoelectric field.

The propagation constant γ and characteristic impedance Z_C of the pipeline can be calculated as follows:

$$\gamma=\sqrt{ZY}, \quad Z_C=\sqrt{Z/Y} \tag{4-1}$$

The transmission line equations of the pipeline under the external electric field are described as follows:

$$\begin{aligned} \frac{\mathrm{d}V(x)}{\mathrm{d}x}+ZI(x)&=E_t(x) \\ \frac{\mathrm{d}I(x)}{\mathrm{d}x}+YV(x)&=0 \end{aligned} \tag{4-2}$$

where V and I are the voltage and current along the pipeline, defined as PSP and GIC in pipeline induction, respectively.

Suppose the length of the pipe is L, and set the left end $x=0$. The solution of the transmission line equations[148] is

$$\begin{bmatrix} V(x) \\ I(x) \end{bmatrix} = \mathbf{\Phi}(x) \begin{bmatrix} V(0) \\ I(0) \end{bmatrix} + \int_0^x \mathbf{\Phi}(x-z) \begin{bmatrix} E_{\mathrm{t}}(z) \\ 0 \end{bmatrix} \mathrm{d}z \tag{4-3}$$

where the chain-parameter matrix $\mathbf{\Phi}(x)$ of the pipeline is calculated by

$$\mathbf{\Phi}(x) = \begin{bmatrix} \cosh(\gamma x) & -Z_{\mathrm{C}} \sinh(\gamma x) \\ -\sinh(\gamma x)/Z_{\mathrm{C}} & \cosh(\gamma x) \end{bmatrix} \tag{4-4}$$

Thus, the relationship of the induced voltage and current between the two terminals of the pipeline (i, k) is as follows:

$$V_k = \cosh(\gamma L) V_i - Z_{\mathrm{C}} \sinh(\gamma L) I_i + \int_0^L \cosh\left(\gamma\left(L-z\right)\right) E_{\mathrm{t}}(z) \mathrm{d}z \tag{4-5}$$

$$I_k = -\frac{\sinh(\gamma L)}{Z_{\mathrm{C}}} V_i + \cosh(\gamma L) I_i - \int_0^L \frac{\sinh\left(\gamma(L-z)\right)}{Z_{\mathrm{C}}} E_{\mathrm{t}}(z) \mathrm{d}z \tag{4-6}$$

where the convolution term is the equivalent source to characterize the effect of the geoelectric field.

The pipeline excited by the induced geoelectric field can be modeled as an equivalent pi-circuit in order to achieve reduction of network induction models. For discontinuities in the pipeline, such as bends, insulating flanges, leakage points, and branch points, additional nodes can be added to divide the pipeline into multiple segments, and the equivalent pi-circuit model is established for each segment.

Boteler proposed the equivalent pi-circuit model for the pipeline with uniform geoelectric field $E_{\mathrm{t}}(x) = E_0$[24], as shown in Figure 4-2. The external uniform geoelectric field is characterized by an equivalent current source I^E, which is computed as follows:

$$I^E = \frac{E_0}{Z} \tag{4-7}$$

For the more general case of nonuniform geoelectric field, we establish an equivalent pi-circuit with two equivalent current sources for the pipeline as depicted in Figure 4-3, whose parameters are derived in detail below.

The relationship betweent the two ends of the equivalent pi-circuit in Figure 4-3 can be obtained according to Kirchhoff's voltage and current laws:

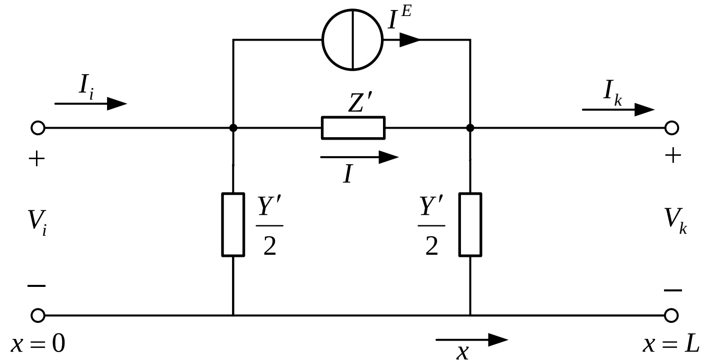

Figure 4-2 Equivalent pi-circuit for induction in a pipeline with uniform geoelectric field proposed by Boteler[24].

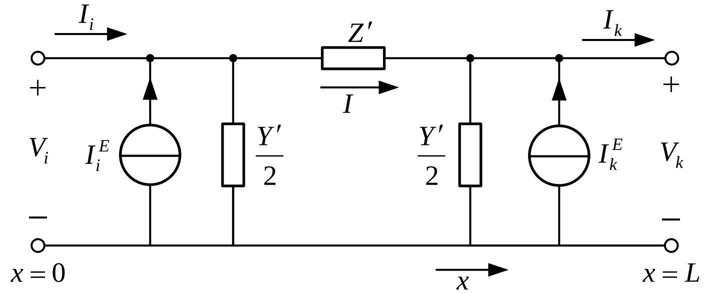

Figure 4-3 Equivalent pi-circuit for induction in a pipeline with nonuniform geoelectric field.

$$\begin{aligned} V_k &= V_i - IZ' \\ I_i &= I + V_i\frac{Y'}{2} - I_i^E \\ I_k &= I - V_k\frac{Y'}{2} + I_k^E \end{aligned} \tag{4-8}$$

Thus, the voltage and current at node *k* can be expressed by those at node *i* as

$$V_k = \left(1 + \frac{Y'Z'}{2}\right) V_i - Z'I_i - Z'I_i^E \tag{4-9}$$

$$I_k = -\,Y'\left(1 + \frac{Y'Z'}{4}\right) V_i + \left(1 + \frac{Y'Z'}{2}\right) I_i + \left(1 + \frac{Y'Z'}{2}\right) I_i^E + I_k^E \tag{4-10}$$

Comparing the coefficients in (4-9)-(4-10) with the results in (4-5)-(4-6) via transmission line theory, the parameters of the equivalent pi-circuit can be derived as

$$Z' = Z_\mathrm{C}\sinh(\gamma L) \tag{4-11a}$$

$$\frac{Y'}{2} = \frac{\cosh(\gamma L) - 1}{Z_\mathrm{C}\sinh(\gamma L)} \tag{4-11b}$$

$$I_i^E = -\frac{1}{Z_{\mathrm{C}}\sinh(\gamma L)}\int_0^L \cosh\left(\gamma(L-z)\right) E_{\mathrm{t}}(z)\mathrm{d}z \tag{4-11c}$$

$$I_k^E = \frac{1}{Z_{\mathrm{C}}\sinh(\gamma L)}\int_0^L \cosh\left(\gamma z\right) E_{\mathrm{t}}(z)\mathrm{d}z \tag{4-11d}$$

To calculate the equivalent current sources, different weights are given to the electric field along the line, hence the nonuniform electric field causes the difference in the amplitude of the two current sources. The effect of the nonuniform geoelectric field depends on pipeline lengths: for an electrically short pipeline satisfying $L \ll 1/\gamma$[23], we obtain $\cosh\gamma z \approx 1\ (0 \le z \le L)$, thereby the influence of the non-uniformity of geoelectric field is relatively small in this case; whereas the opposite is true for an electrically long pipeline.

In particular, for a uniform electric field $E_{\mathrm{t}}(x) = E_0$, the equivalent current sources in (4-11c)-(4-11d) can be simplified as

$$I_i^E = -\frac{E_0}{Z}, \quad I_k^E = \frac{E_0}{Z} \tag{4-12}$$

When the parallel admittance Y of the transmission line tends to 0, the parameters of the modified equivalent pi circuit in (4-11c)-(4-11d) can be simplified as (4-13a)-(4-13d), which is equivalent to the circuit model of the power line in Figure 3-1. It means that the derived two-port equivalent model of the distributed parameter circuit in this chapter is compatible with the power grid model, and the latter one can be considered as a special case.

$$Z' = ZL \tag{4-13a}$$

$$\frac{Y'}{2} = 0 \tag{4-13b}$$

$$I_i^E = -\frac{1}{ZL}\int_0^L E_{\mathrm{t}}(z)\mathrm{d}z \tag{4-13c}$$

$$I_k^E = \frac{1}{ZL}\int_0^L E_{\mathrm{t}}(z)\mathrm{d}z \tag{4-13d}$$

4.1.2 Calculation of Geomagnetic Induction in Pipeline Networks Using Modified Equivalent PI-Circuit

1） Calculating Nodal PSP via Admittance Matrix Method

The equivalent pi-circuits of pipelines are interconnected to form a network, as illustrated in Figure 4-4, where the equivalent current sources on the connected pipelines are integrated into the nodal current injection.

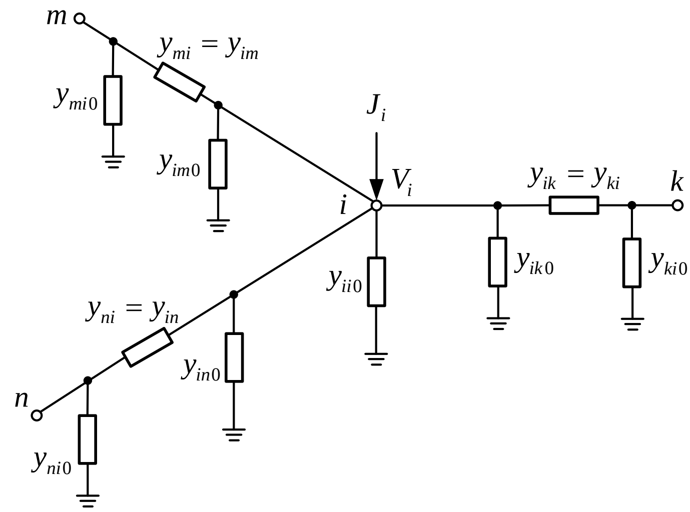

Figure 4-4 Schematic diagram of the pipeline network, where node i is connected to node k, m, and n through pipelines.

The pipeline network is represented as an undirected graph $G_{\mathrm{p}} = \left(N_{\mathrm{p}}, L_{\mathrm{p}}\right)$, where N_{p} is a set containing n_{p} nodes and L_{p} is a set containing n_e edges. The voltage of each node in the network can be calculated using the nodal admittance matrix method[3, 24]:

$$\mathbf{V} = \mathbf{Y}^{-1}\mathbf{J} \tag{4-14}$$

where $\mathbf{J} \in \mathbb{R}^{n_{\mathrm{p}}\times 1}$ is the current source vector, and J_i is the sum of the equivalent current sources injected into node i via (4-15); $\mathbf{Y} \in \mathbb{R}^{n_{\mathrm{p}}\times n_{\mathrm{p}}}$ is the nodal admittance matrix, and the diagonal element Y_{ii} and the off-diagonal element Y_{ki} are calculated via (4-16).

$$J_i = \sum_{k\in N_{\mathrm{nei}}(i)} j_{ik} \tag{4-15}$$

where $N_{\mathrm{nei}}(i)$ the set of all neighboring nodes that are directly connected to node i, and j_{ik} is the equivalent current source at node i of pipeline (i, k).

$$Y_{ii} = y_{ii0} + \sum_{k\in N_{\mathrm{nei}}(i)} (y_{ik} + y_{ik0}), \quad Y_{ki} = -y_{ki} \tag{4-16}$$

where y_{ik} and y_{ik0} are parameters of the equivalent pi-circuit of pipeline (i, k) as depicted in Figure 4-4, and y_{ii0} is the admittance of the additional grounding branch of node i.

The proposed equivalent-pi circuit avoids discretization of pipelines excited by nonuniform geoelectric fields, which can greatly reduce the number of nodal voltage equations.

2） Calculating PSP and GIC Along Pipelines

Different from the induction analysis in the power grid that regards the GIC along a line as an invariant, all PSP and GIC results along a line are usually required in the pipeline analysis. Once the nodal voltage in the pipeline network is obtained through the admittance matrix method, the voltage along each pipeline can be determined using the terminal voltages and local geoelectric fields, which can be solved by (4-17)-(4-18) based on the transmission line theory[23]. In addition, this step can be performed only on some pipelines of interest in the network.

$$V(x) = Z_{\mathrm{C}} \left((A + P(x))\, e^{-\gamma x} - (B + Q(x))\, e^{\gamma x} \right) \tag{4-17}$$

$$I(x) = (A + P(x))\, e^{-\gamma x} + (B + Q(x))\, e^{\gamma x} \tag{4-18}$$

where

$$\begin{aligned} P(x) &= \frac{1}{2Z_{\mathrm{C}}} \int_0^x e^{\gamma z} E_{\mathrm{t}}(z) \mathrm{d}z \\ Q(x) &= -\frac{1}{2Z_{\mathrm{C}}} \int_L^x e^{-\gamma z} E_{\mathrm{t}}(z) \mathrm{d}z \end{aligned} \tag{4-19}$$

The voltages at two terminals of the pipeline via the nodal admittance matrix method are used as boundary conditions:

$$\begin{aligned} V_i &= Z_{\mathrm{C}} \left(A - (B + Q(0)) \right) \\ V_k &= Z_{\mathrm{C}} \left((A + P(L))\, e^{-\gamma L} - B e^{\gamma L} \right) \end{aligned} \tag{4-20}$$

Thus, the coefficients of the general solution *A* and *B* can be calculated as follows:

$$\begin{aligned} A &= \frac{\left(V_k - V_i e^{\gamma L} \right) / Z_{\mathrm{C}} - P(L) e^{-\gamma L} - Q(0) e^{\gamma L}}{e^{-\gamma L} - e^{\gamma L}}, \\ B &= \frac{\left(V_k - V_i e^{-\gamma L} \right) / Z_{\mathrm{C}} - P(L) e^{-\gamma L} - Q(0) e^{-\gamma L}}{e^{-\gamma L} - e^{\gamma L}} \end{aligned} \tag{4-21}$$

Especially, for a uniform electric field, the voltage and current along the pipeline in (4-17)-(4-18) can be simplified into

$$V(x) = \frac{V_k - V_i e^{\gamma L}}{e^{-\gamma L} - e^{\gamma L}} e^{-\gamma x} - \frac{V_k - V_i e^{-\gamma L}}{e^{-\gamma L} - e^{\gamma L}} e^{\gamma x} \tag{4-22}$$

$$I(x) = \frac{V_k - V_i e^{\gamma L}}{Z_{\mathrm{C}} \left(e^{-\gamma L} - e^{\gamma L} \right)} e^{-\gamma x} + \frac{V_k - V_i e^{-\gamma L}}{Z_{\mathrm{C}} \left(e^{-\gamma L} - e^{\gamma L} \right)} e^{\gamma x} + \frac{E_0}{\gamma Z_{\mathrm{C}}} \tag{4-23}$$

3） Procedure of Induction in Pipeline Network Algorithm

The detailed procedure to calculate the PSP and GIC in pipeline networks generated by the nonuniform induced geoelectric field is shown in Algorithm 4-1.

Algorithm 4-1 Geomagnetic induction in pipeline networks

```
Data: A pipeline network $G_p = (N_p, L_p)$ with topology, spatial coordinates of each
      node and transmission line parameters of each pipeline; spatial distribution of
      horizontal electric field vector $\mathbf{E}$.
Result: PSP and GIC of each pipeline.
for $(i, k)$ in $L_p$ do
    Calculate the parameters of equivalent pi-circuit for pipeline $(i, k)$ using
      (4-11a)-(4-11d);
end
Make the nodal current injection vector $\mathbf{J}$ and the network admittance matrix $\mathbf{Y}$ as in
  (4-15)-(4-16);
Calculate the nodal PSP in the pipeline network via (4-14);
for $(i, k)$ in $L_p$ do
    Calculate the induced voltage and current along the pipeline $(i, k)$ via
      (4-17)-(4-18);
end
```

For a uniform geoelectric field, the simplified (4-12) can be used to calculate the current sources in the equivalent pi-circuit, and (4-22)-(4-23) can be used to calculate the PSP and GIC along the pipeline instead.

For an actual pipeline network on the 2-D ground surface given the nodal coordinates, the 1-D line integrals of the tangential electric field in the above equations need to be extended to the 2-D line integrals of the electric field vector. The line integrals along the pipeline (i, k) of the product of a certain function $g(\mathbf{x})$ and the geoelectric field can be calculated as follows:

$$\int_{\mathbf{x}_i}^{\mathbf{x}_k} g(\mathbf{x})\mathbf{E}(\mathbf{x})\mathrm{d}\mathbf{l} = \int_{\mathbf{x}_i}^{\mathbf{x}_k} g(\mathbf{x})E_x(\mathbf{x})\mathrm{d}x + \int_{\mathbf{x}_i}^{\mathbf{x}_k} g(\mathbf{x})E_y(\mathbf{x})\mathrm{d}y \tag{4-24}$$

where dx and dy represent the northward and eastward lengths of d$\mathbf{l}$ respectively, which can be calculated via Reference [79] if nodal coordinates are expressed in latitude and longitude.

4.2 A Model Reduction Method for the Calculation of Low-Frequency EMI on Pipeline Networks Considering Nonlinear Polarization Effect

Realistic pipelines may form a multi-branch interconnected network, and their interactions need to be considered. In addition, nonlinear polarization occurs between the metal and the soil at coating defects, which is also required to be included into the circuit of the pipe network. In this section, the nodal voltage analysis is used to evaluate the voltage and current responses of a pipeline network affected by EMI.

4.2.1 Generalized Equivalent Circuit for Inductive and Conductive Coupling to a Pipeline

1） Inductive Coupling Model of Pipeline

The cause of inductive coupling is the magnetic coupling of external source currents to the pipe. It thus induces electric fields according to Faraday's law of induction, which in turn drive stray currents in the pipe.

Let us assume that the pipe is along the x-axis, then a single cell equivalent structure of a pipe excited by electric fields is depicted in Figure 4-5.

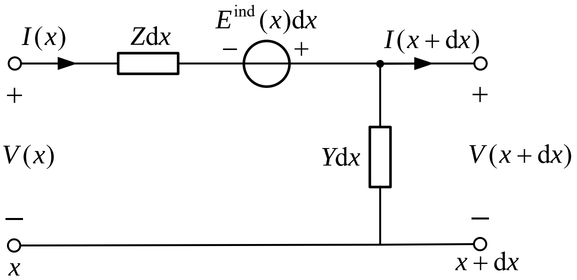

Figure 4-5 Equivalent TL circuit of a pipeline affected by inductive interference.

The remote earth at infinite depth is taken as the potential reference point. The voltage of the metal tube to the remote earth is denoted as V and the longitudinal current along the pipeline is I. The tangential electric field at location x induced by the external source current along the pipeline is denoted as $E^{\mathrm{ind}}(x)$, which can be modeled as distributed voltage sources in the longitudinal branch of the circuit. Accordingly, the TL equations for inductive coupling can be written as[97]

$$\frac{\mathrm{d}V(x)}{\mathrm{d}x} + ZI(x) = E^{\mathrm{ind}}(x) \tag{4-25}$$

$$\frac{\mathrm{d}I(x)}{\mathrm{d}x} + YV(x) = 0 \tag{4-26}$$

where Z and Y are the per-unit-length longitudinal impedance and transverse admittance, respectively. The transverse admittance Y is contributed by both the coating and the soil[105], and the former is usually much lower than the latter for well-insulated pipes.

2） Conductive Coupling Model of Pipeline

The conductive EMI is generated by the soil potential difference along the pipeline due to external grounding currents. It can also be modeled based on TL theory, as shown in the top panel of Figure 4-6.

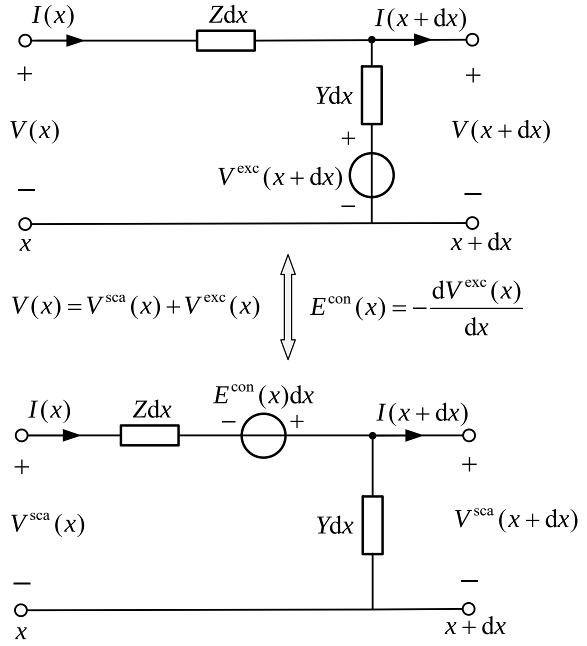

Figure 4-6 Original (top) and modified (bottom) TL circuit models of a pipeline affected by conductive interference.

In the original TL circuit model, the remote earth at infinite depth is taken as the potential reference point. The coating can be considered as a branch with a large resistance between the soil and the metal tube. The soil potential rise at location x along the pipeline due to the external earthing current, namely the excitation voltage $V^{\mathrm{exc}}(x)$, can be modeled as a transverse voltage source in the circuit. The voltage of the metal side of the coating to the remote earth is denoted as $V(x)$. Thus, the TL equations for the conductive coupling are given by[105]

$$\frac{\mathrm{d}V(x)}{\mathrm{d}x}+ZI(x)=0 \tag{4-27}$$

$$\frac{\mathrm{d}I(x)}{\mathrm{d}x}+YV(x)=YV^{\mathrm{exc}}(x) \tag{4-28}$$

We can find that for inductive and conductive coupling, the voltage source is placed on the longitudinal and transverse branches in the original TL circuit, respectively. Correspondingly, the source term is imposed in the first and second TL equation, respectively.

The original TL equations are about the voltage $V(x)$ of the metal side to the remote earth.

We can treat the excitation voltage on the soil side of the coating as local earth. Then, the voltage $V(x)$ can be decomposed into two parts as in (4-29), namely, the scattered voltage $V^{\mathrm{sca}}(x)$ on the metal side to local earth, and the excitation voltage $V^{\mathrm{exc}}(x)$ to remote earth. In this case, the excitation voltages are created by the external source currents, whereas the scattered voltages[149] are created by other currents and charges in the pipeline and the ground.

$$V(x) = V^{\mathrm{sca}}(x) + V^{\mathrm{exc}}(x) \tag{4-29}$$

Moreover, the tangential electric field $E^{\mathrm{con}}(x)$ along the pipe generated by the external earthing current can be expressed as a negative gradient of the excitation voltage:

$$E^{\mathrm{con}}(x) = -\frac{\mathrm{d}V^{\mathrm{exc}}(x)}{\mathrm{d}x} \tag{4-30}$$

Substituting (4-29) and (4-30) into the original TL equations (4-27)-(4-28), the modified TL equations about the scattered voltage $V^{\mathrm{sca}}(x)$ can be derived as

$$\frac{\mathrm{d}V^{\mathrm{sca}}(x)}{\mathrm{d}x} + ZI(x) = E^{\mathrm{con}}(x) \tag{4-31}$$

$$\frac{\mathrm{d}I(x)}{\mathrm{d}x} + YV^{\mathrm{sca}}(x) = 0 \tag{4-32}$$

We can find that the modified TL equations (4-31)-(4-32) for conductive coupling have the same form as those for inductive coupling in (4-25)-(4-26), which yields a modified circuit as depicted in the bottom panel of Figure 4-6.

In addition, the original TL model of capacitive coupling[99], although not discussed in detail in this research, is similar to that of conductive coupling. Thus, the circuit transformation in this subsection is also applicable to the capacitive coupling.

A proof of the modified TL circuit of a pipeline affected by conductive interference is given as follows. For the top panel of Figure 4-6, we can obtain the two-port representation of the original TL circuit model

$$I(x) = [V(x) - V(x + \mathrm{d}x)]\frac{1}{Z\mathrm{d}x} \tag{4-33}$$

$$I(x + \mathrm{d}x) = I(x) - [V(x + \mathrm{d}x) - V^{\mathrm{exc}}(x + \mathrm{d}x)] \cdot Y\mathrm{d}x \tag{4-34}$$

The scattered voltage is defined as the difference between the voltage of the metal side to the remote earth and the excitation voltage of the nearby soil:

$$V^{\mathrm{sca}}(x) := V(x) - V^{\mathrm{exc}}(x) \tag{4-35}$$

$$V^{\mathrm{sca}}(x+\mathrm{d}x) := V(x+\mathrm{d}x) - V^{\mathrm{exc}}(x+\mathrm{d}x) \tag{4-36}$$

Substituting equations (4-35)-(4-36) into (4-33)-(4-34), the two-port representation can be rewritten as

$$I(x) = \left[V^{\mathrm{sca}}(x) - V^{\mathrm{sca}}(x+\mathrm{d}x)\right]\frac{1}{Z\mathrm{d}x} + \left[V^{\mathrm{exc}}(x) - V^{\mathrm{exc}}(x+\mathrm{d}x)\right]\frac{1}{Z\mathrm{d}x} \tag{4-37}$$

$$I(x+\mathrm{d}x) = I(x) - V^{\mathrm{sca}}(x+\mathrm{d}x)\cdot Y\mathrm{d}x \tag{4-38}$$

The circuit interpretation of equations (4-37)-(4-38) is depicted in Figure 4-7(a), where an equivalent current source is added to the longitudinal branch of the modified structure. Then, by converting from Norton to Thevenin equivalent circuit, we can obtain the voltage source representation as shown in Figure 4-7(b).

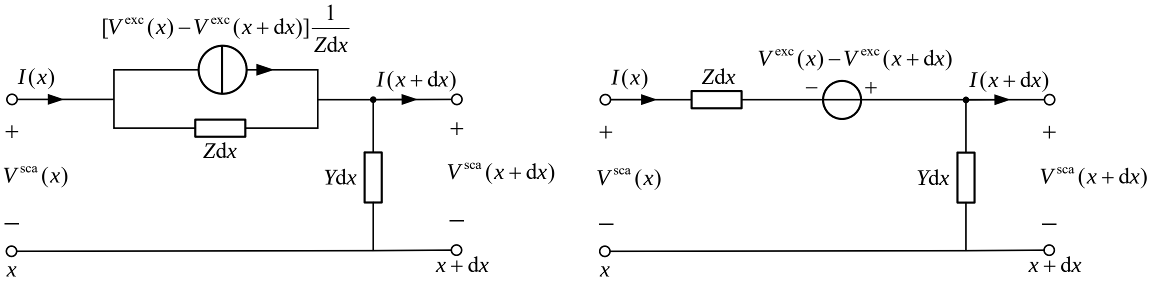

(a) Current source interpretation (b) Voltage source interpretation

Figure 4-7 Modified circuit models of a pipeline affected by the conductive interference.

Using the approximation of a difference operator

$$E^{\mathrm{con}}(x) := -\frac{\mathrm{d}V^{\mathrm{exc}}(x)}{\mathrm{d}x} = -\frac{V^{\mathrm{exc}}(x+\mathrm{d}x) - V^{\mathrm{exc}}(x)}{\mathrm{d}x} \tag{4-39}$$

the voltage source can be rewritten as

$$V^{\mathrm{exc}}(x) - V^{\mathrm{exc}}(x+\mathrm{d}x) = E^{\mathrm{con}}(x)\mathrm{d}x \tag{4-40}$$

In summary, for a pipeline affected by conductive interference, the top panel of Figure 4-6 can be interpreted as the equivalent circuit in the bottom panel of Figure 4-6.

3） Pipeline Affected by Both Inductive and Conductive EMI

Pipelines may be subject to both inductive and conductive EMI in some scenarios. For instance, an AC power line may have a ground fault near the pipe[103, 104], or geomagnetic disturbances and HVDC earth return currents may occur simultaneously[18]. Thus, the sources are present both longitudinally and transversely in the original circuit model, as shown in the top panel of Figure 4-8. Correspondingly, both TL equations are imposed with the source term:

$$\frac{\mathrm{d}V(x)}{\mathrm{d}x} + ZI(x) = E^{\mathrm{ind}}(x) \tag{4-41}$$

$$\frac{\mathrm{d}I(x)}{\mathrm{d}x} + YV(x) = YV^{\mathrm{exc}}(x) \tag{4-42}$$

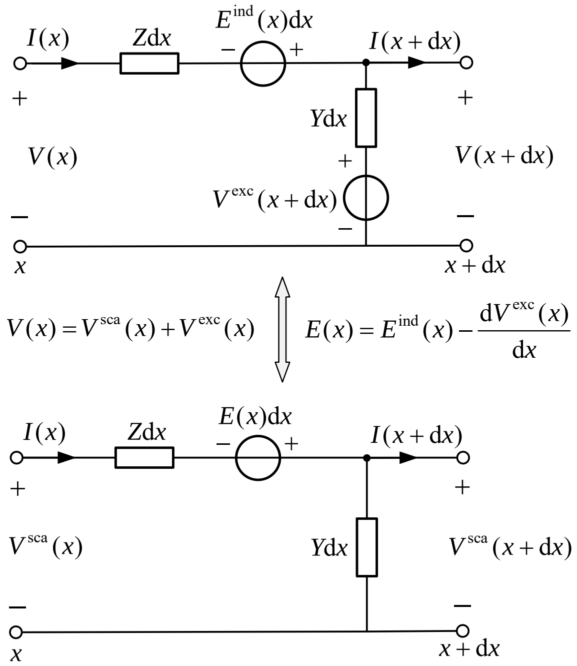

Figure 4-8 Original (top) and modified (bottom) TL circuit models of a pipeline affected by both inductive and conductive interference.

In this case, the voltage and current responses of the pipe are contributed by both the induced electric field E^{ind} in the pipe and the soil potential rise V^{exc}. We can use the total exciting electric field E tangential to the pipe, which is the sum of the inductive part E^{ind} and the conductive part E^{con}:

$$E(x) := E^{\mathrm{ind}}(x) + E^{\mathrm{con}}(x) = E^{\mathrm{ind}}(x) - \frac{\mathrm{d}V^{\mathrm{exc}}(x)}{\mathrm{d}x} \tag{4-43}$$

It allows us to obtain the modified TL equations about the scattered voltages, which are defined in (4-29), as follows:

$$\frac{\mathrm{d}V^{\mathrm{sca}}(x)}{\mathrm{d}x}+ZI(x)=E(x) \tag{4-44}$$

$$\frac{\mathrm{d}I(x)}{\mathrm{d}x}+YV^{\mathrm{sca}}(x)=0 \tag{4-45}$$

A proof of the modified TL circuit of a pipeline affected by both inductive and conductive interference is given as follows. For the top panel of Figure 4-8, we can obtain the two-port representation of the original TL circuit model

$$I(x)=[V(x)-V(x+\mathrm{d}x)+E^{\mathrm{ind}}(x)\mathrm{d}x]\frac{1}{Z\mathrm{d}x} \tag{4-46}$$

$$I(x+\mathrm{d}x)=I(x)-[V(x+\mathrm{d}x)-V^{\mathrm{exc}}(x+\mathrm{d}x)]\cdot Y\mathrm{d}x \tag{4-47}$$

Substituting equations (4-35)-(4-36) into (4-46)-(4-47), the two-port representation can be rewritten as

$$\begin{aligned}I(x)=&[V^{\mathrm{sca}}(x)-V^{\mathrm{sca}}(x+\mathrm{d}x)]\frac{1}{Z\mathrm{d}x}+\\&[E^{\mathrm{ind}}(x)\mathrm{d}x+V^{\mathrm{exc}}(x)-V^{\mathrm{exc}}(x+\mathrm{d}x)]\frac{1}{Z\mathrm{d}x}\end{aligned} \tag{4-48}$$

$$I(x+\mathrm{d}x)=I(x)-V^{\mathrm{sca}}(x+\mathrm{d}x)\cdot Y\mathrm{d}x \tag{4-49}$$

The circuit interpretation of equations (4-48)-(4-49) is depicted in Figure 4-9(a), where an equivalent current source is added to the longitudinal branch, which can be further converted into the voltage source representation shown in Figure 4-9(b).

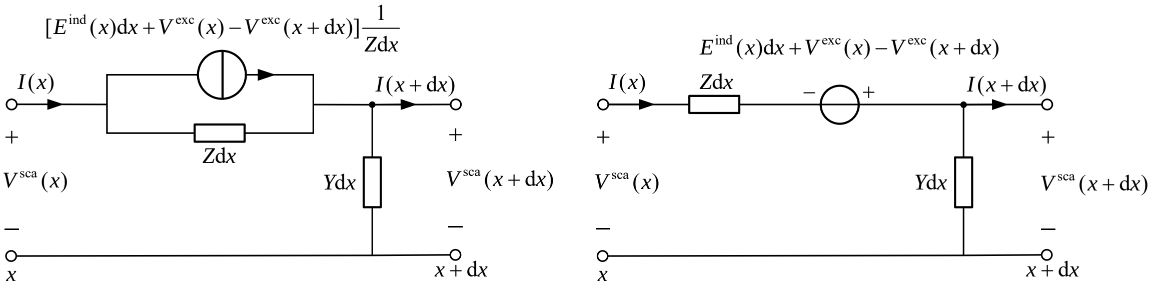

(a) Current source interpretation (b) Voltage source interpretation

Figure 4-9 Modified circuit models of a pipeline affected by both inductive and conductive interference.

Given the total exciting electrical field tangential to the pipeline

$$E(x) := E^{\mathrm{ind}}(x) + E^{\mathrm{con}}(x) = E^{\mathrm{ind}}(x) - \frac{\mathrm{d}V^{\mathrm{exc}}(x)}{\mathrm{d}x} = E^{\mathrm{ind}}(x) - \frac{V^{\mathrm{exc}}(x+\mathrm{d}x) - V^{\mathrm{exc}}(x)}{\mathrm{d}x} \tag{4-50}$$

the voltage source can be rewritten as

$$E^{\mathrm{ind}}(x)\mathrm{d}x + V^{\mathrm{exc}}(x) - V^{\mathrm{exc}}(x+\mathrm{d}x) = E(x)\mathrm{d}x \tag{4-51}$$

To summarize, the top panel of Figure 4-8 can be interpreted as the equivalent circuit in the bottom panel of Figure 4-8.

The above equations (4-44)-(4-45) can be regarded as a general form of (4-25)-(4-26) for the inductive coupling and (4-31)-(4-32) for the conductive coupling analysis. For purely inductive coupling, we have $V(x) = V^{\mathrm{sca}}(x)$. In summary, by modifying the TL model, the excitation is unified as the only longitudinal voltage source in terms of the electric fields. This transformation is applied to arbitrary spatially nonuniform induced fields E^{ind} and soil excitation potential V^{exc}. Furthermore, the simplified equivalent method proposed in Section 4.1.1 for inductive coupling of pipelines can be extended to the analysis of other types of EMI.

In addition, the modified TL equations (4-44)-(4-45) are about the scattered voltages $V^{\mathrm{sca}}(x)$, which is proportional to the leakage current density $i^{\mathrm{leak}}(x)$ and pipe-to-soil potential (PSP) $V^{\mathrm{psp}}(x)$ as in (4-52)-(4-53). For well-insulated pipelines, i.e. when the resistivity of the coating is far larger than that of the soil, the approximation $V^{\mathrm{psp}}(x) \approx V^{\mathrm{sca}}(x)$ is generally considered valid. Thus, $V^{\mathrm{sca}}(x)$ is more concerned in engineering practice compared to the total voltage $V(x)$ to the remote earth in the original TL equations (4-41)-(4-42).

$$i^{\mathrm{leak}}(x) = \frac{YV^{\mathrm{sca}}(x)}{2\pi r} \tag{4-52}$$

$$V^{\mathrm{psp}}(x) = \frac{Y}{Y_{\mathrm{coat}}}V^{\mathrm{sca}}(x) \tag{4-53}$$

where r and Y_{coat} are the outer radius and transverse admittance of the insulation coating, respectively.

4） Handling Additional Grounded Branches at Pipe Nodes

The pipe node may be connected to the groundbed in engineering practice. Assuming an additional grounded branch connects the pipeline node k to the groundbed. Let us denote the voltage of the metal side of pipe node k to the remote earth as V_k, and the soil potential rise near node k as V_k^{exc}. And the soil potential rise of the groundbed is V_k^{gnd}. The grounding impedance of node k is Z_k, and the grounding current is I_k^{gnd}.

For the original circuit model of the grounded branch at node *k* as depicted in Figure 4-10(a), the voltage of the metal side of pipe node *k* to the remote earth can be written as

$$V_k = I_k^{\mathrm{gnd}} Z_k + V_k^{\mathrm{gnd}} \tag{4-54}$$

Hence, the scattered voltage of node *k* can be derived as

$$V_k^{\mathrm{sca}} := V_k - V_k^{\mathrm{exc}} = I_k^{\mathrm{gnd}} Z_k + \left(V_k^{\mathrm{gnd}} - V_k^{\mathrm{exc}}\right) \tag{4-55}$$

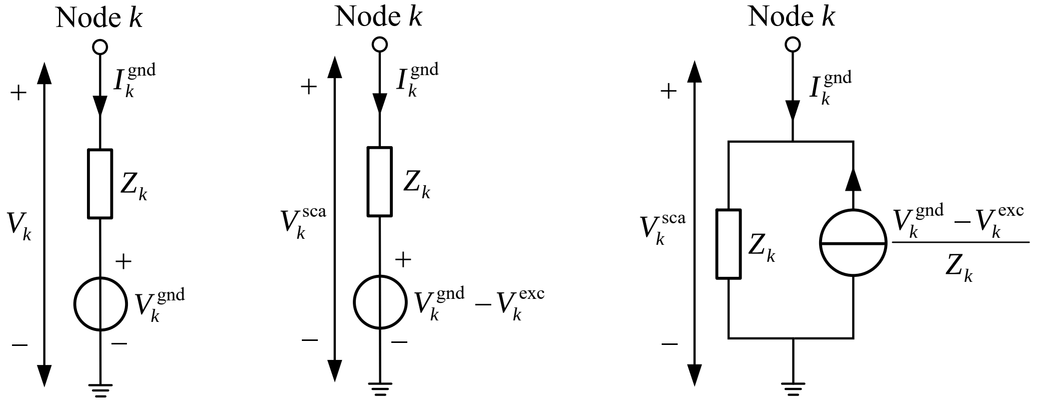

(a) Original circuit

(b) Modified circuit using the voltage source interpretation

(c) Modified circuit using the current source interpretation

Figure 4-10 Circuit models of the additional grounded branch of a pipe node.

The circuit interpretation of equation (4-55) is depicted in Figure 4-10(b), where a voltage source is added to characterize the difference in excitation voltage between the pipe and the groundbed. It can be further converted into a current source shown in Figure 4-10(c) with Norton equivalent system, which can be easily incorporated into the nodal current injection vector in equation (4-60). Especially, if the pipe node *k* is close to the groundbed, i.e. their soil potential rises are approximately equal ($V_k^{\mathrm{exc}} \approx V_k^{\mathrm{gnd}}$), then the additional current source is zero.

5） Equivalent PI-Circuit for Linear Pipe Segments

The distributed TL model of each linear homogeneous pipe segment can be reduced to a lumped circuit with symmetric admittance parameters. Consider a pipeline with two terminal nodes *i* and *k*, which is excited by the external tangential electric field $E(x)$ as described in (4-44)-(4-45).

For such an active two-port circuit, the relationship between the voltages and currents of the two ports can be reproduced by using an equivalent pi-circuit, where the effect of the external electric field is characterized by two lumped current sources at the ports, as shown in Figure 4-11. The analytical solution of the parameters of the equivalent pi-circuit can be obtained by (4-56a)-(4-56d), and the derivation is detailed in Section 4.1.1.

$$y_{ik} = \frac{1}{Z_\mathrm{C}\sinh(\gamma L)} \tag{4-56a}$$

$$y_{ik0} = y_{ki0} = \frac{1}{Z_\mathrm{C}}\tanh(\frac{\gamma L}{2}) \tag{4-56b}$$

$$j_{ik}^{E} = \frac{-1}{Z_\mathrm{C}\sinh(\gamma L)}\int_0^L \cosh\left[\gamma(L-x)\right] E(x)\mathrm{d}x \tag{4-56c}$$

$$j_{ki}^{E} = \frac{1}{Z_\mathrm{C}\sinh(\gamma L)}\int_0^L \cosh\left(\gamma x\right) E(x)\mathrm{d}x \tag{4-56d}$$

where $Z_\mathrm{C} = \sqrt{Z/Y}$ is the characteristic impedance, $\gamma = \sqrt{ZY}$ is the propagation constant, and L is the length of the pipe.

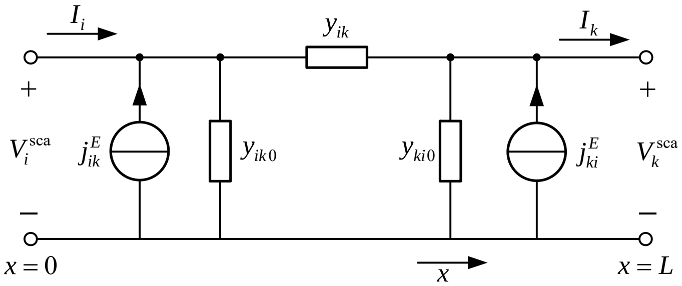

Figure 4-11 Equivalent pi-circuit of a pipeline excited by external electric fields.

Compared to the single-port Thevenin equivalent circuit[23, 97], the equivalent pi-circuit has the advantage that it can be performed for each single-conductor pipe individually according to its own TL parameters and tangential exciting electric field.

Moreover, the equivalent structure can be easily established in circuit simulation software for an intact pipeline, rather than manual segmentation of the distributed circuits[104]. If the pipeline is electrically short at the frequency of the incident field, a single lumped cell is adequate. Otherwise the usual options are (i) using the cascade connection of basic cells or (ii) relying on advanced macromodeling tools allowing to generate black-box behavioral models defined by mathematical relations.

In addition, it is also applicable to pipeline with some nonlinear grounded branches, e.g., on the coating defects. In this case, the pipeline can be simply divided into several segments at these defect nodes, and each segment can be reduced to an equivalent pi-circuit separately.

4.2.2 Calculation of EMI Coupling to Pipeline Network Considering Nonlinear Polarization Effect

1） Nonlinear Polarization of Coating Breakdown

The insulation coating is added between the metal tube and the soil in the intact pipe segments. However, the coating may be damaged due to mechanical collision during the transport and burial process, as well as insulation aging. The schematic diagram of the coating breakdown is depicted in Figure 4-12(a). The damaged part is generally small, with a radius of several centimeters. Thus, each damaged part can be considered as a discrete node in the circuit[107]. For the breakdown node l, its influence on the pipe can be modeled as an additional grounded branch, as shown in Figure 4-12(b), which includes contributions from the interface and the soil.

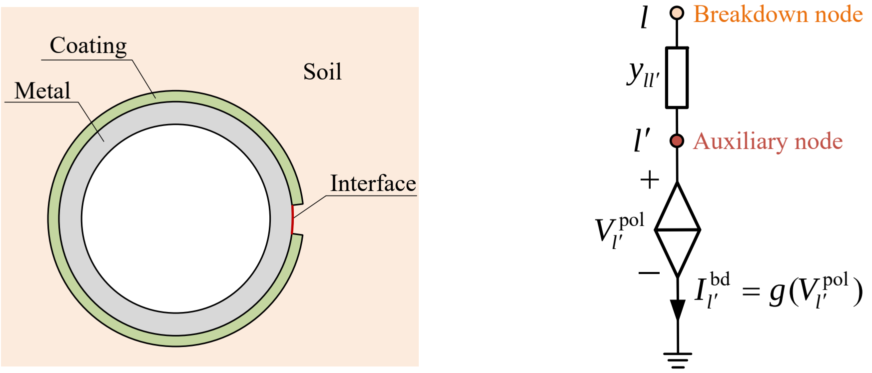

(a) Schematic diagram of the cross-section of the damaged part of the pipe

(b) Equivalent circuit of the breakdown node

Figure 4-12 Coating breakdown considering polarization effect at the interface. In the equivalent circuit of the breakdown node l, $y_{ll'}$ is the linear soil conductance, $V_{l'}^{\mathrm{pol}}$ is the polarization voltage, and $I_{l'}^{\mathrm{bd}}$ is the leakage current.

At the interface where the coating is damaged, polarization effects occur due to the electrochemical reaction between the metal and the soil. An auxiliary node l' is added to describe it in the circuit. The potential difference across the interface, namely the polarization voltage $V_{l'}^{\mathrm{pol}}$, is related to the leakage current density i^{leak}. Their relationship is usually nonlinear and can be obtained through electrochemical tests. For EMI calculation of pipelines, the piecewise interpolation method or the Butler-Volmer model in (4-57)[108, 109, 112] can be used to fit the test data.

$$i^{\mathrm{leak}} = i_0[\exp(\frac{V_{l'}^{\mathrm{pol}} - V_{\mathrm{corr}}^{\mathrm{pol}}}{\beta_{\mathrm{a}}}) - \exp(-\frac{V_{l'}^{\mathrm{pol}} - V_{\mathrm{corr}}^{\mathrm{pol}}}{\beta_{\mathrm{c}}})] \tag{4-57}$$

where the corrosion electrochemical parameters i_0, $V_{\mathrm{corr}}^{\mathrm{pol}}$, β_{a}, β_{c} are the exchange current density, the natural corrosion potential, and the Tafel slope of the anode reaction and of the cathode reaction, respectively. They can be obtained by electrochemical tests. These parameters vary with the resistivity and pH value of the soil[109].

Assuming that the current is uniformly distributed at a breakdown node, then the polarization effect at the interface can be modeled as a nonlinear voltage-controlled current source. For instance, if the Butler-Volmer model is adopted, the leakage current $I_{l'}^{\mathrm{bd}}$ of node l' can be determined by

$$\begin{aligned} I_{l'}^{\mathrm{bd}} &= g(V_{l'}^{\mathrm{pol}}) = S \cdot i^{\mathrm{leak}} \\ &= S \cdot i_0[\exp(\frac{V_{l'}^{\mathrm{pol}} - V_{\mathrm{corr}}^{\mathrm{pol}}}{\beta_{\mathrm{a}}}) - \exp(-\frac{V_{l'}^{\mathrm{pol}} - V_{\mathrm{corr}}^{\mathrm{pol}}}{\beta_{\mathrm{c}}})] \end{aligned} \tag{4-58}$$

where S is the area of the damaged coating.

In addition, the linear admittance of the soil outside a defect depends on the soil parameters and the area of damaged part. It can be calculated by (4-59) for the analysis of DC or quasi-DC interference[107].

$$y_{ll'} = \frac{4\sigma S}{4d + \sqrt{\pi S}} \tag{4-59}$$

where σ is the soil conductivity and d is the coating thickness.

2） Nodal Voltage Analysis of the Pipeline Network

The nodal voltage analysis is performed for the electromagnetic coupling analysis of the pipeline network, which contains linear pipe segments and coating breakdown with nonlinear polarization. As for node sets, N_{nml} is the set of normal nodes, including terminals, bends, and junctions, N_{bd} is the set of breakdown nodes, and N'_{bd} is the set of auxiliary breakdown nodes. The cardinal numbers of these node sets are denoted as $n_1 = |N_{\mathrm{nml}}|$ and $n_2 = |N_{\mathrm{bd}}| = |N'_{\mathrm{bd}}|$. Thus, the set of full nodes in the network is denoted as $N_{\mathrm{p}} = N_{\mathrm{nml}} \cup N_{\mathrm{bd}} \cup N'_{\mathrm{bd}}$, and the total number of nodes is $n = n_1 + 2n_2$.

A demonstrative example of the pipeline network is depicted in Figure 4-13. The original pipeline network consists of four normal nodes $\{h, i, k, m\}$ and three pipes $\{(h, k), (i, k), (k, m)\}$. Assume there exists a breakdown point l on the pipe (k, m), then the pipe can be divided into two segments (k, l) and (l, m). Meanwhile, an additional grounded branch, including an auxiliary node l', is added at node l.

The equivalent pi-circuit can be established for each pipe segment according to (4-56a)-(4-56d). The current sources in the equivalent pi-circuit of each segment due to the external electric fields are integrated in the nodal current injection vector $\mathbf{J} \in \mathbb{R}^{(n_1+n_2)\times 1}$ for the node sets N_{nml} and N_{bd} as

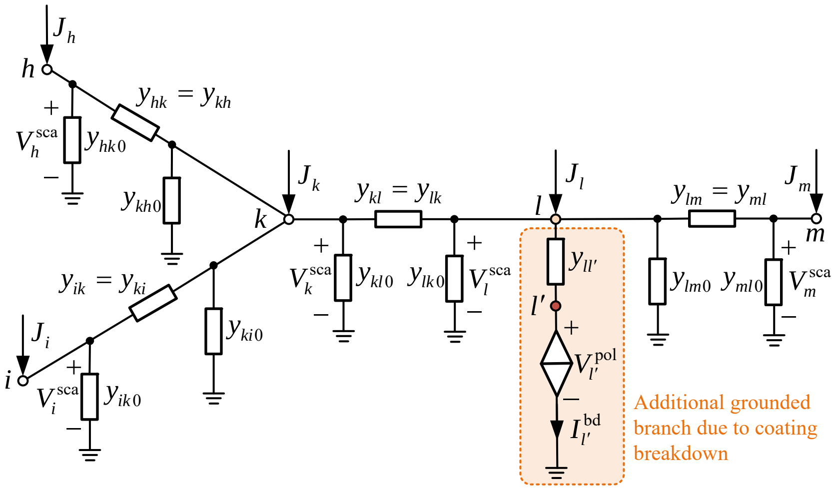

Figure 4-13 Schematic diagram of the circuit model of a illustrative pipeline network considering nonlinear polarization at breakdown node l.

$$J_i = \sum_{k \in N_{\mathrm{nei}}(i)} j_{ik}^{E} \tag{4-60}$$

where $N_{\mathrm{nei}}(i)$ the set of all neighboring nodes that are directly connected to node i.

Then the voltage equation can be formulated for each node. For the normal node $i \in N_{\mathrm{nml}}$, according to Kirchhoff's current law, we can obtain

$$\sum_{k \in N_{\mathrm{nei}}(i)} [y_{ik}(V_i^{\mathrm{sca}} - V_k^{\mathrm{sca}}) + y_{ik0} V_i^{\mathrm{sca}}] = J_i \tag{4-61}$$

Similarly, for the breakdown node $l \in N_{\mathrm{bd}}$, one can get

$$\sum_{k \in N_{\mathrm{nei}}(l), k \neq l'} [y_{lk}(V_l^{\mathrm{sca}} - V_k^{\mathrm{sca}}) + y_{lk0} V_l^{\mathrm{sca}}] + y_{ll'}(V_l^{\mathrm{sca}} - V_{l'}^{\mathrm{pol}}) = J_l \tag{4-62}$$

For the auxiliary node $l' \in N'_{\mathrm{bd}}$, one can get

$$y_{ll'}(V_l^{\mathrm{sca}} - V_{l'}^{\mathrm{pol}}) = I_{l'}^{\mathrm{bd}} = g(V_{l'}^{\mathrm{pol}}) \tag{4-63}$$

The variables to be solved include the scattered voltages $\mathbf{V}^{\mathrm{sca}} \in \mathbb{R}^{(n_1+n_2)\times 1}$ and the polarization voltages $\mathbf{V}^{\mathrm{pol}} \in \mathbb{R}^{n_2 \times 1}$. They can be collectively denoted as the full-node voltages $\tilde{\mathbf{V}} \in \mathbb{R}^{n \times 1}$.

To sum up, the voltage equations (4-61)-(4-63) for all n nodes can be expressed in a compact matrix form with respect to $\tilde{\mathbf{V}}$:

$$\mathbf{f}(\tilde{\mathbf{V}}) := \mathbf{Y}^{\text{init}}\tilde{\mathbf{V}} + \begin{bmatrix} -\mathbf{J} \\ \mathbf{I}^{\text{bd}} \end{bmatrix} = \mathbf{0}, \text{ where } \tilde{\mathbf{V}} = \begin{bmatrix} \mathbf{V}^{\text{sca}} \\ \mathbf{V}^{\text{pol}} \end{bmatrix} \tag{4-64}$$

$\mathbf{Y}^{\text{init}} \in \mathbb{R}^{n\times n}$ is the initial admittance matrix ignoring the grounded branch of the auxiliary breakdown nodes N'_{bd}. The diagonal entries of $\mathbf{Y}^{\text{init}}$, which depend on the node type, are given as

$$Y_{ii}^{\text{init}} = \sum_{k\in N_{\text{nei}}(i)} (y_{ik} + y_{ik0}), \qquad \text{if } i \in N_{\text{nml}} \tag{4-65}$$

$$Y_{ll}^{\text{init}} = y_{ll'} + \sum_{k\in N_{\text{nei}}(l), k\neq l'} (y_{lk} + y_{lk0}), \qquad \text{if } l \in N_{\text{bd}} \tag{4-66}$$

$$Y_{l'l'}^{\text{init}} = y_{ll'}, \qquad \text{if } l' \in N'_{\text{bd}} \tag{4-67}$$

and the off-diagonal entries are given as

$$Y_{ik}^{\text{init}} = \begin{cases} -y_{ik}, & \text{if } k \in i \wedge k \neq i \\ 0, & \text{if } k \notin i \wedge k \neq i \end{cases} \tag{4-68}$$

and $\mathbf{I}^{\text{bd}} \in \mathbb{R}^{n_2\times 1}$ is the earthing current of the node set N'_{bd}, and its l'-th entry $I_{l'}^{\text{bd}}$ depends on the polarization voltage $V_{l'}^{\text{pol}}$ as in (4-58).

3） Solving Nodal Voltages via Newton-Raphson Method

The nodal voltage equation (4-64) has no closed-form solution in the presence of the nonlinear term $\mathbf{I}^{\text{bd}}$. Such a set of nonlinear algebraic equations can be solved by numerical methods such as Newton-Raphson iteration[150]. The nodal voltages $\tilde{\mathbf{V}}$ iterates from the initial guess and gradually converges to the exact solution.

One possible method to determine the initial guess of the nodal voltages $\tilde{\mathbf{V}}^{(0)}$ is by neglecting the leakage currents at the breakdown nodes as in (4-69). Alternatively, a different initial guess of nodal voltages can be obtained by replacing the controlled voltage source with other linear admittance.

$$\mathbf{Y}^{\text{init}}\tilde{\mathbf{V}}^{(0)} = \begin{bmatrix} \mathbf{J} \\ \mathbf{0} \end{bmatrix} \tag{4-69}$$

where $\mathbf{0} \in \mathbb{R}^{n_2\times 1}$ is a zero vector.

Then, the nodal voltages can then be continuously corrected according to the mismatch in

(4-64). At step k, the nodal voltages iterates in the following format:

$$\left.\begin{aligned}\mathbf{Y}^{(k)}\Delta\tilde{\mathbf{V}}^{(k)} &= -\mathbf{f}(\tilde{\mathbf{V}}^{(k)})\\ \tilde{\mathbf{V}}^{(k+1)} &= \tilde{\mathbf{V}}^{(k)} + \Delta\tilde{\mathbf{V}}^{(k)}\end{aligned}\right\}(k=0,1,2,\ldots) \tag{4-70}$$

where $\mathbf{Y} \in \mathbb{R}^{n\times n}$ is the Jacobian matrix, which consists of the first-order partial derivatives of the functions in (4-64) with respect to the nodal voltages:

$$\mathbf{Y} := \frac{\partial \mathbf{f}(\tilde{\mathbf{V}})}{\partial \tilde{\mathbf{V}}} \tag{4-71}$$

It can be found that the Jacobian matrix $\mathbf{Y}$ is actually the nodal admittance matrix containing the dynamic conductance of the grounded branch of the auxiliary breakdown nodes. Thus, the Jacobian matrix $\mathbf{Y}^{(k)}$ at the k-th iteration can be obtained by small corrections to the initial admittance matrix $\mathbf{Y}^{\text{init}}$: the diagonal entries corresponding to the auxiliary nodes N'_{bd} needs be updated as in (4-72) if the Butler-Volmer equation (4-57) is used to characterized the polarization effect, whereas other entries in the matrix remain unchanged.

$$\begin{aligned}Y_{l'l'}^{(k)} &= Y_{l'l'}^{\text{init}} + \left.\frac{\mathrm{d}g(\tilde{V}_{l'})}{\mathrm{d}\tilde{V}_{l'}}\right|_{\tilde{V}_{l'}=\tilde{V}_{l'}^{(k)}}\\ &= Y_{l'l'}^{\text{init}} + S\cdot i_0[\frac{1}{\beta_{\text{a}}}\exp(\frac{\tilde{V}_{l'}^{(k)}-V_{\text{corr}}^{\text{pol}}}{\beta_{\text{a}}}) + \frac{1}{\beta_{\text{c}}}\exp(-\frac{\tilde{V}_{l'}^{(k)}-V_{\text{corr}}^{\text{pol}}}{\beta_{\text{c}}})], \quad \forall l' \in N'_{\text{bd}}\end{aligned} \tag{4-72}$$

The nodal voltages are considered to have converged if the following criterion is satisfied:

$$\|\mathbf{f}(\tilde{\mathbf{V}}^{(k)})\|_\infty = \max_i |f_i(\tilde{\mathbf{V}}^{(k)})| < \varepsilon \tag{4-73}$$

where ε is the tolerance error of the mismatch.

4） Voltages and Currents Along Intact Pipe Segments

Once the nodal scattered voltages are obtained, we can further calculate the responses along the pipeline of interest. The voltages and currents along the pipe (i,k) can be solved from the terminal voltages V_i^{sca} and V_k^{sca}:

$$I(x) = [A+P(x)]\,e^{-\gamma x} + [B+Q(x)]\,e^{\gamma x} \tag{4-74}$$

$$V^{\text{sca}}(x) = Z_{\text{C}}\left\{[A+P(x)]\,e^{-\gamma x} - [B+Q(x)]\,e^{\gamma x}\right\} \tag{4-75}$$

where

$$A = \frac{y_{ik}}{2}(V_i^{\text{sca}} e^{\gamma L} - V_k^{\text{sca}}) - \frac{j_{ik}^E}{2} \tag{4-76a}$$

$$B = \frac{y_{ik}}{2}(V_i^{\text{sca}} e^{-\gamma L} - V_k^{\text{sca}}) + \frac{j_{ki}^E}{2} e^{-\gamma L} \tag{4-76b}$$

$$P(x) = \frac{1}{2Z_{\mathrm{C}}} \int_0^x e^{\gamma\xi} E(\xi) \mathrm{d}\xi \tag{4-76c}$$

$$Q(x) = \frac{1}{2Z_{\mathrm{C}}} \int_x^L e^{-\gamma\xi} E(\xi) \mathrm{d}\xi \tag{4-76d}$$

where y_{ik}, j_{ik}^E and j_{ki}^E are the parameters of the equivalent pi-circuit for pipe (i, k) as in (4-56a)-(4-56d).

5） Procedure for EMI Calculation of Pipeline Network

The procedures for calculating the electromagnetic coupling to the pipeline network are summarized in Algorithm 4-2. Some preprocessing is required to obtain the inputs before starting the algorithm. Firstly, the spatial distribution of the external exciting electric field needs to be simulated by using the source currents and earth resistivity structure, etc. Secondly, the breakdown nodes and auxiliary nodes are added for each pipeline, which can be determined by coating defect detector[107] or related engineering experience[109]. Thus, it yields a new graph $G_{\mathrm{p}} = \left(N_{\mathrm{p}}, L_{\mathrm{p}}\right)$ for the pipe network, where N_{p} is a set of full nodes and L_{p} is a set of all pipe segments.

4.3 Induction Results in Pipeline Networks Excited by Nonuniform Geoelectric Fields

4.3.1 Validation of Pipeline Geomagnetic Induction Model

1） Verification of Pipeline Induction Model Using GIC Measurement

The geomagnetic induction model of the pipeline was verified using publicly available GIC measurement data. The Finnish Meteorological Institute measured and released the longitudinal GIC of the pipeline at the Mäntsälä compressor station in Finland (60.6 N°, 25.2 E°) from 1999 to 2022[151]. In this study, these measured data are compared with calculated GIC values from the DSTL model.

We selected 14 strong magnetic storm events in the 24th cycle of solar activity (2008-2018) according the Dst index. The measured magnetic field data were obtained from the geomagnetic observatory at Nurmijärvi (NUR) near the Finnish pipeline. The induced geo-

Algorithm 4-2 Electromagnetic coupling to pipeline networks considering nonlinear polarization effect

```
   Data:
       1. A pipeline network $G_\mathrm{p} = \left(N_\mathrm{p}, L_\mathrm{p}\right)$ with topology and nodal coordinates;
       2. TL parameters of each pipeline;
       3. Polarization characteristics of coating breakdown;
       4. Spatial distribution of exciting electric field;
       5. Tolerable error $\varepsilon$ and maximum iteration $N_\mathrm{iter}$ for Newton-Raphson method.
   Result: PSPs and currents along the pipes of interest.
 1 Initialization;
 2 // Calculate the initial guess of nodal voltages using modified equivalent pi circuit
 3 for $(i, k)$ in $L_\mathrm{p}$ do
 4     Calculate the parameters of equivalent pi-circuit for pipeline $(i, k)$ using
         (4-56a)-(4-56d);
 5 end
 6 Make the nodal current injection vector $\mathbf{J}$ via (4-60) and initial network admittance
     matrix $\mathbf{Y}^\mathrm{init}$ via (4-65)-(4-68);
 7 Obtain the initial guess of full-node voltages $\tilde{\mathbf{V}}^{(0)}$ in the pipeline network by solving
     (4-69);
 8 // Solve the nodal voltages using Newton-Raphson method
 9 Initialize counter $k \leftarrow 0$ for Newton-Raphson iteration;
10 repeat
11     Initialize the Jacobian matrix $\mathbf{Y}^{(k)} \leftarrow \mathbf{Y}^\mathrm{init}$;
12     for $l'$ in $\mathrm{N}'_\mathrm{bd}$ do
13         Update $Y^{(k)}_{l'l'}$ using $\tilde{V}^{(k)}_{l'}$ as in (4-72);
14     end
15     Calculate the updated voltages $\tilde{\mathbf{V}}^{(k+1)}$ via (4-70);
16     Increment iteration counter step $k \leftarrow k + 1$;
17     if $k \geq N_\mathrm{iter}$ then
18         The Newton-Raphson algorithm does not converge. Re-select the initial
             guess of nodal voltages $\tilde{\mathbf{V}}^{(0)}$ and goto line 9;
19     end
20 until $\|\mathbf{f}(\tilde{\mathbf{V}}^{(k)})\|_\infty < \varepsilon$;
21 Extract $\mathbf{V}^\mathrm{sca}$ and $\mathbf{V}^\mathrm{pol}$ from $\tilde{\mathbf{V}}^{(k)}$;
22 // Calculate the response along each intact pipe segment
23 for $(i, k)$ in $L_\mathrm{p}$ do
24     Calculate the longitudinal currents and scattered voltages along the intact pipe
         segment $(i, k)$ using $V_i^\mathrm{sca}$ and $V_k^\mathrm{sca}$ as in (4-74)-(4-75);
25     Calculate the leakage current density and PSP along the pipe $(i, k)$ using the
         scattered voltages via (4-52)-(4-53);
26 end
27 // Calculate the response at each coating defect
28 for $l'$ in $N'_\mathrm{bd}$ do
29     Calculate the leakage current density at the breakdown node $l'$ using $V_{l'}^\mathrm{pol}$ as in
         (4-57);
30 end
```

electric field is then calculated using a two-layer earth conductivity model. The resistivities of the top and bottom layers of earth are 38.5 and 0.385 Ω·m respectively. The thickness of the surface layer of earth is 150 km. Then, assuming the electric field is spatially uniform, the pipe GIC can be calculated using linear superposition:

$$I(t) = aE_x(t) + bE_y(t) \tag{4-77}$$

where the coefficients a = -70 A/(V/km) and b = 88 A/(V/km) are calculated using the topology and parameters of the Finnish pipeline network based on the DSTL model[151].

The geomagnetic waveform at NUR observatory during the magnetic storm from September 26 to 27, 2011 is shown in Figure 4-14. The calculated and measured pipeline GIC waveforms are compared in Figure 4-15, and their changing patterns show consistency. The scatter plot of GIC in Figure 4-16 shows that the two waveforms have a strong correlation, and the corresponding linear correlation coefficient is 0.8602.

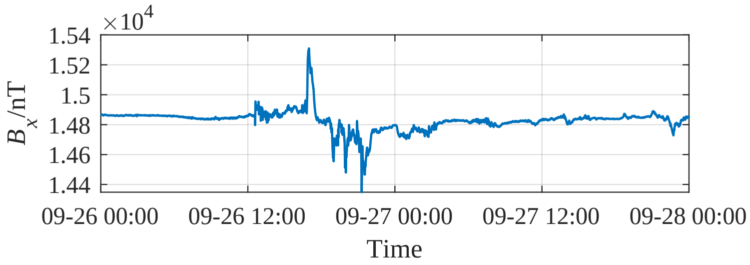

(a) Northward geoelectric field

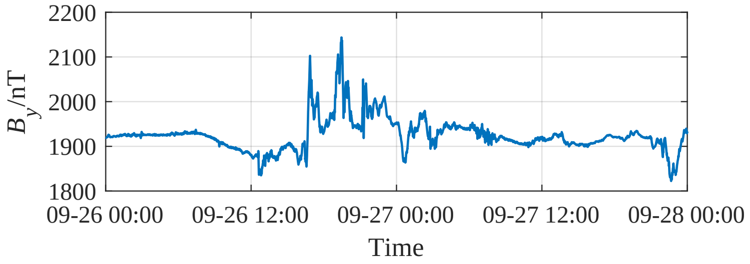

(b) Eastward geoelectric field

Figure 4-14 Measured geomagnetic field waveform at NUR observatory from September 26 to 27, 2011.

Table 4-1 lists the correlation coefficients of measured and calculated GIC waveforms in all 14 GMD events. These correlation coefficients are in the range of 0.63-0.86, which illustrates the applicability of the classic DSTL model. The difference between the calculated and measured GIC waveforms may be caused by the simplification of the earth model and the neglect of current injection from the cathodic protection system.

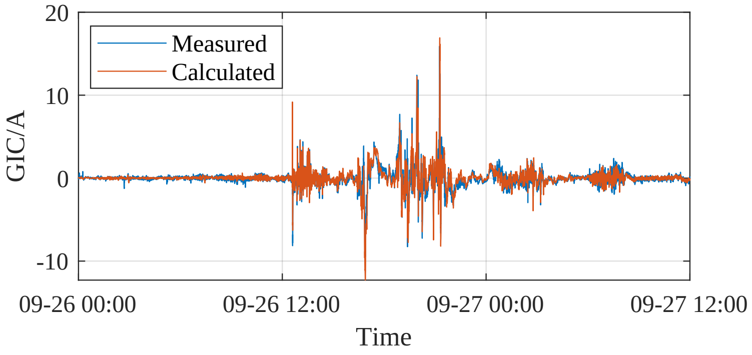

Figure 4-15 Measured and calculated GIC waveform in pipeline at the Mäntsälä compressor station from September 26 to 27, 2011.

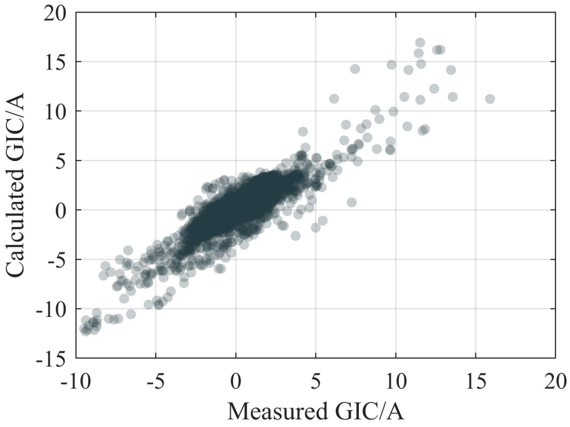

Figure 4-16 Scatter plot of the measured and calculated GIC in pipeline at the Mäntsälä compressor station from September 26 to 27, 2011.

Table 4-1 Correlation coefficients of measured and calculated GIC waveforms in pipeline at the Mäntsälä compressor station

GMD event	Duration	Dst index/nT	Correlation coefficient
1	2011.09.26-2011.09.27	-118	0.8602
2	2012.03.09	-145	0.8339
3	2012.07.15-2012.07.16	-139	0.7312
4	2012.10.01	-122	0.6570
5	2012.10.09	-109	0.7974
6	2012.11.14	-102	0.6898
7	2013.03.17	-132	0.8257
8	2013.06.01	-124	0.7065
9	2013.06.29	-108	0.7868
10	2015.10.07	-124	0.8013
11	2015.12.20	-155	0.7585
12	2016.01.01	-177	0.7073
13	2016.01.20	-104	0.6340
14	2016.10.13	-105	0.8270

2） Validation of Proposed Modified Equivalent PI-Circuit for Pipelines

A single pipeline along the north direction with insulated ends is used to validate the induction algorithm for nonuniform geoelectric field. The pipeline length is 500 km. The series impedance Z is 0.005 Ω/km, and the parallel admittance Y is 0.05 S/km. The above parameters are from a typical case of electrically long pipes in Reference [23], since the nonuniform geoelectric field has a relatively greater effect on electrically long pipes as discussed in Section III-A.

The spatial distribution of the nonuniform geoelectric field is assumed to be $E_{\mathrm{t}}(x) = 0.001x$ V/km, where x is the distance along the pipeline in kilometers.

The induction algorithms in this research are implemented in MATLAB R2019b. The following two methods are used for comparison:

1. Nonuniform method: an equivalent pi-circuit model with nonuniform geoelectric field is established via (4-11a)-(4-11d), resulting in a 2-node network;
2. Piecewise uniform method: the pipeline is equally divided into 500 sections by length, and the geoelectric field of each segment is taken as the value located at the midpoint. An equivalent pi-circuit model with uniform geoelectric field is established for each segment using (4-7), resulting in a network of 501 nodes.

The PSP and GIC along the pipeline obtained by the two methods are highly consistent, as shown in Figure 4-17, which illustrates the accuracy of the proposed model in the case of spatially nonuniform fields.

In addition, the former method can reduce the order of the nodal admittance matrix in (4-14) by simplifying each pipeline into an equivalent circuit, thereby decreasing the computational burden.

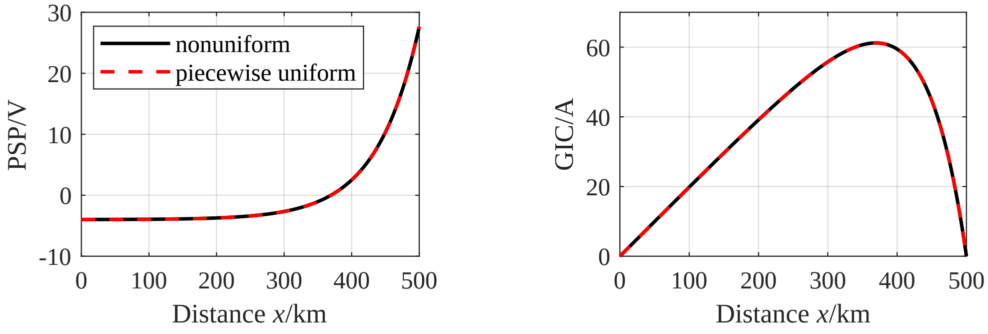

(a) PSP along pipeline (b) GIC along pipeline

Figure 4-17 Comparison of PSP and GIC results with respect to distance x along the pipeline using nonuniform and piecewise uniform algorithms.

4.3.2 Influence of Nonuniform Geomagnetic Fields on Geomagnetic Induction

1） Locally Enhanced and Gradually Changing Nonuniform Geoelectric Field Scenarios

The spatial distribution of the nonuniform geoelectric field used in this section is from the EPRI report[60], provided in a 0.5° × 0.5° regular grid, which includes two scenarios visualized in Figure 4-18.

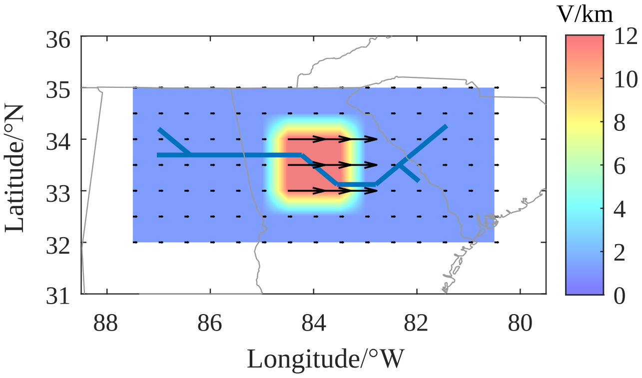

(a) Scenario 1: Eastward local enhancement

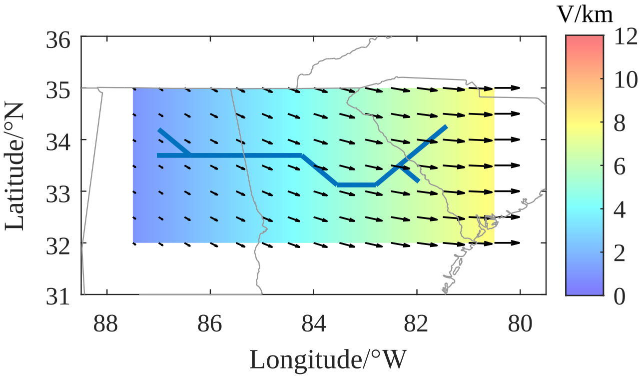

(b) Scenario 2: Southeast geoelectric field

Figure 4-18 Spatial distribution of the nonuniform geoelectric field. The arrow in the figure indicates the electric field vector from the EPRI report[60]; the colored map visualizes the spatial distribution of the interpolated geoelectric field; the blue line shows the location of the pipes, and the gray curve is the base map.

In scenario 1, there is a local enhancement in the geoelectric field magnitude to 12 V/km in an area of 1° × 1°, while the remaining area is 1.2 V/km, and the geoelectric field direction is modified to east in this research. This type of geoelectric field is caused by the local enhancement of the geomagnetic field occurring in areas of hundreds of kilometers at high latitudes, rather than the lateral changes in earth conductivity[32]. In scenario 2, both the magnitude and direction of the geoelectric field vary gradually with the spatial coordinates. The spatial distribution of space currents at high latitudes is quite complicated, and the above two scenarios are regarded as typical geoelectric field caused by nonuniform geomagnetic source fields in this research.

The nodal spatial coordinates of the synthetic modified 9-node and 8-line networks are shown in Table 4-2. The spatial coordinates of network 1 and network 2 are expressed in latitude-longitude and distance, respectively. And the pipeline lengths in network 1 are changed into twice the original data from Reference [24].

Table 4-2 Nodal coordinates of synthetic test pipeline networks

Node	Network 1		Network 2	
	Latitude/°N	Longitude/°E	*x*/km	*y*/km
1	34.200	-87.000	-3.536	-258.744
2	33.693	-87.035	-31.820	-260.460
3	33.693	-86.388	-31.820	-230.460
4	33.693	-84.231	-31.820	-130.460
5	33.122	-83.547	-63.640	-98.640
6	33.122	-82.797	-63.640	-63.640
7	33.503	-82.341	-42.426	-42.426
8	34.263	-81.424	0	0
9	33.185	-81.961	-60.104	-24.749

2） Synthetic Test Pipeline Network 1

A modified 9-node and 8-line test pipeline network presented in Figure 4-19 is used for induction analysis in this section, whose spatial cooridnates are listed in Table 4-2, including a main line “3-4-5-6-7-8” and three branch lines “1-3”, “2-3” and “7-9”.

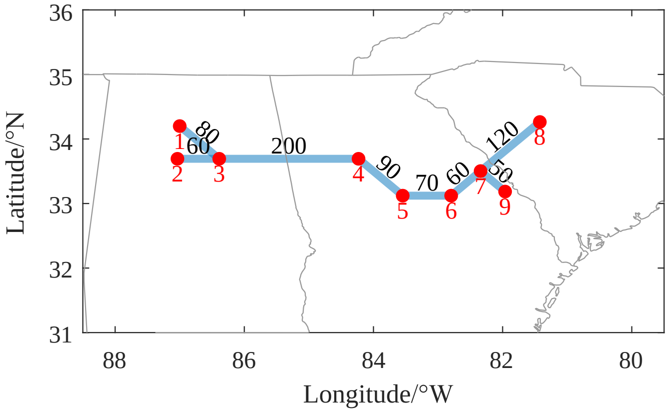

Figure 4-19 The synthetic 9-node and 8-pipeline network 1. The red labels indicate the number of nodes, and the black labels are pipeline lengths in kilometers.

The original data are obtained from Boteler’s paper [24], and some parameters have been adjusted. The length of each pipeline has been modified into twice the original length to match the footprint of the geoelectric field in this section. The series resistance of the main and branch pipeline is 0.00492 and 0.01544 Ω/km, and the parallel conductance is 0.012 and 0.006 S/km, respectively.

3） Induction Results With Nonuniform Geoelectric Field

For the two nonuniform geoelectric field scenarios, the induction results in the pipe network are compared with the corresponding uniform geoelectric field. The nodal PSP and maximum line GIC are shown in Table 4-3 and Table 4-4, and the PSP and GIC along the main pipeline 3-8 are shown in Figure 4-20.

Table 4-3 Nodal PSP in volts in pipeline network 1

Node	Geoelectric field scenario 1		Geoelectric field scenario 2	
	Nonuniform	Uniform	Nonuniform	Uniform
1	-266.76	-124.84	-297.46	-495.81
2	-299.47	-140.62	-284.65	-508.07
3	-274.63	-88.61	-236.49	-320.09
4	-104.01	4.86	-87.45	3.61
5	228.72	5.93	-7.83	57.37
6	345.66	34.40	130.34	161.00
7	246.97	44.77	165.08	166.21
8	250.29	111.31	504.54	342.27
9	260.46	79.56	384.28	322.46

Table 4-4 Maximum line GIC in amperes in pipeline network 1

From Node	To Node	Geoelectric field scenario 1		Geoelectric field scenario 2	
		Nonuniform	Uniform	Nonuniform	Uniform
3	4	979.27	173.49	613.02	649.59
4	5	995.50	173.07	665.63	649.26
5	6	914.65	167.49	666.27	617.93
6	7	617.87	150.90	619.45	528.45
7	8	333.41	104.35	434.52	340.14
1	3	123.42	48.57	123.25	185.57
2	3	100.31	40.05	92.10	144.70
7	9	74.39	18.15	79.83	71.30

If we compare the induction results of nonuniform geoelectric field scenario 1 with those of 1.2 V/km eastward uniform base case, we can see that the PSP of almost all nodes and the maximum GIC of all pipelines in the network have increased significantly due to local geoelectric field enhancement. The spatially locally enhanced geoelectric field covers all of the pipeline 4-5 and a part of the pipeline 3-4 and 5-6. The induction results of these pipelines are directly affected by the nonuniform geoelectric field, while the changes in the results of other pipelines are mainly caused by network interconnection. In the case of a uniform geoelectric field, the peak of PSP is at the end of the main pipe, which is called the corner effect, while the peak of GIC appears in the middle of the pipe. After the geoelectric field is locally enhanced, the PSP peak appears at the edge of the geoelectric field enhanced area, and the GIC increse of the pipeline located in the geoelectric field enhanced area is higher than that of other pipelines.

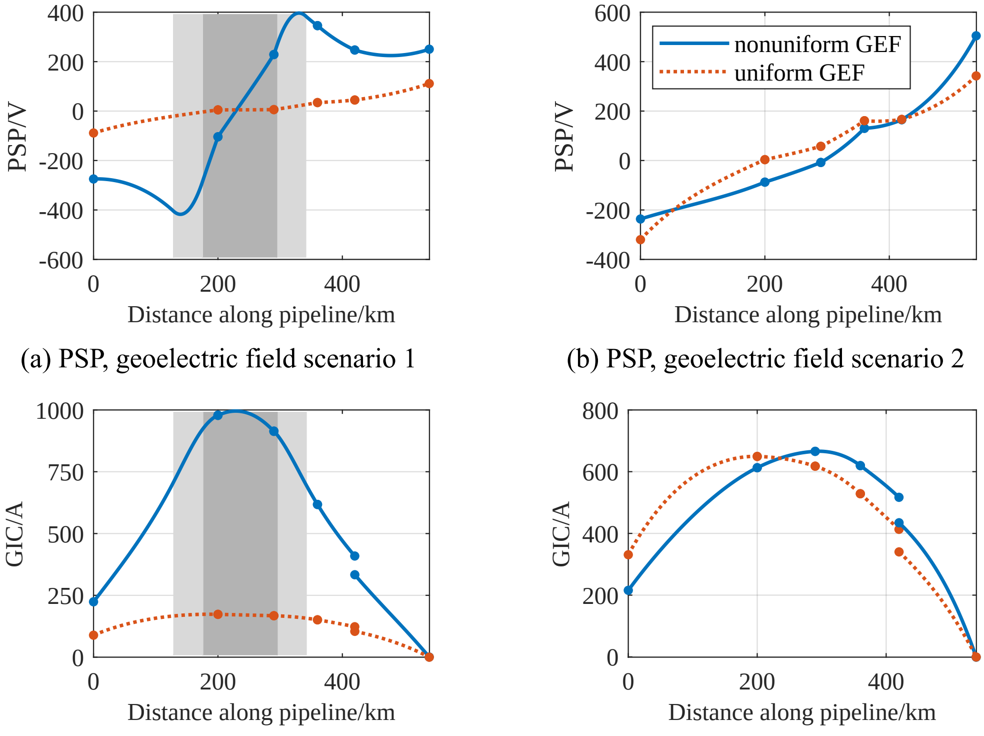

(a) PSP, geoelectric field scenario 1

(b) PSP, geoelectric field scenario 2

(c) GIC, geoelectric field scenario 1

(d) GIC, geoelectric field scenario 2

Figure 4-20 Comparison of PSP and GIC results with distance along the main pipeline “3-8” of network 1 in the case of nonuniform and uniform geoelectric field (GEF). The points in the figure indicate the positions of nodes along the main pipeline. (In subfigure (a) and (c), the dark gray part of the pipeline is located in the 12 V/km enhanced area, the white part is located in the 1.2 V/km base area, and the light gray part is located in the linear transition area from 12 V/km to 1.2 V/km.)

For the nonuniform geoelectric field scenario 2, the spatial distribution of the geoelectric field amplitude is characterized by being smaller in the west and larger in the east. As a comparison, the uniform geoelectric field case is taken as the average value of scenario 2, resulting in a southeast geoelectric field of $E_x = -0.945$ V/km, $E_y = 4.337$ V/km. The induction results along the main pipeline under nonuniform and uniform geoelectric field are compared in Figure 4-20. It can be seen that the overall spatial distributions of PSP and GIC are similar in the two cases, but there is a deviation in amplitude. The spatial averaging of the geoelectric field leads to an underestimation of the PSP and GIC magnitudes in the east of the network, corresponding to the area with a larger local geoelectric field, whereas the induction results are overestimated in the area with a smaller local geoelectric field.

4.3.3 Effects of Lateral Conductivity Variations on Geomagnetic Induction

1） Induction Results Considering Coast Effect

This section adopts the synthetic test pipe network 2 from Reference [24] for induction analysis, as shown in Figure 4-21, and the nodal coordinates are detailed in Table 4-2.

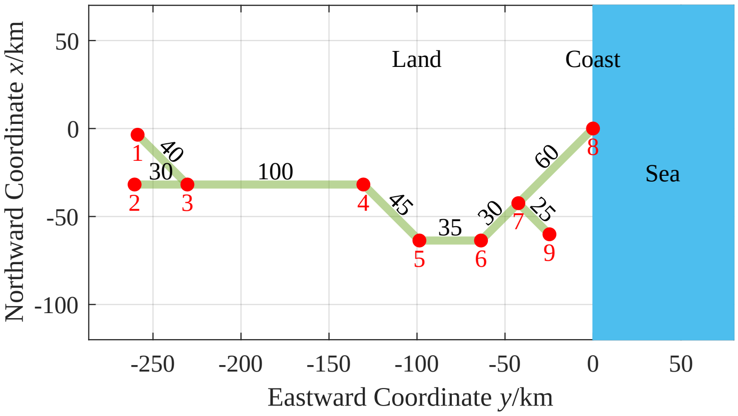

Figure 4-21 The synthetic 9-node and 8-pipeline network 2. The red labels indicate the number of nodes, and the black labels are pipeline lengths in kilometers.

The geoelectric field results obtained by the thin-sheet model and the block model, denoted as E_{3D} and E_{1D}, are used as inputs to analyze the induction in the pipe network. Due to the phase difference between the geoelectric field at different locations on the surface, the real and imaginary parts of the geoelectric field are used for the induction calculation separately, which are then combined to obtain the final amplitudes of the PSP and GIC in the pipelines. The PSP along the main pipeline is shown in Figure 4-22. The PSP of node 8 near the coast is analyzed as an example: for H-polarization, due to coast effect, the PSP of node 8 increases to 138.0% of that in the case of 1-D uniform land; whereas for E-polarization, it decreases to 33.8% of the original. The induction results of other pipes have relatively small changes due to the larger distance from the coast.

Then, the influence of coast at different frequencies on the induction in the pipe network is analyzed. The PSP of node 8 using thin-sheet and block model, denoted by PSP_{3D} and PSP_{1D}, is presented in Figure 4-23. The change of the PSP magnitude in percentage is smaller than that of the geoelectric field, since the coast effect weakens as the distance from the coast increases. As the frequency increases, the enhancement effect of H-polarization on the PSP

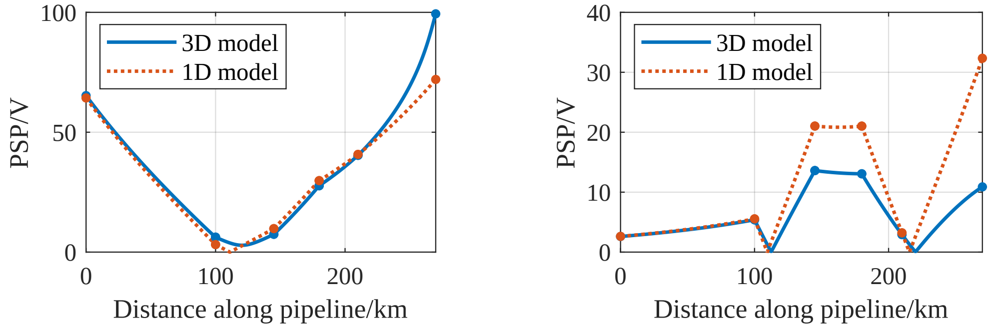

(a) PSP, H-polarization (b) PSP, E-polarization

Figure 4-22 Comparison of PSP with distance along the main pipeline 3-8 of network 2 at 0.001 Hz in the case of 3-D and 1-D earth model.

amplitude gradually weakens, which is consistent with the geoelectric field change shown in Figure 2-19(a); whereas for E-polarization, the weakening of the PSP amplitude is slight at higher frequencies, which is different from the geoelectric field change depicted in Figure 2-19(b), mainly due to the shorter effective distance of the coast effect at higher frequencies. The above results are similar to the impact of the coast on GICs in the power grid[66, 67]. In summary, for the pipe network example presented, the coast affects the PSP of node 8 more at lower frequencies (10^{-4} Hz-10^{-3} Hz), regardless of H-polarization or E-polarization.

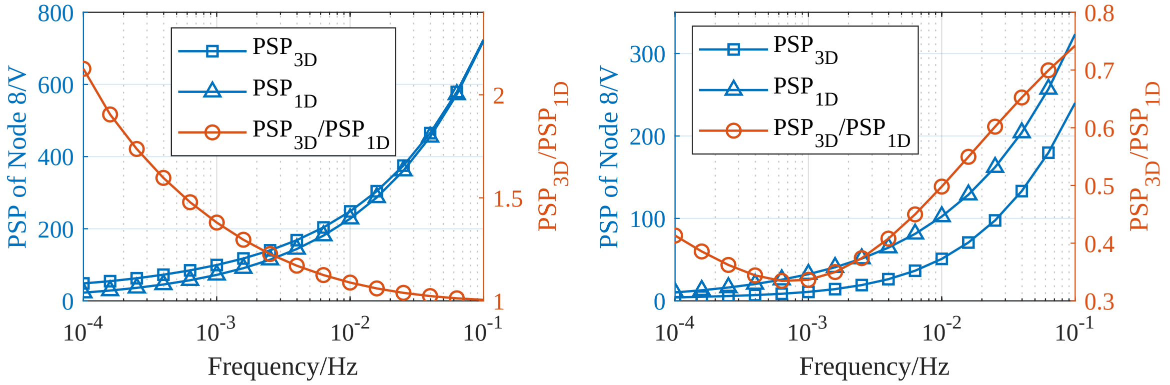

(a) PSP of node 8, H-polarization (b) PSP of node 8, E-polarization

Figure 4-23 Comparison of PSP of node 8 using 3-D and 1-D earth model with respect to the frequencies.

2） Effects of Geoelectric Field Spatial Distribution on Inductions in Pipeline Networks Using Measured Magnetotelluric Responses

The regional geoelectric field is usually spatially averaged due to the lack of magnetotelluric measurements or the simplification of induction simulation models[3, 152, 153]. This section analyzes its influence on the induction results in pipeline networks based on EMTF data measured near an actual coast.

The EMTF data at 1,112 USArray sites were obtained from the IRIS Data Services website[154]. The geomagnetic time series at the Ottawa (OTT) observatory from NRCan[155] during March 13-14, 1989 was selected to calculate the geoelectric field. The calculation process of the geoelectric field spatial distribution is as follows: first calculate the geoelectric field waveform at each EMTF site, and then perform spatial smoothing, i.e., the updated geoelectric field result at each site is the average value at the sites within a given distance, finally the geoelectric field is scaled according to the geomagnetic latitude of each site via (4-78). For GMD risk assessment, the empirical formula (4-78) can be used to scale the geoelectric field to characterize the intensity of geomagnetic activities at different geomagnetic latitudes[32].

$$\alpha(\lambda) = \begin{cases} 0.1, & \text{if } \lambda \leq 40^\circ \\ 0.001 \times e^{0.115\lambda}, & \text{if } 40 < \lambda < 60^\circ \\ 1, & \text{if } \lambda \geq 60^\circ \end{cases} \tag{4-78}$$

where λ is the geomagnetic latitude in degrees.

A geoelectric field peak at 1:17 on March 14, 1989 is selected for the induction analysis of the pipeline network. The spatial distributions of original geoelectric field at the EMTF sites and the geoelectric field under different smoothing distances are shown in Figure 4-24. Spatial smoothing weakens the sharp peak of the geoelectric field and also causes the loss of local details of the geoelectric field spatial distribution.

This section adopts another modification of the synthetic pipeline network from Reference[24], denoted as network 3. Network 3 is obtained by spatial translation of network 1 maintaining the pipe lengths. The geographic coordinate of node 1 in network 3 is (41°N, 81°W), and the pipe network passes through the geoelectric field enhancement area on the east coast. All nodes in the test network 3 are located within the envelope of the EMTF sites in order to avoid spatial extrapolation of the geoelectric field.

EMTF sites are usually scattered points with irregular spatial distribution. In this respect, in the pipeline induction calculation, the geoelectric field vector along the pipeline is obtained by interpolation of the value at the EMTF sites based on the Delaunay triangulation[65].

First, we compare the induction results along the main pipeline of network 3 under geoelectric field smoothing at different distances, where the geoelectric field is linearly interpolated along each pipeline. As shown in Figure 4-25, as the smoothing distance increases, the peak PSP and GIC amplitudes of the pipeline tend to decrease. The geoelectric field spatial

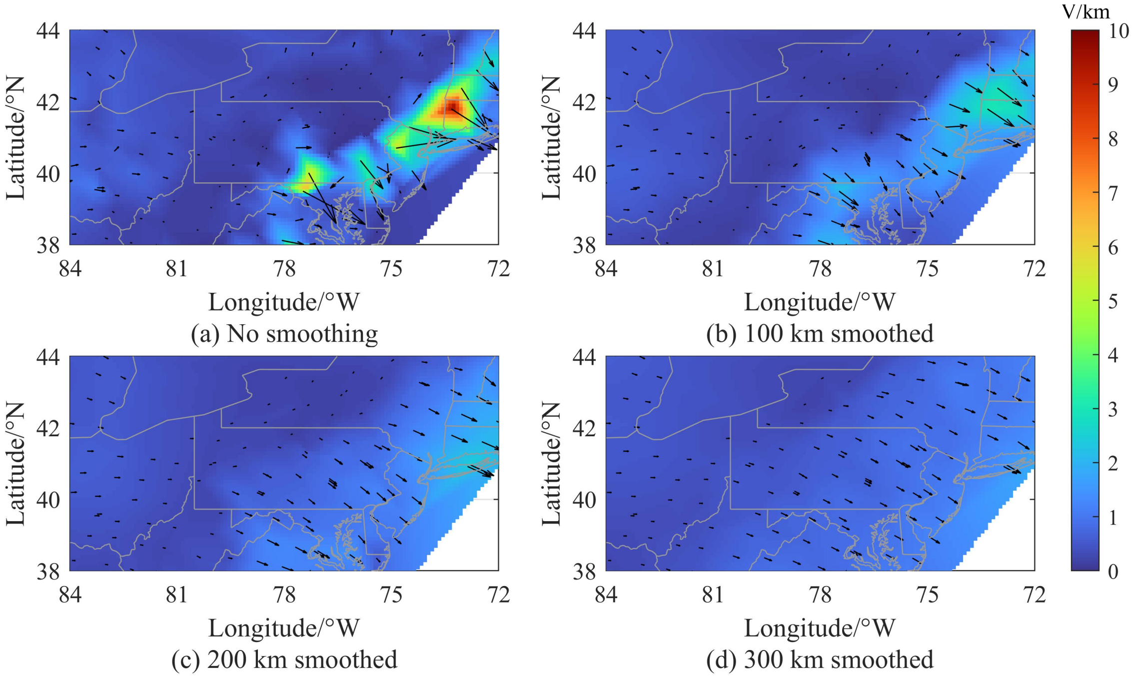

(a) No smoothing

(b) 100 km smoothed

(c) 200 km smoothed

(d) 300 km smoothed

Figure 4-24 Snapshots of the simulated geoelectric field spatial distribution on the east coast under different spatial smoothing distances at 1989-03-14 01:17. The arrow in the figure indicates the geoelectric field vector at the EMTF sites[154]; the color map visualizes the spatial distribution of linear interpolated geoelectric field; and the gray curve is the base map.

averaging may smooth out the fluctuating details of the induction results along the line, causing some risky sections of the pipeline to be unrecognizable.

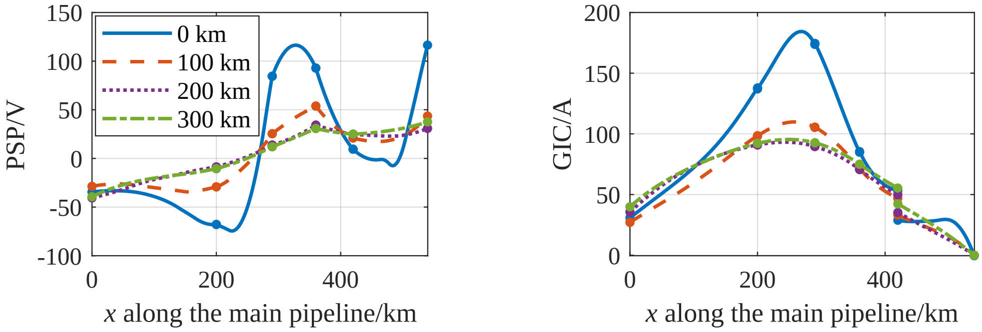

(a) PSP along the main pipeline

(b) GIC along the main pipeline

Figure 4-25 Comparison of PSP and GIC results along the main pipeline of network 3 in the cases of different spatial smoothing distances.

In addition, the influence of different interpolation methods of geoelectric field on the induction of pipe network is analyzed. The original geoelectric fields at the EMTF sites are interpolated along the pipeline using linear, nearest neighbor, and natural neighbor interpolation methods[156], respectively. Figure 4-26 shows the difference in pipeline induction results using different interpolation methods, where nearest neighbor interpolation method yields larger values. Hence, the modeling and measurement of geoelectric fields at finer spatial granularity are important for accurate assessment of geomagnetic induction in pipeline networks.

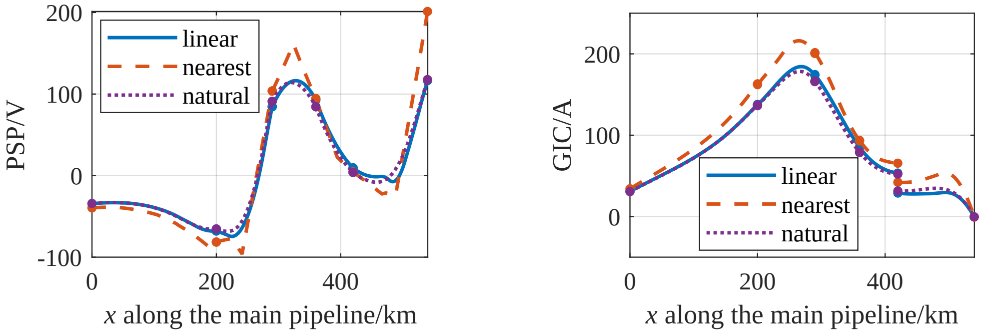

(a) PSP along the main pipeline

(b) GIC along the main pipeline

Figure 4-26 Comparison of PSP and GIC results along the main pipeline of network 3 in the cases of linear, nearest neighbor and natural neighbor interpolation of geoelectric fields.

4.4 Induction Results in Pipeline Networks Considering Nonlinear Polarization Effects

In this section, the proposed computational model is applied to the EMI analysis of long pipelines and interconnected networks. First we analyze the response of a pipeline to typical conductive and inductive interference, including HVDC earth return currents and geomagnetic disturbances. We then analyze the influence of the coating breakdown and illustrate the significance of the polarization effects.

4.4.1 Model Validation of the Generalized Equivalent Circuit for Pipeline

The proposed equivalence method for pipelines has been verified in Section 4.3.1 in the case of inductive EMI caused by geomagnetic disturbances. Hence, this section further illustrates its validity for conductive coupling analysis.

The authors of [106] carried out a field test of the interference of DC current sources on a short buried pipeline, as depicted in Figure 4-27. The length of the pipeline is 39.3 m, and the buried depth is 0.8 m. The outer diameter of the steel tube is 200 mm, and its wall thickness is 5 mm. The steel resistivity is 1.75×10^{-7} Ω·m. The steel tube is wrapped with 3PE insulation coating. Its thickness is 3 mm and its resistivity is 3.33×10^{7} Ω·m. The insulation coating is intact along the pipe. The left and right ends of the pipe were respectively connected to a vertical grounding rod with a length of 1.5 m and a diameter of 10 mm. Four potential measurement points were arranged along the pipe, including M1, M2, M3 and M4. The point M1 was taken as the origin. The 1D layered soil resistivity structure, as shown in Table 4-5, was measured by the Wenner method.

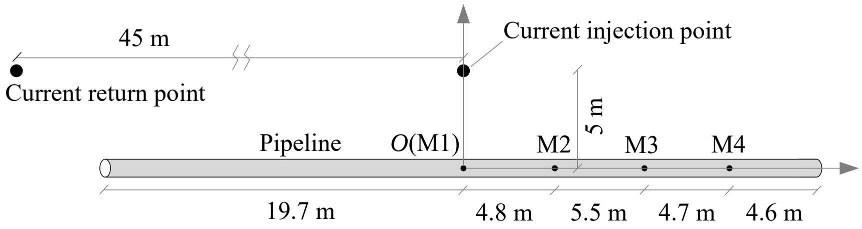

Figure 4-27 Schematic diagram of the field test of a short pipeline[106].

Table 4-5 Two-layer horizontal soil resistivity structure[106]

Layer	Resistivity/Ω·m	Thickness/m
1	31	2.5
2	79	∞

The PSPs along the pipeline are calculated using the proposed model and the classical model, which are compared with the measured data. It is worth noting that in this study, PSP is defined by subtracting the outer soil potential from the inner metal potential of the coating, whereas [106] takes the opposite reference direction. Besides, the slight asymmetry of potential distribution along the pipeline is affected by the current return point. In the proposed model, the pipeline is reduced to an equivalent pi-circuit. Thus, the voltage response can be solved based on a two-node admittance matrix. In contrast, in the classical model, the pipeline is discretized based on the original TL equations (4-27)-(4-28). Hence, the proposed method enables a considerable reduction in model size. As shown in Figure 4-28, the results of the two computational models are highly consistent, and they both agree well with the test data, which validates the accuracy of the proposed method.

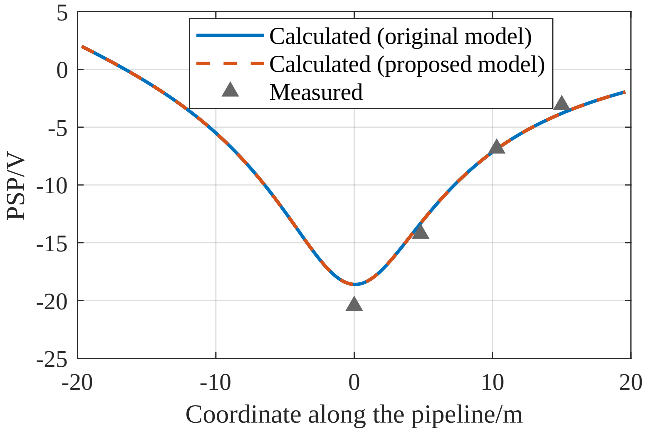

Figure 4-28 Comparison of calculated and measured PSPs along the pipeline.

4.4.2 Comparison of Pipeline Response to HVDC Earth Return Currents and GMDs

Let us consider a more realistic 200 km pipeline as shown in Figure 4-29. The outer diameter of the steel tube is 1016 mm, and its wall thickness is 12 mm[108]. The steel resistivity is 1.75×10^{-7} Ω·m. The coating has a thickness of 3 mm and a resistivity of 3.33×10^{7} Ω·m. In this subsection, the coating is assumed to be intact. The pipeline is buried in a 100 Ω·m homogeneous earth at a depth of 1.5 m.

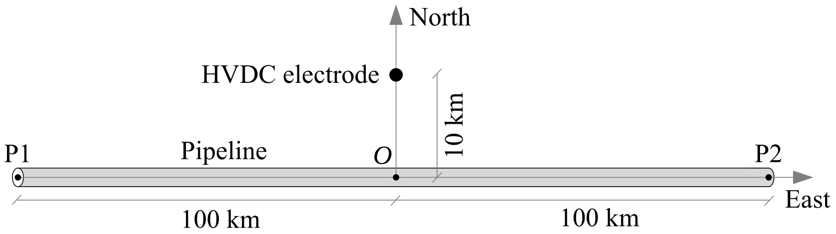

Figure 4-29 Schematic diagram of a simulation case including a long pipeline and a HVDC grounding electrode.

The first type interference is caused by a nearby HVDC grounding electrode. The electrode is 10 km away from the midpoint of the pipeline. Its buried depth is 3 m, and the earthing current is -5 kA. The resulting excitation voltage and tangential exciting electric field along the pipeline are shown in Figure 4-30. It can be seen that the excitation voltage has a peak value of -7.96 V at the center of the pipe and that the tangential electric field reaches a peak of 0.31 V/km at a distance of 7.1 km from the midpoint. The second type interference is geomagnetic disturbances, which correspond to a uniform 0.1 V/km eastward geoelectric field. The pipeline response to the two types of disturbances are then calculated separately. The above is the default simulation configuration in this section unless otherwise specified.

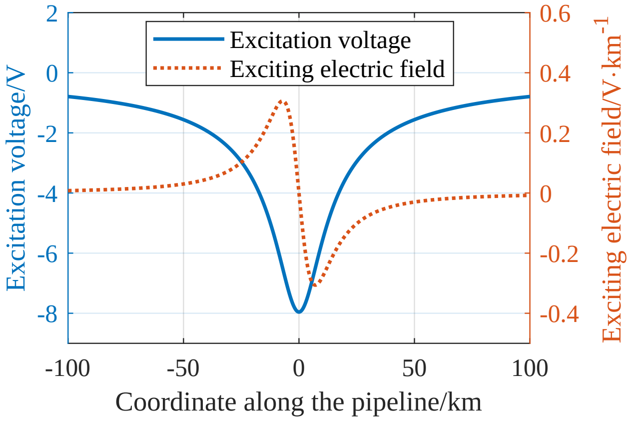

Figure 4-30 The excitation voltage and tangential exciting electric field along the pipeline caused by the HVDC earth return currents.

Figure 4-31 compares the PSP and longitudinal current along the pipe in the two interference cases. In the case of interference from the HVDC grounding electrode, the peak value of PSP is 5.16 V, which appears at the midpoint of the pipeline. In the case of geomagnetic disturbances, the peak value of PSP amplitude is 6.82 V, which appears at the two ends of the pipe. The leakage current density along the pipe is proportional to the PSP, and its peak values in the two interference cases are 5.2×10^{-5} A/m^2 and 6.87×10^{-5} A/m^2, respectively. The peak of the longitudinal current is located at the zero crossing point of the PSP.

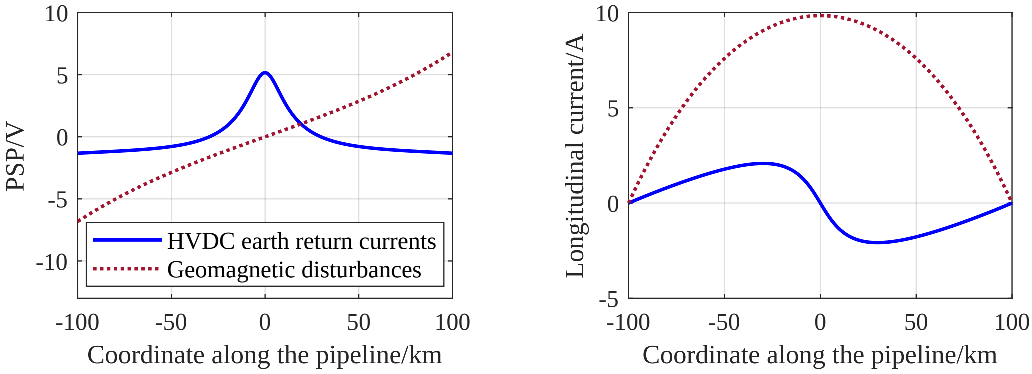

(a) PSP (b) Longitudinal current

Figure 4-31 Pipeline's responses to HVDC earth return currents and geomagnetic disturbances.

4.4.3 Influence of Nonlinear Polarization Effect on Pipeline Response

The influence of coating breakdown is analyzed in this subsection. The damage points are assumed to be equally spaced at an interval of 10 km. The area of the damaged coating of each node is 5 cm^2. Based on the electrochemical test data for the 100 Ω·m soil, the fitted Butler-Volmer polarization equation is given by[108]

$$i = 3.66 \times [\exp(\frac{V_{l'}^{\text{pol}} + 0.304}{2.45}) - \exp(-\frac{V_{l'}^{\text{pol}} + 0.304}{4.94})] \tag{4-79}$$

The corresponding nonlinear polarization curve is shown in Figure 4-32. When the leakage current density is zero, the interface of the coating defect works at the natural corrosion potential -0.304 V. When the leakage current density is in the range of 0∼0.702 A/m^2, the polarization curve is in the second quadrant, which means it behaves as a negative resistance.

Then, we calculate the polarization voltage and leakage current density of the coating defects using two calculation models. In the first model, the polarization effect at the damaged interface is neglected, and only the external soil resistance is considered[102]. In the second model, however, both effects are considered.

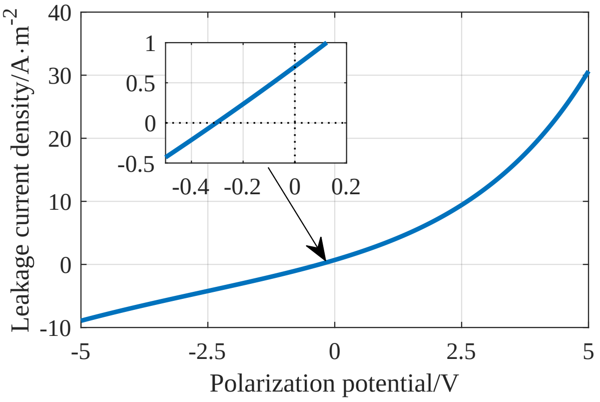

Figure 4-32 Polarization curve of the pipe steel in 100 Ω·m soil.

The response of the coating defects to the HVDC earth return currents and geomagnetic disturbances are shown in Figure 4-33 and Figure 4-34, respectively. If the polarization effect is neglected, the PSPs at the interface of the damaged coating are considered to be zero. In addition, the leakage current density of the coating defects at the midpoint of the pipe is overestimated by 22.6% for the HVDC interference; and the leakage current densities at the left and right ends are overestimated by 46.3% and 22.9% for the geomagnetic disturbances, respectively. Moreover, the magnitude of the leakage current density of the coating defects is much higher than that of the intact coating in Figure 4-31.

We then discuss the influence of the area of damaged coating. The area of each coating defect ranges from 5 cm^2 to 100 cm^2. The total number and distance of the defects are the same as in the previous subsection. Figure 4-35 shows the leakage current density of the coating defects at the left and right ends of the pipe due to geomagnetic disturbances. As the damaged area increases, the leakage current density at both ends decreases gradually.

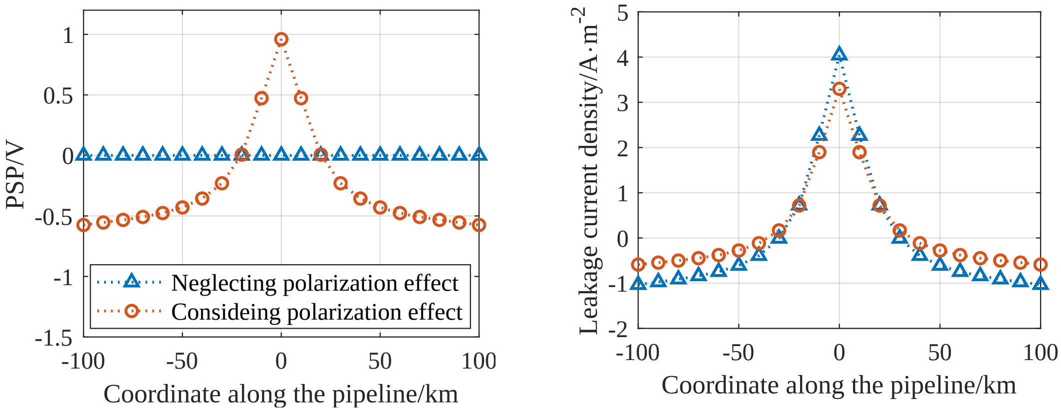

(a) PSP of the interface

(b) Leakage current density

Figure 4-33 Response of the coating defects due to HVDC ground return currents.

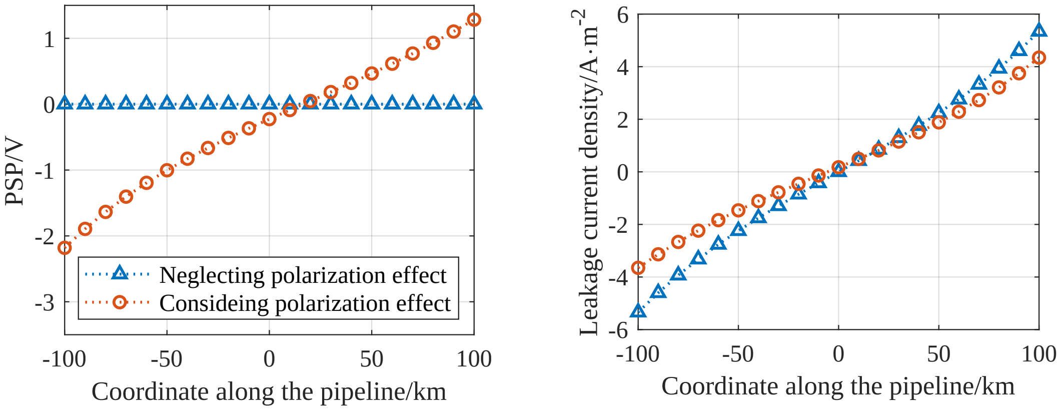

(a) PSP of the interface

(b) Leakage current density

Figure 4-34 Response of the coating defects due to geomagnetic disturbances.

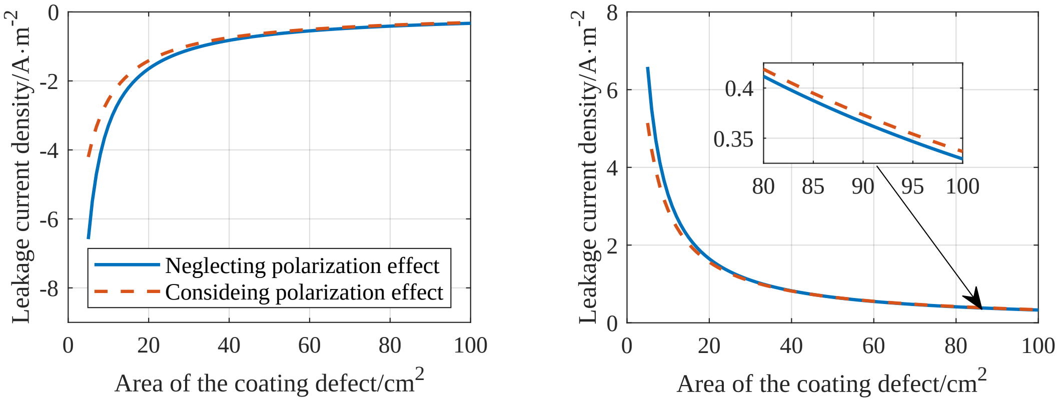

(a) Left end of the pipe

(b) Right end of the pipe

Figure 4-35 Leakage current density induced by geomagnetic disturbances with respect to the area of the coating defect.

In order to indicate the contribution of the polarization effect more clearly, we further adopt a normalized metric, i.e. the ratio of the leakage current density of the coating defects without and with consideration of the polarization effect. Figure 4-36 depicts the variation of this ratio with respect to the area of coating defects. It can be seen that the ratio of leakage current density at the left and right ends decreases with the increase of the damaged area and that the polarization effect has a stronger influence on the current leakage density of the left end than that of the right end. Also, note that for the coating defects at the right end, the ratio may be less than 1 when the damaged area is large, since it works in the second quadrant in Figure 4-32 in this case.

Next, the applicability of the proposed method is illustrated with an interconnected pipeline network with nine nodes and eight lines, as depicted in Figure 4-37. The TL parameters and nodal coordinates of the pipeline network can be found in Table 4-2. The network contains a

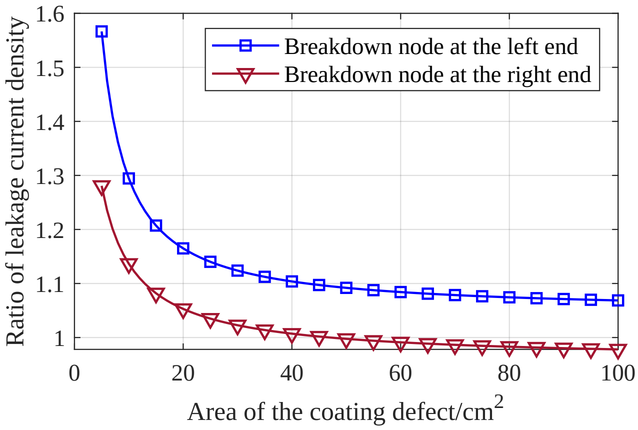

Figure 4-36 Ratio of the leakage current density induced by geomagnetic disturbances neglecting and considering the polarization effect with respect to the area of coating defect.

main pipeline "3-4-5-6-7-8" and three branch lines "1-3", "2-3" and "7-9". The coating defects are assumed to be equally spaced at an interval of 10 km on each pipeline. The area of the damaged coating of each node is 5 cm^2. The external nonuniform geoelectric field is caused by the spatially local enhancement of the geomagnetic variations. The electric field data are provided in report [60] with a 0.5° × 0.5° grid, and the values in this study are scaled to 1% of the original as a representative level of more frequent medium and small geomagnetic disturbances. A finer spatial distribution of the electric field is obtained by linear interpolation.

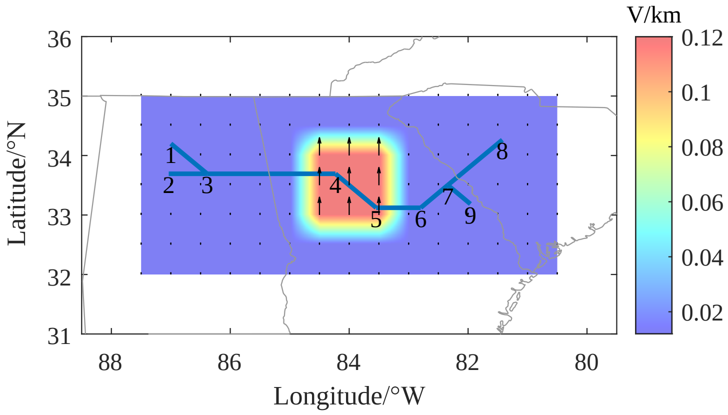

Figure 4-37 Spatial distribution of pipeline networks and nonuniform geoelectric fields[60]. The black arrows show the direction and magnitude of the geoelectric field. The black number is the node index in the pipeline network.

Figure 4-38 shows the leakage current density along the main pipeline "3-8". It can be seen that the amplitude of the leakage current density reaches the extreme value at nodes 4 and 5. Ignoring the polarization effect leads to an overestimation of the leakage current density by 18.5% and 52.8% at nodes 4 and 5, respectively.

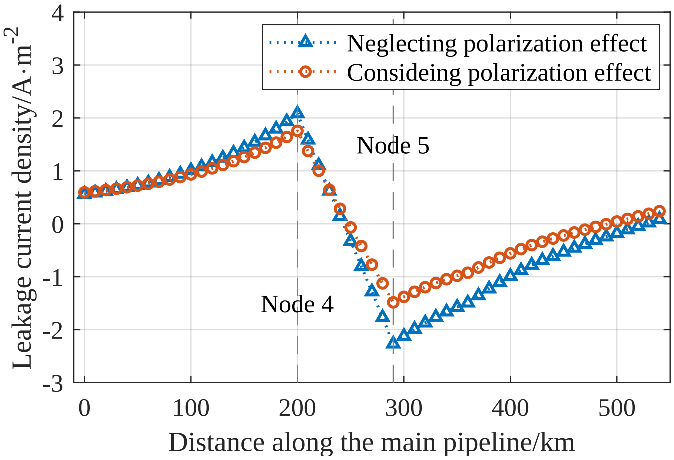

Figure 4-38 Leakage current density of the coating defects along the main pipeline “3-8”.

Finally, the computational performance of the classical discretization method and the proposed equivalence method is compared using a historical geomagnetic disturbance event. The geomagnetic data with 1-minute time cadence measured at Beijing Ming Tombs (BMT) observatory during the event on July 15-16, 2000 are used as inputs, and the corresponding number of time instants is 2880. In the classical method, the pipe between two adjacent coating defects is divided into 100 segments. The algorithms are tested using MATLAB R2019b software on a desktop with a 3.0 GHz Intel i7-9700 CPU and 8 GB RAM. Table 4-6 provides the details of these two calculation methods, including the size of the system of equations, memory requirements and computation times. It shows that the proposed equivalence method can improve computational performance, especially when fine discretization is required to capture the complex spatial non-uniform distribution of the exciting electric field.

Table 4-6 Computational performance of the classical discretization method and the proposed equivalence method for the pipeline network test case

Calculation methods	Size of the coefficient matrix	Memory of the sparse coefficient matrix/kB	Computation times/s
Classical	7375×7375	404.44	132.24
Proposed	148×148	9.21	4.51

4.5 Concluding Remarks

In this chapter, first, we propose a calculation method for the geomagnetic induction in pipeline networks with nonuniform geoelectric field. The influence of the typical nonuniform geoelectric field distribution due to geomagnetic source fields such as local enhancement and gradual variation on the induction results in the pipe network is investigated, which shows that there is a relatively large difference in PSP and GIC compared with uniform geoelectric field. In addition, the lateral conductivity variations also have a great impact on induction in pipe networks, especially at low frequencies, and H-polarization and E-polarization cause increase and decrease of the PSP near the interface, respectively. Moreover, using the induction results in the pipeline network based on magnetotelluric response measurements, the influence of the spatial smoothing and interpolation method of the geoelectric field on the pipeline induction is analyzed. The model proposed in this research can be used to evaluate the geomagnetic induction in pipelines passing through complex geology if geoelectric field distribution with finer spatial granularity is available.

Then, we proposes a generalized modeling and equivalence technique for the analysis of EMI on pipeline networks due to nonuniform fields. The computational model is reduced through the equivalent pi-circuit. The proposed method is validated by comparison with the classical discretization method and field tests. Based on the proposed model, we compare the responses of buried pipelines to HVDC earth return currents and geomagnetic disturbances. In addition, the influence of the coating breakdown and the polarization effect are analyzed. The results show that when the damaged area is small, the leakage current density is relatively large and the influence of the polarization effect is strong, which needs to be considered in the corrosion assessment for pipelines. The proposed calculation method can be extended to other EMI analysis of pipelines. It can also significantly reduce the computational burden and help in the optimization of mitigation measures, where a large number of different configurations need to be analyzed.

5 Modeling of Geomagnetic Induction in Integrated Power-Gas Systems

Nowadays, the integrated power-gas systems (IPGS) are promising for improving the flexibility of energy supply. The power systems and natural gas pipeline networks are increasingly coupled both spatially and functionally, which has not been taken into full account in geomagnetic induction modeling and its effect assessment. On the one hand, common corridors of power lines and buried pipelines have been built to save the land. Thus, the earthing GIC from the power grid and buried pipes may interact with each other, thereby redistributing the induced voltages and currents in the IPGS. On the other hand, natural gas-fired power generation and power-to-gas technology raise the functional dependencies[157]. For instance, the potential transformer outage during a GMD event may lead to cascading failures in the IPGS. Hence, as a first step, rigorous and efficient modeling of geomagnetic induction in the IPGS is of great importance for the GMD risk assessment and mitigation.

However, the interaction between the earthing currents from substation grounding grids and pipelines is not considered in the classical geomagnetic induction models developed for power grids or pipelines separately. Hence, the classical models are not suitable for the geomagnetic induction analysis of the IPGS, where the AC substation may be very close to the pipeline, e.g. only several hundred meters to several kilometers away. Their conductive coupling is relatively strong in this case, thus the classical models may yield biased estimates of the level of the induced voltages and currents in integrated systems and their effects. It may further lead to the result that the mitigation and protection measures developed on this basis do not match the actual magnitude and spatial distribution of the induction results.

In this respect, we propose a novel geomagnetic induction model for the IPGS. To the best of our knowledge, this research is the first attempt to address this issue. The ground transfer resistances between the substation grounding grids and the buried pipelines are considered when we characterize their conductive coupling. Then, a nodal voltage analysis method is proposed to calculate the induced voltages and currents in the IPGS. The proposed circuit approach is verified by using the finite element analysis. In fact, this approach can provide more accurate results of induced voltages and currents in integrated systems compared to the classical models, which can help planners and operators in the energy sector develop comprehensive risk assessment and mitigation strategies for transformers, pipelines and other equipment.

This chapter is organized as follows. Section 5.1 details the proposed geomagnetic induction model for the IPGS. In Section 5.2, the proposed circuit model of the IPGS based on the ground transfer resistance is verified by using the finite element analysis. Then, the geomagnetic induction calculation is performed for a several IPGS test cases in Section 5.3. The induction results in the integrated systems calculated by the proposed model are compared with those by the classical models without considering the influence of earthing currents from the other network, and it clearly demonstrates the importance of considering the coupling between AC power grids and pipelines. Finally, Section 5.4 concludes this chapter.

5.1 Geomagnetic Induction Model for IPGS

5.1.1 Coupling Between Power Grid and Pipeline Network During GMD

GMD hazards may pose a threat to the reliability of the ground-based technological systems, including power grids and pipeline networks[3, 4, 33]. GIC in power grids could give rise to half-cycle saturation of the transformers, causing hot-spot heating, reactive power loss and harmonic distortion, etc[75, 76, 78, 158-160]. The pipe-to-soil potentials (PSP) may accelerate the corrosion of the pipes and interfere with the cathodic protection system[22-24, 161].

In the general context, electromagnetic interference between AC power grids and pipeline networks has attracted much attention, e.g. fault currents[98], harmonic interference[101, 162], lightning strikes[163], and HVDC ground return currents[40]. However, the existing geomagnetic induction models are developed separately for power grids and pipeline networks according to their grounding nature without adequately considering their conductive coupling.

The power grid is discretely grounded through the substation grounding grids in the GIC model. For a general power grid with multiple voltage levels, the full-node models, including the Lehtinen-Pirjola method[76, 158] and the nodal admittance matrix method[75], are proposed to calculate the GIC. Furthermore, the bus admittance matrix method[78] and the reduced nodal admittance matrix method in Section 3.1 are proposed to speed up the GIC computation through model order reduction. In most GIC calculations, the coupling between the substation grounding grids through the earth is usually considered negligible. Some literature analyzed the influence of mutual resistances between substations on GIC in the cases of the uniform earth[159] and horizontally layered earth[160].

On the contrary, the pipelines are continuously grounded through the insulation coating in the geomagnetic induction model. Boteler and Cookson[22] first proposed the distributed source transmission line model to calculate the PSP and GIC along the pipeline. For the analysis of large-scale pipeline networks, some efficient equivalent methods have been proposed for pipes, including the Thevenin equivalent circuit[23], and the equivalent-pi circuit with uniform geoelectric field[24].

There are two main types of coupling between power grids and pipeline networks during GMD. The first category is conductive coupling. The quasi-DC earthing currents from substation grounding grids and pipelines, driven by the geoelectric field, can produce additional electric fields in the soil. Thus, they can generate a potential difference between other grounding bodies. The second type is inductive coupling[161]. GIC in the power grid could lead to half-cycle saturation of the transformer, and the resulting harmonics flowing through the overhead power transmission lines can be inductively coupled to adjacent pipelines, which can be evaluated using well-established methods[101, 162]. Hence, this research focuses on the modeling of conductive coupling in the IPGS.

5.1.2 Calculation of Ground Transfer Resistance Between Grounded Nodes

The conductive coupling in the IPGS during GMD can be modeled through the ground transfer resistance. We discuss its calculation methods for different earth models, including uniform, 1D layered and 3D structures.

Green's function is the basis for the calculation of transfer resistance, which refers to the ground potential V generated by a unit point current source I[164]. If the distance between two grounding bodies is much larger than their size, the earthing current can be regarded as a point current source for ground transfer resistance calculations. Thus, the ratio of V/I can be defined as the ground transfer resistance between the source and field points. Otherwise, it is required to consider the detailed current distribution inside the grounding body to obtain the earth potential rise.

The Green's function depends on the earth resistivity structure. It can be solved analytically for the uniform earth and the 1D layered earth, as depicted in Figure 5-1. These two simplified resistivity structures are widely used in GMD studies[3].

For a homogeneous soil model with resistivity ρ in Figure 5-1(a), the point current source I is assumed to be at the depth z_s. We build a cylindrical coordinate system with the point directly above it situated on the earth surface as the origin, i.e. the earth surface is set to $z = 0$. Thus, the potential at the coordinate (r, z) in the soil can be calculated analytically via the method of images as[165]

$$V(r,z) = \frac{\rho I}{4\pi} \cdot \left[\frac{1}{\sqrt{r^2 + (z - z_\mathrm{s})^2}} + \frac{1}{\sqrt{r^2 + (z + z_\mathrm{s})^2}} \right] \tag{5-1}$$

where r is the horizontal distance between the source and field point, and z is the depth of the

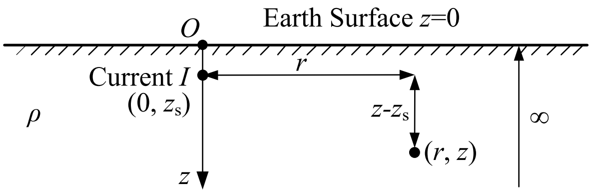

(a) Uniform earth

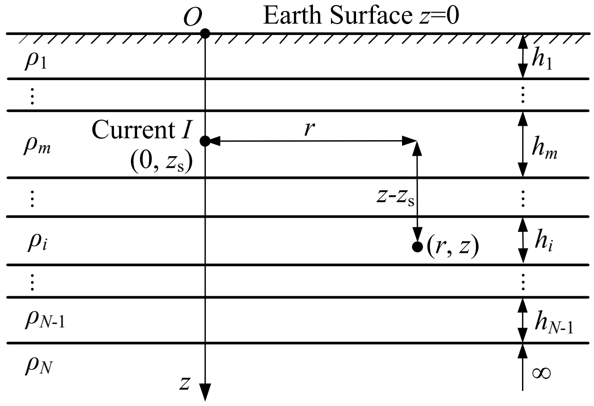

(b) 1D Horizontally layered earth

Figure 5-1 Schematic diagram of earth resistivity structures. The point current source I is added for Green’s function analysis.

field point.

This simple uniform earth can provide us some valuable insights. The interaction between the ground bodies is stronger as the resistivity increases and the distance decreases.

For a layered earth model in Figure 5-1(b), the point current source I is assumed to be located in the m-th layer. According to the potential equation and boundary conditions in the soil, the potential at the coordinate (r, z) in the i-th layer can be deduced as[164]

$$
\begin{aligned}
V_i^m(r,z) = & \frac{\rho_m I}{4\pi}\int_0^\infty \delta(m-i)\, e^{-\lambda|z-z_s|} J_0(\lambda r)\,\mathrm{d}\lambda \\
& + \frac{\rho_i I}{4\pi}\int_0^\infty \phi(\lambda)\, e^{-\lambda(z-z_s)} J_0(\lambda r)\,\mathrm{d}\lambda \\
& + \frac{\rho_i I}{4\pi}\int_0^\infty \psi(\lambda)\, e^{\lambda(z-z_s)} J_0(\lambda r)\,\mathrm{d}\lambda
\end{aligned}
\tag{5-2}
$$

where $\delta(0) = 1$ and $\delta(m-i) = 0$ for $m \neq i$; $J_0(\cdot)$ is the zero-order Bessel’s function of the first kind; $\phi(\lambda)$ and $\psi(\lambda)$ are kernel functions that depend on the soil resistivity parameters and depth of the source point[166].

Substation grounding grids and natural gas pipelines are typically buried at a depth of several meters. Thus, if the source and field points of interest are both in the top layer of soil, the general solution for the potential in (5-2) can be rewritten as[167]

$$V(r,z)=\frac{\rho_1 I}{4\pi}\left\{\frac{1}{\sqrt{r^2+(z-z_{\mathrm{s}})^2}}+\frac{1}{\sqrt{r^2+(z+z_{\mathrm{s}})^2}}\right.$$
$$\left.+\int_0^{\infty}f(\lambda)\left[e^{-\lambda(z-z_{\mathrm{s}})}+e^{-\lambda(z+z_{\mathrm{s}})}+e^{\lambda(z-z_{\mathrm{s}})}+e^{\lambda(z+z_{\mathrm{s}})}\right]J_0\left(\lambda r\right)\mathrm{d}\lambda\right\} \tag{5-3}$$

where $f(\lambda)$ depends on the earth resistivity parameters, which can be obtained in a recursive manner from the bottom layer to the top layer[167].

Note that there is an improper integral in the potential solution (5-3) with an infinite upper limit and an oscillatory kernel function. Thus, the numerical integration method is computationally expensive. As an alternative, the complex image method[168] can be used to efficiently obtain approximate solutions.

For the earth structure with 3D complex resistivity distributions, there is usually no analytical solution for the potential distribution. Instead, it can be solved by numerical approaches such as finite element or boundary element analysis. According to the current conservation law, the governing equations can be written as

$$\nabla\cdot\mathbf{J}_{\mathrm{c}}=0 \tag{5-4}$$

$$\mathbf{J}_{\mathrm{c}}=\sigma\mathbf{E}+\mathbf{J}_{\mathrm{e}} \tag{5-5}$$

$$\mathbf{E}=-\nabla V \tag{5-6}$$

where $\mathbf{J}_{\mathrm{c}}$ is the conduction current density, $\mathbf{E}$ is the electric field intensity, $\mathbf{J}_{\mathrm{e}}$ is the externally generated current density, σ is the conductivity, and V is the electrical potential.

And the earth surface is subject to the boundary condition of electrical insulation:

$$\mathbf{n}\cdot\mathbf{J}_{\mathrm{c}}=0 \tag{5-7}$$

where $\mathbf{n}$ is the normal vector of the earth's surface.

5.1.3 Nodal Voltage Analysis of the IPGS Under GMD

Geomagnetic induction modeling in technological systems can usually be divided into two steps: a geophysical step and an engineering step[33]. In the geophysical step, the induced geoelectric field on the earth's surface is calculated based on the space current system and the earth resistivity structure[59]. In practice, it is difficult to obtain the accurate spatiotemporal distribution of the space current system. Thus, the geoelectric field $\mathbf{E}(\omega)=[E_x(\omega),\ E_y(\omega)]^{\mathrm{T}}$ can be calculated by using the measured geomagnetic field $\mathbf{B}(\omega)=[B_x(\omega),\ B_y(\omega)]^{\mathrm{T}}$ under the plane-wave assumption[3, 65, 128]:

$$\mathbf{E}(\omega) = \mathbf{K}(\omega) \cdot \mathbf{B}(\omega) \tag{5-8}$$

where **K** is the magnetotelluric transfer function, ω is the angular frequency, sub-x and sub-y refer to the components in the north and east directions.

Then in the engineering step, the low-frequency geoelectric field drives the induced currents in the IPGS, which can be calculated by utilizing the resistive circuit analysis. The equivalent circuit of Figure 5-2 provides a simple illustrative IPGS example involving a small portion of both the power grid and the gas pipeline network. We adopt current-controlled voltage sources to characterize the coupling of earthing currents of the substations and pipelines, and the derivation of the rest of the circuit can be found in[3, 24].

We consider a general power grid with multiple voltage levels, as shown in Figure 5-2(a). The buses and substation grounding grids are regarded as nodes, and the node sets are denoted as N_b and N_s, respectively. The GIC flow path inside the substation depends on the type and connection group of the transformers. Figure 5-2(a) gives a typical example, where substation i contains a GY-GY transformer and substation k contains an auto-transformer. The transformer neutral point is connected to the substation grounding grid, and a capacitive or resistive GIC blocking device can be installed on this branch to mitigate the GIC.

The buried natural gas pipelines are continuously grounded through the insulation coating. Thus, we can discretize the pipes to establish a circuit model, as depicted in Figure 5-2(b), and the resulting set of pipe nodes is denoted as N_p.

Thus, we can perform a nodal voltage analysis for the full-node set, including buses, substation grounding grids, and pipe nodes, which can be denoted as $N_\mathrm{full} = N_\mathrm{b} \cup N_\mathrm{s} \cup N_\mathrm{p}$. The numbers of the three types of nodes are denoted as n_b, n_s, and n_p, respectively.

The effect of the geoelectric field on the power grid can be modeled as a voltage source in the power line[3]. Then the voltage source can be converted into the current injections $\mathbf{J}_\mathrm{b}$ at buses with Norton equivalent system. The current injections at the substation grounding grids due to geoelectric fields are zero, since they are not directly connected to the long horizontal conductors. Thus, the nodal current injections in the power grid can be written in matrix form as

$$\mathbf{J}^\mathrm{b} = \mathbf{\Gamma}^\mathrm{b}\mathbf{E}, \quad \mathbf{J}^\mathrm{s} = \mathbf{0} \tag{5-9}$$

where $\mathbf{\Gamma}^\mathrm{b}$ is the incident matrix for buses depending on power grid topology and power line resistances. In the illustrative example of Figure 5-2(a), vector $\mathbf{J}^\mathrm{b}$ collects the current injections

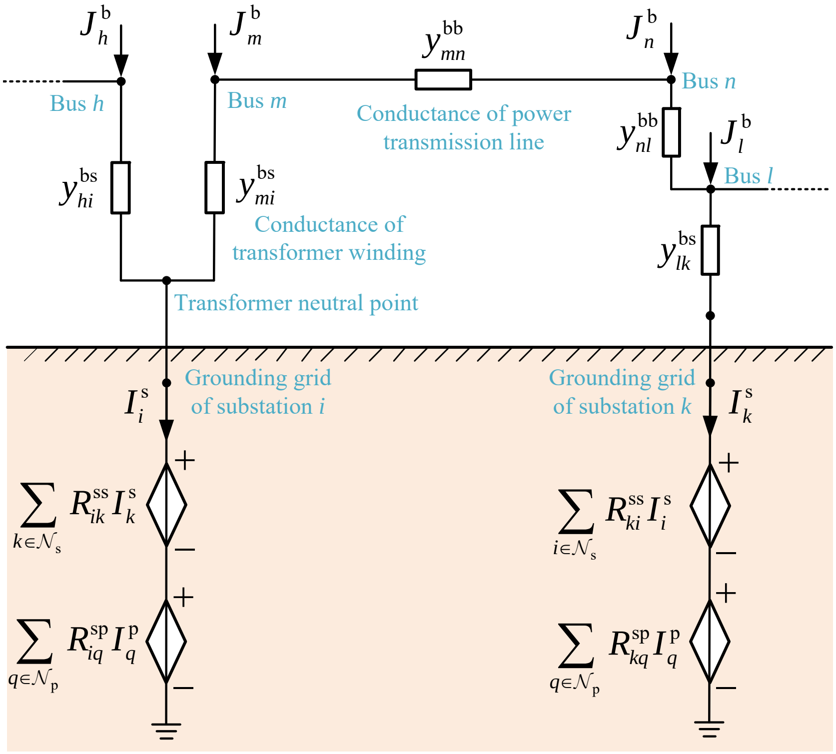

(a) Model of a power grid with multiple voltage levels

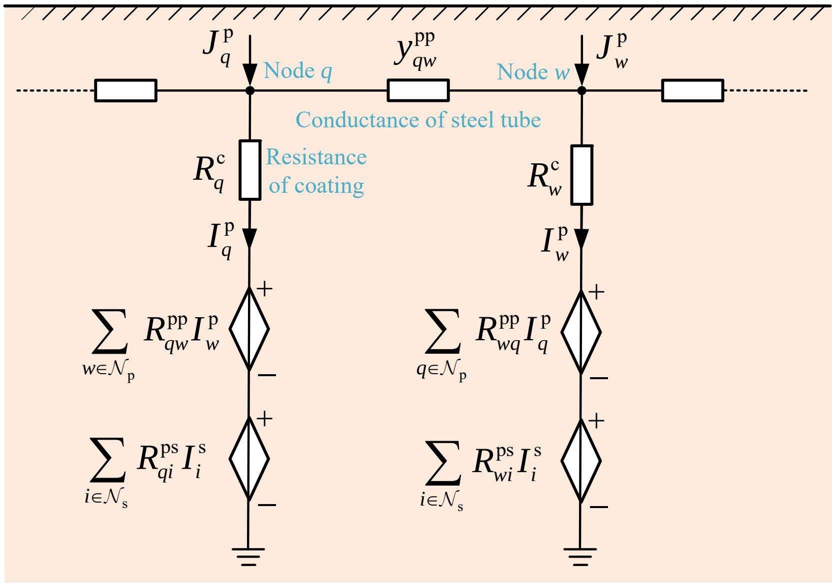

(b) Model of a buried pipe section of the gas pipeline network

Figure 5-2 Equivalent circuit of the IPGS for the geomagnetic induction analysis considering the conductive coupling through the earth. The superscript of the variables refers to the type of the node ('b' for bus, 's' for substation grounding grid, and 'p' for pipe node), and the subscript refers to the index of the node, e.g. J_m is the current injection at node m, I_i is the earthing current of node i, y_{mn} is the admittance of the branch (m, n), R_{ik} is the ground transfer resistance between the grounded nodes i and k, and R_q^{c} is the coating resistance of the pipe node q.

at buses h, m, n and l, yielding $\mathbf{J}^{\mathrm{b}} = [\ldots, J_h^{\mathrm{b}}, J_m^{\mathrm{b}}, J_n^{\mathrm{b}}, J_l^{\mathrm{b}}, \ldots]^{\top}$.

Similar to the buses, we can get the current injections at the pipe nodes

$$\mathbf{J}^{\mathrm{p}} = \mathbf{\Gamma}^{\mathrm{p}}\mathbf{E} \tag{5-10}$$

where $\mathbf{\Gamma}^{\mathrm{p}}$ is the incident matrix for pipelines. For the example of Figure 5-2(b), vector $\mathbf{J}^{\mathrm{p}}$ collects the current injections at pipe nodes q and w, yielding $\mathbf{J}^{\mathrm{p}} = [\ldots, J_q^{\mathrm{p}}, J_w^{\mathrm{p}}, \ldots]^{\top}$.

The current injections due to the geoelectric field can produce GIC in the loop between the IPGS and the earth. The substation grounding grid and pipes are buried, and the earthing currents from them, $\mathbf{I}^{\mathrm{s}}$ and $\mathbf{I}^{\mathrm{p}}$, can produce a ground potential rise and thereby affect other grounded nodes. Such a conductive coupling is modeled as a current-controlled voltage source based on the ground transfer resistance, as depicted in Figure 5-2. For instance, the grounding current I_i^{s} of the substation i results in an earth potential rise $R_{qi}^{\mathrm{ps}} I_i^{\mathrm{s}}$ near the pipe node q, where the transfer resistance R_{qi}^{ps} characterizes the coupling strength between these two nodes.

The ground transfer resistance between the grounded nodes depends on their spatial coordinates and the earth resistivity structures. The transfer resistance in the circuit model of IPGS, as shown in Figure 5-2, can be applied to the cases of arbitrary earth structures.

A nodal voltage analysis can be performed for the IPGS based on the equivalent circuit in Figure 5-2. For the ungrounded bus node $m \in N_{\mathrm{b}}$, according to the Kirchhoff’s current law, we can obtain

$$\sum_{n \in N_{\mathrm{b}}, n \neq m} y_{mn}^{\mathrm{bb}}(V_m^{\mathrm{b}} - V_n^{\mathrm{b}}) + \sum_{i \in N_{\mathrm{s}}} y_{mi}^{\mathrm{bs}}(V_m^{\mathrm{b}} - V_i^{\mathrm{s}}) = J_m^{\mathrm{b}} \tag{5-11}$$

where V_m^{b} and V_n^{b} are the voltages of buses m and n, V_i^{s} is the voltage of substation grounding grid node i, y_{mn}^{bb} is the admittance of the branch from bus m to bus n, y_{mi}^{bs} is the admittance of the branch from bus m to substation grounding grid node i, and J_m^{b} is the current injection at bus m.

Similarly, for the substation grounding grid node $i \in N_{\mathrm{s}}$, one can get

$$\sum_{m \in N_{\mathrm{b}}} y_{im}^{\mathrm{sb}}(V_i^{\mathrm{s}} - V_m^{\mathrm{b}}) + I_i^{\mathrm{s}} = 0 \tag{5-12}$$

where I_i^{s} is the current flowing into the earth from the substation grounding grid node i.

For the pipeline node $q \in N_{\mathrm{p}}$, one can get

$$\sum_{w \in N_{\mathrm{p}}, w \neq q} y_{qw}^{\mathrm{pp}}(V_q^{\mathrm{p}} - V_w^{\mathrm{p}}) + I_q^{\mathrm{p}} = J_q^{\mathrm{p}} \tag{5-13}$$

where V_q^{p}, V_w^{p} are the voltages of the pipe nodes q and w, and y_{qw}^{pp} is the admittance of the steel tube between nodes q and w, I_q^{p} is the earthing current from the pipe node q, and J_q^{p} is the current injection at pipe node q.

In a nutshell, (5-11)-(5-13) for nodal voltages and earthing currents of the full nodes N can be written in matrix form as

$$\begin{bmatrix} \mathbf{Y}^{\mathrm{bb}} & \mathbf{Y}^{\mathrm{bs}} & \mathbf{0} \\ \mathbf{Y}^{\mathrm{sb}} & \mathbf{Y}^{\mathrm{ss}} & \mathbf{0} \\ \mathbf{0} & \mathbf{0} & \mathbf{Y}^{\mathrm{pp}} \end{bmatrix} \cdot \begin{bmatrix} \mathbf{V}^{\mathrm{b}} \\ \mathbf{V}^{\mathrm{s}} \\ \mathbf{V}^{\mathrm{p}} \end{bmatrix} + \begin{bmatrix} \mathbf{0} \\ \mathbf{I}^{\mathrm{s}} \\ \mathbf{I}^{\mathrm{p}} \end{bmatrix} = \begin{bmatrix} \mathbf{J}^{\mathrm{b}} \\ \mathbf{0} \\ \mathbf{J}^{\mathrm{p}} \end{bmatrix} \tag{5-14}$$

where the diagonal and off-diagonal entries of the blocks in the network admittance matrix $\mathbf{Y}$ are given by

$$\mathbf{Y}_{mm}^{\mathrm{bb}} = \sum_{n \in N_{\mathrm{b}}, n \neq m} y_{mn}^{\mathrm{bb}} + \sum_{i \in N_{\mathrm{s}}} y_{mi}^{\mathrm{bs}}, \quad \mathbf{Y}_{mn}^{\mathrm{bb}} = -y_{mn}^{\mathrm{bb}}, \tag{5-15a}$$

$$\mathbf{Y}_{ii}^{\mathrm{ss}} = \sum_{m \in N_{\mathrm{b}}} y_{im}^{\mathrm{sb}}, \quad \mathbf{Y}_{ik}^{\mathrm{ss}} = 0, \tag{5-15b}$$

$$\mathbf{Y}_{qq}^{\mathrm{pp}} = \sum_{w \in N_{\mathrm{p}}, w \neq q} y_{qw}^{\mathrm{pp}}, \quad \mathbf{Y}_{qw}^{\mathrm{pp}} = -y_{qw}^{\mathrm{pp}}, \tag{5-15c}$$

$$\mathbf{Y}_{mi}^{\mathrm{bs}} = \mathbf{Y}_{im}^{\mathrm{sb}} = -y_{mi}^{\mathrm{bs}} = -y_{im}^{\mathrm{sb}}. \tag{5-15d}$$

Furthermore, by considering the interaction of different grounding bodies through the ground transfer resistance in Section 5.1.2, we can get a set of equations on the voltages and earthing currents of the grounded nodes. The voltage of substation grounding grid i can be expressed as

$$V_i^{\mathrm{s}} = \sum_{k \in N_{\mathrm{s}}} R_{ik}^{\mathrm{ss}} I_k^{\mathrm{s}} + \sum_{q \in N_{\mathrm{p}}} R_{iq}^{\mathrm{sp}} I_q^{\mathrm{p}} \tag{5-16}$$

where R_{ii}^{ss} is the self-grounding resistance of the substation i, R_{ik}^{ss} is the mutual resistance between the substation grounding grid nodes i and k, and R_{iq}^{sp} is the mutual resistance between the substation grounding grid node i and the pipe node q.

Similarly, the voltage of the pipe node q can be expressed as

$$V_q^{\mathrm{p}} = R_q^{\mathrm{c}} I_q^{\mathrm{p}} + \sum_{w \in N_{\mathrm{p}}} R_{qw}^{\mathrm{pp}} I_w^{\mathrm{p}} + \sum_{i \in N_{\mathrm{s}}} R_{qi}^{\mathrm{ps}} I_i^{\mathrm{s}} \tag{5-17}$$

where R_q^{c} is the resistance of insulation coating of the pipe node q, and R_{qw}^{pp} is the mutual resistance between the pipe nodes q and w.

To sum up, the relationship between the nodal voltages and earthing currents (5-16)-(5-17) can be written in matrix form as

$$\begin{bmatrix} \mathbf{V}^{\mathrm{s}} \\ \mathbf{V}^{\mathrm{p}} \end{bmatrix} = \begin{bmatrix} \mathbf{R}^{\mathrm{ss}} & \mathbf{R}^{\mathrm{sp}} \\ \mathbf{R}^{\mathrm{ps}} & \mathbf{R}^{\mathrm{c}} + \mathbf{R}^{\mathrm{pp}} \end{bmatrix} \cdot \begin{bmatrix} \mathbf{I}^{\mathrm{s}} \\ \mathbf{I}^{\mathrm{p}} \end{bmatrix} \tag{5-18}$$

where $\mathbf{R}^{\mathrm{ss}}$, $\mathbf{R}^{\mathrm{sp}}$, $\mathbf{R}^{\mathrm{ps}}$, and $\mathbf{R}^{\mathrm{pp}}$ are ground transfer resistance matrices consisting of the self-grounding resistances and mutual resistances, and $\mathbf{R}^{\mathrm{c}}$ is a diagonal matrix of the coating resistance.

Then, equations (5-14) and (5-18) can be combined to solve for the induced voltages and currents. Two solution schemes are discussed below.

1） Solution Scheme 1 by Eliminating the Voltages of Grounded Nodes

If (5-18) is directly substituted into (5-14), then the final equations can be obtained by eliminating the voltages of the grounded nodes, as can be seen in (5-19). We can observe that the design matrix is asymmetric, so (5-19) can be solved based on LU factorization. The induced voltages and currents can be obtained by forward and backward substitution algorithms.

$$\begin{bmatrix} \mathbf{Y}^{\mathrm{bb}} & \mathbf{Y}^{\mathrm{bs}}\mathbf{R}^{\mathrm{ss}} & \mathbf{Y}^{\mathrm{bs}}\mathbf{R}^{\mathrm{sp}} \\ \mathbf{Y}^{\mathrm{sb}} & \mathbf{Y}^{\mathrm{ss}}\mathbf{R}^{\mathrm{ss}} + \mathbf{1}_{n_{\mathrm{s}}} & \mathbf{Y}^{\mathrm{ss}}\mathbf{R}^{\mathrm{sp}} \\ \mathbf{0} & \mathbf{Y}^{\mathrm{pp}}\mathbf{R}^{\mathrm{ps}} & \mathbf{Y}^{\mathrm{pp}}\left(\mathbf{R}^{\mathrm{c}} + \mathbf{R}^{\mathrm{pp}}\right) + \mathbf{1}_{n_{\mathrm{p}}} \end{bmatrix} \cdot \begin{bmatrix} \mathbf{V}^{\mathrm{b}} \\ \mathbf{I}^{\mathrm{s}} \\ \mathbf{I}^{\mathrm{p}} \end{bmatrix} = \begin{bmatrix} \mathbf{J}^{\mathrm{b}} \\ \mathbf{0} \\ \mathbf{J}^{\mathrm{p}} \end{bmatrix} \tag{5-19}$$

where $\mathbf{1}_{n_{\mathrm{s}}}$ and $\mathbf{1}_{n_{\mathrm{p}}}$ are $n_{\mathrm{s}} \times n_{\mathrm{s}}$ and $n_{\mathrm{p}} \times n_{\mathrm{p}}$ identity matrices, respectively.

2） Solution Scheme 2 by Eliminating the Grounding Currents

In the second solution scheme, first we transform (5-18) into

$$\begin{bmatrix} \mathbf{I}^{\mathrm{s}} \\ \mathbf{I}^{\mathrm{p}} \end{bmatrix} = \begin{bmatrix} \mathbf{G}^{\mathrm{ss}} & \mathbf{G}^{\mathrm{sp}} \\ \mathbf{G}^{\mathrm{ps}} & \mathbf{G}^{\mathrm{pp}} \end{bmatrix} \cdot \begin{bmatrix} \mathbf{V}^{\mathrm{s}} \\ \mathbf{V}^{\mathrm{p}} \end{bmatrix} \tag{5-20}$$

where the ground transfer conductance matrices $\mathbf{G}^{\mathrm{ss}}$, $\mathbf{G}^{\mathrm{sp}}$, $\mathbf{G}^{\mathrm{ps}}$, and $\mathbf{G}^{\mathrm{pp}}$ are given as

$$\begin{bmatrix} \mathbf{G}^{\mathrm{ss}} & \mathbf{G}^{\mathrm{sp}} \\ \mathbf{G}^{\mathrm{ps}} & \mathbf{G}^{\mathrm{pp}} \end{bmatrix} = \begin{bmatrix} \mathbf{R}^{\mathrm{ss}} & \mathbf{R}^{\mathrm{sp}} \\ \mathbf{R}^{\mathrm{ps}} & \mathbf{R}^{\mathrm{c}} + \mathbf{R}^{\mathrm{pp}} \end{bmatrix}^{-1} \tag{5-21}$$

Substituting (5-20) into (5-14), we can obtain the nodal voltage equation by eliminating the earthing currents:

$$\begin{bmatrix} \mathbf{Y}^{\mathrm{bb}} & \mathbf{Y}^{\mathrm{bs}} & \mathbf{0} \\ \mathbf{Y}^{\mathrm{sb}} & \mathbf{Y}^{\mathrm{ss}} + \mathbf{G}^{\mathrm{ss}} & \mathbf{G}^{\mathrm{sp}} \\ \mathbf{0} & \mathbf{G}^{\mathrm{ps}} & \mathbf{Y}^{\mathrm{pp}} + \mathbf{G}^{\mathrm{pp}} \end{bmatrix} \cdot \begin{bmatrix} \mathbf{V}^{\mathrm{b}} \\ \mathbf{V}^{\mathrm{s}} \\ \mathbf{V}^{\mathrm{p}} \end{bmatrix} = \begin{bmatrix} \mathbf{J}^{\mathrm{b}} \\ \mathbf{0} \\ \mathbf{J}^{\mathrm{p}} \end{bmatrix} \tag{5-22}$$

The design matrix in (5-22) is symmetric positive definite, thus it can be solved by Cholesky factorization, which is more efficient than general LU factorization. In geomagnetic induction analysis, (5-22) usually needs to be solved repeatedly, taking into account the time-varying geoelectric field, changes in power grid topology, uncertain resistance parameters, etc. Thus, the solution scheme 2 is more computationally efficient than scheme 1.

As a special case, if we ignore the coupling between grounding bodies, i.e. all the mutual resistance entries are assumed to be zero, then (5-22) reduces to the classical nodal admittance matrix method.

Once the nodal voltages are solved, we can further obtain some auxiliary outputs of interest. For instance, the transformer effective GIC[75] are the weighted sum of the currents in the windings:

$$\mathbf{I}^{\mathrm{eff}} = \mathbf{\Phi} \cdot \begin{bmatrix} \mathbf{V}^{\mathrm{s}} \\ \mathbf{V}^{\mathrm{b}} \end{bmatrix} \tag{5-23}$$

where $\mathbf{\Phi}$ is the transformation matrix, and n_{t} is the number of transformers of interest.

In the pipeline networks, PSP refers to the voltage inside and outside the insulation coating, which can be calculated as

$$\mathbf{V}^{\mathrm{psp}} = \mathbf{R}^{\mathrm{c}}\mathbf{I}^{\mathrm{p}} = \mathbf{R}^{\mathrm{c}}\left(\mathbf{G}^{\mathrm{ps}}\mathbf{V}^{\mathrm{s}} + \mathbf{G}^{\mathrm{pp}}\mathbf{V}^{\mathrm{p}}\right) \tag{5-24}$$

5.1.4 Procedures of the Induction Calculation for the IPGS

Figure 5-3 summarizes the procedures of geomagnetic induction modeling in IPGS based on the nodal voltage analysis method. The inputs of the algorithm include: 1) the space current system or the surface geomagnetic field; 2) the earth resistivity structure; 3) the spatial coordinates, topology and resistance parameters of the IPGS. The outputs are the induced currents and voltages in the IPGS.

It can be seen that the earth resistivity structure plays a key role in the algorithm. It can affect both the nodal current injections and the ground transfer conductance matrix of the

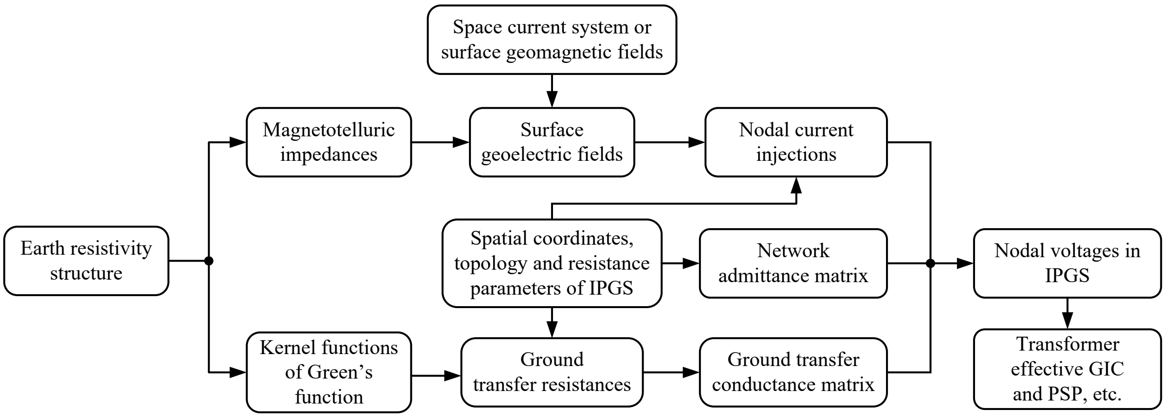

Figure 5-3 Flow chart of geomagnetic induction algorithm for the IPGS.

IPGS. Hence, accurate earth resistivity parameters are required for the geomagnetic induction calculation.

In this research, the conductive coupling between the substation grounding grids and the buried pipelines are modeled by the transfer resistance in the circuit model of IPGS. And the proposed circuit approach is validated by using the finite element analysis in Section 5.2.

5.2 Model Validation via Finite Element Analysis

In this section, the proposed circuit model of the IPGS based on the ground transfer resistance is verified by using the finite element method (FEM). The electrical potential distribution is solved based on the finite element solution for (5-4)-(5-7).

First, we establish 3D models for the uniform 1000 Ω·m earth model and the 1D layered Testing earth structure in Table 5-1 in finite element software, respectively. A unit point current excitation is applied to the earth surface, and the potential generated at the surface is used to calculate the transfer resistance.

Table 5-1 1D layered testing resistivity structure[40]

Layer	Thickness/m	Resistivity/Ω·m
1	6	70
2	25	120
3	60	90
4	300	220
5	500	500
6	3500	2500
7	13100	34385
8	17100	5324
9	97600	83095
10	∞	813

The ground transfer resistance results at the earth surface obtained by the FEM are presented in Figure 5-4, which are in good agreement with the analytical solutions from (5-1) and (5-3). The established finite element model can be further used to analyze the earth with 3D complex resistivity distribution.

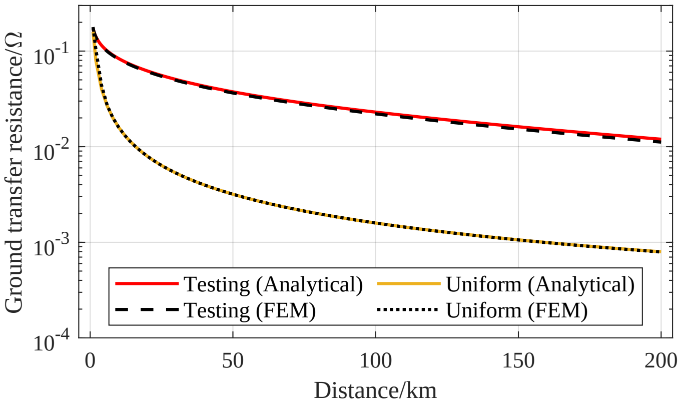

Figure 5-4 Comparison of the ground transfer resistances of the uniform 1000 Ω·m earth and the 1D layered Testing earth obtained by analytical solution and FEM.

Then, we built a comprehensive finite element model that includes the uniform earth and the pipeline, and the schematic diagram is shown in Figure 5-5(a). A 0.001 Hz and 10 A point current is injected at the origin to represent the substation grounding current. The horizontal distance from the current source to the center of the buried pipeline is 15 m. The pipeline is along the *y*-axis and its two ends are insulated. The length of the pipeline is 100 m, and its buried depth is 1.5 m. The cross section of the pipe is shown in Figure 5-5(b), where the conductivity and thickness of the steel tube and coating are taken from [23].

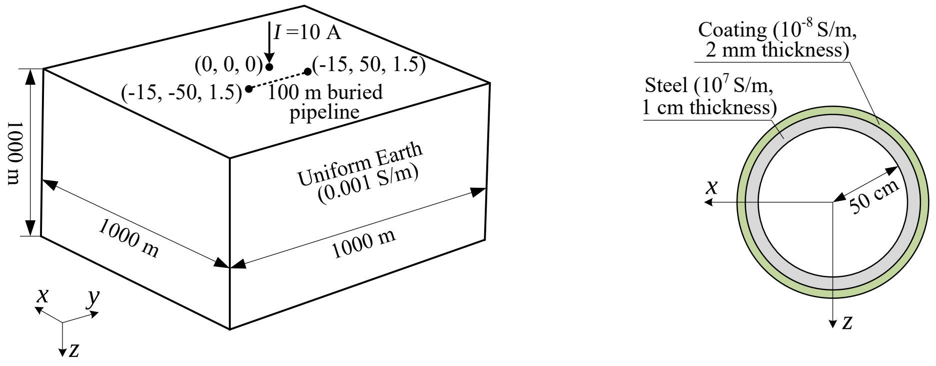

(a) Schematic diagram of the whole model

(b) Cross section of the pipeline

Figure 5-5 The finite element model that involves the uniform earth, a buried pipeline, and one point current excitation.

The potential distribution on the *yOz* plane of the pipeline calculated by the FEM is shown in Figure 5-6. It can be observed that there is a large potential difference between the steel side and the soil side of the coating, which illustrates the influence of the earthing GIC from the power grid on the pipe. The PSP results of the FEM are compared with those of the proposed circuit method in Figure 5-7. The results of the two methods are highly consistent, which indicates that the circuit method adopted in this research is reasonable to analyze the conductive coupling in IPGS during GMD.

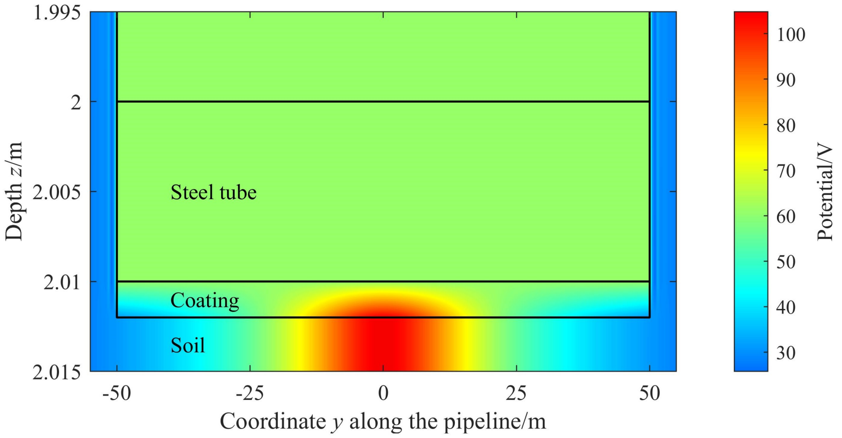

Figure 5-6 Potential distribution in the *yOz* plane of the pipeline obtained by FEM.

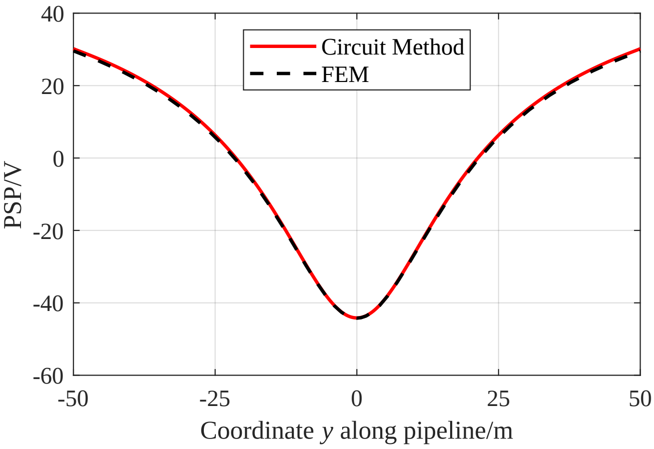

Figure 5-7 Comparison of the PSP results along the pipeline obtained by circuit method and FEM.

5.3 Case Studies of Geomagnetic Induction in IPGS

In this section, first, a simple case with a single power transmission line and a single buried pipeline is given in Section 5.3.1, and the influences of IPGS characteristics and earth resistivity structures are discussed. In Section 5.3.2, the geomagnetic induction calculation is performed for a realistic large-scale IPGS test case.

5.3.1 Simple IPGS Test Cases With Single Power Line and Single Pipeline

1） IPGS With Different Spatial Patterns

Let us start with a simple synthetic IPGS case with double-circuit power transmission lines, a single pipeline, two substations S1 and S2, two pipeline terminals P1 and P2. The default parameters for the power grid and pipeline are set as follows. The voltage level of the power grid is 750 kV. The length of the power line is 100 km, and the resistance per unit length of single-circuit line is 0.01205 Ω/km per phase. Each substation contains two auto-transformers, and the equivalent winding resistance of each transformer is 0.3852 Ω per phase, and the substation grounding resistance is 0.2 Ω[169]. The series impedance and parallel admittance of the pipeline are 0.005 Ω/km and 0.05 S/km, respectively[23]. The buried depth of the pipeline is 1.5 m, and both terminals of the pipe are electrically insulated. The power line is parallel to the pipeline in the east-west direction, and the minimum distance between the substation and the pipeline is 1 km.

In engineering practice, there are various spatial intersections between power grids and pipelines. Three typical spatial patterns are considered in the test cases, as shown in Figure 5-8:

1. The east terminal of the power line is close to the west terminal of the pipeline, i.e. the substation S2 is close to the pipe node P1.
2. The east terminal of the power line is near the center of the pipeline.
3. The west terminal of the power line is near that of the pipeline, and so is the east terminal.

The IPGS cases are assumed to be located on a 1D horizontally layered Testing earth structure from[40], as shown in Table 5-1. The resistivity of shallow soil can be inverted by electrical sounding methods, such as the four-electrode Wenner method[168], whereas the deep earth structure is obtained by magnetotelluric survey.

2） Results of Different Geomagnetic Induction Models

To illustrate the interaction of the power grid and pipelines in geomagnetic induction, we compare the results of three induction models for the IPGS test case in Figure 5-8:

1. In the proposed induction model 1, the mutual resistances between all grounded nodes, including substation grounding grids and buried pipelines, are preserved.
2. In the classical induction model 2, the mutual resistances between all grounded nodes are neglected. This assumption is widely adopted by existing geomagnetic induction

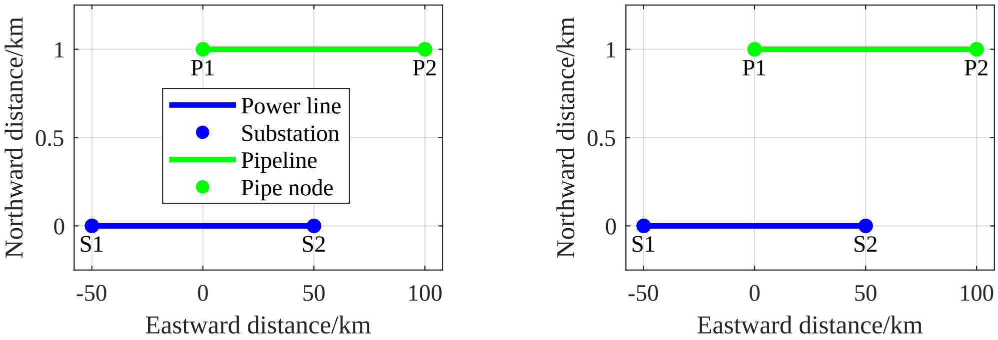

(a) Spatial pattern 1 (b) Spatial pattern 2

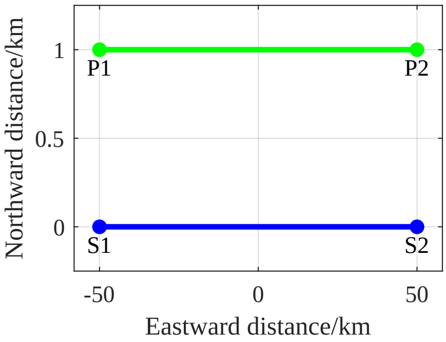

(c) Spatial pattern 3

Figure 5-8 Three typical spatial patterns of IPGS with single power line and single pipeline.

studies.

3. In the induction model 3, the mutual resistances between the substation grounding grid nodes and the mutual resistance between the pipeline nodes are preserved, whereas the mutual resistances between these two types of nodes are neglected.

The induction models 2 and 3 are used as references to illustrate the impact of the interaction between different grounding nodes on the results of geomagnetic induction. For pipelines, the difference in the induction results of the induction models 2 and 3 represents the contribution of interaction between the pipe nodes, whereas the difference of the induction models 1 and 3 reveals the contribution of coupling from the substation grounding grid. The same goes for the power grid.

The PSP along the pipeline calculated by the three induction models are compared in Figure 5-9. By comparing the PSP results of induction models 2 and 3, it can be seen that ignoring the coupling between the pipe nodes could lead to a slight increase in the PSP amplitude. It means that the classical distributed source transmission line model[22] for pipelines can usually provide a more conservative estimate for PSP.

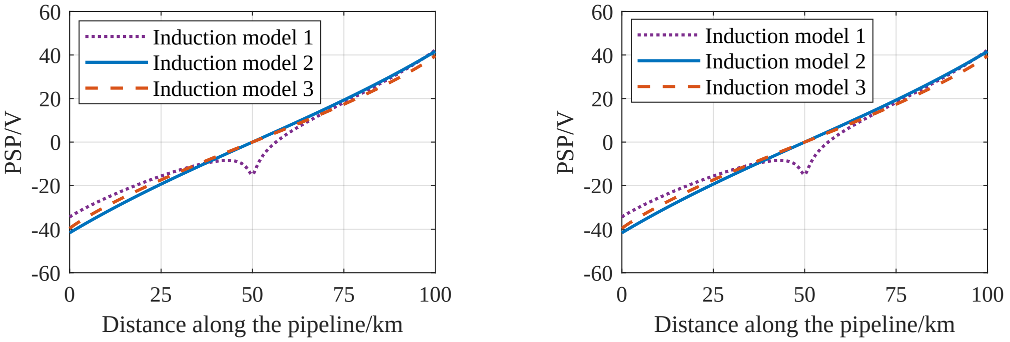

(a) PSP of spatial pattern 1

(b) PSP of spatial pattern 2

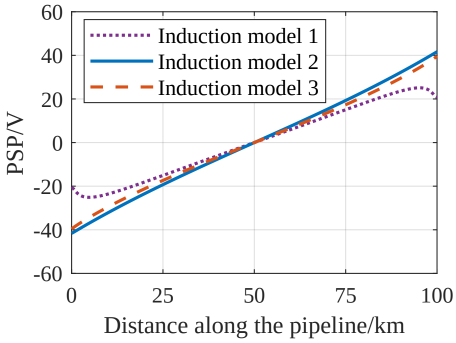

(c) PSP of spatial pattern 3

Figure 5-9 Comparison of PSP along the pipeline P1-P2 obtained by three induction models. (Induction model 1: with all the mutual resistance in the IPGS. Induction model 2: without all mutual resistance in the IPGS. Induction model 3: with mutual resistance of the pipe nodes only)

By comparing the PSP of induction models 1 and 3 in Figure 5-9, we can see that the presence of the power grid greatly affects the PSP along the pipeline, whose charscteristics depend on the spatial pattern of IPGS:

1. For IPGS spatial pattern 1, the grounding current of substation S2 is in the opposite direction to the earthing current of pipe node P1. In this case, if the influence of the power grid is considered, the PSP of node P1 changes from -39.69 V to -56.06 V (41.24% increase in PSP amplitude).
2. For IPGS spatial pattern 2, the earthing current in the middle of the pipeline is zero when the power grid does not exist. However, in the presence of the power grid, a PSP spike with an amplitude of -14.92 V is generated near the middle of the pipeline. The substation grounding GIC may cause significant changes in the induction results in nearby pipeline segments.
3. For IPGS spatial pattern 3, the grounding current of substation S2 is in the same direction as the earthing current of pipe node P1. In this case, the PSP of node P1 changes from -39.69 V to -21.08 V in the presence of the power grid (46.89% reduction in PSP

amplitude).

In addition, the GIC in the power grid is also calculated by using three induction models. The grounding GIC of substation S2 obtained by induction models 2 and 3 are 137.13 A and 146.36 A, respectively. It means that ignoring the conductive coupling between the substation grounding grids could lead to an underestimate of the GIC by 6.73%.

A comparison of the results of induction models 1 and 3 characterizing the contribution of the pipeline is shown in Table 5-2. The GIC variation mainly depends on the direction and magnitude of the earthing current in the pipeline near the substation. Overall, the influence of the power grid on the pipeline in geomagnetic induction is greater than that of the pipeline on the power grid.

Table 5-2 Substation grounding GIC in the cases of different spatial patterns of the IPGS

Spatial pattern of the IPGS	GIC of S2/A	Increment/%
1	150.06	2.53
2	146.33	-0.02
3	140.98	-3.68

3） Influence of Pipeline Parameter

In addition to the spatial pattern, the resistance parameters of the IPGS may also have a large impact on the induction results. For instance, the parallel admittance of pipelines depends on the material and thickness of the insulation coating. The insulation performance of the coating could degrade with age in service, and leakage points may even appear.

A typical range of parallel admittance, 0.05-0.25 S/km, from[23] is chosen to analyze its influence on the induction results of the IPGS in Figure 5-8(a). The normalized metrics, including percentage increment in PSP amplitude at pipe node P1 due to the power grid and the percentage increment in GIC amplitude at substation S2 due to the pipeline, are adopted to quantify the strength of the coupling between the power grid and the pipeline. It can be seen from Figure 5-10 that with the increase of the parallel admittance of the pipeline, the coupling between the power grid and the pipeline is stronger due to the increase of the earthing currents of the pipeline.

In the above analysis, both terminals P1 and P2 of the pipeline are assumed to be electrically insulated. In engineering practice, additional grounding devices may be added to the pipe nodes. Thus, the influence of different grounding modes of pipe terminals on the induction results are analyzed in Table 5-3. The grounding resistance of the pipe terminal is set to 0.5 Ω, which is chosen from its typical range[170]. It can be seen that if the pipe node P1 is

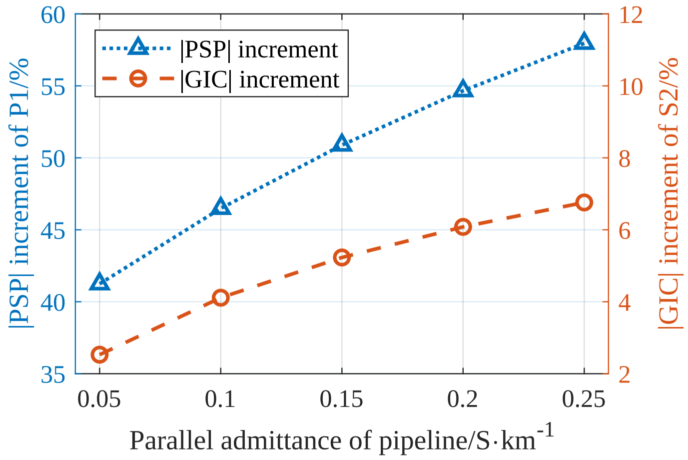

Figure 5-10 The increment of the PSP amplitude of the pipe node P1 and the increment of the GIC amplitude of the substation S2 with respect to the parallel admittance of the pipeline.

grounded, the GIC in the power grid may increase significantly, which is mainly contributed by the earthing current concentrated at the node P1.

Table 5-3 Substation grounding GIC in the cases of different grounding modes of pipe nodes

Grounding mode of pipe nodes	GIC of S2/A	Increment/%
P1 insulated and P2 insulated	150.06	2.53
P1 insulated and P2 grounded	151.16	3.28
P1 grounded and P2 insulated	161.68	10.47
P1 grounded and P2 grounded	165.00	12.74

4） Influence of Earth Resistivity Structures

The resistivity structure of different geological zones varies greatly, especially in the shallow earth. Thus, we analyze the influence of four different earth structures on the geomagnetic induction. The variation of earth resistivity with depth is shown in Figure 5-11 and the original data can be found in[40, 160]. The Testing, Guangdong, and Hubei models are 1D horizontally stratified. In addition, a uniform earth with 1000 Ω·m resistivity is considered, which is widely used in engineering standards to provide an estimate of the geoelectric field in the absence of knowledge about the geological structure[171].

Correspondingly, the ground transfer resistances of the four earth structures with respect to the horizontal distance are compared in Figure 5-12. As the horizontal distance increases, the transfer resistance of the uniform earth decreases rapidly, whereas the transfer resistance of the Testing and Guangdong models decreases relatively slowly. This is mainly due to the presence of high resistivity layers in the deep earth for these two structures. In addition, the transfer resistance of the Hubei model is generally much smaller than the other three due to its overall lower earth resistivity.

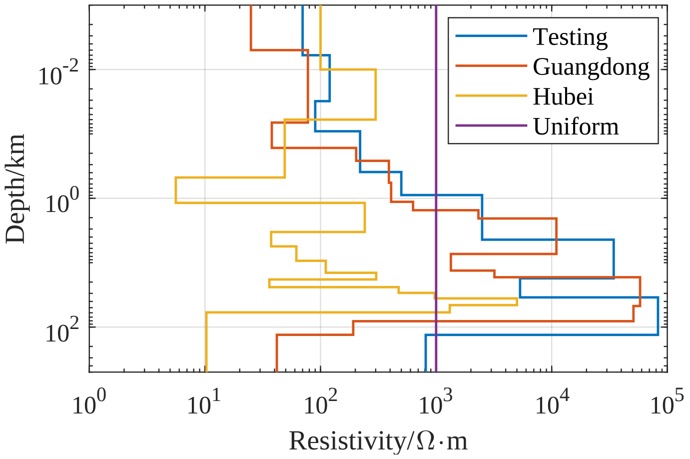

Figure 5-11 Profiles of four typical earth resistivity structures.

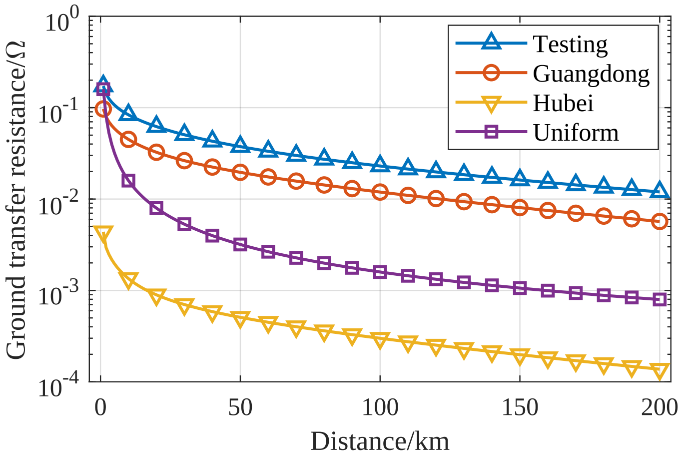

Figure 5-12 The ground transfer resistance of the four earth resistivity structures with respect to the horizontal distance from the source point to the field point on the earth surface.

Then, for IPGS with spatial pattern 1 in Figure 5-8(a), the influence of the shortest distance from the substation to the pipeline on the induction is discussed. The output of interest is the percentage increment of the PSP amplitude of pipe node P1 due to the power grid, as shown in Figure 5-13. It can be seen that when the distance from the substation S2 to the pipe node P1 is 1 km, the increment of PSP amplitude at node P1 of the uniform earth is higher than that of the three layered earth models. With the increase of the distance, the change of PSP decreases rapidly in the case of uniform earth, whereas the Testing and Guangdong earth models correspond to a larger effective coupling distance between the power grid and the pipeline. Hence, the detailed resistivity structure is required when designing the safe distance between the power grid and the pipeline for GMD in the IPGS planning stage.

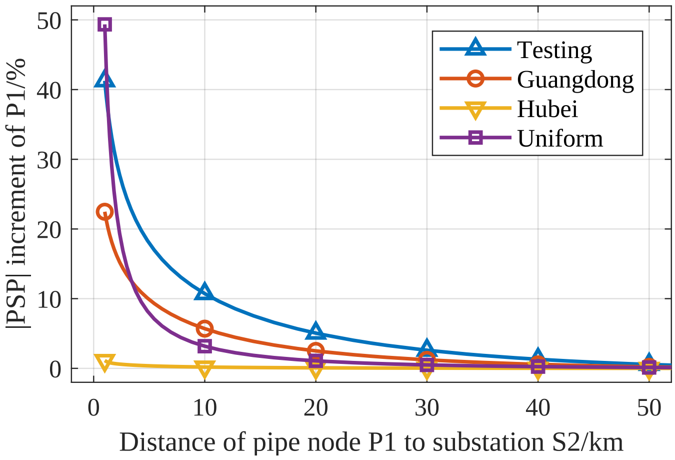

Figure 5-13 The percentage increment of the PSP amplitude of the pipe node P1 in the cases of different earth resistivity structures.

5.3.2 A Realistic Large-Scale IPGS Case

In this section, a realistic IPGS case from [40] is adopted for geomagnetic induction analysis. The spatial coordinates and topology of the power grid and pipelines are shown in Figure 5-14.

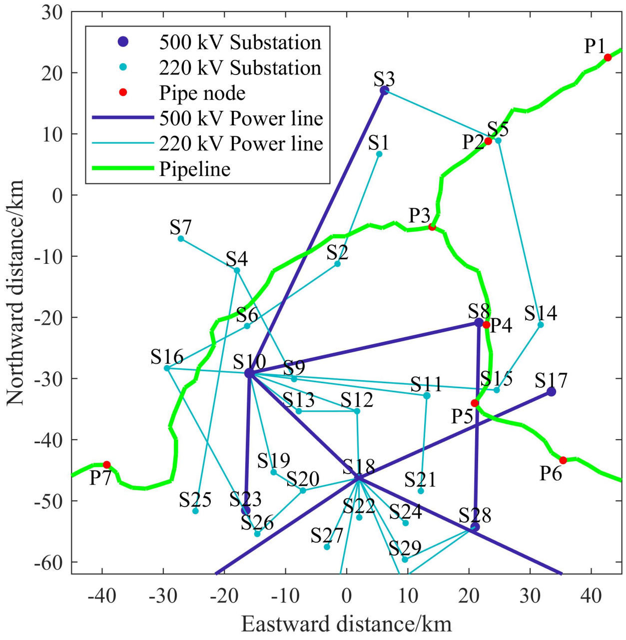

Figure 5-14 Spatial location and topology of the IPGS test case[40].

The AC transmission grid consists of two voltage levels: 500kV and 220kV. There are thirty-three substations in total, including nine 500kV and twenty-four 220kV ones. And the total number of power transmission lines is seventy-three, including sixteen 500kV and fiftyseven 220kV ones. The three pipelines are interconnected and intersect at pipe node P3. There is an insulating joint at the pipe node P5, thus the pipeline P4-P5 and the pipeline P5-P6 are electrically insulated. The IPGS is located on the Testing earth resistivity structure in Table 5-1.

First, the geomagnetic induction in the IPGS is analyzed in the case of 1 V/km northward geoelectric field. The spatial distribution of GIC in the power grid considering the influence of pipelines is shown in Figure 5-15. Large grounding GIC can be found at substations S5, S8 and S15 near the pipeline.

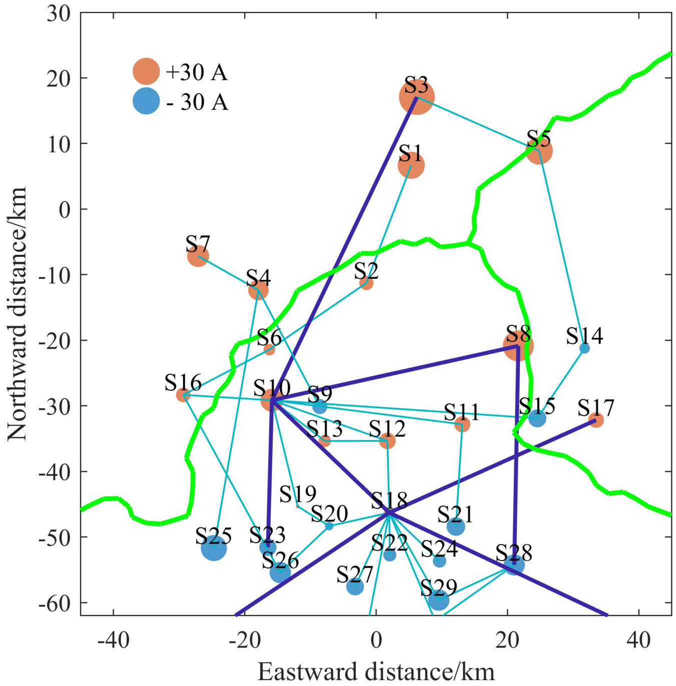

Figure 5-15 Snapshot of the substation grounding GIC considering pipelines in the case of 1 V/km northward geoelectric field.

The substation grounding GIC with and without the pipelines are compared in Figure 5-16. The GIC increment of each substation with respects to its shortest distance to the pipeline is shown in Figure 5-17. The GIC amplitudes of substations S6 and S16 increase by more than 20% due to the pipeline, whereas the relative variation of GIC amplitude at most substations are basically within 10%.

Figure 5-18 shows the PSP along the pipeline P1-P5 with 1 V/km northward geoelectric field. Under the influence of the power grid, the PSP amplitude of node P2 increases by 69.07%, while the PSP amplitude of node P5 decreases by 7.00%. It mainly depends on the size and orientation of the substation grounding GIC adjacent to the pipe nodes. Hence, the interaction between the substation ground grids and buried pipelines may redistribute induced voltages and currents in the integrated system, and The proposed comprehensive geomagnetic induction model can overcome the bias of the traditional uncoupled model.

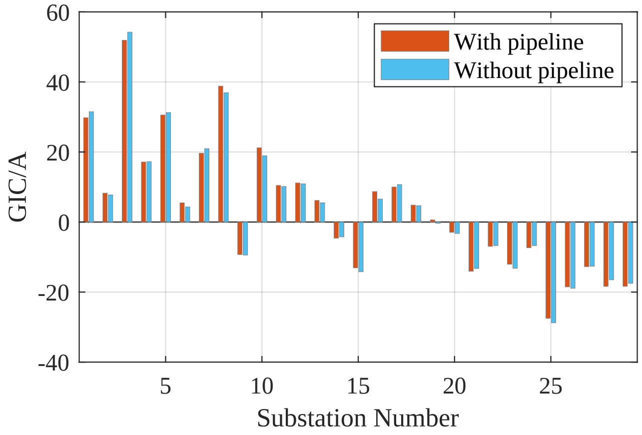

Figure 5-16 Substation grounding GIC with and without pipelines.

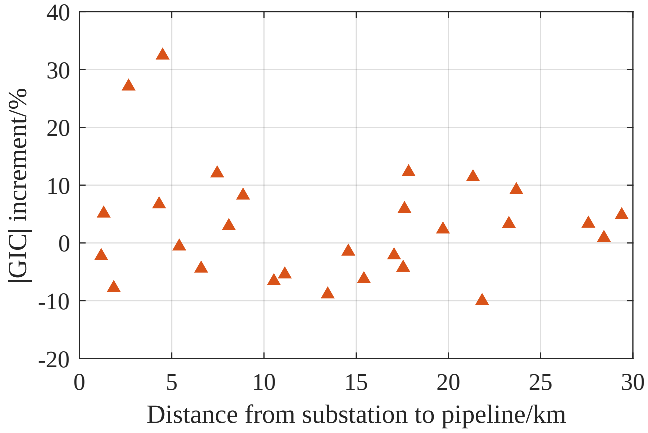

Figure 5-17 The GIC increment of each substation due to the pipelines with respect to its distance to the pipeline.

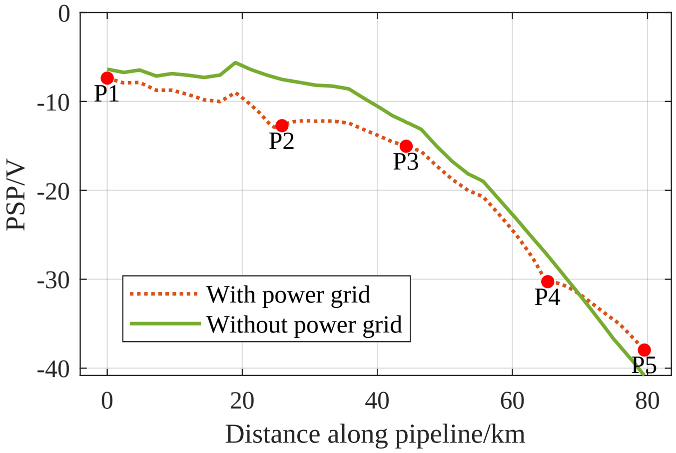

Figure 5-18 PSP along the pipeline P1-P5 with and without the power grid in the case of 1 V/km northward geoelectric field.

Similarly, PSP along the pipeline P1-P5 in the case of 1 V/km eastward geoelectric field is given in Figure 5-19. The polarities of the PSP at node P4 and P5 are even reversed due to the power grid. Overall, the contribution from the power grid to the PSP along the pipeline differs significantly in the cases of northward and eastward geoelectric fields.

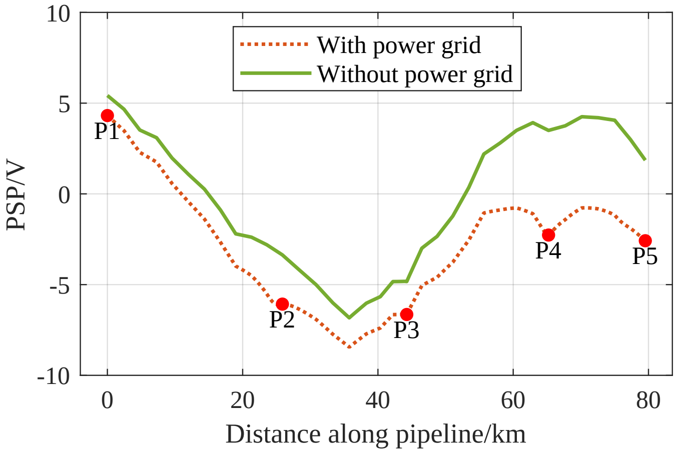

Figure 5-19 PSP along the pipeline P1-P5 with and without the power grid in the case of 1 V/km eastward geoelectric field.

In addition, we evaluated the induction results in the IPGS during the historical GMD event on July 15-16, 2000. Figure 5-20 shows the geomagnetic variations at Beijing Ming Tombs (BMT) observatory from SuperMAG.

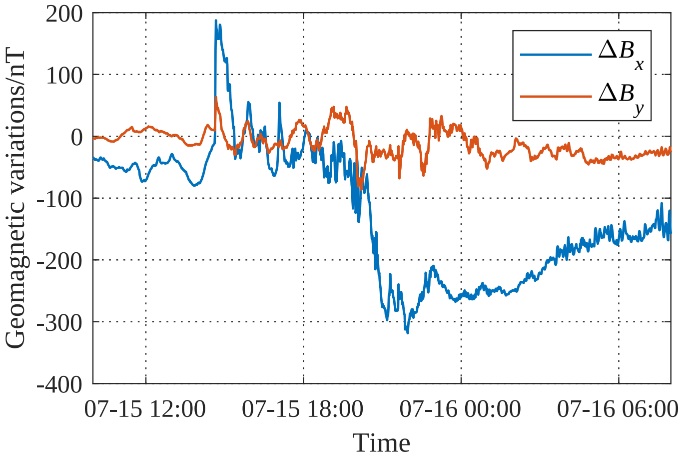

Figure 5-20 Geomagnetic variations at BMT observatory during the historical GMD event on July 15-16, 2000.

Figure 5-21 compares the PSP waveforms of the pipe node P2 with and without consideration of the power grid, which shows that ignoring the power grid may lead to an underestimation of the PSP level.

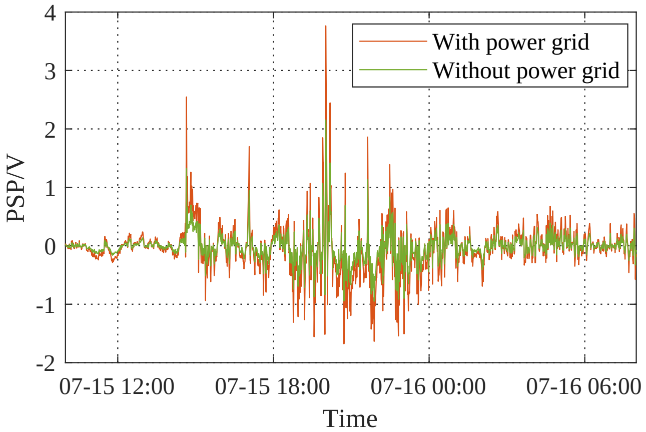

Figure 5-21 Comparison of the PSP waveforms at the pipe node P2 with and without power grid during the GMD event on July 15-16, 2000.

5.4 Concluding Remarks

This chapter proposes a geomagnetic induction model for the IPGS by considering the interaction of the power grids and buried pipelines. The proposed model can assist the energy sector in assessing the GMD risks of the IPGS in a more comprehensive manner, thus developing more effective and targeted mitigation measures. Several IPGS test cases are used to illustrate the contribution of the conductive coupling through the earth to the induction results. The results show that for the geomagnetic induction analysis in infrastructure networks, it is necessary to take into account the influence of other adjacent conductor systems.

The spatial pattern of the IPGS, including the location of power lines, substations, and pipelines, could affect the increase or decrease trend of PSP and GIC. The resistance parameters of the power grid and pipelines may affect the strength of the coupling. In addition, the effective coupling distance between the substations and the pipelines depends on the earth resistivity structure.

6 Conclusions and Perspectives

6.1 Summary

GMD generated by solar activity induces quasi-DC voltages and currents in the interconnected conductor systems, which can affect the reliability and operating conditions of ground-based energy infrastructure, including AC transmission networks and gas pipeline networks. In order to comprehensively and accurately assess the impact of extreme GMD, this study proposes several efficient modeling methods suitable for geomagnetic induction in large-scale power grids and pipeline networks by considering the geophysical step and engineering step. First, the return levels of extreme geomagnetic variations are estimated by combining extreme value statistics and the theoretical upper limit of the Dst index, and then the spatio-temporal distribution of the induced geoelectric field is further obtained taking into account the 3D complex earth conductivity distribution. Then, several model reduction methods are proposed for the geomagnetic induction calculations in large-scale circuit systems with lumped and distributed parameters under spatially non-uniform electric field excitation. Finally, a comprehensive circuit model is proposed for the integrated power-gas system that considers the coupling between substations and buried pipelines. The main research conclusions of this dissertation are as follows:

(1) The induced geoelectric field environment strongly depends on reasonable estimation of geomagnetic activity intensity and accurate earth conductivity models, which is of great importance for the geomagnetic induction calculation of energy systems with long conductors. The 100-year, 200-year and 10,000-year return levels of geomagnetic variations are estimated using historical geomagnetic observations based on extreme value statistics. In order to deal with the problem of excessively wide confidence intervals due to limited observations, the theoretical upper limit of the Dst index is introduced. The intensity of extreme GMDs at different latitudes such as the Sanhua area of China and the UK is compared. A Bayesian method for interpreting the horizontally layered earth structure is proposed. It can provide more comprehensive statistical properties of soil parameters to be estimated, such as confidence intervals and probability distributions, compared to classic optimization-based methods. Some multilayer earth test cases illustrate its capability to statistically quantify the impacts of measurement noise and shielding effects on the estimation performance of the soil parameters. Finally, the nonuniform geoelectric field distribution is calculated taking into account vertical and lateral variations in the earth conductivity. The results of several test cases show that when the geo-

magnetic field is parallel to interfaces such as the coast, the geoelectric field on the land side may be significantly enhanced, which means that the geomagnetic risk of energy systems near the coast deserves more attention.

(2) The evaluation of GICs in the power grid and their impact is subject to uncertainty in DC and AC parameters. The RNAM method is proposed for GIC model reduction of large-scale transmission system, which can be used to efficiently quantify the influence of uncertain substation grounding resistance parameters. The proposed RNAM method is compared with the classic GIC calculation methods, including the LP method, the NAM method and the BAM method. Several power grid test cases show that it can save 25%-40% of the simulation time compared with the classical NAM method. The RNAM method can also simplify the GIC calculation of multi-area power grids with multiple tie lines by eliminating the external system. Furthermore, the impact of transformer reactive power loss caused by GIC on the voltage security is evaluated. An efficient surrogate model of AC voltage is proposed based on the sparse generalized polynomial chaos expansion method in order to efficiently quantify the influence of random parameters such as induced geoelectric fields, substation grounding resistances and AC loads. For large-scale power grid analysis, multiple AC voltage outputs are compressed based on principal component analysis, which can reduce the number of PCE-based surrogate models to be built.

(3) Classical geomagnetic induction calculations for pipeline typically assume uniform geoelectric fields and linear components, without considering the effects of nonuniform electric fields and nonlinear polarization effect, which may significantly affect the distribution of response in long-distance pipelines. A modified equivalent-pi circuit model is derived for the buried pipelines to efficiently solve the response of interconnected pipeline networks excited by nonuniform geoelectric fields, which does not require discretization of the original distributed parameter circuit model. The results show that the accurate spatial distribution of the geoelectric field is important for predicting the voltage and current distribution in the pipeline. Furthermore, the proposed equivalent circuit model can be used to efficiently evaluate the nonlinear polarization effects of coating breakdown. The simulation results show that the nonlinear polarization effect may significantly affect the leakage current density at the coating defects. In addition, the differences in the voltage and current distribution along pipelines caused by GMD and HVDC earth return currents are compared.

(4) The classical geomagnetic induction models are developed separately for power grids and gas pipeline networks, which is not suitable for the IPGS analysis. A novel induction model that considers the coupling effect between the two networks is proposed in order to rigorously

evaluate the geomagnetic response in the integrated system. The ground transfer resistance is adopted to characterize the conductive coupling between the substation grounding grid and buried pipelines, which is verified using the finite element method. The results of several test cases show that the substation grounding GIC may redistribute the induced voltage and current in adjacent buried pipelines. The influence of different layered earth resistivity structures on the coupling strength of the substation grounding grid and buried pipelines is quantified. The proposed induction model allows for a more comprehensive evaluation of geomagnetic hazards on integrated systems.

6.2 Future Work

The research of this dissertation mainly focuses on the modeling and calculation of the induced voltage and current response of extreme GMD in large-scale transmission grids and gas pipeline networks. In future work, further research can be conducted on the following aspects:

(1) The accuracy of geomagnetic induction in energy networks is limited by a large number of uncertain input parameters, e.g. geomagnetic variation strength and direction, earth conductivity, AC load, pipe coating defects, etc. During GMD, the parameters in the geomagnetic induction model can be calibrated online using the measurements from power lines, transformers and pipelines. It can further reduce the uncertainty in the results of calculated induced voltages and currents.

(2) This study mainly focuses on the impact of transformer reactive power loss caused by GIC on the AC voltage security of the power system. In addition, the half-wave saturation of the transformer can also result in the odd and even harmonics, hot-spot heating, vibration and noise, etc. These may cause the risk of cascading failures for relay protection and reactive power compensation equipment. It is therefore necessary to establish a more comprehensive assessment model for power systems that incorporates GIC-related fault chains and develop comprehensive probabilistic risk assessment metrics.

(3) The proposed geomagnetic induction model can be combined with the early warning system for space weather activities to achieve pre-event and online assessment of GMD impacts. The assessment results can assist the robust decision-making and operation of the energy system, and the operating mode can be optimized and adjusted in advance to mitigate geomagnetic risks.

Acknowledgements

I would like to start by expressing my sincere gratitude to my supervisors for their excellent guidance while writing this dissertation. I feel fortunate to have Prof. Yanzhao Xie as my PhD supervisor at XJTU. I am very grateful for his unwavering support, valuable discussions, and continuous encouragement throughout my academic studies and personal life. I am equally thankful to my PoliTO supervisors, Prof. Igor S. Stievano, Prof. Flavio Canavero, and Prof. Riccardo Trinchero for accepting me as their student under the co-tutelle PhD project. Their insightful comments and suggestions have been instrumental in shaping the outcome of my research. Their dedication toward research and teaching has undoubtedly contributed to my further growth as a researcher and has left a deep impression on my academic pursuit.

I would like to extend my appreciation to all professors, staffs, and colleagues in HPEMC group at XJTU and EMC group at PoliTO. In particular I would like to thank Dr. Qing Liu from Xi'an University of Science and Technology, Dr. Kejie Li from Hefei University of Technology and Dr. Yuhao Chen, Dr. Jun Guo, Dr. Shaofei Wang, Dr. Ning Dong, Dr. Ziweihua Du, Dr. Shaoyin He, Dr. Yi Zhou and Dr. Tao Liang from Xi'an Jiaotong University. Their comments and suggestions have greatly enriched the quality of my work.

I would like to thank Zongyang Wang, Yuying Wu, Yifan Yang, Hongye Zhang, Mingxiang Gao, Yanpeng Ge, Xiaoyu Ge, Qi Li, Yangxin Qiu, Ruijiang Sun, Henan Liu, Mingyue Gou, Zeqi Lv, Daozhong Zhang, and Zain Anwer Memon for their consistent collaboration and lasting friendships.

Next, I would like to thank Prof. Bing Wei and Prof. Bingqiang Li for taking time from their busy schedules to review my dissertation carefully.

Finally, I want to thank my parents for their endless love and support throughout my life. This accomplishment would not have been possible without their unwavering understanding and encouragement.

References

[1] Ariannik M, Rezaei-Zare A, Werle P. Processing magnetometer signals for accurate wide-area geomagnetic disturbance monitoring and resilience analysis[J]. IEEE Transactions on Power Delivery, 2021, 36(4): 2550-2558.

[2] Dehghanian P, Zhang A, Fatima R, et al. An integrated assessment of a G3 GMD event on large-scale power grids: From magnetometer data to geomagnetically induced current analysis[J]. IEEE Transactions on Industry Applications, 2024, 60(1): 1634-1644.

[3] Boteler D, Pirjola R. Modeling geomagnetically induced currents[J]. Space Weather, 2017, 15(1): 258-276.

[4] Pulkkinen A, et al. Geomagnetically induced currents: Science, engineering, and applications readiness[J]. Space Weather, 2017, 15(7): 828-856.

[5] Kappenman J. Geomagnetic storms and their impacts on the US power grid[R]. Meta-R-319. Goleta, CA, USA: Metatech Corporation, 2010.

[6] IEEE Power and Energy Society Technical Council Task Force on Geomagnetic Disturbances. Geomagnetic disturbances: Their impact on the power grid[J]. IEEE Power and Energy Magazine, 2013, 11(4): 71-78.

[7] Yu N, Zhang X, Kong W, et al. Multidisciplinary advancements in geomagnetically induced currents research[J]. Journal of Jilin University (Earth Science Edition), 2024, 54(1): 54-67.

[8] Bu W, Zhang H, Huang Q. Review of geomagnetically induced currents[J]. Reviews of Geophysics and Planetary Physics, 2022, 53(1): 53-65.

[9] Zhu T, Wang F. Calculation of temperature rise of large transformer under geomagnetically induced current[J]. Transactions of China Electrotechnical Society, 2022, 37(8): 1915-1925.

[10] Huang T, Wang Z, Li Y. The influence of converter transformer DC bias on eddy current loss of tank[J]. Transactions of China Electrotechnical Society, 2023, 38(8): 2004-2014.

[11] Juvekar G P, Klauber C, Davis K R, et al. GIC-inclusive state estimator for power system awareness during geomagnetic disturbance events[J]. IEEE Transactions on Power Systems, 2021, 36(4): 2966-2974.

[12] Wang Z, Si Y, Liu L. Influence of geomagnetic storms on the stability of power system[J]. Transactions of China Electrotechnical Society, 2022, 37(7): 1780-1788.

[13] Xin W, Wang Z, Liu C, et al. Quantitative evaluation method of voltage stability of UHV AC power network under geomagnetic storm[J]. Transactions of China Electrotechnical Society, 2023, 38(21): 5771-5780.

[14] Xin W, Liu C, Wang Z, et al. Correction for voltage setting value of pilot node in EHV and UHV AC power grid during strong geomagnetic storm[J]. Power System Technology, 2023, 47(10): 4284-4290.

[15] Si Y, Wang Z, Liu L, et al. Impacts of uncertain geomagnetic disturbances on transient power angle stability of DFIG integrated power system[J]. IEEE Transactions on Industry Applications, 2023, 59(2): 2615-2625.

[16] Rajput V N, Boteler D H, Rana N, et al. Insight into impact of geomagnetically induced currents on power systems: Overview, challenges and mitigation[J]. Electric Power Systems Research, 2021, 192(1): 1-11.

[17] Guillon S, Toner P, Gibson L, et al. A colorful blackout: The Havoc caused by auroral electrojet generated magnetic field variations in 1989[J]. IEEE Power and Energy Magazine, 2016, 14(6): 59-71.

[18] Liu C M, Liu L G, Pirjola R. Geomagnetically induced currents in the high-voltage power grid in China[J]. IEEE Transactions on Power Delivery, 2009, 24(4): 2368-2374.

[19] Gaunt C T, Coetzee G. Transformer failures in regions incorrectly considered to have low GIC-risk[C]//2007 IEEE Lausanne Power Tech. 2007: 807-812.

[20] Marsal S, Torta J M, Curto J J, et al. Validating GIC modeling in the Spanish power grid by differential magnetometry[J]. Space Weather, 2021, 19(12): 1-17.

[21] Clilverd M A, Rodger C J, Brundell J B, et al. Long-lasting geomagnetically induced currents and harmonic distortion observed in New Zealand during the 7–8 September 2017 disturbed period[J]. Space Weather, 2018, 16(6): 704-717.

[22] Boteler D, Cookson M. Telluric currents and their effects on pipelines in the Cook Strait region of New-Zealand[J]. Materials Performance, 1986, 25(3): 27-32.

[23] Pulkkinen A, Pirjola R, Boteler D, et al. Modelling of space weather effects on pipelines[J]. Journal of Applied Geophysics, 2001, 48(4): 233-256.

[24] Boteler D. A new versatile method for modelling geomagnetic induction in pipelines[J]. Geophysical Journal International, 2013, 193(1): 98-109.

[25] Fernberg P A, Samson C, Boteler D H, et al. Earth conductivity structures and their effects on geomagnetic induction in pipelines[J]. Annales Geophysicae, 2007, 25(1): 207-218.

[26] Yu Z, Hao J, Liu L, et al. Monitoring experiment of electromagnetic interference effects caused by geomagnetic storms on buried pipelines in China[J]. IEEE Access, 2019, 7(1): 14603-14610.

[27] Boteler D. Geomagnetic effects on the pipe-to-soil potentials of a continental pipeline[J]. Advances in Space Research, 2000, 26(1): 15-20.

[28] National Space Weather Strategy and Action Plan[R]. Executive Office of the President Washington DC, 2019.

[29] UK severe space weather preparedness strategy[R]. UK Department for Business, Energy & Industrial Strategy, 2021.

[30] Viljanen A, Pirjola R, Prácser E, et al. Geomagnetically induced currents in Europe-Modelled occurrence in a continent-wide power grid[J]. Journal of Space Weather and Space Climate, 2014, 4(1): 1-9.

[31] IEEE guide for establishing power transformer capability while under geomagnetic disturbances[S]. New York, NY, USA, 2015: 1-50.

[32] Transmission system planned performance for geomagnetic disturbance events[S]. Atlanta, GA, USA, 2020.

[33] Pirjola R. Geomagnetically induced currents during magnetic storms[J]. IEEE Transactions on Plasma Science, 2000, 28(6): 1867-1873.

[34] Pulkkinen A, Bernabeu E, Eichner J, et al. Generation of 100-year geomagnetically induced current scenarios[J]. Space Weather, 2012, 10(4): 1-19.

[35] Thomson A W P, Dawson E B, Reay S J. Quantifying extreme behavior in geomagnetic activity[J]. Space Weather, 2011, 9(10): 1-12.

[36] Oughton E J, Hapgood M, Richardson G S, et al. A risk assessment framework for the socioeconomic impacts of electricity transmission infrastructure failure due to space weather: An application to the United Kingdom[J]. Risk Analysis, 2019, 39(5): 1022-1043.

[37] Cannon P, Angling M, Barclay L, et al. Extreme space weather: impacts on engineered systems and infrastructure[R]. London, UK: Royal Academy of Engineering, 2013: 42.

[38] Dawalibi F, Blattner C J. Earth resistivity measurement interpretation techniques[J]. IEEE Transactions on Power Apparatus and Systems, 1984, PAS-103(2): 374-382.

[39] IEEE Guide for Safety in AC Substation Grounding[S]. New York, NY, USA, 2015: 55-66.

[40] Zhang B, Cao F, Zeng R, et al. DC current distribution in both AC power grids and pipelines near HVDC grounding electrode considering their interaction[J]. IEEE Transactions on Power Delivery, 2019, 34(6): 2240-2247.

[41] Del Alamo J. A second order gradient technique for an improved estimation of soil parameters in a two-layer earth[J]. IEEE Transactions on Power Delivery, 1991, 6(3): 1166-1170.

[42] Zhang B, Cui X, Li L, et al. Parameter estimation of horizontal multilayer earth by complex image method[J]. IEEE Transactions on Power Delivery, 2005, 20(2): 1394-1401.

[43] Lagace P, Fortin J, Crainic E. Interpretation of resistivity sounding measurements in N-layer soil using electrostatic images[J]. IEEE Transactions on Power Delivery, 1996, 11(3): 1349-1354.

[44] Lagace P, Vuong M H, Lefebvre M, et al. Multilayer resistivity interpretation and error estimation using electrostatic images[J]. IEEE Transactions on Power Delivery, 2006, 21(4): 1954-1960.

[45] Yang J, Zou J. Parameter estimation of a horizontally multilayered soil with a fast evaluation of the apparent resistivity and its derivatives[J]. IEEE Access, 2020, 8(1): 52652-52662.

[46] Del Alamo J. A comparison among eight different techniques to achieve an optimum estimation of electrical grounding parameters in two-layered earth[J]. IEEE Transactions on Power Delivery, 1993, 8(4): 1890-1899.

[47] Gonos I, Stathopulos I. Estimation of multilayer soil parameters using genetic algorithms[J]. IEEE Transactions on Power Delivery, 2005, 20(1): 100-106.

[48] Calixto W P, Neto L M, Wu M, et al. Parameters estimation of a horizontal multilayer soil using genetic algorithm[J]. IEEE Transactions on Power Delivery, 2010, 25(3): 1250-1257.

[49] Calixto W P, Coimbra A P, Alvarenga B, et al. 3-D soil stratification methodology for geoelectrical prospection[J]. IEEE Transactions on Power Delivery, 2012, 27(3): 1636-1643.

[50] He W, Zhang R, Zhu L, et al. Parameter estimation of horizontal multilayer earth based on complex image method and improved particle swarm optimization[J]. IEEJ Transactions on Electrical and Electronic Engineering, 2013, 8(5): 456-462.

[51] Pereira W R, Soares M G, Neto L M. Horizontal multilayer soil parameter estimation through differential evolution[J]. IEEE Transactions on Power Delivery, 2016, 31(2): 622-629.

[52] Coelho R R A, Pereira A E C, Neto L M. A high-performance multilayer earth parameter estimation rooted in Chebyshev polynomials[J]. IEEE Transactions on Power Delivery, 2018, 33(3): 1054-1061.

[53] Li Z X, Rao S W. The inversion of one-dimensional soil parameters in the frequency domain with considering multilayered earth based on simulated annealing algorithm[J]. IEEE Transactions on Electromagnetic Compatibility, 2020, 62(2): 425-432.

[54] Jesenik M, Hamler A, Trlep M. Analyzing of a soil model using the finite element method for simulation of soil resistivity measurement[J]. IEEE Transactions on Magnetics, 2021, 57(7): 1-4.

[55] Jesenik M, Trlep M. Testing of multi layered soil models based on data obtained from finite element models with known soil structures using metaheuristics for parameters' determination[J]. Applied Soft Computing, 2020, 95(1): 1-21.

[56] Dan Y, Zhang Z, Yin J, et al. Parameters estimation of horizontal multilayer soils using a heuristic algorithm[J]. Electric Power Systems Research, 2022, 203(1): 1-11.

[57] Dan Y, Yin J, Yang J, et al. Influence analysis of calculated horizontally layered soil parameters on grounding parameters[J]. High Voltage, 2023, 8(2): 421-430.

[58] Meliopoulos A P, Papalexpoulos A D. Interpretation of soil resistivity measurements: Experience with the model SOMIP[J]. IEEE Transactions on Power Delivery, 1986, 1(4): 142-151.

[59] Zheng K, Pirjola R J, Boteler D H, et al. Geoelectric fields due to small-scale and large-scale source currents[J]. IEEE Transactions on Power Delivery, 2013, 28(1): 442-449.

[60] Arritt R, Leonardi B. Geomagnetic disturbance (GMD) non-uniform field benchmark test case: Benchmarking geomagnetically induced currents with non-uniform geoelectric fields[R]. 3002018 766. Palo Alto, CA, USA: Electric Power Research Institute, 2020.

[61] Amm O, Viljanen A. Ionospheric disturbance magnetic field continuation from the ground to the ionosphere using spherical elementary current systems[J]. Earth, Planets and Space, 1999, 51(6): 431-440.

[62] Marti L, Yiu C, Rezaei-Zare A, et al. Simulation of geomagnetically induced currents with piecewise layered-earth models[J]. IEEE Transactions on Power Delivery, 2014, 29(4): 1886-1893.

[63] Kelbert A, Balch C C, Pulkkinen A, et al. Methodology for time-domain estimation of storm time geoelectric fields using the 3-D magnetotelluric response tensors[J]. Space Weather, 2017, 15(7): 874-894.

[64] Kelbert A. The role of global/regional earth conductivity models in natural geomagnetic hazard mitigation[J]. Surveys in Geophysics, 2020, 41(1): 115-166.

[65] Sun R, Balch C. Comparison between 1-D and 3-D geoelectric field methods to calculate geomagnetically induced currents: A case study[J]. IEEE Transactions on Power Delivery, 2019, 34(6): 2163-2172.

[66] Liu C, Wang X, Lin C, et al. Proximity effects of lateral conductivity variations on geomagnetically induced electric fields[J]. IEEE Access, 2019, 7(1): 6240-6248.

[67] Liu C, Wang X, Zhang S, et al. Effects of lateral conductivity variations on geomagnetically induced currents: H-polarization[J]. IEEE Access, 2019, 7(1): 6310-6318.

[68] Gilbert J L. Simplified techniques for treating the ocean−land interface for geomagnetically induced electric fields[J]. IEEE Transactions on Electromagnetic Compatibility, 2015, 57(4): 688-692.

[69] Karami H, Sheshyekani K, Rezaei-Zare A, et al. Effect of mixed propagation path on electromagnetic fields at ground surface produced by electrojet[J]. IEEE Transactions on Electromagnetic Compatibility, 2018, 60(6): 2019-2024.

[70] Pirjola R J. Modelling the electric and magnetic fields at the earths surface due to an auroral electrojet[J]. Journal of Atmospheric and Solar-Terrestrial Physics, 1998, 60(11): 1139-1148.

[71] Pirjola R, Viljanen A, Boteler D. Series expansions for the electric and magnetic fields produced by a line or sheet current source above a layered earth[J]. Radio Science, 1999, 34(2): 269-280.

[72] Boteler D H. The evolution of Québec earth models used to model geomagnetically induced currents[J]. IEEE Transactions on Power Delivery, 2015, 30(5): 2171-2178.

[73] Dong B, Danskin D, Pirjola R, et al. Evaluating the applicability of the finite element method for modelling of geoelectric fields[J]. Annales Geophysicae, 2013, 31(10): 1689-1698.

[74] Wang X, Boteler D H, Pirjola R J. Distributed-source transmission line theory for modeling the coast effect on geoelectric fields[J]. IEEE Transactions on Power Delivery, 2023, 38(5): 3541-3550.

[75] Overbye T J, Shetye K S, Hutchins T R, et al. Power grid sensitivity analysis of geomagnetically induced currents[J]. IEEE Transactions on Power Systems, 2013, 28(4): 4821-4828.

[76] Boteler D H, Pirjola R J. Comparison of methods for modelling geomagnetically induced currents[J]. Annales Geophysicae, 2014, 32(9): 1177-1187.

[77] Blake S P, Gallagher P T, Campanyà J, et al. A detailed model of the Irish high voltage power network for simulating GICs[J]. Space Weather, 2018, 16(11): 1770-1783.

[78] Marsal S, Torta J M, Canillas-Pérez V, et al. A new standalone tool for DC-equivalent network generation and GIC calculation in power grids with multiple voltage levels[J]. Space Weather, 2022, 20(3): 1-14.

[79] Horton R, Boteler D, Overbye T J, et al. A test case for the calculation of geomagnetically induced currents[J]. IEEE Transactions on Power Delivery, 2012, 27(4): 2368-2373.

[80] Boteler D, Lackey A, Marti L, et al. Equivalent circuits for modelling geomagnetically induced currents from a neighbouring network[C]//2013 IEEE Power & Energy Society General Meeting. 2013: 1-5.

[81] Guo S X, Liu L G, Pirjola R J, et al. Impact of the EHV power system on geomagnetically induced currents in the UHV power system[J]. IEEE Transactions on Power Delivery, 2015, 30(5): 2163-2170.

[82] Kazerooni M, Zhu H, Overbye T J, et al. Transmission system geomagnetically induced current model validation[J]. IEEE Transactions on Power Systems, 2017, 32(3): 2183-2192.

[83] Klauber C, Shetye K, Overbye T J, et al. A GIC estimator for electric grid monitoring during geomagnetic disturbances[J]. IEEE Transactions on Power Systems, 2020, 35(6): 4847-4855.

[84] Rezaei-Zare A. Enhanced transformer model for low- and mid-frequency transients—Part I: Model development[J]. IEEE Transactions on Power Delivery, 2015, 30(1): 307-315.

[85] Bernabeu E E. Single-phase transformer harmonics produced during geomagnetic disturbances: Theory, modeling, and monitoring[J]. IEEE Transactions on Power Delivery, 2015, 30(3): 1323-1330.

[86] Haddadi A, Rezaei-Zare A, Gérin-Lajoie L, et al. A modified IEEE 118-bus test case for geomagnetic disturbance studies–Part I: Model data[J]. IEEE Transactions on Electromagnetic Compatibility, 2020, 62(3): 955-965.

[87] Haddadi A, Hassani R, Mahseredjian J, et al. Evaluation of simulation methods for analysis of geomagnetic disturbance system impacts[J]. IEEE Transactions on Power Delivery, 2021, 36(3): 1509-1516.

[88] Dong X, Liu Y, Kappenman J. Comparative analysis of exciting current harmonics and reactive power consumption from GIC saturated transformers[C]//2001 IEEE Power Engineering Society Winter Meeting. Conference Proceedings (Cat. No.01CH37194): vol. 1. 2001: 318-322.

[89] Overbye T J, Hutchins T R, Shetye K, et al. Integration of geomagnetic disturbance modeling into the power flow: A methodology for large-scale system studies[C]//2012 North American Power Symposium (NAPS). 2012: 1-7.

[90] Zheng K, Boteler D, Pirjola R J, et al. Effects of system characteristics on geomagnetically induced currents[J]. IEEE Transactions on Power Delivery, 2014, 29(2): 890-898.

[91] Liu Q, Xie Y z, Dong N, et al. Uncertainty quantification of geo-magnetically induced currents in UHV power grid[J]. IEEE Transactions on Electromagnetic Compatibility, 2020, 62(1): 258-265.

[92] Ingham M, Rodger C J. Telluric field variations as drivers of variations in cathodic protection potential on a natural gas pipeline in New Zealand[J]. Space Weather, 2018, 16(9): 1396-1409.

[93] Ingham M, Divett T, Rodger C J, et al. Impacts of GIC on the New Zealand gas pipeline network[J]. Space Weather, 2022, 20(12): 1-17.

[94] Trichtchenko L, Trishchenko A, Hejda P, et al. Evaluation of telluric-associated corrosion on buried pipelines[J]. Journal of Atmospheric and Solar-Terrestrial Physics, 2023, 248(1): 1-14.

[95] Coelho L, Sotelo G, Lima A C. Detailed versus simplified representation of a pipeline for assessment of inductive and conductive couplings to an overhead transmission lines during steady-state and fault conditions[J]. International Journal of Electrical Power & Energy Systems, 2022, 142(1): 1-17.

[96] Rabah D, Lahdeb M, Ghoneim S, et al. Combined effects of electrostatic and electromagnetic interferences of high voltage overhead power lines on aerial metallic pipeline[J]. Facta universitatis - series: Electronics and Energetics, 2022, 35(3): 349-377.

[97] Taflove A, Dabkowski J. Prediction method for buried pipeline voltages due to 60 Hz AC inductive coupling part I-analysis[J]. IEEE Transactions on Power Apparatus and Systems, 1979, PAS-98(3): 780-787.

[98] Dawalibi F, Southey R. Analysis of electrical interference from power lines to gas pipelines. II. parametric analysis[J]. IEEE Transactions on Power Delivery, 1990, 5(1): 415-421.

[99] Lucca G. Electromagnetic interference from power lines on pipelines: influence of pipe insulating coating degradation[J]. International Transactions on Electrical Energy Systems, 2016, 26(12): 2699-2712.

[100] Wang C, Liang X, Radons R. Minimum separation distance between transmission lines and underground pipelines for inductive interference mitigation[J]. IEEE Transactions on Power Delivery, 2020, 35(3): 1299-1309.

[101] Boteler D, Charalambous C A, Lax K. New insights into calculations of ac interference at fundamental and harmonic frequencies taking account of the phase relationships of the currents[J]. IEEE Transactions on Power Delivery, 2022, 37(2): 851-859.

[102] Ma C, Liu C. Influence of pipeline insulation leakage points on the distribution of geomagnetically induced current and pipe-soil potential[J]. IEEE Access, 2019, 7(1): 147470-147480.

[103] Chrysostomou D, Dimitriou A, Kokkinos N D, et al. Short-term electromagnetic interference on a buried gas pipeline caused by critical fault events of a wind park: A realistic case study[J]. IEEE Transactions on Industry Applications, 2020, 56(2): 1162-1170.

[104] Moraes C M, Matos G H d S, Martins-Britto A G, et al. Total AC interferences between a power line subject to a single-phase fault and a nearby pipeline with multilayered soil[J]. IEEE Transactions on Electromagnetic Compatibility, 2023, 65(2): 585-594.

[105] Lagace P, Houle J L, Greiss H, et al. Computer aided evaluation of pipeline current near toroidal HVDC ground electrodes[J]. IEEE Transactions on Power Delivery, 1989, 4(1): 216-222.

[106] Meng X, Zhang B, Liao Y, et al. Potential influence of ground return current from HVDC grounding electrode on buried pipeline[J]. Proceedings of the Chinese Society of Electrical Engineering, 2019, 39(20): 6113-6121.

[107] Yu Z, Liu L, Wang Z, et al. Evaluation of the interference effects of HVDC grounding current on a buried pipeline[J]. IEEE Transactions on Applied Superconductivity, 2019, 29(2): 1-5.

[108] Li X, Lu J, Bai F, et al. Modeling and calculation of the coupled voltage and current on the oil and gas pipeline from the HDVC/UHDC electrode grounding currents while considering the nonlinear polarization effect[J]. Proceedings of the Chinese Society of Electrical Engineering, 2022, 42(3): 1198-1209.

[109] Li X, Lu J, Cao F, et al. Corrosion effects of HVDC grounding currents on oil and gas pipelines under different soil resistivity conditions considering nonlinear polarization[J]. Power System Technology, 2022, 46(12): 5021-5028.

[110] Zaboli A, Vahidi B, Yousefi S, et al. Evaluation and control of stray current in DC-electrified railway systems[J]. IEEE Transactions on Vehicular Technology, 2017, 66(2): 974-980.

[111] Haubrich H J, Flechner B, Machczynski W. A universal model for the computation of the electromagnetic interference on earth return circuits[J]. IEEE Transactions on Power Delivery, 1994, 9(3): 1593-1599.

[112] Dickinson E J, Wain A J. The Butler-Volmer equation in electrochemical theory: Origins, value, and practical application[J]. Journal of Electroanalytical Chemistry, 2020, 872(1): 1-15.

[113] Coles S. An Introduction to Statistical Modeling of Extreme Values[M]. London, U.K.: Springer, 2001: 74-91.

[114] Gilleland E, Katz R W. ExtRemes 2.0: An extreme value analysis package in R[J]. Journal of Statistical Software, 2016, 72(8): 1-39.

[115] Vasyliūnas V M. The largest imaginable magnetic storm[J]. Journal of Atmospheric and Solar-Terrestrial Physics, 2011, 73(11): 1444-1446.

[116] Kelly G S, Viljanen A, Beggan C D, et al. Understanding GIC in the UK and French high-voltage transmission systems during severe magnetic storms[J]. Space Weather, 2017, 15(1): 99-114.

[117] Gjerloev J W. The SuperMAG data processing technique[J]. Journal of Geophysical Research: Space Physics, 2012, 117(1): 1-19.

[118] Radasky W A, Savage E B. Understanding of the geomagnetic storm environment as it impacts the electric power grid[C]//2017 IEEE International Symposium on Electromagnetic Compatibility & Signal/Power Integrity (EMCSI). 2017: 1-43.

[119] Kappenman J G. Storm sudden commencement events and the associated geomagnetically induced current risks to ground-based systems at low-latitude and midlatitude locations[J]. Space Weather, 2003, 1(3): 1-16.

[120] Beggan C D, Beamish D, Richards A, et al. Prediction of extreme geomagnetically induced currents in the UK high-voltage network[J]. Space Weather, 2013, 11(7): 407-419.

[121] Elster C, et al. A guide to Bayesian inference for regression problems[R]. Deliverable of EMRP project NEW04, 2015.

[122] Wagner P R, Nagel J, Marelli S, et al. UQLab user manual – Bayesian inversion for model calibration and validation[R]. UQLab-V1.3-113. Switzerland: ETH Zurich, 2019.

[123] Bishop C. Pattern Recognition and Machine Learning[M]. Cambridge, UK: Springer, 2006.

[124] Goodman J, Weare J. Ensemble samplers with affine invariance[J]. Communications in Applied Mathematics and Computational Science, 2010, 5(1): 65-80.

[125] Martin O. Bayesian Analysis with Python: Introduction to Statistical Modeling and Probabilistic Programming Using PyMC3 and ArviZ[M]. Second. Birmingham, UK: Packt Publishing, 2018.

[126] Dan Y, Zhang Z, Duanmu Z, et al. Segmented sampling least squares algorithm for Green’s function of arbitrary layered soil[J]. IEEE Transactions on Power Delivery, 2021, 36(3): 1482-1490.

[127] Gilbert J L, Radasky W A, Savage E B. A technique for calculating the currents induced by geomagnetic storms on large high voltage power grids[C]//2012 IEEE International Symposium on Electromagnetic Compatibility. 2012: 323-328.

[128] Marti L, Rezaei-Zare A, Boteler D. Calculation of induced electric field during a geomagnetic storm using recursive convolution[J]. IEEE Transactions on Power Delivery, 2014, 29(2): 802-807.

[129] Gustavsen B, Semlyen A. Rational approximation of frequency domain responses by vector fitting[J]. IEEE Transactions on Power Delivery, 1999, 14(3): 1052-1061.

[130] Grivet-Talocia S, Gustavsen B. Time-domain simulation[G]//Passive Macromodeling: Theory and Applications. First. Hoboken, NJ: John Wiley & Sons, 2016: 522-536.

[131] Zheng K. Reaearch on influence factors and modelling methods of geomagnetically induced currents in large power grid[D]. Beijing, China: North China Electric Power University, 2014.

[132] Beamish D. The 1:625k near-surface bedrock electrical conductivity map of the UK[R]. OR/12/037. British Geological Survey, 2012: 23.

[133] Beggan C. Sensitivity of geomagnetically induced currents to varying auroral electrojet and conductivity models[J]. Earth, Planets and Space, 2015, 67(1): 1-12.

[134] Dorfler F, Bullo F. Kron reduction of graphs with applications to electrical networks[J]. IEEE Transactions on Circuits and Systems I: Regular Papers, 2013, 60(1): 150-163.

[135] Birchfield A B, Xu T, Gegner K M, et al. Grid structural characteristics as validation criteria for synthetic networks[J]. IEEE Transactions on Power Systems, 2017, 32(4): 3258-3265.

[136] He J, Zeng R, Gao Y, et al. Seasonal influences on safety of substation grounding system[J]. IEEE Transactions on Power Delivery, 2003, 18(3): 788-795.

[137] Rezaei-Zare A, Etemadi A H. Optimal placement of GIC blocking devices considering equipment thermal limits and power system operation constraints[J]. IEEE Transactions on Power Delivery, 2018, 33(1): 200-208.

[138] Rezaei-Zare A. Behavior of single-phase transformers under geomagnetically induced current conditions[J]. IEEE Transactions on Power Delivery, 2014, 29(2): 916-925.

[139] Rezaei-Zare A. Reactive power loss versus GIC characteristic of single-phase transformers[J]. IEEE Transactions on Power Delivery, 2015, 30(3): 1639-1640.

[140] Boteler D H, Bradley E. On the interaction of power transformers and geomagnetically induced currents[J]. IEEE Transactions on Power Delivery, 2016, 31(5): 2188-2195.

[141] Marelli S, Lüthen N, Sudret B. UQLab user manual – Polynomial chaos expansions[R]. UQLab-V2.0-104. Switzerland: ETH Zurich, 2022.

[142] Memon Z A, Trinchero R, Manfredi P, et al. Machine learning for the uncertainty quantification of power networks[J]. IEEE Letters on Electromagnetic Compatibility Practice and Applications, 2020, 2(4): 138-141.

[143] Manfredi P, Grivet-Talocia S. Fast stochastic surrogate modeling via rational polynomial chaos expansions and principal component analysis[J]. IEEE Access, 2021, 9(1): 102732-102745.

[144] Boteler D, Bui-Van Q, Lemay J. Directional sensitivity to geomagnetically induced currents of the Hydro-Quebec 735 kV power system[J]. IEEE Transactions on Power Delivery, 1994, 9(4): 1963-1971.

[145] Wang B, Fang X, Zhao X, et al. Bi-level optimization for available transfer capability evaluation in deregulated electricity market[J]. Energies, 2015, 8(12): 13344-13360.

[146] Birchfield A B, Gegner K M, Xu T, et al. Statistical considerations in the creation of realistic synthetic power grids for geomagnetic disturbance studies[J]. IEEE Transactions on Power Systems, 2017, 32(2): 1502-1510.

[147] Birchfield A B, Schweitzer E, Athari M H, et al. A metric-based validation process to assess the realism of synthetic power grids[J]. Energies, 2017, 10(8): 1-14.

[148] Paul C R. Incident field excitation of two-conductor line[G]//Analysis of Multiconductor Transmission Lines. Second. Hoboken, NJ: John Wiley & Sons, Inc., 2008: 578-592.

[149] Nucci C, Rachidi F, Rubinstein M. Derivation of telegrapher's equations and field-to-transmission line interaction[G]//Electromagnetic Field Interaction with Transmission Lines: From Classical Theory to HF Radiation Effects. Southampton, UK: WIT Press, 2008: 1-22.

[150] Wang X F, Song Y, Irving M. Load flow analysis[G]//Modern Power Systems Analysis. Boston, MA: Springer US, 2008: 71-128.

[151] Viljanen A, Pulkkinen A, Pirjola R, et al. Recordings of geomagnetically induced currents and a nowcasting service of the Finnish natural gas pipeline system[J]. Space Weather, 2006, 4(10): 1-9.

[152] Gannon J, Leonardi B, Arritt R. Improving conductivity models for geomagnetically induced current (GIC) estimation: Guidance for validation of GIC models[R]. 3002017897. Palo Alto, CA, USA: Electric Power Research Institute, 2020.

[153] Gannon J, Arritt R, Leonardi B. Use of magnetotelluric measurement data to validate/improve existing earth conductivity models[R]. 3002019425. Palo Alto, CA, USA: Electric Power Research Institute, 2020.

[154] Kelbert A, Egbert G, Schultz A. IRIS DMC data services products: EMTF, The magnetotelluric transfer functions[Z]. https://doi.org/10.17611/DP/EMTF.1. Accessed on: Jul. 24, 2021. 2011.

[155] Magnetic Data[Z]. https://geomag.nrcan.gc.ca/. Accessed on: Jun. 9, 2021.

[156] Amidror I. Scattered data interpolation methods for electronic imaging systems: A survey[J]. Journal of Electronic Imaging, 2002, 11(2): 157-176.

[157] Zeng Z, Ding T, Xu Y, et al. Reliability evaluation for integrated power-gas systems with power-to-gas and gas storages[J]. IEEE Transactions on Power Systems, 2020, 35(1): 571-583.

[158] Lehtinen M, Pirjola R J. Currents produced in earthed conductor networks by geomagnetically-induced electric fields[J]. Annales Geophysicae, 1985, 3(1): 479-484.

[159] Pirjola R. Effects of interactions between stations on the calculation of geomagnetically induced currents in an electric power transmission system[J]. Earth, Planets and Space, 2008, 60(7): 743-751.

[160] Pan Z, Zhang L, Wang X, et al. HVDC ground return current modeling in AC systems considering mutual resistances[J]. IEEE Transactions on Power Delivery, 2015, 31(1): 165-173.

[161] Trichtchenko L, Boteler D H. Coupling between power systems and pipelines during geomagnetic disturbances[R]. Open File 7453. Geological Survey of Canada, 2013.

[162] Yong J, Xia B, Yong H, et al. Harmonic voltage induction on pipelines: Measurement results and methods of assessment[J]. IEEE Transactions on Power Delivery, 2018, 33(5): 2170-2179.

[163] Dimitriou A, Charalambous C A. Interpreting coating stress voltages on underground gas pipelines due to lightning strikes on adjacent power lines[C]//2018 34th International Conference on Lightning Protection (ICLP). 2018: 1-7.

[164] Li W, Pan Z, Lu H, et al. Influence of deep earth resistivity on HVDC ground-return currents distribution[J]. IEEE Transactions on Power Delivery, 2017, 32(4): 1844-1851.

[165] Zeng R, He J, Zhang B. Methodology and technology for power system grounding[M]. John Wiley & Sons, 2012.

[166] Takahashi T, Kawase T. Calculation of earth resistance for a deep-driven rod in a multi-layer earth structure[J]. IEEE Transactions on Power Delivery, 1991, 6(2): 608-614.

[167] Zhang B, Zeng R, He J, et al. Numerical analysis of potential distribution between ground electrodes of HVDC system considering the effect of deep earth layers[J]. IET Generation, Transmission & Distribution, 2008, 2(2): 185-191.

[168] Zhang B, Cui X, Li L, et al. Parameter estimation of horizontal multilayer earth by complex image method[J]. IEEE Transactions on Power Delivery, 2005, 20(2): 1394-1401.

[169] Liu Q. Study on the rules of geomagnetically induced currents in power grid based on uncertainty quantification method[D]. Xi'an, China: Xi'an Jiaotong University, 2020.

[170] Liu Z, Li B, Zou J, et al. Research on calculation method of electromagnetic influence on buried metal pipeline networks due to HVDC grounding electrode current[J]. Power System Technology, 2021, 45(4): 1613-1617.

[171] Lee R H W, Shetye K S, Birchfield A B, et al. Using detailed ground modeling to evaluate electric grid impacts of late-time high-altitude electromagnetic pulses (E3 HEMP)[J]. IEEE Transactions on Power Systems, 2019, 34(2): 1549-1557.

Achievements

[1] **Liu MZ**, Xie YZ, Yang YF, Trinchero R, Stievano I S. Reduced nodal admittance matrix method for probabilistic GIC analysis in power grids[J]. IEEE Transactions on Power Systems, 2023, 38(5):4950-4953 (SCI).

[2] **Liu MZ**, Xie YZ, Dong N, Wang ZY, Yang YF. Numerical analysis of nonuniform geoelectric field impacts on geomagnetic induction in pipeline networks[J]. IEEE Transactions on Electromagnetic Compatibility, 2022, 64(4):999-1009 (SCI).

[3] **Liu MZ**, Xie YZ, Chen YH, Trinchero R, Stievano I S. Modeling of induction in integrated power-gas systems due to geomagnetic disturbances[J]. IEEE Transactions on Power Delivery, 2023, 38(6): 3847-3859 (SCI).

[4] **Liu MZ**, Xie YZ, Wu YY, Trinchero R, Stievano I S. A generalized equivalence method for the calculation of low-frequency EMI on pipeline networks considering polarization effect[J]. IEEE Transactions on Power Delivery, 2024, 39(3):1827-1839 (SCI).

[5] **Liu MZ**, Xie YZ, Chen YH, Liu Q. Modeling the 10,000-year geomagnetic disturbance scenarios based on extreme value analysis[J]. IEEE Letters on Electromagnetic Compatibility Practice and Applications, 2020, 2(4):156-160 (Best Student Paper Award of 6th IEEE Global Electromagnetic Compatibility Conference).

[6] Chen YH, Xie YZ, **Liu MZ**, Wang ZY, Liu Q, Qiu AC. Geomagnetically induced current calculation of high voltage power system with long transmission lines using Kriging method[J]. IEEE Transactions on Power Delivery, 2022, 37(1):650-657 (SCI).

[7] Chen YH, Wang XY, **Liu MZ**, Xie YZ. Parameters estimation of horizontal multilayer earth based on Kriging model updating method[J]. Electric Power Systems Research, 2024, 233(1):1-10 (SCI).

[8] Liu Q, Xie YZ, Dong N, Chen YH, **Liu MZ**, Li Q. Uncertainty quantification of geo-magnetically induced currents in UHV power grid[J]. IEEE Transactions on Electromagnetic Compatibility, 2020, 62(1):258-265 (SCI).

[9] Wang ZY, Xie YZ, Chen YH, Dong N, **Liu MZ**. Vulnerability assessment of equipment excited by disturbances for class imbalance problem based on improved kernel density estimation[J]. IEEE Transactions on Electromagnetic Compatibility, 2024, 66(2):382-391 (SCI).

[10] **Liu MZ**, Xie YZ, Wang ZY, Chen YH. Estimation of horizontal multilayer soil parameters using Bayesian inference[J]. IEEE Transactions on Electromagnetic Compatibility (Under Review).